UNIVERSITY OF SOUTHAMPTON

DISTRIBUTED FIBRE SENSING USING MICROWAVE HETERODYNE DETECTION OF SPONTANEOUS BRILLOUIN BACKSCATTER

by Sally M. Maughan

A thesis submitted for the degree of

DOCTOR OF PHILOSOPHY

FACULTY OF ENGINEERING AND APPLIED SCIENCE

DEPARTMENT OF ELECTRONICS AND COMPUTER SCIENCE

SEPTEMBER 2001

UNIVERSITY OF SOUTHAMPTON

ABSTRACT

FACULTY OF ENGINEERING AND APPLIED SCIENCE

DEPARTMENT OF ELECTRONICS AND COMPUTER SCIENCE

Doctor of Philosophy

DISTRIBUTED FIBRE SENSING USING MICROWAVE HETERODYNE DETECTION OF SPONTANEOUS BRILLOUIN BACKSCATTER

by Sally M. Maughan

Brillouin scattering has been used for many years in optical fibre temperature and strain sensing applications, due to the dependence of both the power and the frequency shift of the scattered radiation on these two quantities. Simultaneous temperature and strain sensing is possible if both the power and frequency shift are measured. Much work has been published which presents either power or frequency shift measurements alone. Simultaneous measurement, however, has been less well documented, with all recent cases using direct detection of the backscattered power.

This thesis discusses heterodyne detection of spontaneous Brillouin backscatter, presenting the first simultaneous temperature and strain sensing results using this technique. Microwave beat frequencies of ~11GHz were used, with the use of a high bandwidth (20GHz) detector. Since the approximate value of the Brillouin frequency shift is ~11GHz, the backscatter may be mixed directly with the heterodyne local oscillator, avoiding the need for the complicated optical shifting used in previous heterodyne sensors. The high beat frequency also means that the signal is shifted out of the self-beat noise of the local oscillator and that independent measurement of either Stokes or anti-Stokes Brillouin power is possible.

A 25km microwave distributed heterodyne sensor was constructed with a spatial resolution of 20m, which demonstrated a temperature resolution of <4K and a strain resolution of <100με. Frequency shift measurements alone were also obtained for a 57km sensing length, capable of <2.5K resolution at the distal end of the fibre in the absence of strain. Theoretical modelling of the noise properties of this sensor agreed well with experiment and provided a comparison of the sensor's performance with those of direct detection and low beat frequency heterodyne detection.

As the input pulse power is increased, nonlinear processes ensue, compromising the accuracy of the sensor. These processes were investigated both experimentally and theoretically for a range of input pulse durations, focussing on their effect on Brillouin power and frequency shift measurement.

Acknowledgements

I would like to start by thanking my supervisor, Dr Trevor Newson and co-workers Huai Hoo Kee, Keith De Souza and Gareth Lees for all their help during my time at the Optoelectronics Research Centre. Sincere thanks also go to Arthur Hartog and Peter Wait of York Sensors for useful discussions and feedback as well as to Stuart Russell for all his generous aid and constructive debate, despite working in another research group. I am also in debt to Radiodetection, more specifically to Andrew Lewis, Bob Clarke and Barry Fleury for their refreshing outlook on life and, more helpfully, their sharing nature with regard to electronics know-how.

Mention also goes to Professor Dave Richardson, Dr John Dakin, Shaif-Ul Alam, Carlos Alegria, Ed Austin, Trevor Austin, Gabriele Bonfrate, Daniele Faccio, Grant Harris, Mike Langton, Joe Stefanov and Ed Weatherby and who have all at some point either lent me something or other I have very much needed, given willing advice or completed urgent PAT testing or a fibre rewind without (much) grumbling.

Of course, there are also those who help lift the spirit without directly affecting work. These include many of the above, but also my family and the following: Jude Abanulo, Gabriele Biffi, Gilberto Brambilla, Paul Brown, Alex Cockerill, Cristiana Contardi, Greg Emmerson, Vittoria Finazzi, Alexander Fu, Corin Gawith, Mark Gunning, Oliver Hadeler, Arshad Mairaj, Daniel Milanese, Mamoun Naim, Li Na Ng, Chris Pownall, Carsten Rohde, Dave Sager, Anna Sheridan, Andy Strong, Sam Watts and Joe Zhong and of course all my friends from Cambridge (you know who you are).

Before I run out of space, I would like to thank Reading University's Dr John Macdonald, Dr Sean O'Leary and Professor Alan Lettington, who used to run a superlative MSc Optics course before it was forced to terminate, all of whom have left their mark.

Finally, and most importantly, I extend every gratitude to Pete Houston who has been tireless in his moral support, proof reading, love and exercise of culinary skills and without whom I would certainly not have completed this work, which I dedicate to my grandfather, Thomas Chesterton Page, who died on the 26th February 2001, aged 88.

CONTENTS

Chapter One Introduction 1

Chapter Two Distributed Optical Fibre Sensing: Overview 4

2.1 INTRODUCTION 4
2.2 RAYLEIGH SCATTERING 5
2.2.1 Fibre Loss and the Origins of Rayleigh Scattering 5
2.2.2 Optical Time-Domain Reflectometry (OTDR) 7
2.2.3 Coherent Optical Time-Domain Reflectometry (COTDR) 11
2.2.4 Coherent Rayleigh Noise (CRN) 12
2.2.5 Rayleigh Distributed Temperature Sensors 14
2.3 RAMAN SCATTERING 15
2.3.1 Origins of Raman Scattering 16
2.3.2 Raman DOFS 17
2.4 BRILLOUIN SCATTERING 19
2.4.1 Origins of Brillouin Scattering 19
2.4.2 Brillouin Measurements for Temperature and Strain Sensing 22
2.4.3 Why Use Brillouin Scattering Rather Than Raman? 24
2.4.4 Stimulated Scattering and Nonlinear Effects 25
2.4.4.1 Stimulated Brillouin Scattering and Stimulated Raman Scattering *26*
2.4.4.2 Self-Phase Modulation *30*
2.4.5 Direct Detection of Spontaneous Brillouin Backscatter 31
2.4.5.1 Fabry-Perot Interferometer *32*
2.4.5.2 Mach-Zehnder Interferometer *37*
2.4.5.3 Fibre Bragg Grating *40*
2.4.6 Direct Detection of Stimulated Brillouin Backscatter 41
2.4.7 Coherent Detection of Spontaneous Brillouin Backscatter 43
2.5 THE STATE OF THE ART: SUMMARY 46
2.6 REFERENCES 47

Chapter Three Constituents and Design of a Coherent Brillouin Sensor **54**

3.1 INTRODUCTION 54
3.2 USING A MICROWAVE BEAT FREQUENCY 54
3.3 SOURCE 55
3.3.1 Choice of Source 56
3.4 MODULATOR 57
3.4.1 AOM 57
3.4.2 EOM 59
3.4.3 Choice of Modulator 60
3.5 ERBIUM DOPED FIBRE AMPLIFIER 60
3.5.1 Choice of Pump Laser 63
3.6 DETECTION SYSTEM 64
3.7 HETERODYNE THEORY 66
3.8 POLARISATION EFFECTS 71
3.8.1 Polarisation Scrambler 73

3.9 Brillouin Frequency Shift Dependence on Source Wavelength 78
3.10 The First Sensor 80
3.11 Data processing 82
3.12 Conclusions 85
3.13 References 87

Chapter Four Theoretical Analysis of the Sensor 89

4.1 Introduction 89
4.2 Optical Properties of The Sensing Regimes 89
4.2.1 Sensor Configurations 89
4.2.2 ASE Powers and Spectra 92
4.2.2.1 EDFA 92
4.2.2.2 ASE Filtering in Coherent Detection 95
4.2.2.3 ASE Filtering in Direct Detection 96
4.2.3 Summary 98
4.3 Noise Analysis 101
4.3.1 Detector Specifications and SNR 101
4.3.1.1 Coherent Detection 101
4.3.1.2 Direct Detection 104
4.3.1.3 Summary 105
4.3.2 Noise Components 106
4.3.2.1 Shot Noise and Thermal Noise 106
4.3.2.2 ASE Beat Terms 107
4.3.2.3 Brillouin, Rayleigh and Local Oscillator Self-Beat Terms 110
4.3.2.4 Brillouin, Rayleigh and Local Oscillator Cross-Beat Terms 111
4.3.3 SNR and Noise Comparisons 111
4.4 Frequency Shift and Power Errors 121
4.5 Conclusions 125
4.6 References 127

Chapter Five Temperature and Strain Sensing: Experiments 128

5.1 Introduction 128
5.2 Problems with the First Sensor and Their Solutions 128
5.2.1 Undesirable Heterodyne Peaks 128
5.2.2 Polarisation Noise Due to Incomplete Scrambling 131
5.2.3 The Second Sensor 133
5.3 Initial Measurements over 57km 135
5.4 Temperature Calibration 140
5.4.1 Oven Temperature Stability 140
5.4.2 Frequency Shift Dependence 141
5.4.3 Power Dependence 142
5.5 Noise on the Rayleigh Trace 145
5.6 Multiple Peaks 147
5.7 Linewidth Dependence on Temperature and Fibre Length 149
5.8 Dual Source and the Third Sensor 151
5.9 Strain Calibration of Brillouin Frequency Shift and Power 153
5.10 Simultaneous Temperature and Strain Sensing 156
5.11 Measurement Time Considerations 160

5.12 Scrambler Replacement 160
5.13 Satellite Peaks 163
5.14 Conclusions 164
5.15 References 165

Chapter Six Nonlinear Effects and Threshold Powers 167

6.1 Introduction 167
6.2 Continuous Wave Stimulated Brillouin Scattering 167
6.3 Nonlinear Effects in Coherent Sensing: Theory and Experiment 172
6.3.1 Stimulated Brillouin Scattering 172
6.3.1.1 Theory 172
6.3.1.2 Experiment 173
6.3.2 Stimulated Raman Scattering 174
6.3.2.1 Theory 174
6.3.2.2 Experiment 176
6.3.3 Self Phase Modulation 176
6.3.3.1 Theory 176
6.3.3.2 Experiment 182
6.4 Summary and Conclusions 194
6.5 References 195

Chapter Seven Conclusions 197

7.1 Summary and Conclusions 197
7.2 Future Work 199
7.3 References 201

Appendix A Polarization Scrambling 202

Appendix B Sagnac Loop Mirror 208

Appendix C Full Theoretical Noise Breakdowns 210

List of Publications 217

Glossary

AOM	Acousto-Optic Modulator
ASE	Amplified Spontaneous Emission
ASSR	Anti-Stokes/Stokes Ratio
BOTDA	Brillouin Optical Time-Domain Analysis
COTDR	Coherent Optical Time-Domain Reflectometry
CRN	Coherent Rayleigh Noise
DCOBS	Distributed COherent Brillouin Spectroscopy
DOFS	Distributed Optical Fibre Sensing
DOP	Degree Of Polarisation
EDFA	Erbium-Doped Fibre Amplifier
EMI	ElectroMagnetic Interference
EOM	Electro-Optic Modulator
FBG	Fibre Bragg Grating
FC	Fourier Component
FP	Fabry-Perot interferometer
FSAV	Frequency Shift AVeraging
FSR	Free Spectral Range
FWHM	Full Width at Half Maximum
FWM	Four Wave Mixing
GVD	Group Velocity Dispersion
IF	Intermediate Frequency
LED	Light Emitting Diode
LPF	Low Pass Filter
LPR	Landau Placzek Ratio
LO	Local Oscillator (optical or electrical)
MZ	Mach-Zehnder interferometer
NA	Numerical Aperture
OLO	Optical Local Oscillator
OTDR	Optical Time-Domain Reflectometry
PDL	Polarisation Dependent Loss
PZT	PiezoElectric Transducer
RBW	Resolution BandWidth
RMS	Root Mean Square
SBS	Stimulated Brillouin Scattering
SOP	State Of Polarisation
SNR	Signal to Noise Ratio
SPM	Self-Phase Modulation
SRS	Stimulated Raman Scattering
VBW	Video BandWidth
WDM	Wavelength Division Multiplexor

Chapter One

Introduction

Distributed optical fibre sensing is a versatile technique which allows the spatially continuous measurement of temperature, strain or both, along the length of a single optical fibre. The optical scattering properties of the fibre itself are dependent on the ambient temperature and strain; in such a distributed sensor, it is the scattered light which is detected and analysed. Both the input light and the scattered light are guided along the same (sensing) fibre, so all measurements may be performed at a single location; all that need be in the field is the fibre itself. Since optical fibre is lightweight, flexible and immune to electromagnetic interference (EMI), as well as having a very small cross-sectional area, it is an attractive transducer for many applications; its low heat capacity per unit length makes it a prime candidate for use in temperature sensors. Distributed optical fibre sensors can be used to monitor temperature profiles along power cables and near furnaces; distributed strain measurements would be important in the continuous, preventative, monitoring of large structures, for example: bridges and dams. Sensors with lengths of many kilometres are possible, due to the low optical loss of modern fibres.

Brillouin scattering is the only scattering process in optical fibre which is significantly sensitive to both temperature and strain; both the Brillouin power and its frequency shift are affected, to different degrees, by both. Spontaneous Brillouin backscatter has been optically separated from the dominant Rayleigh component using high-performance interferometers and its power directly measured to high accuracy, for the purpose of temperature sensing. In 1998, a temperature error of 0.9K was demonstrated by Lees et al. for a spatial resolution of 3.5m and a sensing length of 16km (see §2.4.5.2). The Brillouin frequency shift has also been measured, for the purpose of either temperature or strain sensing, using direct detection, heterodyne detection, and Brillouin gain/loss methods. The best frequency shift results have been obtained using heterodyne detection: in 1996, Izumita et al demonstrated a 20με resolution for a spatial resolution of 100m and a sensing length of 30km (see §2.4.7)

by heterodyne detection of spontaneous Brillouin backscatter. To measure temperature and strain simultaneously, both the Brillouin power and frequency shift must be measured. This work discusses the first simultaneous results obtained using heterodyne detection but direct detection techniques yielded, in May 2000, a temperature resolution of 4K for a spatial resolution of 10m and a sensing length of 15km (see §2.4.5.2).

The principal aim of this research was to develop a heterodyne distributed Brillouin fibre sensor capable of simultaneous temperature and strain measurement to ±5K and ±100με over at least 25km, at 20m spatial resolution, surpassing previous achievement. To date, all heterodyne systems have arranged for the Brillouin/optical local oscillator (OLO) beat frequency to lie within the detection bandwidth of a conventional receiver (~100MHz). This was done by deriving both the pulses and the OLO from a single source and optically shifting one component in frequency; the use of two separate sources would result in inherent frequency instability. This research instead focuses on heterodyne sensing at the ~11GHz unshifted beat frequency by using a 20GHz bandwidth detector and a 26GHz rf spectrum analyser, which have only become available relatively recently. This approach serves to simplify the optics and ensure gain flatness over the range of frequency shift change expected (up to 500MHz).

Chapter Two of this work provides an overview of the background to this research. The processes of Rayleigh, Raman and Brillouin scattering within an optical fibre are described as well as their characteristics and suitability for distributed sensing. A review of previous research into sensing techniques is also presented, with particular emphasis being given to Brillouin-based sensors. Sensors based on spontaneous scattering are limited in range or spatial resolution by the onset of nonlinear optical effects for sufficiently large input pulse power or energy. These effects include stimulated Raman scattering (SRS), stimulated Brillouin scattering (SBS) and self-phase modulation (SPM). A brief description and comparison of these phenomena is included in this chapter as an introduction to the nonlinear work presented in Chapter Six.

Chapter Three describes constituent parts and basic theory of the microwave heterodyne sensor. The properties of optical source, coupler, pulse modulator, optical amplifier and detection system are all detailed. Heterodyne theory is discussed and techniques for overcoming persistent noise due to polarisation of the backscattered light are described. The chapter concludes with preliminary traces obtained by the newly constructed sensor and a discussion of potential data processing methods to extract Brillouin frequency shift and power information from the collected data.

Chapter Four provides a detailed theoretical noise analysis of the sensor which consequently allows a comparison of different sensor designs, from both microwave coherent and direct detection regimes. For the coherent detection case, the theoretical behaviour of the noise on the extracted power and frequency shift traces is modelled as a function of the signal-to-noise ratio determined earlier in the chapter. This model allows calculation of expected errors on the power and frequency shift traces, provided that the powers and spectra of all optical signals at the detector are known.

Chapter Five describes temperature and strain sensing results achieved with the new sensor as well as improvements in design. Calibrations of measured Brillouin frequency shift and power with temperature and strain are provided and the results compared to existing values. Measuring frequency shift only, temperature sensing results are presented for fibre lengths of 57km and 27km, followed by simultaneous temperature and strain sensing results for a sensing length of 31km.

Chapter Six describes the action of nonlinear optical effects on the Brillouin spectra, for several pulse durations, as pulse power is increased. Theoretical and experimental results are presented, allowing a threshold power to be estimated for a given pulse duration and sensing length.

Chapter Seven summarises and concludes the work, providing also a brief outline of potential future research in this field.

The work in this thesis consists primarily of the author's own research. Any material from other sources is referenced accordingly.

Chapter Two

Distributed Optical Fibre Sensing: Overview

2.1 Introduction

As mentioned in Chapter One, distributed optical fibre sensing (DOFS) exploits the properties of optical fibre itself to obtain information about a certain required measurand, such as temperature or strain, continuously along the length of the sensing fibre. Optical time-domain reflectometry (OTDR) is the simplest form of DOFS, where the required measurand is the fibre's own loss distribution along its length. OTDR is a diagnostic procedure employed to measure splice or connector losses, for instance, or to locate the position of a suspected break in a long length of fibre. The basic method involves launching a short pulse of light down the fibre under test, via a fibre coupler, then detecting the backscattered Rayleigh signal (§2.2.2). This signal comprises the elastically scattered light which is captured within the numerical aperture of the fibre, in the backward direction, as the pulse propagates and which is subsequently transmitted back through the coupler. The backscatter trace is continuous in time, with each point in time corresponding to a particular distance along the fibre. The time axis may be easily converted into a distance axis by considering the velocity of light within the fibre at the appropriate wavelength.

Rayleigh scattering is an elastic process (i.e. there is no frequency shift on scattering) and is relatively insensitive to changes in temperature. However, the temperature-sensitive processes of both Brillouin and Raman scattering occur in addition to the Rayleigh (and at a much lower power, for spontaneous scattering). Both of these processes are inelastic, three-wave interactions involving the incident wave, the backscattered wave and thermal molecular vibrations within the fibre. These molecular vibrations are described by acoustic phonons for Brillouin scattering and optical phonons for Raman scattering. Since phonon density is, by its very nature, temperature-dependent, Brillouin and Raman scattering may be used as bases for

distributed temperature sensors, provided that their signals are separated from the Rayleigh. Brillouin scattering may also be used to measure distributed tensile strain, due to the dependence of the acoustic velocity on this quantity (§2.4.1).

This chapter will describe in more detail the different scattering mechanisms used in DOFS and review existing experimental techniques for sensor realisation.

2.2 Rayleigh Scattering

2.2.1 Fibre Loss and the Origins of Rayleigh Scattering

Rayleigh scattering is an elastic process caused by randomly-occurring inhomogeneities in the refractive index of the glass on a scale which is much smaller than the wavelength of the propagating light. These inhomogeneities arise from fluctuations in density and composition which are frozen into the glass when it is cooled during fabrication. Improvements to fabrication techniques may reduce but not completely eliminate Rayleigh loss, which is detrimental in optical transmission applications. However, Rayleigh scattering is used advantageously in many areas of DOFS, not only OTDR, commonly to provide a temperature- and strain-invariant reference attenuation distribution.

Rayleigh scattering is characterised by an attenuation coefficient which is proportional to λ^{-4} and is therefore dominant at short wavelengths. This coefficient is given, for radiation of wavelength λ propagating in a single component glass, as [2.1]

$$\gamma_R = \frac{8\pi^3}{3\lambda^4} n^8 p^2 \beta_c K T_F \qquad \{2.1\}$$

where $K = 1.381 \times 10^{-23}$ J K^{-1} is Boltzmann's constant and the other quantities, along with typical values (for silica fibre) are given in Table 2.1, below. The use of these values results in $\gamma_R = 4.56 \times 10^{-5}$ m^{-1} for λ=1550nm, equivalent to 0.197 dBkm^{-1}, a significant fraction of the total fibre loss at this wavelength (~0.2dBkm^{-1}).

Description	Symbol	Value
Fibre refractive index	n	1.46
Average photoelastic coefficient	p	0.286
Fictive temperature	T_F	1950 K
Isothermal compressibility at T_F	β_c	7×10^{-11} m^{2}N^{-1}

Table 2.1 Physical parameters of silica fibre used in Equation {2.1}, taken from [2.1]

This coefficient, γ_R, is related to the Rayleigh contribution, T_R, to the transmissivity of the fibre (in the absence of nonlinear effects) by

$$T_R = \exp(-\gamma_R L) \qquad \{2.2\}$$

where L is the fibre length.

It is informative to observe the contribution which Rayleigh scattering makes to overall fibre loss for a wide range of wavelengths in the near infra-red (where the fibre loss is lowest). A typical overall attenuation spectrum for high purity silica fibre is shown in Figure 2.1, as presented in [2.2]. It can be seen that, discounting the significant peak at 1.4μm caused by hydroxyl group (OH) absorption, Rayleigh scattering is the dominant contributor to fibre loss between 0.8μm and 1.55μm.

Two low-loss 'windows' are exploited in telecommunications. These are located at 1.3μm and 1.55μm and are visible in Figure 2.1 on either side of the 1.4μm OH peak. The 1.3μm band corresponds to the region of zero material dispersion of silica and the 1.55μm band to the lowest fibre loss. These two windows are also used in DOFS to enable longer-range sensors to be built. The 1.55μm band is particularly attractive due to the ease of optical amplification by the use of erbium-doped fibre amplifiers (EDFAs) (§3.5).

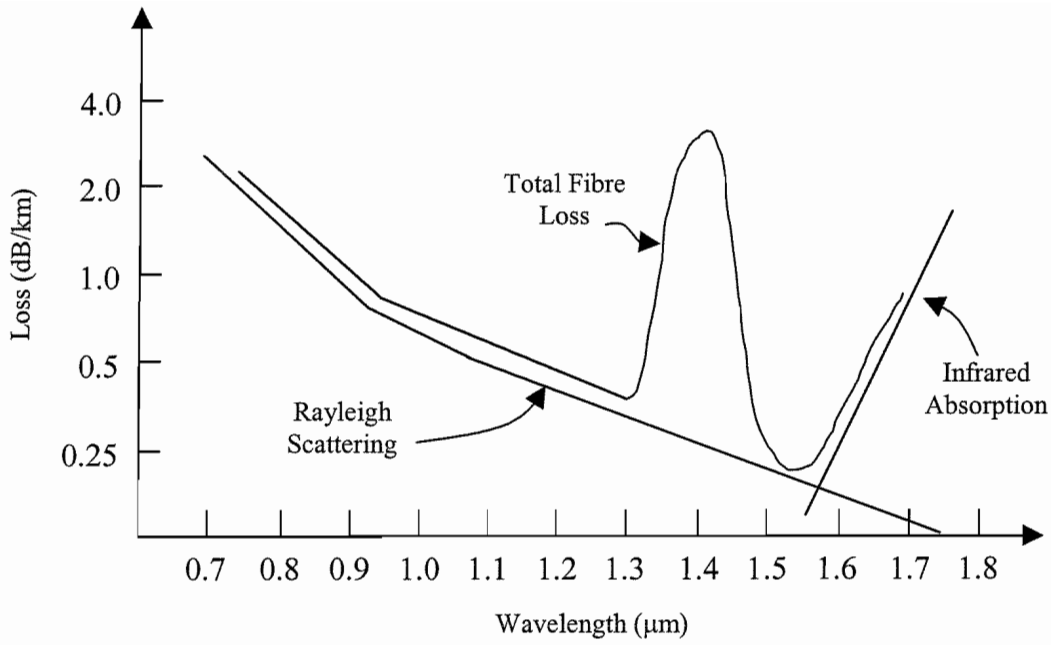

Figure 2.1 Fibre loss spectrum for silica glass [2.2], showing the contributions of Rayleigh scattering and infrared absorption to the total loss. The peak at 1.4μm is due to hydroxyl ion absorption.

2.2.2 Optical Time-Domain Reflectometry (OTDR)

As mentioned previously, optical time-domain reflectometry (OTDR) is the simplest form of DOFS and is used to measure the optical loss distribution along the fibre under test, commonly for the purpose of fault detection. It was first proposed in 1976 by Barnoski and Jensen [2.3]. A basic experimental OTDR arrangement is shown in Figure 2.2.

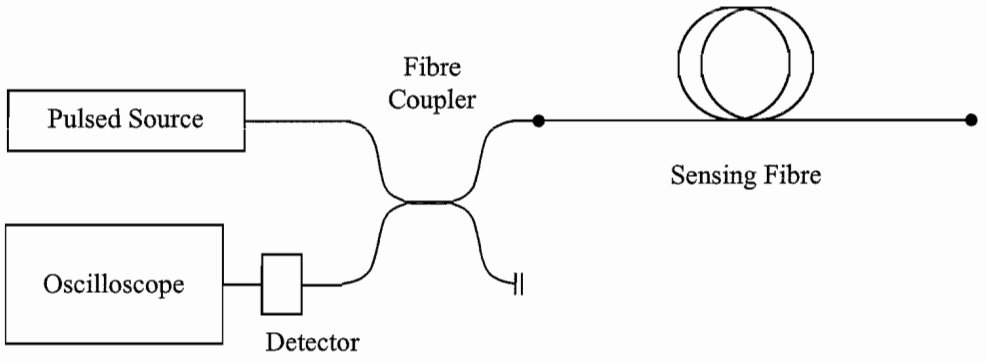

Figure 2.2 Schematic of an OTDR arrangement.

A short pulse of light is launched down the test fibre and the backscattered light is detected as a function of time. The shape of the backscatter trace is a measure of the fibre's optical loss with distance, as is illustrated in Figure 2.3. It can be seen from

this figure that backscatter detection time, t, may be converted to distance along the fibre, x, by use of the equation

$$x = \frac{v_g t}{2} = \frac{c}{2n} t \qquad \{2.3\}$$

if $t = 0$ is set to be the time at which the first backscatter radiation is detected. In this equation, v_g is the group velocity within the fibre, c is the speed of light in vacuo and n is the refractive index of the fibre core.

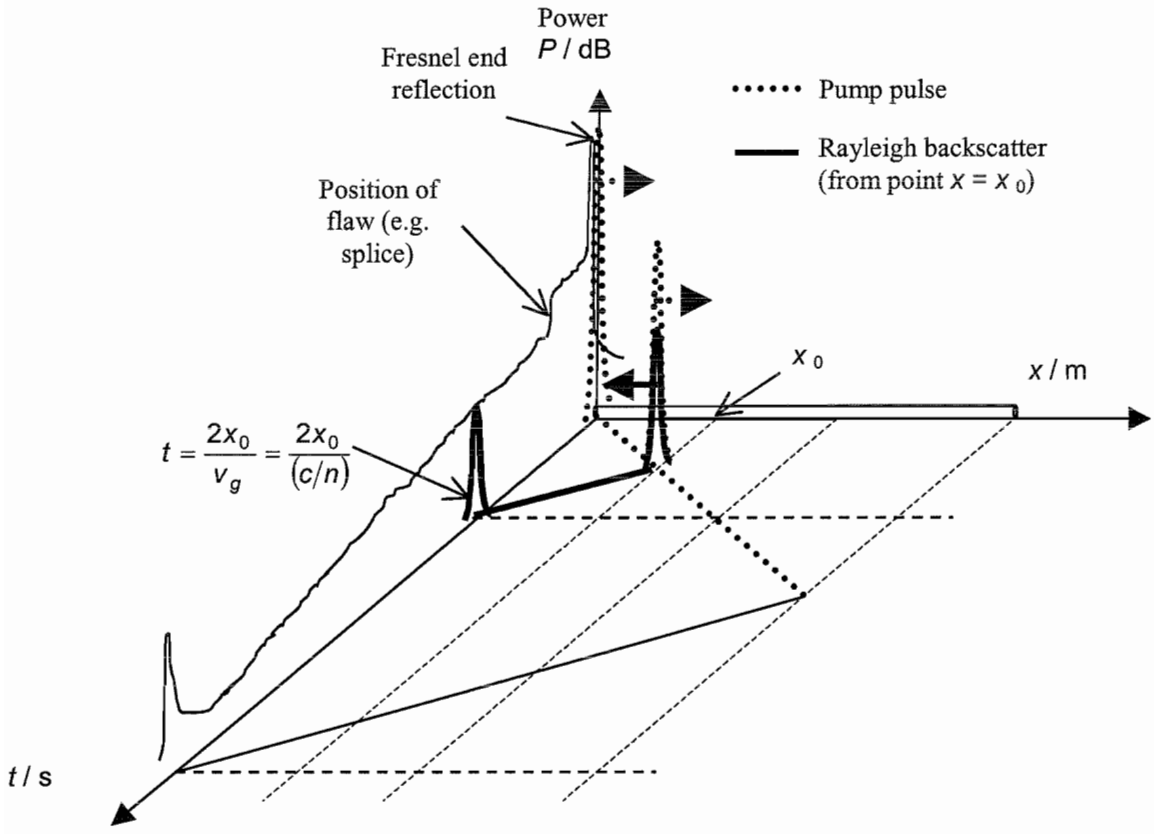

Figure 2.3 Illustration of the relationship between backscatter detection time and scattering position along the sensing fibre.

The backscattered power, P_R, may be described theoretically as a function of time, for an input pulse duration W_0, by the following equation [2.4]

$$P_R(t) = \frac{1}{2} P_i \, S \, \gamma_R \, W_0 \, v_g \exp(-\gamma \, v_g t) = P_R(0) \cdot \exp(-\gamma \, v_g t) \qquad \{2.4\}$$

In this equation, S is the fraction of captured optical power and is defined below (for a step index fibre):

$$S = \frac{(NA)^2}{4n^2} \qquad \{2.5\}$$

Descriptions and typical values of quantities in these equations are given in Table 2.2. The attenuation coefficient, γ, is the measured quantity in OTDR and, from Equation {2.4}, is equal to $1/20^{th}$ of the gradient of a plot of measured Rayleigh backscatter attenuation in dB, $A(t)=10\cdot\log(P_R(t)/P_R(0))$ against distance along the fibre, $x = 0.5v_g t$.

Description	Symbol	Value
Launched pump power / W	P_i	----
Numerical aperture	NA	0.12
Fibre refractive index	n	1.46
Rayleigh scattering coefficient / m^{-1}	γ_R	4.6×10^{-5}
Total attenuation coefficient / m^{-1}	γ	----

Table 2.2 Quantities appearing in Equations {2.4} and {2.5} and sample values (assuming silica fibre and a wavelength of 1.55μm).

Using these values as an example, Equation {2.4} simplifies to

$$P_R(t) = 7.8 \cdot E_P \cdot \exp(-\gamma v_g t) = 7.8 \cdot E_P \cdot \exp(-2\gamma x) \qquad \{2.6\}$$

where $E_P = P_i \cdot W_0$ is the energy of the pulse in Joules. For a pulse of duration 200ns and average power 150mW, this gives $P_R(0)$=230nW. So in this case, even at the near end of the fibre, the Rayleigh signal is 58dB down on the input. Clearly, high optical input powers are needed in order to achieve a detectable signal, particularly for high spatial resolution sensing. Care must be taken, however, not to induce stimulated Raman or Brillouin scattering or other nonlinear effects, e.g. self phase modulation (§2.4.4). An optimum coupling ratio must be found for the maximum pulse power available. For instance, for a very high available pump power, it may be desirable to launch only 5% into the sensing fibre in order to enable detection of 95% of the backscatter signal.

The spatial resolution of an OTDR system is affected by both the input pulse duration and the detection bandwidth. This bandwidth must always be sufficiently large if full benefit is to be gained from the shortness of the pulse. Expressions for the spatial resolution implied by both the pulse width, ΔT, and detector bandwidth, $\Delta\nu$, individually are given below by Δx_{pul} and Δx_{det}, respectively

$$\Delta x_{pul} = \frac{c}{2n} \cdot \Delta T \quad \text{and} \quad \Delta x_{\text{det}} = \frac{c}{2n} \cdot \frac{1}{2\Delta\nu} \qquad \{2.7\}$$

for a flat gain bandwidth with instantaneous cut-off at $\Delta\nu$. For standard silica fibre, $n \approx 1.5$ and these relations simplify to

$$\Delta x_{pul}\ (m) = \frac{\Delta T\ (ns)}{10} \quad \text{and} \quad \Delta x_{\text{det}}\ (m) = \frac{50}{\Delta\nu\ (\text{MHz})} \qquad \{2.8\}$$

For optimum signal to noise Δx_{det} should equal Δx_{pul} and so a pulse length of ΔT requires a detector of bandwidth

$$\Delta\nu\ (\text{MHz}) = \frac{500}{\Delta T\ (ns)} \qquad \{2.9\}$$

Longer wavelength radiation undergoes higher fibre bend loss and so can be used preventatively by allowing early diagnosis of problems. For this reason, sensors operating at 1.6μm have been popular [2.5]. However, 1.55μm sensors have a longer range, since the fibre loss at this wavelength is a minimum.

Broad-band sources, such as light-emitting diodes (LEDs), may be used in OTDR. However, for these larger linewidths, dispersion may become a problem by causing the pulse width to increase and thereby degrading the spatial resolution for more distant parts of the sensing fibre. The main advantage of broad-band sources in OTDR is the absence of coherent Rayleigh noise (§2.2.4) on their backscatter signal.

2.2.3 Coherent Optical Time-Domain Reflectometry (COTDR)

Conventional OTDR may be improved by the use of coherent detection (or heterodyne detection). This technique involves mixing the backscattered signal with an optical local oscillator (OLO) with a fixed frequency difference, $\Delta\nu_{IF}$ (termed the 'intermediate frequency', IF) between the two. A typical COTDR system schematic is illustrated in Figure 2.4.

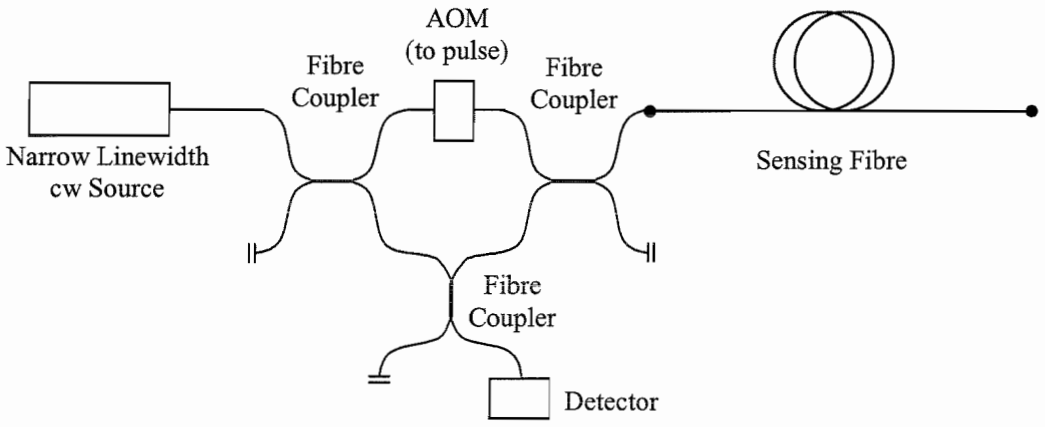

Figure 2.4 Typical COTDR schematic. A frequency shift (IF) is introduced by the pulsing AOM, with the original cw signal acting as LO.

Usually, a single optical source is used to provide both the OLO and the sensing pulses, with the required frequency difference being introduced by the acousto-optic modulator (AOM – §3.4.1) used to form the pulses themselves [2.6]. Optical mixing of the backscatter signal and OLO on the photodetector results in a component, i_S, of the output current, which oscillates at the intermediate frequency $\Delta\nu_{IF}$. This has an amplitude component proportional to $(P_S \cdot P_{LO})^{1/2}$, where P_S is the signal power and P_{LO} is the OLO power. Since P_{LO} is constant, $i_S \propto P_S^{1/2}$. This component of current is then converted to baseband, by first selecting it using an rf bandpass filter (centred at $\Delta\nu_{IF}$) then mixing it with an rf signal at $\Delta\nu_{IF}$ to give the final, DC, output. Alternatively, the signal may be converted to baseband by first mixing with the rf signal at $\Delta\nu_{IF}$ then using a low pass filter to remove high frequency noise.

There are two main advantages of coherent detection over direct measurement of the backscatter signal. The first is that it allows greater dynamic range, since the output current is not proportional to the signal power itself, but to its square root. The second is improved sensitivity, since the low-power backscatter (which would be difficult to detect directly) is effectively amplified by the local oscillator field. This is evident from the fact that $I_S \propto (P_S \cdot P_{LO})^{1/2}$. A disadvantage arises from the requirement that the two interfering frequencies be easily distinguishable, a narrow linewidth source must be used and so coherent Rayleigh noise becomes a problem.

2.2.4 Coherent Rayleigh Noise (CRN)

Coherent Rayleigh noise (or 'fading noise') is a major problem when using a narrow linewidth source in OTDR [2.7]. When using a narrow-band source, with coherence length greater than the pulse length, there is no loss of coherence from start to end of the pulse. As such a pulse propagates down an optical fibre, the detected backscatter signal at any one time is therefore given by the coherent superposition of all the scattered waves reaching the detector, one wave from each scattering centre in the relevant section of fibre. The length of the relevant fibre section will, at all times, be half of that occupied by the optical pulse but its centre will progress down the fibre with time, as the pulse propagates.

Since the scattering centres are randomly situated, the backscattered waves from each centre arrive at the detector with random phase. The waves also arrive with different polarisations, depending on the birefringent properties of the sensing fibre. Standard single-mode fibre has a low birefringence with poorly defined, possibly changing, axes, which means that the state of polarisation is not preserved down the fibre length. The average beat length of such fibre is still as low as ~50m, so the polarisation state of both sensing pulses and backscatter will change on a scale smaller than this. Since both the phase and the polarisation of each wave affects the coherent superposition at the detector, these effects will result in a signal which may be wildly different to the desired incoherent intensity sum. As the scattering fibre section changes with time, so do the phases and polarisations of the scattered waves at the detector and the backscatter trace therefore appears jagged. These fluctuations in backscatter intensity are termed coherent Rayleigh noise (CRN) or 'fading' noise.

CRN is illustrated in Figure 2.5, which shows a OTDR backscatter signal obtained using a 300kHz linewidth laser. Notice the high correlation of the noise in this figure between adjacent traces even though 2048 averages have been taken over a period of ~30s. This evidence supports the fact that conventional signal averaging techniques are not effective in reducing CRN. This is because both the positions of the scattering centres and the birefringent properties of the fibre will change only slowly with time (e.g. due to density/temperature/strain fluctuations).

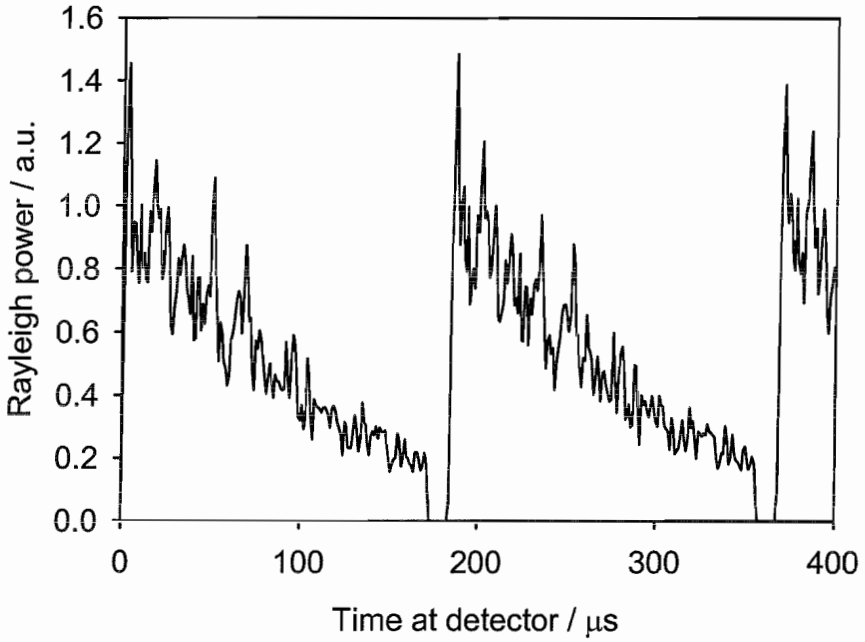

Figure 2.5 Coherent Rayleigh noise visible on the Rayleigh backscatter trace when using a narrow linewidth (300kHz) laser.

In conventional, direct detection, OTDR, CRN may be rendered insignificant by using a sufficiently broad-band source, with a coherence length of much less than the pulse length. A source of wavelength λ with a bandwidth of $\Delta\nu$ (corresponding linewidth $\Delta\lambda$) has a coherence length of

$$L_c = \left|\frac{c}{n \cdot \Delta\nu}\right| = \left|\frac{\lambda^2}{n \cdot \Delta\lambda}\right| \qquad \{2.10\}$$

in a material of refractive index *n*.

Consider an OTDR pulse of duration 100ns, corresponding to a spatial resolution of 10m. From Equation {2.10}, a source of 2nm linewidth has a coherence length of 0.8mm, small compared to the 10m spatial resolution, so the superposition will be incoherent and CRN negligible. A source of bandwidth 1MHz, however, has a coherence length of 200m and will cause significant CRN.

Unfortunately, this method of noise reduction is not possible in heterodyne systems, where the source must necessarily be narrow-band. CRN characteristics, however, are different for independent laser frequencies, so the noise may be considerably reduced by computing the average of many backscatter traces, for each of which the laser is shifted in wavelength. This acts to approximate a broad-band source, which may be said to consist of a continuum of single frequency emitters. This technique is called "frequency shift averaging" (FSAV) and has been investigated, for example, in [2.8]. The amplitude noise has been shown to be inversely proportional to the square root of the number of independent frequencies used [2.6].

Another consideration with heterodyne detection is that the resultant polarisation state of the backscatter affects the heterodyne efficiency, reducing it to zero for orthogonal backscatter and LO polarisations.

2.2.5 Rayleigh Distributed Temperature Sensors

Rayleigh scattering in conventional optical fibres is not significantly temperature dependent so the existence of Rayleigh-based temperature sensors may seem surprising. However, liquid-core fibres do exhibit temperature dependence in their Rayleigh backscatter and so, in the past, distributed fibre temperature sensors have been based on such fibres [2.9].

Unfortunately, there are several problems resulting from their use:

- Expansion and contraction must be catered for, necessitating the use of liquid reservoirs.

- Rapid cooling may result in the formation of voids in the fibre core.
- Any contamination of the liquid would lead to unreliable results.
- The measurable temperature range is restricted by the liquid's freezing and boiling points.
- The numerical aperture of the fibre (which dictates the solid angle over which the backscatter is captured) is also significantly temperature-dependent.

In order to avoid the above-mentioned problems intrinsic to liquid-core fibre temperature sensors, a solid-fibre Rayleigh scattering method has been proposed [2.10]. In sensing fibre with a highly-scattering cladding, the detected Rayleigh backscatter from any location along the fibre will depend upon the total power present in the cladding at that point. Since the refractive index difference between fibre core and cladding is temperature-dependent then so is the fraction of power present in the cladding and therefore, also, the backscattered intensity. A successful field demonstration of this technique was carried out in 1995, when it was used to monitor temperature distributions in power plant machinery and achieved a temperature resolution of ±5K, a spatial resolution of 0.1m and a range of 100m [2.10].

Despite the improvements introduced by the vitreous-core technique, every distributed optical fibre sensor based upon Rayleigh scattering suffers one intrinsic drawback: there is no way to distinguish between those changes in backscatter which arise from temperature fluctuations and those which are caused by intrinsic fibre loss. The Rayleigh backscatter signal is much more profitably used as a temperature-insensitive reference in, for example, Brillouin-based sensors.

2.3 Raman Scattering

The use of Raman scattering results in significantly improved temperature sensing capability compared with Rayleigh techniques; conventional single-mode silica fibre may be used and compensation for intrinsic fibre loss is possible.

2.3.1 Origins of Raman Scattering

Raman scattering in glass [2.11] is a process in which an incident photon is scattered by a molecule within the glass which thereby simultaneously undergoes a transition between two vibrational states and either produces, or absorbs, a phonon. By conservation of energy, a frequency difference must exist between the incident and scattered photons. If a phonon is created during the interaction, the frequency of the photon must decrease on scattering and the scattered radiation is called the "Stokes wave". If a phonon is absorbed, the frequency of the photon increases, resulting in the "anti-Stokes wave". 'Optical' phonons take part in Raman scattering; these are of high energy and so induce large frequency shifts of many THz. In fact, silica, due to its noncrystalline structure, has molecular vibration levels which are spread into bands, resulting in a particularly broad Raman spectrum, with a peak at ~440cm^{-1} (13.2THz at 1.55μm), illustrated in Figure 2.6, as presented in [2.12].

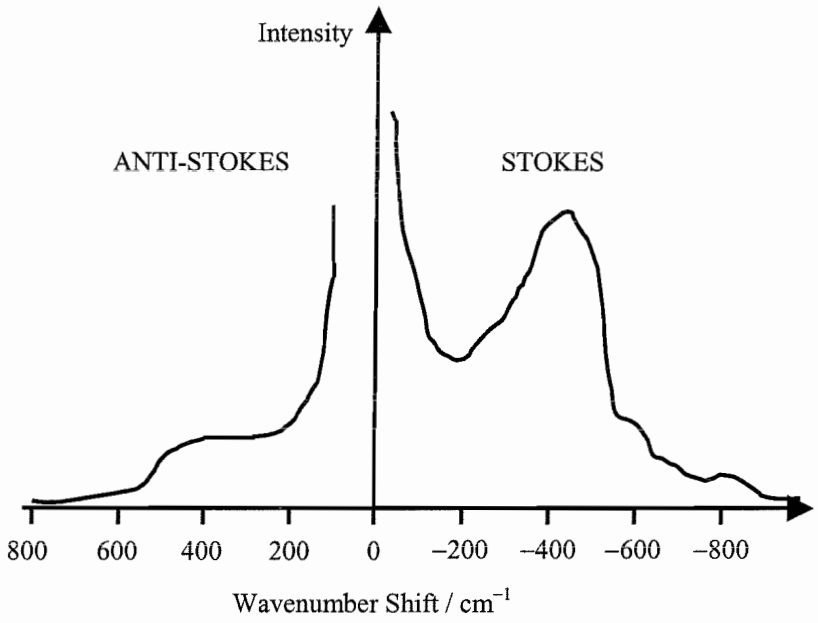

Figure 2.6 Raman spectrum for germanium doped silica glass using a pump wavelength of 514.5nm [2.12].

The principal application of Raman scattering to DOFS is in temperature sensing. The anti-Stokes Raman signal, in particular, is extremely temperature sensitive, due to its intrinsic reliance on the absorption of phonons, which are more prevalent at high temperatures (following the Maxwell-Boltzmann distribution). Consequently, the anti-Stokes signal power is an important quantity in Raman distributed temperature

sensing. However, the ratio of anti-Stokes power to Stokes power is a preferred measurand since it allows determination of absolute temperature (intrinsic fibre losses are cancelled out). This ratio is given by [2.12]

$$R(T) = \frac{P_{AS}}{P_S} = \left(\frac{\lambda_s}{\lambda_a}\right)^4 \exp\left(-\frac{hc}{KT} \cdot \nu^*\right) \qquad \{2.11\}$$

where ν^* is their wavenumber separation from the pump and is given by

$$\nu^* = \frac{\Delta\lambda}{\lambda^2} = \frac{\Delta\nu}{c} \qquad \{2.12\}$$

and λ_s and λ_a are the Stokes and anti-Stokes wavelengths, h = 6.63×10^{-34} Js is Planck's constant, K = 1.381×10^{-23} JK^{-1} is Boltzmann's constant, c is the speed of light in vacuo and T is the absolute temperature.

The percentage change in $R(T)$ for a temperature rise of δT is, from Equation {2.11},

$$100 \cdot \frac{\delta R}{R} = \frac{100hc\nu^*}{KT^2}\delta T \qquad \{2.13\}$$

For $\Delta\nu$=13.2THz ($\Delta\lambda$=106nm) separation from a 1.55μm pump, ν^*=44000 m^{-1} and, from Equation {2.14}, the sensitivity of $R(T)$ to temperature is approximately +0.74%/K for an ambient temperature of 293K.

2.3.2 Raman DOFS

Temperature sensors exploiting spontaneous Raman scattering have been the subject of research since 1985 [2.13], [2.14] and are now commercially available. These sensors commonly use the anti-Stokes/Stokes ratio (ASSR), detailed in §2.2.2, which provides an absolute temperature measurement (intrinsic fibre losses are cancelled out). Alternatively, the anti-Stokes component alone may be used, simplifying the procedure, but requiring careful calibration against known temperatures. Commercial

single-ended Raman-based sensors have reached a temperature accuracy of ±0.5K for 1m spatial resolution and a sensing range of up to 12km (Sensa / York Sensors – current product literature).

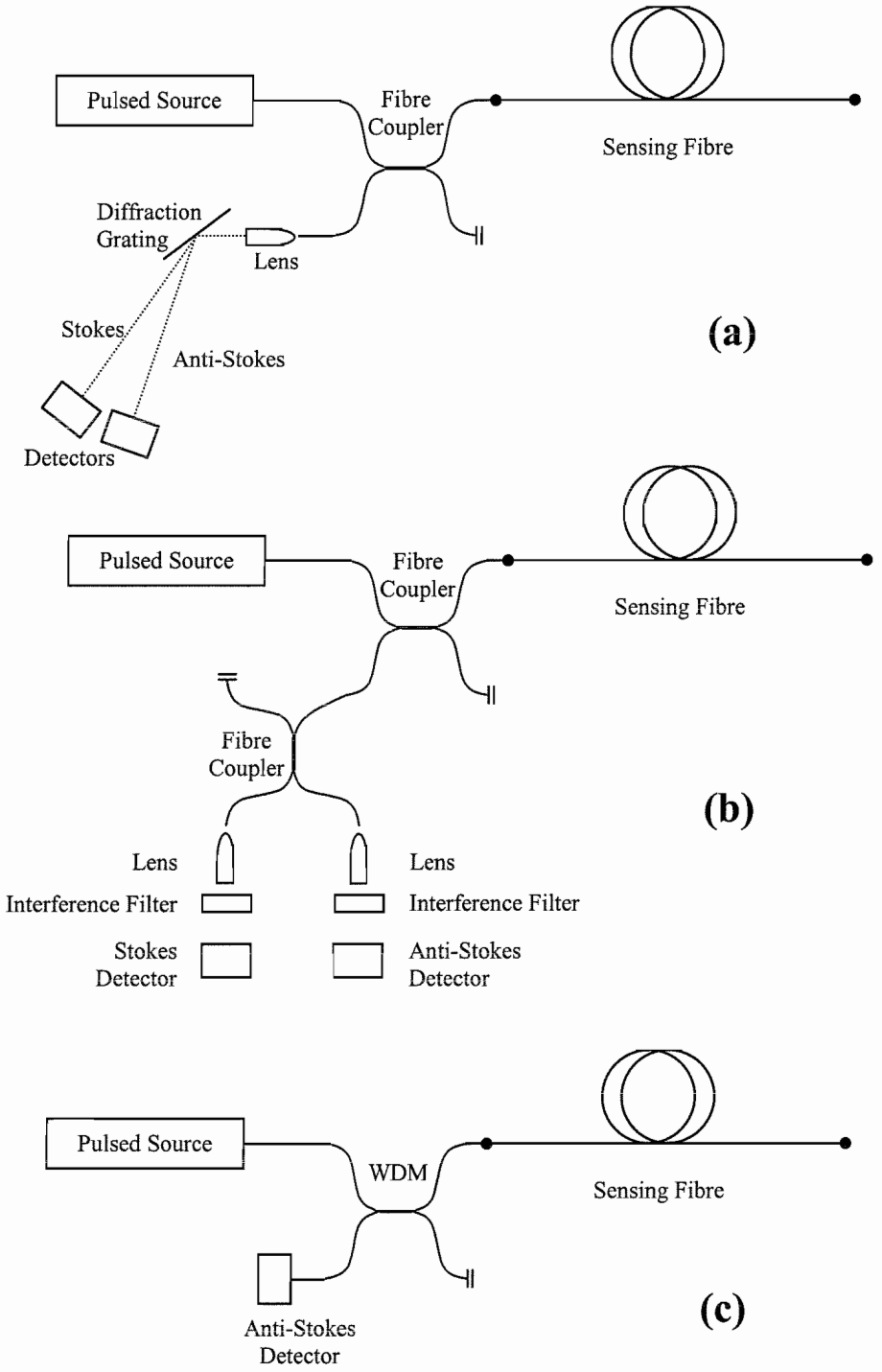

Figure 2.7 Various techniques for isolating the Stokes and/or anti-Stokes Raman signals. These use: (a) a diffraction grating, (b) interference filters and (c) a wavelength division multiplexor (WDM).

In either case, the Raman signal must be separated from the Rayleigh. Due to the large wavelength shift induced by Raman scattering (~100nm), simple methods using diffraction gratings (Figure 2.7a) or interference filters (Figure 2.7b) may be employed in order to isolate the Raman signals. If the anti-Stokes component alone is required, a particularly simple, all-fibre arrangement using a wavelength division multiplexor (WDM) is possible (Figure 2.7c).

The large wavelength shift also causes problems. If both Stokes and anti-Stokes are to be detected, two different time-to-distance scalings must be used, because of significant changes in fibre refractive index due to dispersion. Two different detection clock speeds may be used in order to counteract this problem [2.15]. The fibre losses will also be different at the two wavelengths and must be taken into account before calculating temperatures. Care must be taken not to exceed nonlinear or stimulated scattering thresholds for the pulse width and fibre length used.

2.4 Brillouin Scattering

2.4.1 Origins of Brillouin Scattering

Another type of scattering, first predicted by Brillouin in 1922 [2.16], was first observed in an amorphous, glass-like substance in 1950 by Krishnan when he demonstrated its generation in a specimen of fused quartz [2.17]. Brillouin scattering like Raman scattering, involves an interaction between incident wave, scattered wave and phonons. This time, however, 'acoustic' rather than optical phonons are involved. Acoustic phonons have much lower energies than optical phonons which results in the very small frequency shift characteristic of Brillouin scattering (~11GHz or ~0.086nm at ~1530nm). Again, phonons may either be created or absorbed, resulting in Stokes or anti-Stokes scattered waves. Conservation of energy dictates that

$$\begin{aligned} \nu_P &= \nu_S + \nu_A \\ \nu_P + \nu_A &= \nu_{AS} \end{aligned} \qquad \{2.14\}$$

where ν_P, ν_A, ν_S and ν_{AS} are the frequencies of the pump, acoustic phonon, Stokes wave and anti-Stokes wave, respectively.

Also, conservation of momentum requires that

$$\begin{aligned} \boldsymbol{k}_P &= \boldsymbol{k}_S + \boldsymbol{k}_A \\ \boldsymbol{k}_P + \boldsymbol{k}_A &= \boldsymbol{k}_{AS} \end{aligned} \qquad \{2.15\}$$

where $\boldsymbol{k}_P$, $\boldsymbol{k}_A$, $\boldsymbol{k}_S$ and $\boldsymbol{k}_{AS}$ are the wave vectors of the pump, acoustic phonon, Stokes wave and anti-Stokes wave respectively. This is shown pictorially in Figure 2.8 where, due to the small frequency shifts involved, $|\boldsymbol{k}_S|$ and $|\boldsymbol{k}_{AS}|$ have been set equal to $|\boldsymbol{k}_P|$, reasonable since the three moduli differ only by ~0.01% at 1.55μm.

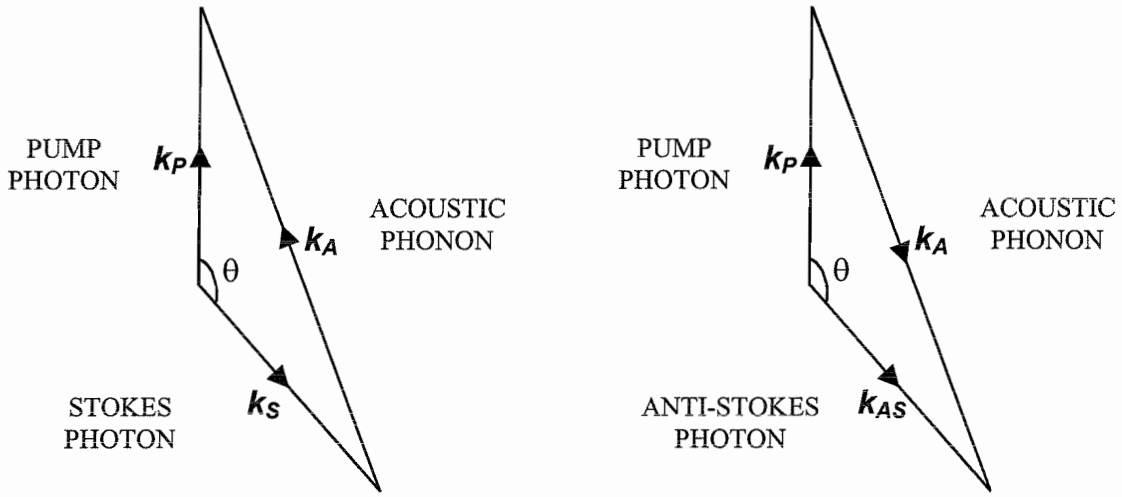

Figure 2.8 Conservation of momentum diagram for Stokes and anti-Stokes Brillouin scattering, with $|\boldsymbol{k}_S| = |\boldsymbol{k}_{AS}| = |\boldsymbol{k}_P|$.

It can be seen geometrically, from Figure 2.8, that for both the Stokes and anti-Stokes cases alike

$$\begin{aligned} |\boldsymbol{k}_A| = \frac{2\pi|\nu_A|}{V_A} = 2|\boldsymbol{k}_P|\sin(\theta/2) = 2\left(\frac{2\pi n}{\lambda_P}\right)\sin(\theta/2) \\ \Rightarrow \ |\nu_A| = \frac{2V_A n}{\lambda_P}\sin(\theta/2) \end{aligned} \qquad \{2.16\}$$

where V_A is the acoustic velocity in the fibre, θ is the angle between the pump and scattered waves, n is the fibre refractive index and λ_P is the pump wavelength in vacuo. From Equation {2.16}, it can be seen that frequency shift, ν_A, reduces to zero in the forward direction and is maximum in the backward direction. Since these two

directions are the only important ones in optical fibre transmission, it follows that Brillouin scattering is a mainly backward process and that its linewidth must be very narrow in order to satisfy conservation of momentum. By setting $\theta = \pi$ in Equation {2.16}, the magnitude of the Brillouin frequency shift is found to be

$$\nu_B = \frac{2V_A n}{\lambda_P} \qquad \{2.17\}$$

A typical spontaneous backscatter spectrum, including the Rayleigh and both Brillouin components, is illustrated in Figure 2.9. The total Brillouin power is typically a factor of ~30 smaller than the Rayleigh power [2.18].

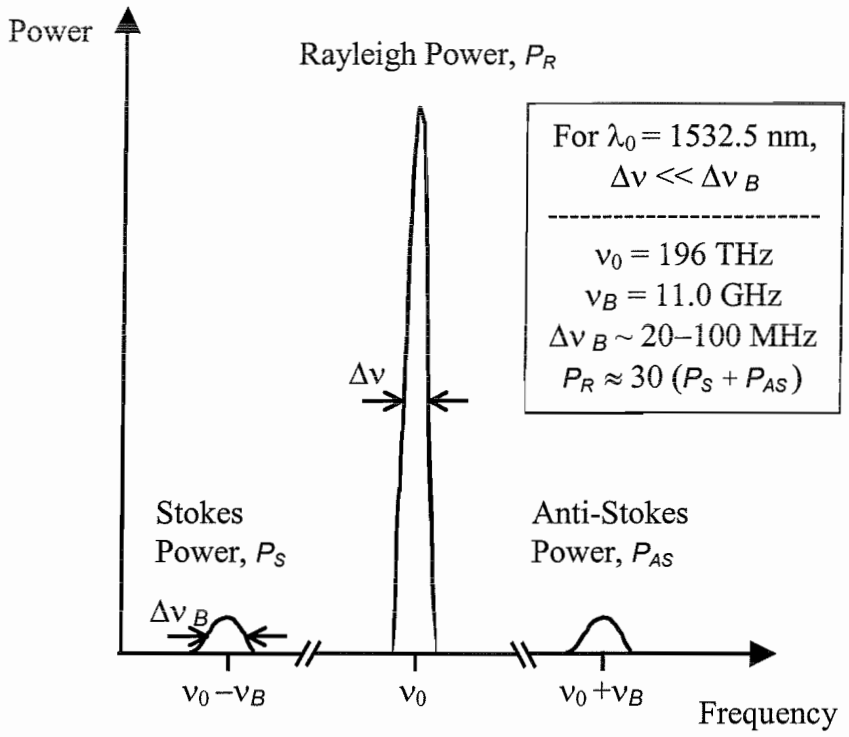

Figure 2.9 Schematic of a combined Brillouin and Rayleigh spectrum (not to scale), with typical values for physical parameters

From Equation {2.17}, it can be seen that, for a given incident wavelength, the Brillouin frequency shift depends solely upon the acoustic velocity and fibre refractive index. In turn, these two quantities are dependent on both intrinsic characteristics (e.g. fibre composition) and environmental factors (such as temperature and strain). The intensities of Brillouin scattered waves are also temperature and strain dependent. Brillouin intensity is given by the formula [2.19]

$$I_B = \frac{I_R T}{T_F(\rho V_A^2 B_T - 1)} \qquad \{2.18\}$$

where I_B and I_R are the Brillouin and Rayleigh intensities, T_F is the fictive temperature of the glass, ρ is the density, B_T is the isothermal compressibility, V_A is the acoustic velocity and T is the absolute temperature. It can be seen in this equation that the Brillouin intensity is explicitly temperature-dependent, but additional temperature and also strain effects also exist via the dependence of the density and acoustic velocity on these quantities. Although relations such as Equation {2.18} exist, it is necessary to undertake experimental calibration of each sensor system to ensure accurate results.

2.4.2 Brillouin Measurements for Temperature and Strain Sensing

Brillouin scattering may be used to measure temperature and/or strain distributions by virtue of their effect on the Brillouin scattered power and frequency shift. If Brillouin power is measured, normalisation is required to account for intrinsic fibre losses: a broad-band Rayleigh OTDR trace is usually used for this purpose. If a system is required to sense temperature and strain simultaneously, both the normalised Brillouin power and the frequency shift must be measured. The following discussion shows how temperature and strain information may be extracted from these measurements.

If the normalised Brillouin power, P_B^{norm}, and the frequency shift, ν_B, vary linearly with temperature, T, and strain, ε, then the following holds

$$\begin{aligned} 100 \times \frac{P_B^{norm}(T(z),\varepsilon(z)) - P_B^{norm}(T_0(z_0),\varepsilon_0(z_0))}{P_B^{norm}(T_0(z_0),\varepsilon_0(z_0))} &= C_{P,T} \cdot [T(z) - T_0(z_0)] + C_{P,\varepsilon} \cdot [\varepsilon(z) - \varepsilon_0(z_0)] \\ \nu_B(T(z),\varepsilon(z)) - \nu_B(T_0(z_0),\varepsilon_0(z_0)) &= C_{\nu,T} \cdot [T(z) - T_0(z_0)] + C_{\nu,\varepsilon} \cdot [\varepsilon(z) - \varepsilon_0(z_0)] \end{aligned} \qquad \{2.19\}$$

where z is the distance down the fibre. $P_B^{norm}(T,\varepsilon)$ and $\nu_B(T,\varepsilon)$ correspond to the distributed sensing measurements and the quantities $P_B^{norm}(T_0,\varepsilon_0)$ and $\nu_B(T_0,\varepsilon_0)$ are reference values determined experimentally for temperature T_0 and strain ε_0 at a distance z_0 along the fibre. The coefficients $C_{P,T}$, $C_{P,\varepsilon}$, $C_{\nu,T}$ and $C_{\nu,\varepsilon}$, are also calibrated experimentally and have been shown to have the expected linear relationship. To

date, the measured values for each coefficient have been within the following ranges, determined or inferred ($\nu_B \propto \lambda^{-1}$) for a pump wavelength of 1.5μm: $C_{P,T} = +0.33 \pm 0.3$ %/K [2.19] [2.20], $C_{P,\varepsilon} = -8 \pm 1\times10^{-4}$ %/με [2.20] [2.21], $C_{\nu,T} = +1.09 \pm 0.08$ MHz/K [2.20] [2.22] and $C_{\nu,\varepsilon} = +0.052 \pm 0.004$ MHz/με [2.20] [2.21] [2.23] [2.24]. The notation in these two equations may be simplified to

$$\begin{aligned} \Delta P_B^{norm} &= C_{P,T}\Delta T + C_{P,\varepsilon}\Delta\varepsilon \\ \Delta\nu_B &= C_{\nu,T}\Delta T + C_{\nu,\varepsilon}\Delta\varepsilon \end{aligned} \qquad \{2.20\}$$

and expressed in matrix form, giving

$$\begin{pmatrix} \Delta P_B^{norm} \\ \Delta\nu_B \end{pmatrix} = \begin{pmatrix} C_{P,T} & C_{P,\varepsilon} \\ C_{\nu,T} & C_{\nu,\varepsilon} \end{pmatrix} \begin{pmatrix} \Delta T \\ \Delta\varepsilon \end{pmatrix} \qquad \{2.21\}$$

If the determinant, $(C_{P,T}\, C_{\nu,\varepsilon} - C_{P,\varepsilon}\, C_{\nu,T})$, of the matrix in this equation is nonzero then its inverse may be found and thereby both temperature and strain determined. Experimentally, $(C_{P,T}\, C_{\nu,\varepsilon})/(C_{P,\varepsilon}\, C_{\nu,T}) \approx -19$ and so the inverse equation

$$\begin{pmatrix} \Delta T \\ \Delta\varepsilon \end{pmatrix} = \frac{1}{\left(C_{P,T}C_{\nu,\varepsilon} - C_{P,\varepsilon}C_{\nu,T}\right)} \begin{pmatrix} C_{\nu,\varepsilon} & -C_{P,\varepsilon} \\ -C_{\nu,T} & C_{P,T} \end{pmatrix} \begin{pmatrix} \Delta P_B^{norm} \\ \Delta\nu_B \end{pmatrix} \qquad \{2.22\}$$

may be used to find ΔT and $\Delta\varepsilon$. Actual values of temperature and strain are then

$$\begin{aligned} T &= T_0 + \Delta T \\ \varepsilon &= \varepsilon_0 + \Delta\varepsilon \end{aligned} \qquad \{2.23\}$$

and their corresponding RMS errors, δT and $\delta\varepsilon$, may be calculated from the measured RMS errors in Brillouin power and frequency shift, $\delta\nu_B$ and δP_B^{norm}, using these equations [2.25]

$$\delta T = \frac{\left|C_{P,\varepsilon}\right|\cdot\delta\nu_B + \left|C_{\nu,\varepsilon}\right|\cdot\delta P_B}{\left|C_{P,T}C_{\nu,\varepsilon} - C_{P,\varepsilon}C_{\nu,T}\right|}, \qquad \delta\varepsilon = \frac{\left|C_{P,T}\right|\cdot\delta\nu_B + \left|C_{\nu,T}\right|\cdot\delta P_B}{\left|C_{P,T}C_{\nu,\varepsilon} - C_{P,\varepsilon}C_{\nu,T}\right|} \qquad \{2.24\}$$

2.4.3 Why Use Brillouin Scattering Rather Than Raman?

There are several advantages of Brillouin scattering over Raman scattering as a basis for a distributed fibre sensor. Perhaps the most fundamental of these is that Brillouin scattering may be used in the measurement of strain as well as temperature, by determining its frequency shift. Indeed, as has been introduced theoretically, simultaneous temperature and strain sensors are possible using Brillouin scattering, whereas Raman scattering is essentially strain-invariant. To aid in a more detailed comparison of the uses of two types of scattering within DOFS, the key properties of Brillouin and Raman scattering are summarised in Table 2.3, and their strain and temperature dependence in Table 2.4.

Quantity (for silica fibre, at 1.55 μm)	**Brillouin**	**Raman**
Gain bandwidth	~ 20-100 MHz	~ 5 THz
Peak gain coefficient	5×10^{-11} m/W	1×10^{-13} m/W
Frequency shift from Rayleigh at peak gain	11 GHz	13 THz
Corresponding free-space wavelength shift	0.09 nm	104 nm
dB weaker than Rayleigh (spontaneous scattering)	~20	~30

Table 2.3 Comparison of Brillouin and Raman scattering characteristics [2.26] [2.27]

Quantity	**Temperature Dependence**	**Strain Dependence**
Brillouin intensity	+0.33% / K	-8×10^{-4} % / με
Brillouin frequency shift	+1.1 MHz / K	+0.05 MHz / με
Raman, Anti-Stokes/Stokes Ratio (ASSR)	+0.8% / K	n/a

Table 2.4 Temperature and tensile strain dependence of Brillouin and Raman scattering [2.19] [2.20] [2.21] [2.22] [2.23] [2.26] [2.27]

It can be seen that the Brillouin frequency shift, at ~11GHz, is much smaller than the Raman, which makes optical isolation of the Brillouin signal more difficult and necessarily requires use of a narrow linewidth source, introducing coherent noise problems. However, the small Brillouin gain bandwidth makes it ideal for electrical

separation in a heterodyne system, rendering careful optical separation unnecessary. Also, the small Brillouin frequency shift means that the incident and Brillouin wavelengths experience almost identical attenuation so, by choosing a 1.55μm source, loss can be kept to a minimum and the range of the sensor increased. Working solely in the 1.55μm band also allows the use of erbium-doped fibre amplifiers (EDFAs) to amplify both pulse and backscatter. With their large wavelength shift, of ~100nm, Raman sensors do not share these advantages and additional problems arise due to the Stokes and anti-Stokes Raman signals having widely different refractive indices. The Brillouin signal is also more than an order of magnitude larger than the Raman, increasing the signal to noise ratio for the same input pulse, allowing improvements in sensor resolution and/or range.

Provided the Brillouin signal can be isolated, either optically or electrically, and any coherent noise counteracted, these advantages strongly outweigh, in many applications, the lower temperature sensitivity (0.33%/K) of Brillouin scattering compared with Raman (0.8%/K).

2.4.4 Stimulated Scattering and Nonlinear Effects

In any distributed optical fibre sensor, there is a threshold of pulse power or energy, above which errors begin to appear in the measurements. This is due to the onset of nonlinear phenomena, which distort the backscattered traces either directly or via changes in the pump depletion and/or spectral profile. There are three main effects which act to limit the launched pulse power/energy: stimulated Brillouin scattering (SBS), stimulated Raman scattering (SRS) and self-phase modulation (SPM). It should be mentioned at this stage, however, that sensors have been constructed which utilise SBS, but these introduce a counterpropagating signal at the Stokes wavelength, rather than an increase in pump power, to induce stimulated scattering (see §2.4.6). In the specific case of a heterodyne sensor performing spontaneous Brillouin spectroscopy, the effect of these nonlinear effects on sensor performance are investigated in detail in Chapter Six.

2.4.4.1 Stimulated Brillouin Scattering and Stimulated Raman Scattering

As pump power is increased, the density of phonons emitted in the Stokes Brillouin interaction increases and the resultant acoustic wave causes the formation of a forward propagating refractive index grating, by the process of electrostriction. This grating, in turn, causes an increase in Stokes Brillouin power due to its increasing Bragg reflectivity (Equation {2.17} is essentially the normal-incidence Bragg equation) and consequent Doppler shifting. Much of the pump power may be transferred in this fashion to the backward-propagating Stokes Brillouin beam for very intense, narrow linewidth radiation [2.28]. This process is termed Stimulated Brillouin Scattering (SBS). Stimulated Raman scattering (SRS) may also occur for high pump powers, with the forward-propagating Stokes Raman signal growing at the expense of the pump. Stimulated scattering of the backward-propagating Stokes Raman is not usually observed since it has a higher threshold than that of stimulated forward scattering [2.11]. The Raman gain may, however, be used to amplify backward propagating signals. Stimulated Brillouin scattering, however, is a purely backward process due to conservation of momentum (§2.4.1).

The threshold for cw stimulated Raman scattering (SRS), defined as the input pump power for which the Stokes power becomes equal to the pump power at the fibre output, is given, approximately, by [2.11]

$$P_{threshold}^{SRS} = \frac{16A_{eff}}{g_R L_{eff}} \qquad \{2.25\}$$

where A_{eff} is the effective core area (mode field area) and g_R is the Raman gain coefficient (Table 2.3). The quantity L_{eff} is the effective interaction length. Due to pump depletion, L_{eff} differs from the actual interaction length, L_{int}, which is the length of fibre for which the pump and Stokes wave overlap. The relationship between the two is

$$L_{eff} = \frac{1}{\alpha_P}\left(1 - \exp(-\alpha_P L_{int})\right) \qquad \{2.26\}$$

where α_P is the pump absorption coefficent ($\sim 5\times10^{-5}$ m^{-1} for silica fibre). This dependence is illustrated in Figure 2.10 which shows that there is a definite upper limit to L_{eff} and so, beyond a certain interaction length, the addition of extra fibre makes very little difference to the threshold.

An equivalent relationship for stimulated Brillouin scattering is given by

$$P_{threshold}^{SBS} = \frac{21A_{eff}}{g_B L_{eff}} \qquad \{2.27\}$$

where g_B is the Brillouin gain coefficient (Table 2.3).

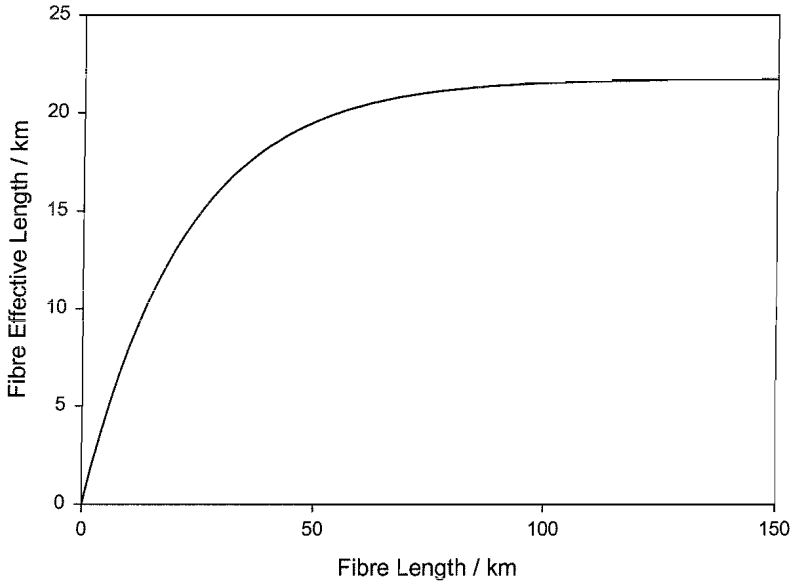

Figure 2.10 Graph showing how effective interaction length varies with actual fibre length. Pump depletion causes the effective length to be less than the actual length and to tend to a constant value for long fibres.

For $A_{eff} = 50\mu m^2$, the SRS and SBS thresholds are simply

$$P_{threshold}^{SRS} = \frac{8000}{L_{eff}} \quad , \quad P_{threshold}^{SBS} = \frac{21}{L_{eff}} \qquad \{2.28\}$$

It would appear from these equations that the Brillouin threshold will always be lower for any given length of fibre and pump wavelength. This is certainly that case for a cw pump, where $L_{int} = L$, the length of the fibre; for L_{eff} near maximum at 21km, the

thresholds for cw SRS and SBS are 381mW and 1mW respectively. For optical pulses, however, L_{int} (and therefore L_{eff}, by Equation {2.26}) is calculated in a different way for each type of scattering.

Owing to the backward-propagating nature of stimulated Brillouin scattering, L_{int} will be half of the fibre length occupied by the pump pulse, or the fibre length itself, whichever is shorter. This means that SBS threshold will increase dramatically for short pulses. In contrast, stimulated Raman scattering is a forward-propagating phenomenon, meaning that the cw interaction length will still be valid for relatively short fibre lengths. With a pulsed input, however, the Raman wave will 'walk off' from the pump after a certain distance, due to the significant difference in dispersion arising from the ~100nm wavelength shift. This 'walk off distance', L_w, after which the Raman and pump pulses are no longer coincident, is given (in km) by [2.26]

$$L_W = \frac{W_0}{D \cdot \Delta\lambda} \qquad \{2.29\}$$

where W_0 is the pulse duration (in ns), $\Delta\lambda$ is the difference in wavelength (~100nm) and D is the fibre's material dispersion parameter (typically 0.02 ns nm^{-1} km^{-1} at 1.5μm [2.29]). For a 20ns pulse, $L_w \approx$10km. The interaction length, L_{int}, will be either the walk off length or the fibre length, whichever is smaller. This means that, for very short pulses, the Raman threshold will be elevated (for a given fibre length, L), but will tend to a steady state value for longer pulses, due to the finite potential interaction length, L. The effective interaction lengths for Raman and Brillouin scattering and the consequent stimulated thresholds are shown as 3-dimensional plots in Figure 2.11. Fibre lengths considered range between 1km and 25km and input optical pulse lengths between 1ns and 400ns.

Figure 2.12(a) shows contour plot of the ratio (expressed in dB) of the SBS to SRS thresholds illustrated in Figure 2.11. This contour plot clearly shows two distinct regions, one where SBS dominates (for longer pulse lengths and shorter fibres) and a second where SRS dominates (for longer fibres and shorter pulse lengths). Figure 2.12(b) shows the equivalent contour plot of actual stimulated scattering threshold, in dBm, defined as the lower of the two SBS and SRS thresholds.

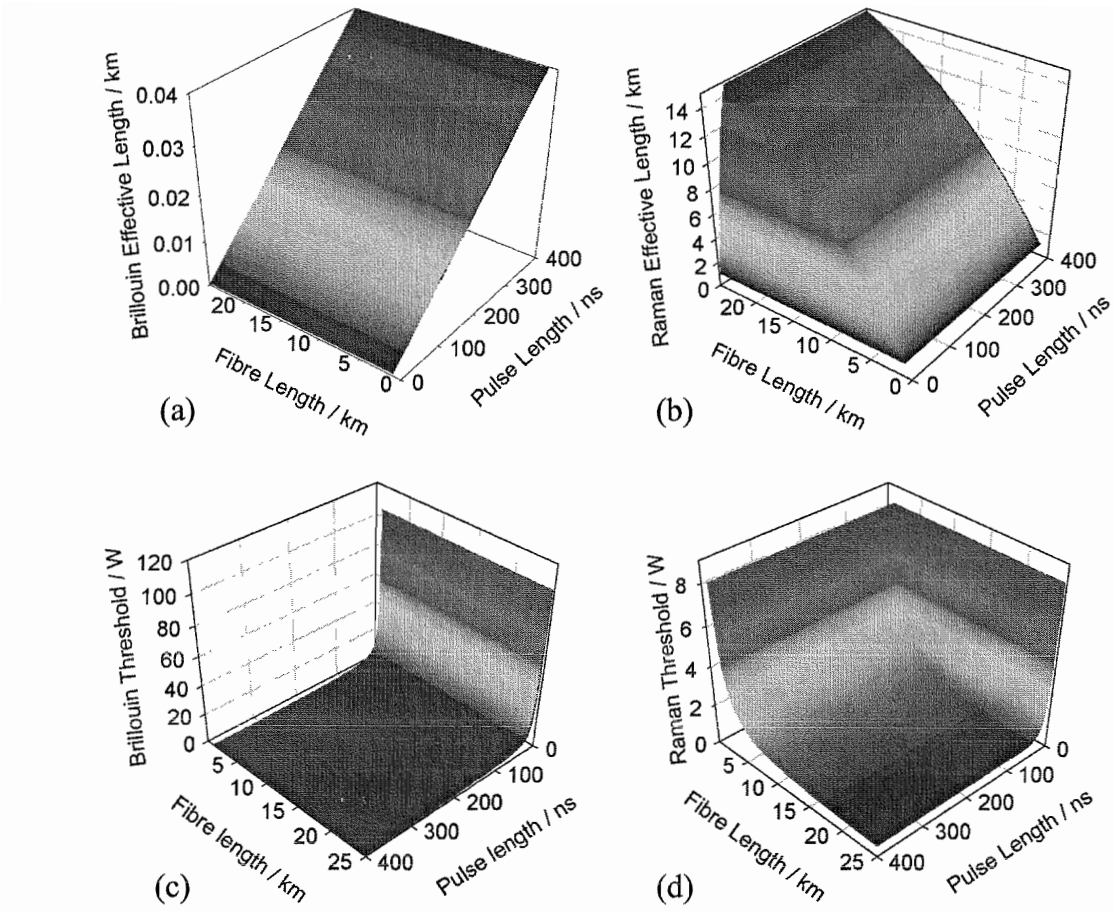

Figure 2.11 Theoretical effective interaction lengths for (a) Brillouin and (b) Raman scattering, along with consequent stimulated (c) Brillouin and (d) Raman scattering thresholds. (Pulse lengths from 1ns to 400ns and fibre lengths from 1km to 25km.)

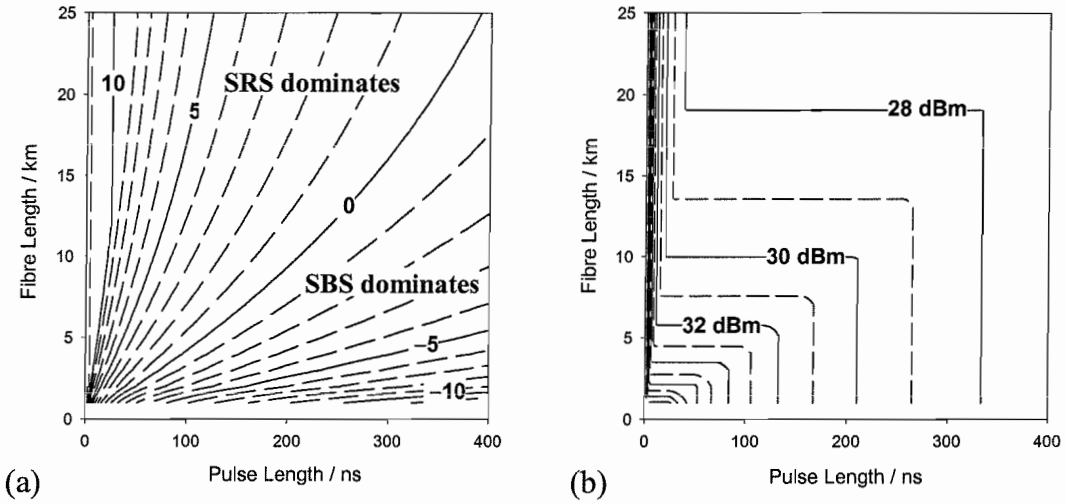

Figure 2.12 (a) Contour plot of ratio of SBS to SRS stimulated scattering thresholds, expressed in dB. (b) Contour plot of stimulated scattering threshold beyond which either SBS or SRS occurs. (Pulse lengths from 1ns to 400ns and fibre lengths from 1km to 25km.)

Finally, before leaving this section, it should be noted that the SBS threshold will increase for sources with linewidths greater than the narrow Brillouin gain bandwidth (between ~20MHz and ~100MHz) and that both the SBS and SRS threshold will increase (by a factor of between 1 and 2) if the polarisation state is not maintained along the fibre [2.11].

2.4.4.2 Self-Phase Modulation

Another nonlinear effect occurring at high pulse powers is self-phase modulation (SPM). This is not a scattering effect, as are SBS and SRS, but instead leads to spectral broadening of the pump pulse. This spectral broadening is due to the significant intensity-dependence of the fibre core refractive index at high powers. The change in refractive index results in an intensity-dependent, and hence time-dependent, phase shift of the light within the fibre. Assuming group velocity dispersion (GVD) to be negligible, this results in a pulse which is unchanged in shape temporally, but widened spectrally: a temporal variation of phase is equivalent to an instantaneous optical frequency variation. GVD is negligible for long, narrow-linewidth pulses and may be estimated, as was the walk-off length for Raman scattering, by considering the material dispersion of the fibre (0.02 ns nm^{-1} km^{-1} at 1.5μm, as mentioned in the previous section).

This effect is important when measurement of the Brillouin frequency shift is to be made since distortion of the spectrum will shift the measured central frequency and hence introduce inaccuracy. In heterodyne detection of the Brillouin spectrum, the frequency spreading and distortion to the lineshape (which is expected to be Lorentzian for a spontaneous signal [2.30][2.31]) is directly visible and may also affect the measurement of Brillouin power.

The frequency distortion is dependent on the input temporal pulse shape. Pulse shapes with higher intrinsic frequency components (steep edges) have greater frequency chirp induced by SPM than smoother pulse shapes. Experimental observations of self-phase modulations are detailed in Chapter Six.

2.4.5 Direct Detection of Spontaneous Brillouin Backscatter

When measuring only temperature, assuming the effects on the Brillouin power due to strain are negligible, knowledge of the frequency shift is not required. From Table 2.4, it can be calculated that a strain of ~400με (0.04%) is required to introduce a temperature error of 1K; the required accuracy in temperature dictates the degree of strain which will be tolerated. Provided the Brillouin signal may be separated from the Rayleigh for the entire range of frequency shifts encountered (due both to temperature and the tolerable small strain changes) the Brillouin power may be directly measured and used as a basis for a calibrated temperature sensor. In fact, the Landau Placzek ratio (LPR), which is the ratio of Rayleigh power to Brillouin power (compensating for intrinsic fibre losses) is a suitable measurand and has been widely used in distributed temperature sensing [2.18] [2.19] [2.32] [2.33].

The linewidth of the source used to measure the Brillouin power must obviously be considerably less than the Brillouin frequency shift (~11GHz), in order to allow separation from the Rayleigh. However, to overcome problems of CRN on the Rayleigh signal, a broad-band pulse is generally used to obtain the Rayleigh trace. To simplify acquisition in such a sensor, a switchable narrow-band/broad-band laser source was built by de Souza et al., using an all-fibre acoustically switched device [2.34]. Although the source linewidth must be narrow for such Brillouin power measurements, it may be much larger than the very narrow linewidths required for accurate Brillouin frequency shift measurement. In practice, sources of 2GHz linewidth have been used successfully.

A typical arrangement for LPR measurement is shown in Figure 2.13. The backscattered radiation from the sensing fibre is split into two arms. One of these is for use with the narrow-band source and separates the Brillouin signal from the Rayleigh. The other enables direct detection of the OTDR signal from the broad-band source.

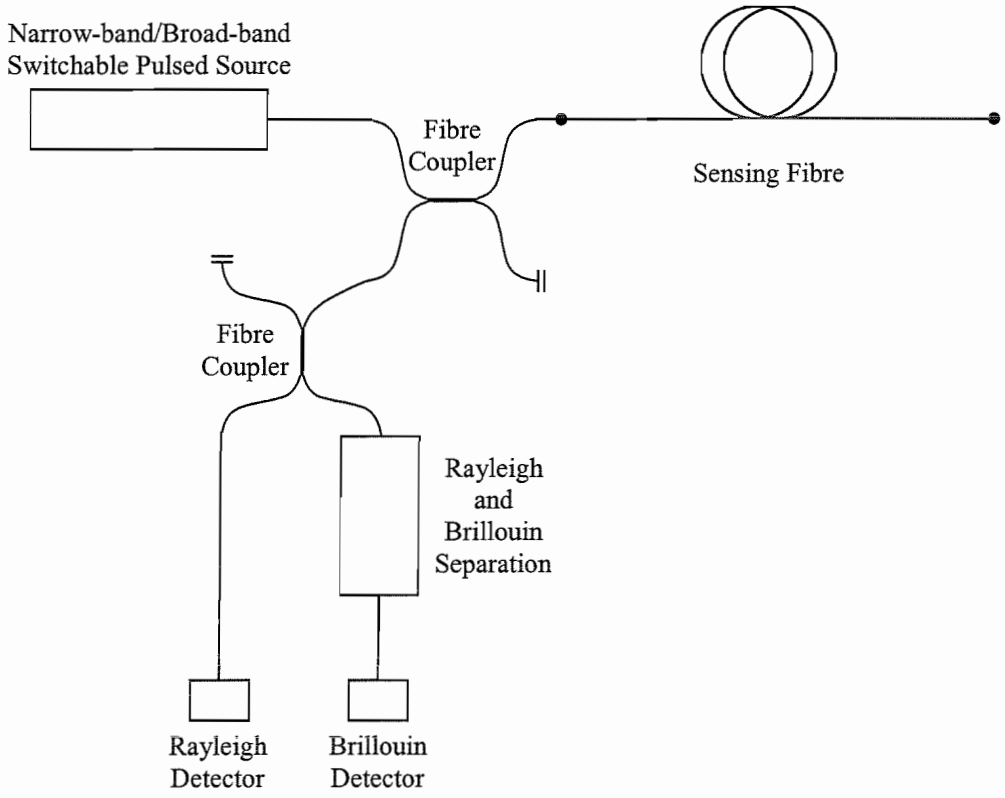

Figure 2.13 Schematic of a Brillouin intensity sensor. A narrow-band source allows isolation of the Brillouin backscatter trace, whereas a broad-band source gives a Rayleigh trace devoid of coherent noise.

Since the frequency shift is so small, a stable optical interferometer or fibre Bragg grating (FBG) must be used to separate the Brillouin from the Rayleigh. Two suitable interferometers are the Fabry-Perot and Mach-Zehnder. It is possible to use these interferometers to obtain frequency shift information as well as power information in order to create a simultaneous strain and temperature sensor. The use in DOFS of these two interferometers, as well as the FBG, will now be discussed.

2.4.5.1 Fabry-Perot Interferometer

The Fabry-Perot (FP) interferometer is, in essence, a pair of parallel, semi-silvered, optical flats, one of which may be moved in order to vary their separation. Radiation entering the interferometer is reflected back and forth many times between the two mirrors. A schematic FP layout is shown in Figure 2.14. Radiation from the input fibre is collimated by a lens and enters the cavity; the emitted radiation is then focussed onto a detector.

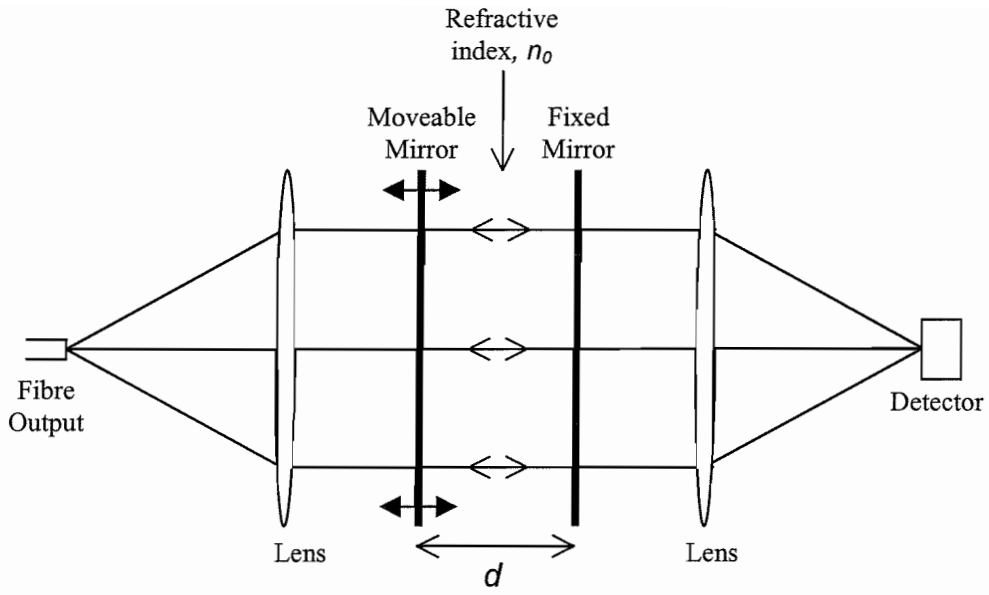

Figure 2.14 Fabry-Perot interferometer schematic.

The interferometer has a different transmissivity for each incident frequency of light, due to the different degrees of phase matching, at the interferometer output, between successive reflections. This frequency-dependent phase difference is given by

$$\Delta\phi(\nu) = k \cdot 2d = \frac{2\pi n_0 \nu}{c} \cdot 2d \qquad \{2.30\}$$

where d is the mirror separation, n_0 is the intercavity refractive index, ν is the input frequency and c is the speed of light in vacuo. If $\Delta\phi=2\pi m$, all reflections are in phase but if $\Delta\phi=2\pi(m+1)$, alternate reflections are out of phase. The reflectivity, R, of the mirrors affects the amplitudes of successive reflections. Taking both phase and amplitude changes into account, the complex amplitude transfer function, $A(\nu)$, of the interferometer may be calculated by summing all the reflected components at the interferometer output. This transfer function is given by

$$A(\nu) = \sqrt{T} \cdot e^{i\frac{\Delta\phi}{2}} \cdot \left(\sum_{j=0}^{\infty} \left(\sqrt{R}^2 e^{i\Delta\phi} \right)^j \right) \cdot \sqrt{T} = T \cdot e^{i\frac{\Delta\phi}{2}} \cdot \left(\sum_{j=0}^{\infty} \left(R\, e^{i\Delta\phi} \right)^j \right) \qquad \{2.31\}$$

where T is the energy transmissivity of each mirror, R is the energy reflectance of each mirror and j is an integer representing the order of the reflected component.

The sum within this equation is a geometric progression with common ratio $R\,e^{i\Delta\phi}$ and therefore the equation evaluates to

$$A(\nu) = T \cdot e^{i\frac{\Delta\phi}{2}} \cdot \left(\frac{1}{1 - R\,e^{i\Delta\phi}} \right) \qquad \{2.32\}$$

which is valid for all $|R| < 1$. (However it can be seen that, for the case of $R = 1$, no radiation will ever enter the cavity and so none will be detected.) The intensity transfer function, $X(\nu)=A(\nu)A^{*}(\nu)$, is then

$$X(\nu) = \frac{T^2}{1 + R^2 - 2R\cos(\Delta\phi)} \qquad \{2.33\}$$

Assuming that $T = 1 - R$, i.e. no absorption, and using Equation {2.30}, $X(\nu)$ becomes

$$X(\nu) = \frac{1}{1 + \frac{4R}{(1-R)^2}\sin^2\left(\frac{2\pi n_0 d}{c} \cdot (\nu - \nu_0) \right)} \qquad \{2.34\}$$

if a suitable reference frequency, ν_0, is chosen (such that $2\pi n_0 d\nu_0 / c = m\pi$, where m is an integer) to shift the centre of the periodic transfer function from 0Hz to the relevant ~200THz, near-infrared region. This transfer function is illustrated in Figure 2.15 for several different mirror reflectivities. It can be seen that equally spaced peaks appear in the transfer function, occurring at frequencies $\nu_{max} = \nu_0 + mc/(2n_0 d)$, with m again an integer. The spacing between them is known as the 'free spectral range', or FSR, of the interferometer and given by

$$\Delta\nu_{FSR} = \frac{c}{2n_0 d} \qquad \{2.35\}$$

Theoretically, each maximum frequency will always have $X(\nu_{max}) = 1$. If the separation of the FP mirrors is chosen such that the FSR of the FP is ~22GHz (i.e. d = 6.8mm, for an air-filled cavity) then the Stokes and anti-Stokes Brillouin signals may be placed at adjacent peaks of the transfer function by fine tuning of the cavity length.

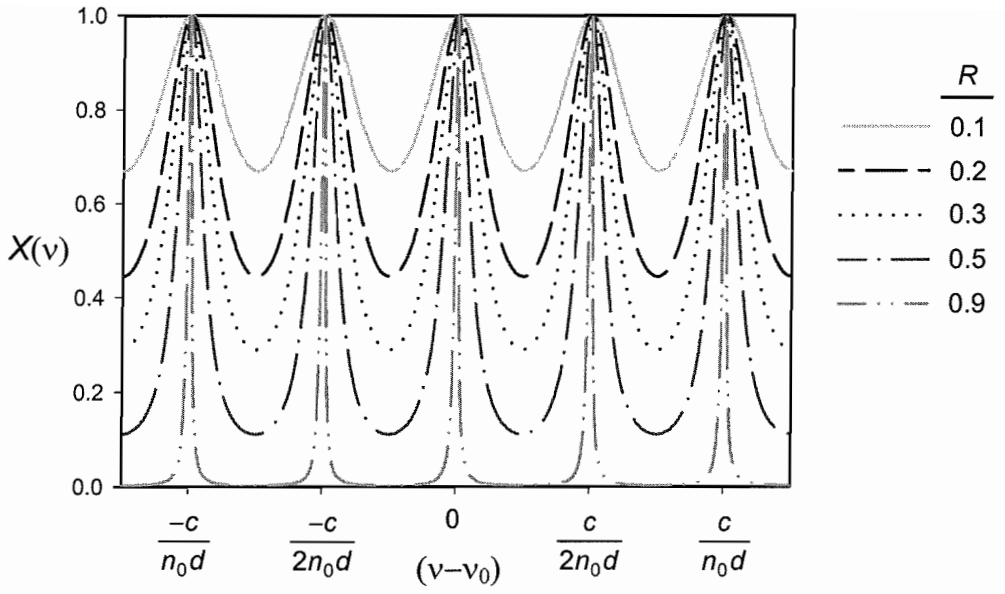

Figure 2.15 Transfer function of the ideal, lossless, Fabry-Perot interferometer, for mirror reflectivities of 0.1, 0.2, 0.3, 0.5 and 0.9, where ν_0 is such that it lies at a peak and shifts the transfer function to the wavelength/frequency range of interest.

The Rayleigh frequency will then coincide with the intervening minimum and be attenuated. From Equation {2.34}, these minima have an intensity transmission of

$$X(\nu_{min}) = \frac{1}{1+\frac{4R}{(1-R)^2}} \qquad \{2.36\}$$

and it can be seen that the degree of attenuation depends solely on mirror reflectivity: the higher the reflectivity the better the Rayleigh rejection. The transfer function and hence the minimum transmissivity may be expressed in terms of a property of the cavity called the 'finesse', $\Im$. This is defined as the FSR divided by the full width half maximum (FWHM) of each fringe of the transfer function and is calculated to be

$$\Im = \frac{\pi\sqrt{R}}{1-R} \qquad \{2.37\}$$

and so, from Equations {2.34} and {2.35}, the transfer function is

$$X(\nu) = \frac{1}{1+\frac{4\Im^2}{\pi^2}\sin^2\left(\frac{\pi\cdot(\nu-\nu_0)}{\Delta\nu_{FSR}}\right)} \qquad \{2.38\}$$

Although the maximum theoretical value of the lossless FP transfer function, which is independent of mirror reflectivity, is always unity, imperfect free-space coupling, diffraction effects and mirror absorption all contribute to the high loss (~10dB) of Fabry-Perot interferometers in Brillouin sensing. Also, the finite signal linewidth may cause problems. For a desired Rayleigh attenuation of 36dB, a finesse of 100 ($R \approx 0.97$) is required, resulting in a fringe FWHM of 220MHz for an FSR of 22GHz. This small FWHM may possibly result in the rejection of some of the signal, depending on the source linewidth, increasing the loss and also the effective Rayleigh attenuation. However, very high finesse Fabry-Perot cavities may be used in simultaneous strain and temperature sensors, in which distributed Brillouin spectroscopy is performed by piezoelectric control of the moveable mirror, and where selective rejection is part of the technique [2.35]. Another problem with the use of FP interferometers arises from the time-dependence of the backscatter signal. The preceding analysis assumes a cw input, such that all the reflected orders are present in the superposition. However, if the backscatter changes rapidly, not all of the reflected components arriving at the detector at the same time will arise from input backscatter of the same characteristics and so the results will be flawed.

Of course, since the stop-bands of a high finesse FP are broad, it is not necessary for both Stokes and anti-Stokes frequencies to lie on a peak: either may be chosen and the sensor will be effective provided only that the Rayleigh rejection is adequate. In 1996, measuring anti-Stokes power alone (FSR=50GHz), Wait and Newson achieved a temperature error of 1.5°C for a sensing length of 12.9km and a spatial resolution of 130m [2.33]. Later, in 1997, a simultaneous temperature and strain sensor based on FP Brillouin spectroscopy was demonstrated by Parker et al. [2.35]. This sensor exhibited errors in temperature and strain of 4K and 100με respectively, for a sensing length of 1.2km and a spatial resolution of 40m.

The Mach-Zehnder interferometer, an all-fibre arrangement which is not based on a multi-reflection cavity, overcomes most of these problems and exhibits a low insertion loss.

2.4.5.2 Mach-Zehnder Interferometer

The fibre Mach-Zehnder (MZ) interferometer comprises two 50/50 fibre couplers spliced together, as in Figure 2.16, such that there is a difference in length, Δx, between the two connecting paths. If the backscatter signal, containing both Rayleigh and Brillouin wavelengths is launched into one port of the MZ and if the path difference is appropriate, the Brillouin and Rayleigh signals will emerge from different output ports.

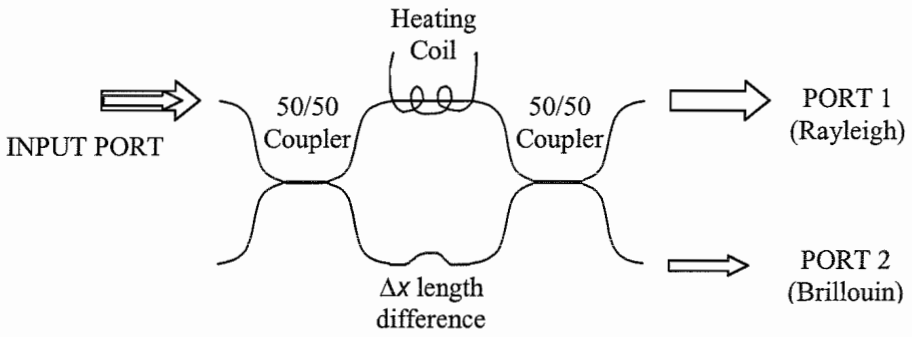

Figure 2.16 Schematic of a fibre Mach-Zehnder interferometric optical filter. The backscattered signal is launched into the input port. The Rayleigh and Brillouin are separated and appear at different output ports. A heating coil is used, with feedback, to stabilise the path difference.

Intensity transfer functions $X^{(1)}(\nu)$ and $X^{(2)}(\nu)$, from the input port to output ports 1 and 2 respectively may be calculated by considering evolution of the complex amplitude through the system. It is well known [2.36] that the cross-coupled wave in a fibre coupler exhibits a $\pi/2$ phase shift, whereas the transmitted wave is not phase shifted. This relative phase shift is in fact a requirement for conservation of energy. Thus, for the MZ illustrated in Figure 2.16 (but with an arbitrary coupling ratio, α) the complex amplitude transfer functions may be calculated as

$$\begin{aligned} A^{(1)}(\nu) &= i\sqrt{1-\alpha}\cdot\exp(i2\pi n\Delta x\nu/c)\cdot i\sqrt{1-\alpha} + \sqrt{\alpha}^{2} \\ A^{(2)}(\nu) &= i\sqrt{1-\alpha}\cdot\exp(i2\pi n\Delta x\nu/c)\cdot\sqrt{\alpha} + \sqrt{\alpha}\cdot i\sqrt{1-\alpha} \end{aligned} \qquad \{2.39\}$$

where n is the fibre refractive index and c is the speed of light in vacuo and common phase differences are ignored.

Since $X(\nu)=A(\nu)A^{*}(\nu)$, the intensity transfer functions are expressed as

$$\begin{aligned} X^{(1)}(\nu) &= \left[\alpha-(1-\alpha)\cdot\exp(i2\pi n\Delta x\nu/c)\right]\cdot\left[\alpha-(1-\alpha)\cdot\exp(-i2\pi n\Delta x\nu/c)\right] \\ &= 2\alpha(1-\alpha)\cdot\left(\frac{1-2\alpha(1-\alpha)}{2\alpha(1-\alpha)}-\cos(2\pi n\Delta x\nu/c)\right) \\ X^{(2)}(\nu) &= \left[i\sqrt{\alpha(1-\alpha)}\cdot(1+\exp(i2\pi n\Delta x\nu/c))\right]\cdot\left[-i\sqrt{\alpha(1-\alpha)}\cdot(1+\exp(-i2\pi n\Delta x\nu/c))\right] \\ &= 2\alpha(1-\alpha)\cdot(1+\cos(2\pi n\Delta x\nu/c)) \end{aligned} \quad \{2.40\}$$

and so, for an ideal MZ ($\alpha = 0.5$), the transfer functions (shown in Figure 2.17) are

$$\begin{aligned} X^{(1)}(\nu) &= \tfrac{1}{2}\left[1-\cos\left(\frac{2\pi(\nu-\nu_0)}{\Delta\nu_{FSR}}\right)\right] \\ X^{(2)}(\nu) &= \tfrac{1}{2}\left[1+\cos\left(\frac{2\pi(\nu-\nu_0)}{\Delta\nu_{FSR}}\right)\right] \end{aligned} \quad \{2.41\}$$

where $\Delta\nu_{FSR} = c/(n\Delta x)$ is the free spectral range of the MZ, i.e. the period of each transfer function, and ν_0 is arranged such that it lies at a peak of $X^{(2)}$.

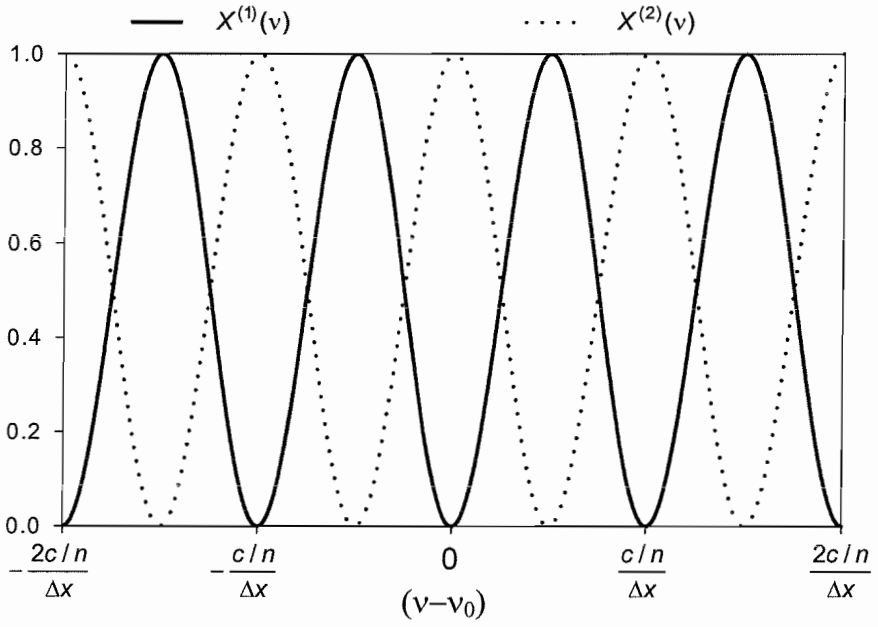

Figure 2.17 Transfer functions $X^{(1)}(\nu)$ and $X^{(2)}(\nu)$ into each output port of the ideal Mach-Zehnder interferometer, where ν_0 is such that it lies at a peak of $X^{(2)}$ and shifts the transfer function to the wavelength/frequency range of interest.

For a Brillouin frequency shift of 11GHz, the Rayleigh and Brillouin may be separated if $\Delta\nu_{FSR}$=22GHz (i.e. $\Delta x \approx$ 9mm) since, with suitable fine-tuning of the path difference, the Stokes and anti-Stokes frequencies (ν_S and ν_{AS} respectively) may be made to lie on successive peaks of $X^{(2)}(\nu)$. When this happens, $X^{(2)}(\nu_S)=X^{(2)}(\nu_{AS})=1$ and $X^{(2)}(\nu_R)=0$ (ν_R is the Rayleigh frequency), whereas $X^{(1)}(\nu_S)=X^{(1)}(\nu_{AS})=0$ and $X^{(1)}(\nu_R)=1$ and so the separation is theoretically perfect (ignoring linewidth considerations). The fine-tuning condition is

$$\Delta x = m \cdot \frac{\lambda_S}{n} \qquad \{2.42\}$$

which means that careful stabilisation of Δx is required to within a fraction of a wavelength. A heating coil is often used for this purpose.

In practice, a finite source linewidth affects the Rayleigh rejection. For example, a 2GHz linewidth Q-switched laser source, the signal is still at half power 1GHz away from the central frequency. Whilst the central frequency, ν_0, is completely rejected, the attenuation of the Rayleigh at ν_0+1GHz is only 14dB (from Equation {2.41}) for an FSR of 22GHz. Care must also be taken to ensure that there is not any significant difference in birefringence-induced polarisation change within the two arms, so that complete interference will take place at the output ports. In 1996, de Souza et al. [2.32] achieved a spatial resolution of 40m for a sensing length of 12.9km with a temperature error of 2.9K.

In order to achieve improved separation, a double pass Mach-Zehnder arrangement [2.37] may be used (as introduced by de Souza et al. [2.38]), where the Brillouin makes two passes of the interferometer, as in Figure 2.18. By 1998, Lees et al. had improved sensor performance, by use of a double-pass MZ and a 2GHz linewidth Q-switched laser source, to achieve a temperature error of only 0.9K for a spatial resolution of 3.5m and a sensing length of 16km [2.39].

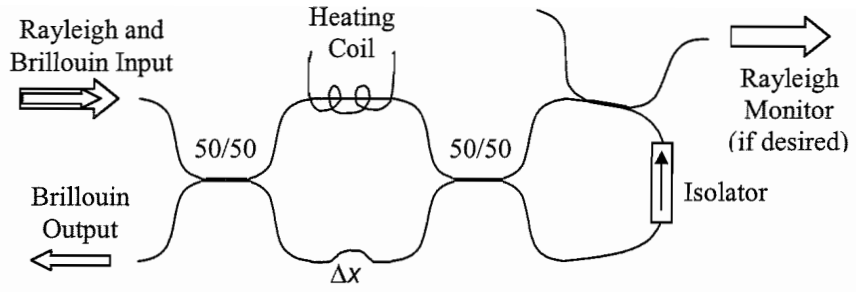

Figure 2.18 Double pass fibre Mach-Zehnder interferometer. Here the output Brillouin signal is refiltered by a second pass through the interferometer.

It is also possible to measure frequency shift using Mach-Zehnder interferometers, thereby creating a simultaneous temperature and strain sensor. The broad peak of the Mach Zehnder transfer function does not allow Brillouin spectroscopy, unlike the narrow fringes in a high finesse Fabry-Perot cavity. However, two Mach-Zehnders may be used in series to enable the measurement of frequency shift, as demonstrated by Kee et al. [2.40]. Firstly, the Brillouin signal was separated from the Rayleigh using a double-pass MZ of 22GHz FSR. Then, the Brillouin was launched into a single-pass MZ with 7GHz FSR to obtain a signal which is dependent on frequency shift. This second MZ was tuned using part of the source radiation (representing the Rayleigh frequency). The Brillouin intensity, independent of frequency shift, was obtained by summing the two traces output from the second MZ when the Rayleigh frequency was tuned to firstly a minimum and secondly a maximum of its transfer function. For unstrained fibre at room temperature, the Brillouin frequencies had X=0.8 and X=0.2 for these two tunings, respectively. If frequency shift increased (higher temperature or larger strain) X decreased for the first tuning and increased for the second. The change in Brillouin frequency shift was therefore obtained by normalising a single output trace to the sum. A 15km simultaneous strain and temperature sensor was demonstrated, with a strain resolution of 290με and a temperature resolution of 4K, for a spatial resolution of 10m [2.40].

2.4.5.3 Fibre Bragg Grating

Another technique to separate optically Brillouin from Rayleigh is the use of a fibre Bragg grating (FBG). This has only very recently been optimised for the creation of a Brillouin temperature sensor. Wait and Hartog demonstrated, in 2001, the use of a

FBG notch filter to suppress the Rayleigh signal whilst transmitting both Stokes and anti-Stokes backscatter [2.41]. Two temperature-stabilised gratings were used, separated by an optical isolator, to achieve adequate rejection. A spatial resolution of 2m was demonstrated, for a sensing length of 25km. They achieved 7K temperature error at 25km for a 10-minute averaging time (actual number of averages was not specified) and a 1K temperature error at 20km for a 180-minute averaging time. Unfortunately this technique can not be used alone to achieve simultaneous temperature and strain sensing since the relatively wide bandwidth (~0.13nm) of the gratings used prevents accurate frequency shift measurement.

2.4.6 Direct Detection of Stimulated Brillouin Backscatter

Stimulated Brillouin scattering, rather than spontaneous, has also been used in distributed sensing. However, instead of using a high input power to create the stimulated scattering condition, which would almost certainly introduce other unwanted nonlinear effects, the Brillouin gain is exploited by using counter-propagating pump and probe radiation, separated by the Brillouin frequency shift. This means that access to both ends of the sensing fibre is necessary, an obvious disadvantage in many applications. Also, the measurement of Brillouin power is more difficult and so it has proved difficult to construct a simultaneous temperature and strain sensor using this technique. The method was first proposed by Horiguchi and Tateda in 1989 [2.42] and they named it Brillouin Optical Time-Domain Analysis (BOTDA). BOTDA is a form of Brillouin spectroscopy which explores the gain spectrum at each point along the sensing fibre. A typical experimental arrangement is shown in Figure 2.19.

The measured quantity in BOTDA is the fluctuation in the cw probe signal power, observed at the detector, as a pump pulse propagates along the sensing fibre. The cw probe is downshifted in frequency by $\Delta\nu$ with respect to the pulsed pump. If the probe frequency happens to lie within the pump pulse's local Brillouin gain spectrum, the pump will cause amplification of the cw probe at that point. This technique has therefore been termed the 'Brillouin gain' method [2.43].

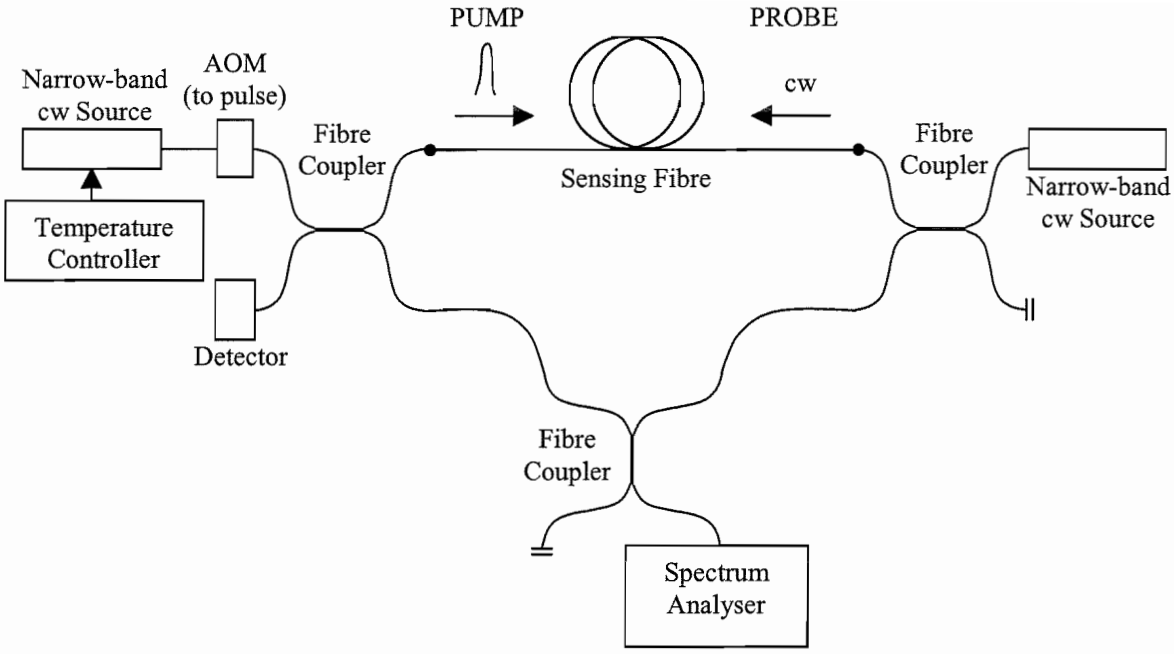

Figure 2.19 Brillouin Optical Time Domain Analysis (BOTDA). A cw probe and pulsed pump are separated by $\Delta\nu$, which is approximately the Brillouin frequency shift, ν_B. When $\Delta\nu=\nu_B$, the cw probe is amplified by the pump pulse. The spectrum analyser monitors $\Delta\nu$.

By taking many traces at stepped values of $\Delta\nu$ (achieved by, for example, temperature-tuning one of the lasers) the Brillouin gain spectrum at each position along the fibre may be obtained. The system may also be operated in 'Brillouin loss' [2.44] mode, where the cw signal becomes the pump and loses intensity at the expense of a Stokes probe pulse, which is amplified when the frequency shift is appropriate. This is claimed to allow the creation of longer sensors, since the probe pulse is amplified, rather than depleted by the Brillouin interaction.

Until recently, this technique had been used merely to measure frequency shift information and so was a single-variable sensor. As a strain sensor, a resolution of 20με was presented in 1994 for a spatial resolution of 5m and a 22km sensing length [2.44]. In 1999, however, a simultaneous temperature and strain sensor was created, using a Brillouin loss technique, by Smith et al. [2.45]. Unfortunately, this sensor exhibited limited performance, with a sensing length of only 50m of polarisation maintaining fibre. Over this 50m length, errors of 3.9K and 178με were measured for a spatial resolution of 3.5m.

2.4.7 Coherent Detection of Spontaneous Brillouin Backscatter

Distributed coherent Brillouin spectroscopy (DCOBS) uses heterodyne detection of spontaneous Brillouin backscatter to create simultaneous distributed temperature and strain sensors: power and frequency shift information may be obtained from each measured spectrum. DCOBS is a similar technique to that of COTDR (§2.2.3), in that the backscatter is mixed with a strong optical local oscillator (OLO) but, in the case of DCOBS, either the optical frequency difference between OLO and backscatter or the electrical local oscillator frequency in the receiver must be scanned so that the Brillouin spectra may be built up. If the optical frequency difference is scanned, stability of each frequency needs to be ensured. Care must also be taken that the same pulse (and OLO) power is used for each frequency or that measured powers are used to normalise the backscatter trace. If the electrical LO frequency is scanned, the gain spectrum of the receiver over the range of interest must be flat or at least calibrated. To date, only relatively narrow band, standard heterodyne detectors have been used in DCOBS sensors, where the OLO must be arranged to be within ~100 MHz of either the Stokes or anti-Stokes Brillouin signal. Using the same source to provide both sensing pulses and OLO gives much greater frequency stability than using two separate laser sources, so it has been necessary to frequency shift either the sensing pulses or OLO optically by ~11GHz. A typical DCOBS schematic is shown in Figure 2.20. The high optical frequency shift has been introduced in several ways.

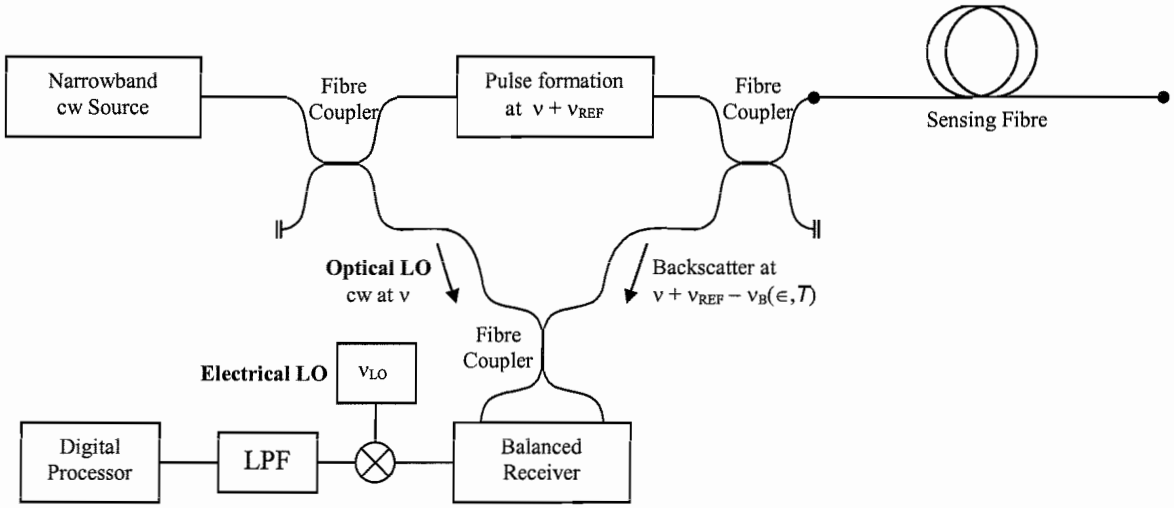

Figure 2.20 Schematic of distributed coherent Brillouin spectroscopy (DCOBS). A single source provides both sensing pulses (shifted in frequency by $\nu_{REF} \sim \Delta\nu_B$ ~11GHz) and optical LO. Here, with ν_{REF} positive, the Stokes spectrum is measured. The mixer and LPF select a frequency component of the Brillouin spectrum and either ν_{REF} or ν_{LO} is scanned such that the distributed Brillouin spectra are built up.

The creation of shifted pulses using a Brillouin laser was implemented by Lecoeuche et al. in 1999 [2.46]. Pulses are emitted from such a laser at the Stokes frequency and hence only the anti-Stokes backscatter signal is in the correct frequency range to be measured. There is also little control over pulse characteristics and repetition rate and almost no scope for scanning of the pulse frequency. This work did not produce a simultaneous sensor since no spectroscopy was undertaken. They merely measured the Brillouin power: no frequency selective filter was present in their detection system and the total beat spectrum power within the 125MHz bandwidth of their detector was the measured quantity. Unfortunately, since there was no measurement of frequency shift, there could be no allowance for the shape of the gain spectrum of the receiver making this design fundamentally flawed. Indeed the authors did not present calibrated temperature sensing results, but claimed a 10m spatial resolution over a sensing length of 16km. Rayleigh measurements were obtained using a narrow-band source and frequency shift averaging. Later, in 2000, this technique was used on a sensing length of 20km with a spatial resolution of 7m and a quoted temperature error of 6K at 19km, although still no calibration was evident [2.47].

In 1996, Izumita et al. [2.24] used a high-frequency electro-optic phase modulator driven by a microwave generator, to create 11GHz sidebands. Both the input polarisation and the modulator drive voltage had to be optimised to maximise rejection of the fundamental. To form pulses and to shift the pulse fundamental frequency away from the source (OLO) frequency, the phase-modulated radiation was passed through two 120MHz AOMs, separated by an EDFA. Since rejection of the fundamental was not perfect, its Rayleigh backscatter produced a beat signal with the OLO at 240MHz, which had to be filtered by an electrical filter. Again, a simultaneous sensor was not created; only frequency shift was measured, by tuning the microwave generator over the Brillouin spectral range. No power measurements were attempted from these data. The authors claimed a spatial resolution of 100m over a sensing length of 30km with an error in frequency shift of ±1MHz.

Shimizu et al. [2.48] [2.49] pioneered the use of an acousto-optic modulator (AOM, §3.4.1) frequency translation ring to create a tunable frequency shift in the required 11GHz range. In this design, shown in Figure 2.21, source radiation is initially pulsed

by AOM 1, before making many passes of AOM 2, multiplying the small frequency shift per circuit to give a total in the 11GHz range. Small changes made to the rf drive frequency of AOM 2 may be used to tune the overall frequency shift. An erbium doped fibre amplifier is inserted into the ring in order to compensate for the losses through AOM 2 and the fibre coupler. A bandpass filter is used to prevent the circulation of unwanted amplified spontaneous emission, although care must still be taken to avoid lasing. A delay line of sufficient length must also be added to the circuit in order for each pulse to be fully contained within the ring, avoiding frequency overlap. To select the appropriately shifted pulse, a further modulator, AOM 3, is used; all three modulators must be carefully timed to allow correct operation of the shifter. Using this method of frequency shifting, the authors demonstrated a spatial resolution of 100m for a 40km sensing fibre [2.49], although no temperature and strain sensing results were presented and power and frequency shift errors were obtained theoretically not explicitly demonstrated.

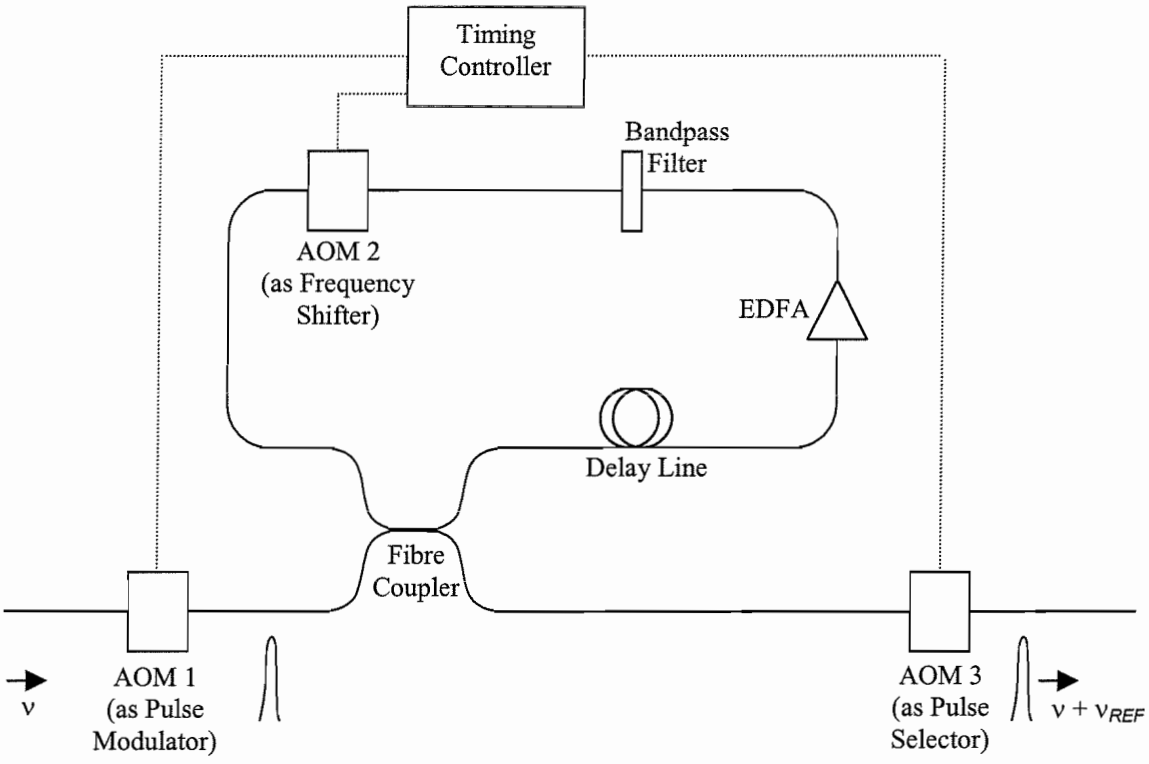

Figure 2.21 AOM ring circuit for frequency translation. AOM 1 forms an initial pulse, part of which is coupled into the ring. AOM 2 shifts the frequency of the circulating pulse on each circuit of the ring. Part of the pulse is coupled out of the ring after each round trip and AOM 3 is timed such that it transmits a pulse with frequency shift approximately equal to the Brillouin frequency shift. This frequency shift may be tuned by making slight changes to the rf frequency applied to AOM 2.

2.5 The State of The Art: Summary

Progress in spontaneous Brillouin temperature and strain sensing to date is summarised in Table 2.5. It can be seen that the best temperature resolution demonstrated is ~1K, the best strain resolution 20με, the best spatial resolution 2m and the best sensing length 30km. However, not all of these have been achieved at the same time. Indeed reported single-ended simultaneous sensors, all of which utilise direct detection techniques, have yet not demonstrated a temperature resolution less than 4K or a sensing range longer than 15km.

Date	Temperature Resolution	Strain Resolution	Spatial Resolution	Sensing Length	No. averages	
Direct detection power only						
Nov 1996	2.9K	-	40m	12.9km	8,192	[2.32]
Jan 1998	1.4K	-	10m	6km	65,536	[2.18]
Jul 1998	0.9K	-	3.5m	16km	not stated	[2.39]
May 2001	1K	-	2m	25km	180 mins	[2.41]
Coherent detection frequency shift only						
Dec 1996	-	20με	100m	30km	720,896	[2.24]
Coherent detection power only						
Oct 2000	6K 3K	-	7m 7m	20km 1km	300,000	[2.47]
Direct detection both power and frequency shift						
Jul 1997	4K	100με	40m	1.2km	1,600 per spectrum	[2.35]
May 2000	4K	290με	10m	15km	65,536	[2.40]

Table 2.5 Summary of progress made in temperature and strain sensing using detection of spontaneous Brillouin backscatter.

It was the principal aim of this work to develop a temperature and strain sensor based on the coherent detection of spontaneous Brillouin backscatter, in order to ascertain its potential as a simultaneous sensor. The sensor would ideally demonstrate a range of greater than 25km, with a temperature resolution of ~5K, a strain resolution of ~100με and a spatial resolution of 20m.

Chapter Three will now describe the basic features of such a sensor.

2.6 References

[2.1] J.M. Senior: "Optical Fiber Communications", Second Edition, *Prentice Hall*, ISBN 0-13-635426-2 (1992)

[2.2] D. Minoli: "Telecommunications Technology Handbook", *Artech House Inc.*, ISBN 0-89006-425-3 (1991)

[2.3] M.K. Barnoski and S.M. Jensen: "Fiber waveguides: a novel technique for investigating attenuation characteristics", *Applied Optics*, Vol. 15, No. 9, pp. 2112-2115 (September 1976)

[2.4] E. Brinkmeyer: "Analysis of the backscattering method for single-mode optical fibers", *Journal of the Optical Society of America*, Vol. 70, No. 8, pp. 1010-1012 (August 1980)

[2.5] T. Sato, T. Horiguchi, Y. Koyamada and I. Sankawa: "A 1.6 μm Band OTDR Using a Synchronous Raman Fiber Amplifier", *IEEE Photonics Technology Letters*, Vol. 4, No. 8, pp. 923-924 (August 1992)

[2.6] H. Izumita, S.-i. Furukawa, Y. Koyamada and I. Sankawa: "Fading Noise Reduction in Coherent OTDR", *IEEE Photonics Technology Letters*, Vol. 4, No. 2, pp. 201-203 (February 1992)

[2.7] P. Healey: "Fading in heterodyne OTDR", *Electronics Letters*, Vol. 20, No. 1, pp. 30-32 (January 1984)

[2.8] J.P. King, D.F. Smith, K. Richards, P. Timson, R.E. Epworth and S. Wright: "Development of a Coherent OTDR Instrument", *Journal of Lightwave Technology*, Vol. LT-5, No. 4, pp. 616-624 (April 1987)

[2.9] A.H. Hartog and D.N. Payne: "Remote measurement of temperature distribution using an optical fibre", *Proc. ECOC'82*, pp. 215-220 (Cannes, France, 1982)

[2.10] A.A. Boiarski, G. Pilate, T. Fink and N. Nilsson: "Temperature Measurements in Power Plant Equipment Using Distributed Fiber Optic Sensing", *IEEE Transactions on Power Delivery*, Vol. 10, No. 4, pp. 1771-1778 (October 1995)

[2.11] G.P. Agrawal: "Nonlinear Fiber Optics", Second Edition, *Academic Press*, ISBN 0-12-045142-5 (1995)

[2.12] J.P. Dakin: "Multiplexed and distributed optical fibre sensor systems", *Journal of Physics E: Scientific Instruments*, Vol. 20, pp. 954-967 (1987)

[2.13] A.H. Hartog, A.P. Leach and M.P. Gold: "Distributed temperature sensing in solid-core fibres", *Electronics Letters*, Vol. 21, No. 23, pp. 1061-1062 (November 1985)

[2.14] J.P. Dakin, D.J. Pratt, G.W. Bibby and J.N. Ross: "Distributed optical fibre Raman temperature sensor using a semiconductor light source and detector", *Electronics Letters*, Vol. 21, No. 13, pp. 569-570 (June 1985)

[2.15] T. Wakami and S. Tanaka: "1.55μm Long-Span Fiber-Optic Distributed Temperature Sensor", *Tenth International Conference on Optical Fiber Sensors*, pp. 134-137 (Glasgow, 1994)

[2.16] L. Brillouin: "Diffusion de la lumière at des rayons x par un corps tranparent homogène – influence de l'agitation thermique", *Annales de Physique (Paris)*, Vol. 17, p. 88-122 (1922)

[2.17] R.S. Krishnan: "Fine Structure of the Rayleigh Line in Amorphous Substances", *Nature*, Vol. 165, No. 4206, pp. 933-934 (June 1950)

[2.18] G.P. Lees, P.C. Wait, M.J. Cole and T.P. Newson: "Advances in Optical Fiber Distributed Temperature Sensing Using the Landau-Placzek Ratio", *IEEE Photonics Technology Letters*, Vol. 10, No.1, pp. 126-128 (January 1998)

[2.19] P.C. Wait and T.P. Newson: "Landau Placzek ratio applied to distributed fibre sensing", *Optics Communications*, Vol. 122, No. 4-6, pp. 141-146 (January 1996)

[2.20] T.R. Parker, M. Farhadiroushan, V.A. Handerek and A.J. Rogers: "Temperature and strain dependence of the power level and frequency of spontaneous Brillouin scattering in optical fibers", *Optics Letters*, Vol. 22, No. 11, pp. 787-789 (June 1997)

[2.21] K. De Souza, P.C. Wait and T.P.Newson: "Characterisation of strain dependence of the Landau-Placzek ratio for distributed sensing", *Electronics Letters*, Vol. 33, No. 7, pp. 615-616 (March 1997)

[2.22] T. Kurashima, T. Horiguchi and M. Tateda: "Thermal Effects of Brillouin Gain Spectra in Single-Mode Fibers", *IEEE Photonics Technology Letters*, Vol. 2, No. 10, pp. 718-720 (October 1990)

[2.23] T. Horiguchi, T. Kurashima and M. Tateda: "Tensile Strain Dependence of Brillouin Frequency Shift in Silica Optical Fibers", *IEEE Photonics Technology Letters*, Vol. 1, No. 5, pp. 107-109 (May 1989)

[2.24] H. Izumita, T. Sato, M. Tateda and Y. Koyamada: "Brillouin OTDR Employing Optical Frequency Shifter Using Side-Band Generation Technique with High-Speed LN Phase-Modulator", *IEEE Photonics Technology Letters*, Vol. 8, No. 12, pp. 1674-1676 (December 1996)

[2.25] J.D.C. Jones: "Review of fibre sensor techniques for temperature-strain discrimination", *Twelfth International Conference on Optical Fiber Sensors*, pp. 36-39 (Williamsburg, Virginia, October 1997)

[2.26] P.C. Wait, K. De Souza and T.P. Newson: "A theoretical comparison of spontaneous Raman and Brillouin based fibre optic distributed temperature sensors", *Optics Communications*, Vol. 144, No. 1-3, pp. 17-23 (December 1997)

[2.27] T. Horiguchi, K. Shimizu, T. Kurashima, M. Tateda and Y. Koyamada: "Development of a Distributed Sensing Technique Using Brillouin Scattering", *Journal of Lightwave Technology*, Vol. 13, No. 7, pp. 1296-1302 (July 1995)

[2.28] D. Cotter: "Observation of stimulated Brillouin scattering in low-loss silica fibre at 1.3μm", *Electronics Letters*, Vol. 18, No. 12, pp. 495-496 (June 1982)

[2.29] J. Gowar: "Optical Communication Systems", Second Edition, *Prentice Hall*, ISBN 0-13-638727-6 (1993)

[2.30] P.C. Wait and T.P. Newson: "Measurement of Brillouin scattering coherence length as a function of pump power to determine Brillouin linewidth", *Optics Communications*, Vol. 117, No. 1-2, pp. 142-146 (May 1995)

[2.31] M. Niklès, L. Thévenaz and P.A. Robert: "Brillouin Gain Spectrum Characterization in Single-Mode Optical Fibres", *Journal of Lightwave Technology*, Vol. 15, No. 10, pp. 1842-1851 (October 1997)

[2.32] K. De Souza, G.P. Lees, P.C. Wait and T.P. Newson: "Diode-pumped Landau-Placzek based distributed temperature sensor utilising an all-fibre Mach-Zehnder interferometer", *Electronics Letters*, Vol. 32, No. 23, pp. 2174-2175 (November 1996)

[2.33] P.C. Wait and T.P. Newson: "Reduction of coherent noise in the Landau Placzek ratio method for distributed fibre optic temperature sensing", *Optics Communications*, Vol. 131, No. 4-6, pp. 285-289 (November 1996)

[2.34] K. De Souza, D.O. Culverhouse and T.P. Newson: "Dual-operation Q-switched erbium-doped fibre laser for distributed fibre sensing", *Electronics Letters*, Vol. 33, No. 24, pp. 2040-2042 (November 1997)

[2.35] T.R. Parker, M. Farhadiroushan, V.A. Handerek and A.J. Rogers: "A Fully Distributed Simultaneous Strain and Temperature Sensor using Spontaneous Brillouin Backscatter", *IEEE Photonics Technology Letters*, Vol. 9, No. 7, pp. 979-981 (July 1997)

[2.36] D.B. Mortimore: "Fiber Loop Reflectors", *Journal of Lightwave Technology*, Vol. 6, No. 7, pp. 1217-1224 (July 1988)

[2.37] C.A. Millar, D. Harvey and P. Urquhart: "Fibre reflection Mach-Zehnder interferometer", *Optics Communications*, Vol. 70, No. 4, pp. 304-308 (March 1989)

[2.38] K. De Souza, P.C. Wait and T.P. Newson: "Double-pass configured fibre Mach-Zehnder interferometric optical filter for distributed fibre sensing", *Electronics Letters*, Vol. 33, No. 25, pp. 2148-2149 (December 1997)

[2.39] G.Lees, P. Wait and T.Newson: "Distributed Temperature Sensing using the Landau-Placzek Ratio", *Proc. ICAPT98*, *ICAPT98T234*, Ottawa, Ontario, Canada (July 1998)

[2.40] H.H. Kee, G.P. Lees and T.P. Newson: "All-fiber system for simultaneous interrogation of distributed strain and temperature sensing by spontaneous Brillouin scattering", *Optics Letters*, Vol. 25, No. 10, pp. 695-697 (May 2000)

[2.41] P.C.Wait and A.H.Hartog: "Spontaneous Brillouin-Based Distributed Temperature Sensor Utilizing a Fiber Bragg Grating Notch Filter for the Separation of the Brillouin Signal", *IEEE Photonics Technology Letters*, Vol. 13, No. 5, pp. 508-510 (May 2001)

[2.42] T. Horiguchi and M. Tateda: "BOTDA - Nondestructive Measurement of Single-Mode Optical Fiber Attenuation Characteristics Using Brillouin Interaction: Theory", *Journal of Lightwave Technology*, Vol. 7, No. 8, pp. 1170-1176 (August 1989)

[2.43] T. Horiguchi, T. Kurashima and M. Tateda: "A Technique to Measure Distributed Strain in Optical Fibers", *IEEE Photonics Technology Letters*, Vol. 2, No. 5, pp. 352-354 (May 1990)

[2.44] X. Bao, D.J. Webb and D.A. Jackson: "22km distributed strain sensor using Brillouin loss in an optical fibre", *Optics Communications*, Vol. 104, No. 4-6, pp. 298-302 (January 1994)

[2.45] J. Smith, A. Brown, M. DeMerchant and X. Bao: "Simultaneous distributed strain and temperature measurement", *Applied Optics*, Vol. 38, No. 25, pp. 5372-5377 (September 1999)

[2.46] V. Lecœuche, D.J. Webb, C.N. Pannell and D.A. Jackson: "25km Brillouin based single-ended distributed fibre sensor for threshold detection of temperature or strain", *Optics Communications*, Vol. 168, No. 1-4, pp. 95-102 (September 1999)

[2.47] V. Lecœuche, M.W. Hathaway, D.J. Webb, C.N. Pannell and D.A. Jackson: "20-km Distributed Temperature Sensor Based on Spontaneous Brillouin Scattering", *IEEE Photonics Technology Letters*, Vol. 12, No. 10, pp. 1367-1369 (October 2000)

[2.48] K. Shimizu, T. Horiguchi and Y. Koyamada: "Technique for translating light-wave frequency by using an optical ring circuit containing a frequency shifter", *Optics Letters*, Vol. 17, No. 18, pp. 1307-1309 (September 1992)

[2.49] K. Shimizu, T. Horiguchi, Y. Koyamada and T. Kurashima: "Coherent Self-Heterodyne Brillouin OTDR for Measurement of Brillouin Frequency Shift Distribution in Optical Fibers", *Journal of Lightwave Technology*, Vol. 12, No. 5, pp. 730-736 (May 1994)

Chapter Three

Constituents and Design of a Coherent Brillouin Sensor

3.1 Introduction

This chapter will describe both the optical and electrical components required to construct a fibre optic sensor based on 11GHz coherent detection of spontaneous Brillouin scattering. Preliminary results from such a sensor will be presented.

This chapter will also include a mathematical description of heterodyne theory, as well as a discussion of how polarisation of the backscatter gives rise to an important problem and how this problem may be alleviated.

A description of how the Brillouin power and frequency shift measurements may be extracted from the collected data will conclude the chapter. Firstly, however, the motivation for using a microwave beat frequency will be discussed.

3.2 Using a Microwave Beat Frequency

There are several advantages to detection of Brillouin backscatter at a microwave beat frequency of ~11GHz, rather than at the previously attempted ~100MHz. These are:

- Detection system gain is effectively flat over the entire frequency range of interest (~500MHz), since this is a small proportion of the whole detector bandwidth.

- The beat frequency is shifted away from the local oscillator self-beat noise, which is prevalent at low frequencies (see §4.3.3).

- Independent measurement of both Stokes and anti-Stokes backscatter is possible since both beat frequencies lie within the detector bandwidth. If a first-order AOM (§3.4.1) is used as a pulse modulator, the Stokes and anti-Stokes separation will be twice the AOM frequency shift.

- Since optical frequency shifting of 11GHz (§2.4.7) is not required in such a sensor, the optics is simplified and particularly stable in frequency.

The work of looking at the beat frequency between Brillouin backscatter and pump radiation was begun by Everard and Thomas in 1989 [3.1], when a special microwave device, a coplanar waveguide three-wave mixer, was used to detect cw stimulated Brillouin backscatter. Pump and SBS radiation were mixed with a microwave oscillator in a photoconductive medium, downconverting the beat frequency between the two optical signals (in this case 33GHz) to ~500MHz, within the passband of their rf spectrum analyser. This work was continued in 1995 [3.2] where the stimulated Brillouin frequency shift of an undisclosed length of high birefringence fibre was calibrated against temperature. No distributed sensing was demonstrated, however, and no error in the measured frequency shift was quoted.

3.3 Source

In the search for a suitable source for our heterodyne spontaneous Brillouin distributed fibre optic sensor, we must consider several characteristics:

- Linewidth
- Wavelength
- Tunability
- Power

As discussed in Chapter Two, heterodyne detection of spontaneous Brillouin backscatter requires that the source linewidth is considerably less than the Brillouin frequency shift. In fact, any source with linewidth comparable to or larger than that of

the Brillouin signal will distort the heterodyne spectral shape from that of the Lorentzian Brillouin gain spectrum. This narrow linewidth necessarily implies a particularly coherent source and hence there is a problem with coherent noise. Additionally, a broad-band source, with several nanometres linewidth, is desirable in order to obtain the reference Rayleigh scattering attenuation spectrum.

Source wavelength is restricted if we wish to construct a long range sensor. As mentioned in §2.2.1, there are two suitable windows of operation if low fibre loss is desired. Of these, the 1.55μm window is the more versatile choice since erbium-doped fibre amplifier (EDFA) technology allows convenient signal amplification. In a heterodyne sensor which, to increase frequency stability, uses a single source to provide both pulses and optical local oscillator, amplification is necessary unless a cw source with the high power of several hundred mW is available for use.

Source tunability is a desirable feature, particularly if any wavelength-sensitive components are to be included in the design. Lasers with a gain medium of erbium doped glass may be constructed for tunability over the entire gain spectrum of the erbium transition (§3.5).

Source power would ideally be as high as possible whilst ensuring the above characteristics. A source of low power may be amplified to a suitable level, although any amplifier will add noise to the signal output.

3.3.1 Choice of Source

The source chosen for these experiments was a continuous wave, fibre coupled, Hewlett Packard tunable laser (1474–1567nm) with a linewidth of 300kHz (~2.3 fm) and a maximum output power of approximately 100μW. Source linewidth was measured by a delayed self-heterodyne technique [3.3] and the resulting heterodyne spectrum is shown in Figure 3.1. A Lorentzian curve was fitted to the experimental data and the source linewidth was measured as 300kHz. For the Rayleigh measurements, a source of amplified spontaneous emission (ASE, §3.5) was chosen.

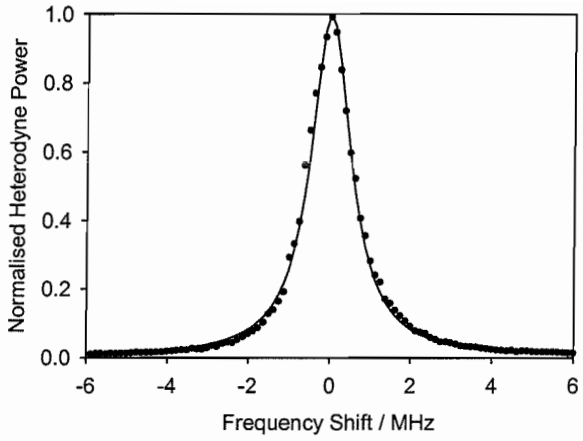

Figure 3.1 Source lineshape measured using a delayed self-heterodyne technique. A fitted Lorentzian curve (solid line) has linewidth 600kHz, so the source linewidth is determined as 300kHz.

3.4 Modulator

Since the optical local oscillator and sensing pulses are to be obtained from the same source, some form of pulse modulation is required. Two contenders for this function are the acousto-optic modulator (AOM) and the electro-optic modulator (EOM).

3.4.1 AOM

An acousto-optic modulator (AOM, Figure 3.2) allows the creation of pulses with rise times typically between ~20ns and ~150ns [3.4]. It is a deflective switch, in which incoming radiation is physically deflected on the application of an rf signal. This rf signal is applied to a transducer attached to a suitable crystal, through which the light to be switched is propagating, causing the creation of an acoustic wave. This wave induces a moving refractive index grating within the crystal, by the photoelastic effect, from which the incident light is diffracted. The rf frequency, ν_{RF}, and angle of indicence, θ_i, of the light within the crystal must be chosen such that Bragg diffraction takes place. The grating, travelling with the acoustic velocity, V_A, has a period, $\Lambda_A = V_A / \nu_{RF}$. For deflection into the first order beam, the Bragg relation is therefore

$$\sin\theta_i = n\sin\theta_B = \frac{\lambda_i}{2\Lambda_A} = \frac{\lambda_i \nu_{RF}}{2V_A} \qquad \{3.1\}$$

where n is the refractive index of the acousto-optic crystal at the incident wavelength and θ_B is the Bragg angle. The angle through which the incident beam is deflected,

$2\theta_i$, is typically only 2-3° for 1550nm radiation, 110MHz and an acoustic velocity of ~4000m/s. Also, since the grating is moving, the deflected light is Doppler shifted by the applied rf frequency, either up or down depending on the relative directions of propagation of the acoustic wave and incident radiation. Figure 3.2 shows an upshifting AOM.

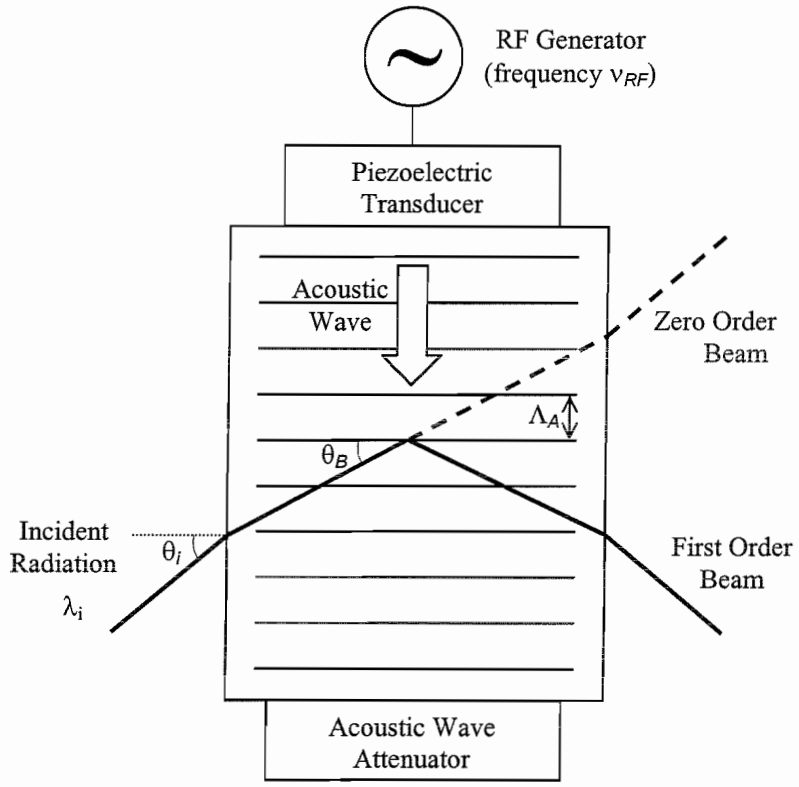

Figure 3.2 Schematic of an upshifting acousto-optic modulator. Radiation incident at the Bragg angle is diffracted from the cavity when an rf signal is applied to the piezoelectric transducer.

The extinction ratio of such a modulator is high, since when no rf signal is applied, no diffraction takes place and no light is coupled into the first order beam. If the rf power is sufficiently high (typically ~3W), the diffraction efficiency of the AOM may reach over 80%. Coupling of the light from input to output fibre adds an extra loss, however, and so the typical insertion loss of an AOM is ~3dB in pulsed mode. Owing to heating of the crystal due to the acoustic wave and consequent damage, the maximum applied rf power is limited. For continuous first order deflection of the AOM, a lower rf power is recommended than for the pulsed regime and so a higher loss, ~5dB, is observed. Acousto-optic modulators are relatively polarisation insensitive, so active polarisation control of the incident radiation is not necessary.

3.4.2 EOM

An electro-optic modulator (EOM), also known as a Pockels cell, may also act as a modulator. This takes advantage of the Pockels effect [3.5], in which a longitudinal electric field applied to an electro-optic (non-centrosymmetric) crystal results in polarisation rotation of transmitted radiation due to induced changes in birefringence. If an electro-optic crystal is placed at 45° between two crossed polarisers, and no electric field is applied (i.e. no polarisation rotation) any radiation entering will be extinguished. If an electric field is then applied to the crystal, such that a 90° polarisation rotation is obtained, then the polariser/crystal combination will have low loss and the switch will be open. The voltages required to produce such electric fields are generally of the order of kilovolts, and so this method is costly and somewhat dangerous. However, the switching times achieved by Pockels cells are very fast – of the order of a few nanoseconds, which make them desirable in sources for high spatial resolution sensing applications.

However, integrated optical EOMs have recently become available, usually constructed from $LiNbO_3$, which utilise single-mode channel waveguide technology and require much smaller voltages: of the order of 10-20V. These EOMs work on the principle of a Mach Zehnder interferometer which is converted into a modulator by applying an electrical voltage, V, to one of the arms. There is a consequent phase shift, by the electro-optic effect, proportional to V. If the magnitude of V is such that the phase difference, on entering the second coupler, between the radiation from each of the two arms is zero, all the radiation will pass into one output arm of the interferometer. If the phase difference is instead arranged, by application of a suitable voltage, to be π, the output radiation switches from one output arm to the other. The modulation bandwidth of such integrated optical EOMs is typically tens of GHz.

Polarisation control is very important in EOM switches, however, and a polarisation controller [3.6] is usually employed prior to switching and is adjusted to achieve maximum extinction ratio. If a good extinction ratio is desired for weakly polarised radiation, such as ASE (§3.5), when using a Mach Zehnder based integrated EOM, a polariser must be used in conjunction with the polarisation controller.

3.4.3 Choice of Modulator

The pulse modulator chosen for the sensor was a 20-25ns rise-time 110MHz downshifting TeO_2 AOM, with an insertion loss of 3dB at 3W applied rf power. The device was fibre coupled for ease of use and stability and had a quoted extinction ratio of >50dB.

3.5 Erbium Doped Fibre Amplifier

In order to launch sensing pulses with maximum tolerable power (before the onset of nonlinear effects) and hence obtain the best signal-to-noise ratio at the detector, optical amplification is required after the initial pulse modulation stage. Indeed, amplification may be required at several positions in the sensor. The first erbium-doped fibre amplifier (EDFA) was presented in 1987 by Mears et al. [3.7]. Such amplifiers, which are now commonplace in the telecommunications industry, utilise the properties of erbium-doped silica to provide efficient amplification in the 1.55μm wavelength window.

Erbium-doping consists of introducing Er^{3+} ions into optical fibre, which may then be pumped at a variety of wavelengths in order to create the population inversion required for gain. It is a three level system and a simplified energy level diagram [3.8] is shown in Figure 3.3. The pump photons excite electrons from the $^4I_{15/2}$ ground state into the metastable level, $^4I_{13/2}$, either directly, or via non-radiative transitions from higher levels. The radiative transition from the metastable level back to the ground state has a very long lifetime, of 8-10ms [3.9], and a significant population inversion may therefore build up.

Five possible pump bands are illustrated in Figure 3.3; these are also evident as peaks in Figure 3.4, which shows a typical absorption spectrum for erbium-doped fibre [3.10]. Pumping at 1490nm directly into the metastable level is possible due to the Stokes shift of the fluorescence band from the absorption band of this transition. The other four pump bands excite electrons to higher energy levels but this is followed by rapid non-radiative decay to the metastable level.

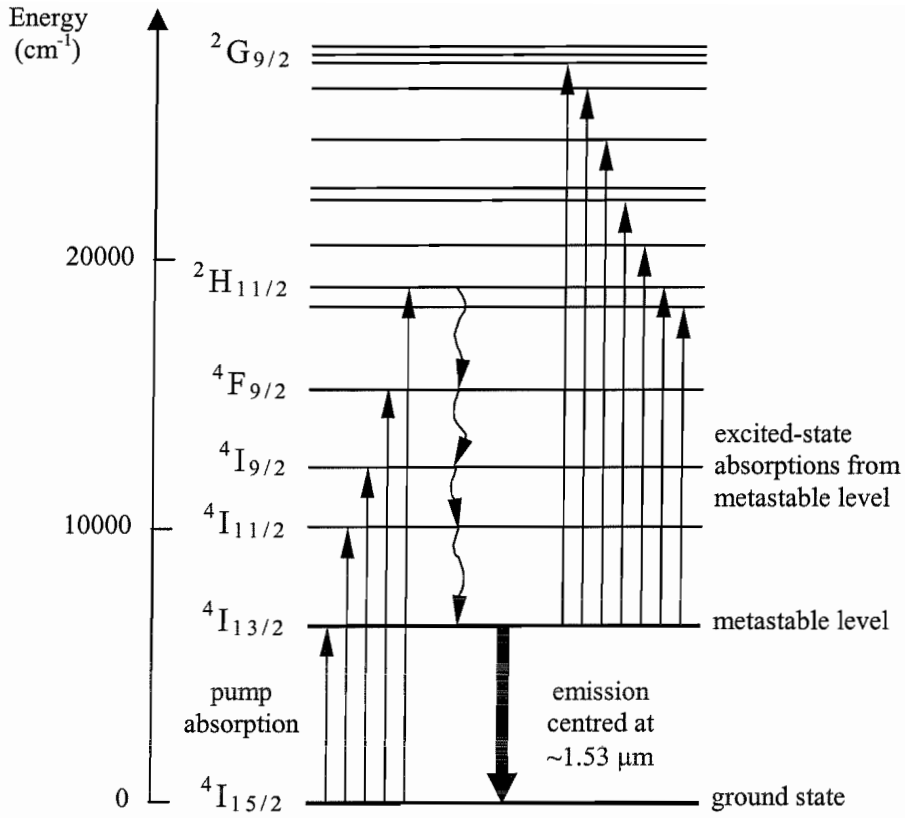

Figure 3.3 Erbium energy level diagram [3.8]. Pumping may take place at various wavelengths with nonradiative decay to the metastable level. The three shortest pump wavelengths cause pump excited state absorption.

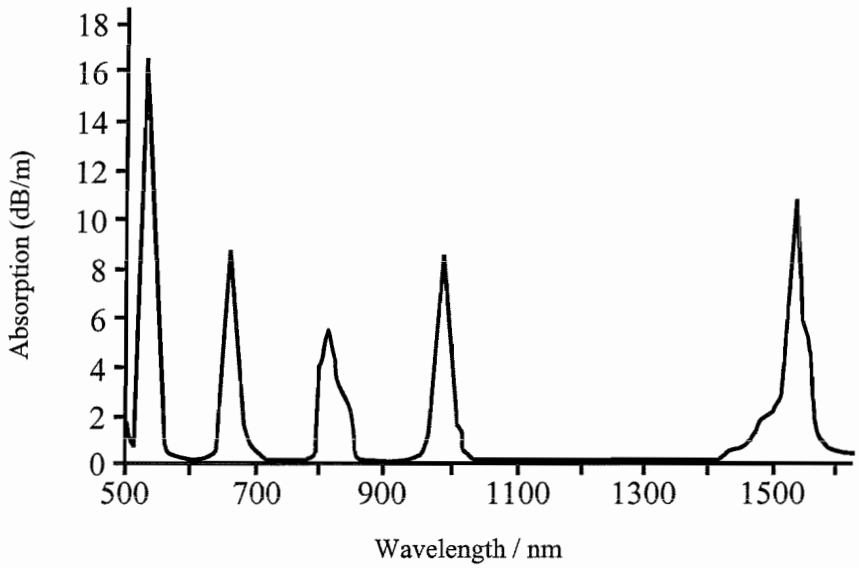

Figure 3.4 Erbium absorption spectrum [3.10], showing peaks corresponding to the five pump transitions in Figure 3.3.

There is less efficient use of pump energy at shorter wavelengths, since more is expended in non-radiative transitions. Longer wavelength pumps are also desirable for other reasons. One of these is that the pump, as well as the signal, may be single mode so there is improved modal overlap and a larger pump absorption cross-section. However, it is pump excited state absorption which is the most detrimental consequence of using a shorter wavelength pump.

Pump wavelengths in the 520nm, 660nm or 810nm bands all cause excited state absorption, where a pump photon excites an electron from the highly populated metastable level rather than from the ground state. This excited electron then returns to the metastable level by nonradiative decay. The original pump photon is wasted and pump efficiency is much reduced. Although it is possible to modify pump excited state absorption by altering the glass host and, in some cases, move the absorption band away from the pump band altogether [3.8], there are now practical semiconductor laser diode pumps widely available at 980nm, making this the pump wavelength of choice.

When a single erbium ion is continuously pumped, it will spontaneously emit 1.55μm-band photons in all directions. In the case of an optical fibre, those travelling in the forward and backward directions will be captured and guided along the fibre. These photons, on encountering other excited erbium ions, will stimulate emission, resulting in amplification of the radiation.

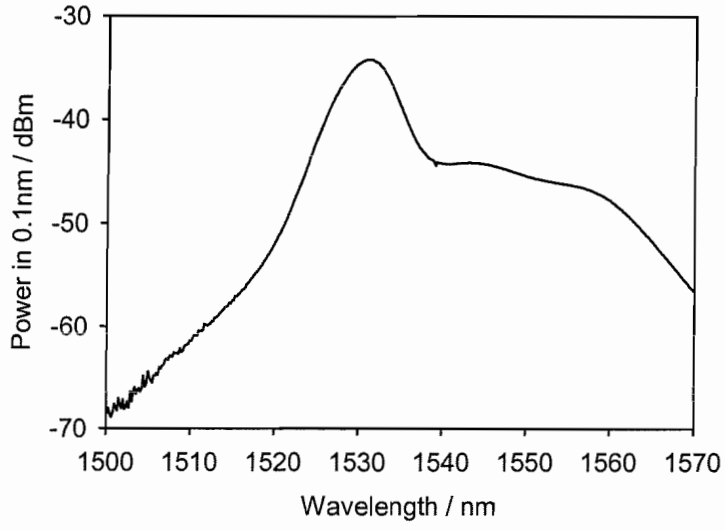

Figure 3.5 Typical ASE spectrum for erbium-doped fibre, in this case pumped at 980nm.

This 1.55μm-band radiation, termed "amplified spontaneous emission" (ASE), is emitted at both ends of the pumped fibre, even with no input signal or optical feedback and results in slight depletion of the population inversion. A typical ASE spectrum is shown in Figure 3.5 showing emitted power in dBm as a function of wavelength. It can be seen that the spectrum is very broad, allowing the pumped erbium fibre to amplify any input optical signal within that bandwidth, although with differing gains.

In an EDFA (Figure 3.6), optical feedback and hence ASE is minimised by the addition of optical isolators (based on the Faraday effect) at both input and output. The pump radiation is coupled into the fibre by use of a wavelength division multiplexor (WDM), which allows the pump to be launched with low loss into the erbium fibre without significant attenuation of the 1.55μm signal. As well as having broad gain bandwidth, EDFAs are polarisation insensitive, have low insertion loss and no cross talk, which justifies their now widespread use in telecommunications as ideal replacements for electrical repeaters.

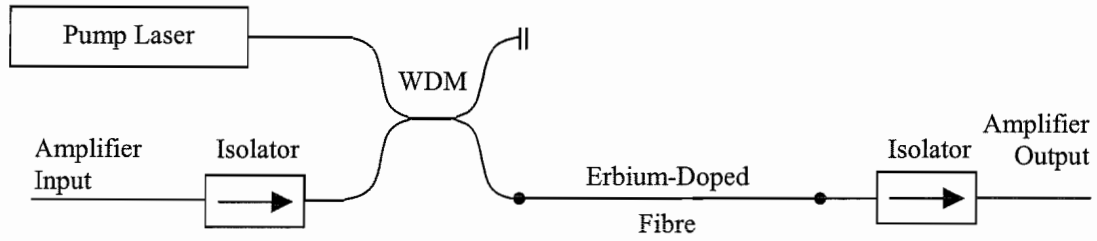

Figure 3.6 Schematic of an EDFA

3.5.1 Choice of Pump Laser

The pump lasers chosen for the amplifiers in the sensor were 980nm fibre-pigtailed laser diode sources with in-fibre maximum output powers of between 75mW and 110mW.

3.6 Detection System

If beat frequencies of ~11GHz are to be observed, firstly a detector of suitable bandwidth is essential. Secondly, some method of time-domain microwave frequency analysis of the detector output voltage is required. The detector used in these experiments was a Hewlett Packard (HP 83440C) 20GHz-bandwidth high-speed lightwave converter. This detector comprised a fibre-connectorised, DC-coupled, hermetically sealed, unamplified InGaAs photodiode, with a responsivity of 0.65A/W at 1550nm and a corresponding gain of 32.5V/W into a 50Ω load. The noise of this detector is dominated by thermal noise and is therefore $27\,\mathrm{pW}/\sqrt{\mathrm{Hz}}$ at 295K for a 50Ω resistor.

The microwave frequency analysis was achieved by a Hewlett Packard (E4407B) 26.5GHz rf/microwave electrical spectrum analyser (ESA). With the analyser set in "zero span" mode at the desired frequency, a corresponding time-domain trace could be obtained. The ESA block diagram is shown in Figure 3.7. The input voltage, at the desired frequency, is first downconverted to a fixed intermediate frequency of 21.4MHz by mixing with a microprocessor-controlled electrical local oscillator. The resolution bandwidth (RBW, band-pass) filter is then applied and the resulting signal amplified. The amplified 21.4MHz signal is then detected and passed through the video bandwidth (VBW, low-pass) filter. The resulting video output voltage is then monitored, in real time, on an oscilloscope.

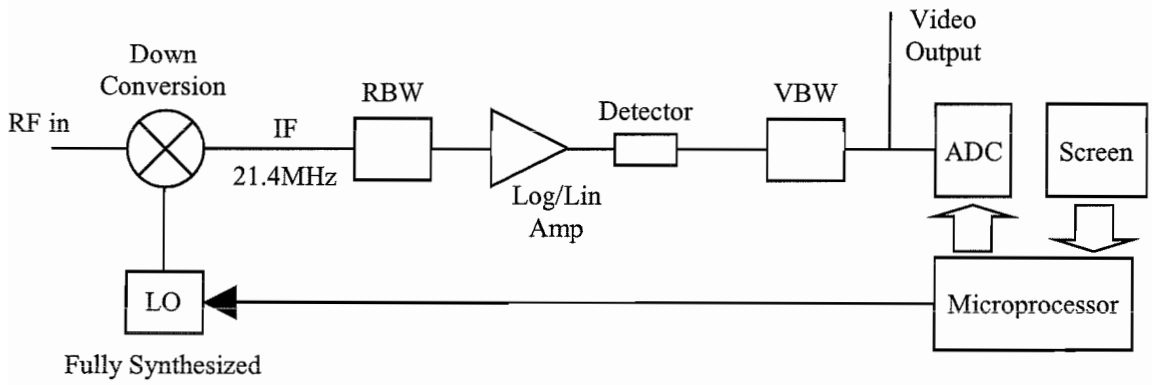

Figure 3.7 Block diagram for the HP E4407B 26.5GHz electrical spectrum analyser. The video output is sent to an oscilloscope for real time backscatter trace acquisition. RF in comes from the HP 83440C 20GHz detector.

The ESA had a maximum resolution bandwidth of 5MHz and a maximum video bandwidth of 3MHz. This places a lower limit on the spatial resolution of the sensor. From Equation {2.8} (§2.2.2), this limit is given by $\Delta x_{det}\,(m) = 50/[\Delta\nu\ (\mathrm{MHz})]$ for a detector of bandwidth $\Delta\nu$. For $\Delta\nu$=3MHz, a theoretical spatial resolution limit of 17m results. In order to measure this limit experimentally, a 110MHz rf signal was modulated into a low-frequency square wave by a switch with a rise time of less than 5ns before being input into the ESA. The rising edge of the corresponding video output voltage, with the ESA centred on 110MHz, is shown in Figure 3.8(a). The 10% to 90% rise time was measured as ~175ns, corresponding to a distance of 17.5m, close to the predicted value of 17m. The 5% to 95% rise time, however, is 200ns and the spatial resolution limit of the ESA will be stated as 20m from this point on.

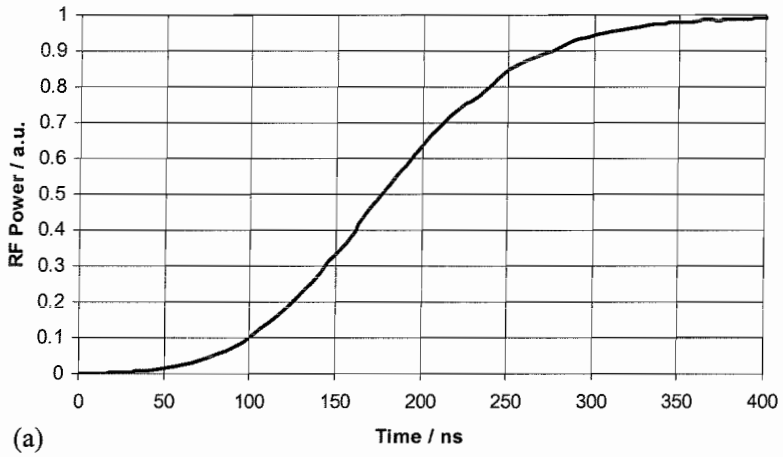

(a)

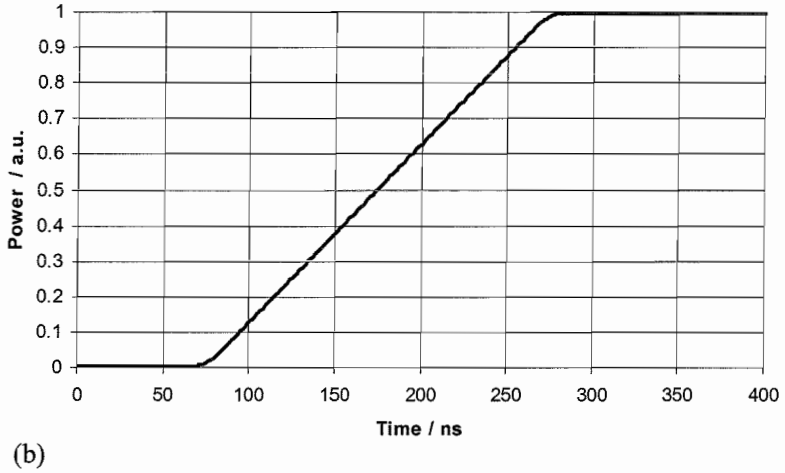

(b)

Figure 3.8 (a) Rising edge of rf power measured with ESA (5MHz resolution bandwidth, 3MHz video bandwidth). ESA set in zero span at 110MHz, with a switched 110MHz rf signal (<5ns rising and falling edges) as input. (b) Simulated actual (not detected) rising edge of optical backscattered power using a 200ns FWHM sensing pulse (20ns rising and falling edges)

A sensing pulse length of 200ns was chosen for use with this detection system; the simulated rise time of the backscatter from such a pulse is shown in Figure 3.8(b), giving a similar spatial resolution to that of the ESA.

For the broad-band Rayleigh trace, a high bandwidth, high gain detector must be used. In these experiments a 3MHz, 10mV/nW, 300μm InGaAs photodiode and transimpedance amplifier combination was used for this purpose. The bandwidth of this receiver matches the ESA bandwidth and so gives the same spatial resolution.

3.7 Heterodyne Theory

Consider interference between two Fourier components (FCs), of identical polarisation, with electric fields, E_1 and E_2, given by

$$\begin{aligned} E_1 &= E_1^0 \cos(2\pi\nu_1 t + \phi_1) \\ E_2 &= E_2^0 \cos(2\pi\nu_2 t + \phi_2) \end{aligned} \qquad \{3.2\}$$

where ϕ_1 and ϕ_2 are the phase of each FC and E_1^0 and E_2^0 are their amplitudes. The sum of these components gives the resultant electric field

$$E = (E_1 + E_2) = E_1^0 \cos(2\pi\nu_1 t + \phi_1) + E_2^0 \cos(2\pi\nu_2 t + \phi_2) \qquad \{3.3\}$$

The optical power $P=\alpha\langle E^2\rangle=\alpha(E^0)^2/2$, where α is the constant of proportionality and $\langle\ \rangle$ indicates a time average. This means that the power of the mixed components (with an averaging time much greater than either $1/\nu_1$ or $1/\nu_2$) is given by

$$P = \alpha\left\langle (E_1 + E_2)^2 \right\rangle = \alpha\left\langle \left(E_1^0 \cos(2\pi\nu_1 t + \phi_1) + E_2^0 \cos(2\pi\nu_2 t + \phi_2)\right)^2 \right\rangle \qquad \{3.4\}$$

This expression may be simplified in the following way

$$P = \alpha\left(E_1^0\right)^2\left\langle\cos^2(2\pi\nu_1 t+\phi_1)\right\rangle + \alpha\left(E_2^0\right)^2\left\langle\cos^2(2\pi\nu_2 t+\phi_2)\right\rangle + 2\alpha E_1^0 E_2^0\left\langle\cos(2\pi\nu_1 t+\phi_1)\cos(2\pi\nu_2 t+\phi_2)\right\rangle$$

$$= \left(2P_1\cdot\frac{1}{2}\right)+\left(2P_2\cdot\frac{1}{2}\right)+2\sqrt{2P_1 2P_2}\left\langle\cos(2\pi\nu_1 t+\phi_1)\cos(2\pi\nu_2 t+\phi_2)\right\rangle \qquad \{3.5\}$$

$$= P_1 + P_2 + 4\sqrt{P_1P_2}\left\langle\cos(2\pi\nu_1 t+\phi_1)\cos(2\pi\nu_2 t+\phi_2)\right\rangle$$

Now, the measured photocurrent at the detector, $I_{det} = P\eta e/(h\nu_s)$, where $\nu_s \approx \nu_1 \approx \nu_2$ is the frequency of the interacting radiation, η is the quantum efficiency of the detector and e is the charge on an electron, so

$$i_{\text{det}}\left(\frac{h\nu_s}{\eta e}\right) = P_1 + P_2 + 4\sqrt{P_1P_2}\left\langle\cos(2\pi\nu_1 t+\phi_1)\cos(2\pi\nu_2 t+\phi_2)\right\rangle$$

$$= P_1 + P_2 + 2\sqrt{P_1P_2}\left\langle\cos\left(2\pi(\nu_2+\nu_1)t+(\phi_2+\phi_1)\right)\right\rangle + 2\sqrt{P_1P_2}\left\langle\cos\left(2\pi(\nu_2-\nu_1)t+(\phi_2-\phi_1)\right)\right\rangle \qquad \{3.6\}$$

The first time-averaged term is negligible, since the integration time is much greater than $1/(\nu_2+\nu_1)$. The detector photocurrent is therefore given by

$$i_{\text{det}} = \left(\frac{\eta e}{h\nu_s}\right)P_1 + \left(\frac{\eta e}{h\nu_s}\right)P_2 + 2\left(\frac{\eta e}{h\nu_s}\right)\sqrt{P_1P_2}\left\langle\cos\left(2\pi(\nu_2-\nu_1)t+(\phi_2-\phi_1)\right)\right\rangle \qquad \{3.7\}$$

If the detector is fast enough to pick up the frequency $(\nu_2-\nu_1)$ accurately then the time average on this term is not necessary and the detector photocurrent will be given by

$$i_{\text{det}} = \left(\frac{\eta e}{h\nu_s}\right)P_1 + \left(\frac{\eta e}{h\nu_s}\right)P_2 + 2\left(\frac{\eta e}{h\nu_s}\right)\sqrt{P_1P_2}\cos\left(2\pi(\nu_2-\nu_1)t+(\phi_2-\phi_1)\right) \qquad \{3.8\}$$

with the RMS current flowing at frequency $(\nu_2-\nu_1)$ being

$$i_{CD}^{rms} = \left(\frac{\eta e}{h\nu_s}\right)\sqrt{2P_1P_2} \qquad \{3.9\}$$

Now, if P_1=P_{LO} is the local oscillator power and P_2=P_B is the backscattered Brillouin signal power, then the rf power, at frequency $(\nu_B - \nu_{LO})$, $P_{rf} = i_{sig}^2 R$ is given by

$$P_{rf} = i_{sig}^2 R = \left(\frac{\eta e}{h\nu_s}\right)^2 \cdot 2RP_{LO}P_B \qquad \{3.10\}$$

This is true for two single Fourier components. However, we will now consider two interacting signals with finite lineshape. The power spectrum for such a signal, shifted to be centred at $\nu = 0$, is defined as

$$S(\nu) = \frac{P \cdot L(\nu)}{\int_{-\infty}^{\infty} L(\nu)\, d\nu} \qquad \{3.11\}$$

where $L(\nu)$ is the lineshape function, again centred at $\nu = 0$, and P is the total signal power. The rf power spectrum $S_{rf}(f)$, is found by summing all the rf frequency components (Equation {3.10}) in the two spectra which are separated by $|f|$. Since relative frequencies of both f and $-f$ must be included, the power spectrum is given by

$$S_{rf}(f) = \left(\frac{\eta e}{h\nu_s}\right)^2 2R\left[\int_{-\infty}^{\infty} S_{LO}(\nu - \nu_{LO}) \cdot S_B(\nu - \nu_B + f)\, d\nu + \int_{-\infty}^{\infty} S_{LO}(\nu - \nu_{LO}) \cdot S_B(\nu - \nu_B - f)\, d\nu\right] \qquad \{3.12\}$$

which is valid for all f>0. Substituting $\delta\nu_B = \nu_B - \nu_{LO}$ gives

$$\begin{aligned} S_{rf}(f) &= \left(\frac{\eta e}{h\nu_s}\right)^2 \cdot 2R \cdot \left[\int_{-\infty}^{\infty} S_{LO}(\nu - \nu_{LO}) \cdot S_B(\nu - \nu_{LO} - \delta\nu_B + f)\, d\nu + \right. \\ &\qquad \left. \int_{-\infty}^{\infty} S_{LO}(\nu - \nu_{LO}) \cdot S_B(\nu - \nu_{LO} - \delta\nu_B - f)\, d\nu\right] \qquad \{3.13\} \\ &= \left(\frac{\eta e}{h\nu_s}\right)^2 \cdot 2R \cdot \left[\int_{-\infty}^{\infty} S_{LO}(\nu) \cdot S_B(\nu - \delta\nu_B + f)\, d\nu + \int_{-\infty}^{\infty} S_{LO}(\nu) \cdot S_B(\nu - \delta\nu_B - f)\, d\nu\right] \end{aligned}$$

Using Equation {3.11} this becomes

$$S_{rf}(f)=\left(\frac{\eta e}{h\nu_s}\right)^2\cdot\frac{2P_{LO}P_BR}{\int_{-\infty}^{\infty}L_{LO}(\nu)\,d\nu\int_{-\infty}^{\infty}L_B(\nu)\,d\nu}\left(\int_{-\infty}^{\infty}L_{LO}(\nu)\cdot L_B(\nu-\delta\nu_B+f)\,d\nu+\int_{-\infty}^{\infty}L_{LO}(\nu)\cdot L_B(\nu-\delta\nu_B-f)\,d\nu\right) \quad \{3.14\}$$

where $L_{LO}(\nu)$ and $L_B(\nu)$ are lineshapes of the local oscillator and signal, respectively, and P_{LO} and P_B are the total powers. The first integral in the numerator is a shifted cross-correlation of the two lineshapes, the second is a mirror image in frequency of a shifted cross-correlation of the two lineshapes. Assuming the local oscillator is a delta function, approximating a very narrow source linewidth, for ease of calculation, this simplifies to

$$S_{rf}(f)=\left(\frac{\eta e}{h\nu_s}\right)^2\cdot\frac{2P_{LO}P_BR}{\int_{-\infty}^{\infty}L_B(\nu)\,d\nu}\left(L_B(f-\delta\nu_B)+L_B(-f-\delta\nu_B)\right) \quad \{3.15\}$$

For the anti-Stokes signal, since f is positive, $\delta\nu_B$ =11GHz and the Brillouin linewidth, $\Delta\nu_B$=35MHz, the second term in the brackets is negligible for all relevant f. For a Lorentzian profile, the second term is >26dB down over the frequency range 10–12GHz and >40dB down for the range 10.8–11.2GHz. For the Stokes signal, $\delta\nu_B$ =–11GHz and the first term is negligible. The anti-Stokes rf spectrum is therefore the same shape as the anti-Stokes Brillouin spectrum and the shape of the Stokes rf spectrum is the mirror image of that of the Stokes Brillouin spectrum. Both spectra are centred at $\delta\nu_B$. The peak rf power in a detection bandwidth B_e is then given, for a symmetrical Brillouin spectrum, where $L_B(f)= L_B(-f)$, by

$$P_{rf}^{peak}=\int_{|\delta\nu_B|-B_e/2}^{|\delta\nu_B|+B_e/2}S_{rf}(f)\,df=\left(\frac{\eta e}{h\nu_s}\right)^2\cdot\frac{2P_{LO}P_sR\int_{|\delta\nu_B|-B_e/2}^{|\delta\nu_B|+B_e/2}L_B(f-|\delta\nu_B|)\,df}{\int_{-\infty}^{\infty}L_B(\nu)\,d\nu} \quad \{3.16\}$$

where $|\delta\nu_B|$ =11GHz for both anti-Stokes and Stokes signals.

For the Lorentzian profile of the Brillouin signal, this simplifies to

$$P_{rf}^{peak} = \left(\frac{\eta e}{h\nu_s}\right)^2 \cdot 2P_{LO}P_B R \cdot \frac{\int_{|\delta\nu_B|-B_e/2}^{|\delta\nu_B|+B_e/2} \frac{1}{\left(2(f-|\delta\nu_B|)/\Delta\nu_B\right)^2+1} df}{\int_{-\infty}^{\infty} \frac{1}{(2\nu/\Delta\nu_B)^2+1} d\nu} \qquad \{3.17\}$$

where $\Delta\nu_B$ is the Brillouin linewidth. Since the integral of a Lorentzian is an arctangent function, this becomes

$$P_{rf}^{peak} = \left(\frac{\eta e}{h\nu_s}\right)^2 \cdot 2P_{LO}P_B R \cdot \frac{\left[\frac{\Delta\nu_B}{2}\tan^{-1}\left(2(f-|\delta\nu_B|)/\Delta\nu_B\right)\right]_{|\delta\nu_B|-B_e/2}^{|\delta\nu_B|+B_e/2}}{\frac{\pi}{2}\Delta\nu_B}$$

$$= \left(\frac{\eta e}{h\nu_s}\right)^2 \cdot 2P_{LO}P_B R \cdot \frac{\left(\tan^{-1}(B_e/\Delta\nu_B) - \tan^{-1}(-B_e/\Delta\nu_B)\right)}{\pi} \qquad \{3.18\}$$

$$= \left(\frac{\eta e}{h\nu_s}\right)^2 \cdot 2P_{LO}P_B R \cdot \frac{2\tan^{-1}(B_e/\Delta\nu_B)}{\pi}$$

which for all bandwidths, $B_e < 0.3\Delta\nu_B$, simplifies, with an accuracy of 97% or greater, to

$$P_{rf}^{peak} = \left(\frac{\eta e}{h\nu_s}\right)^2 \cdot 2P_{LO}R \cdot P_B \frac{2B_e}{\pi\Delta\nu_B} \qquad \{3.19\}$$

This is equivalent to having a Brillouin signal of $P_B^{\text{det}} = 2B_e P_B/(\pi\Delta\nu_B)$ instead of P_B. This is the Brillouin signal contained within the central B_e of its spectrum

$$P_{rf}^{peak} = \left(\frac{\eta e}{h\nu_s}\right)^2 \cdot 2P_{LO}R \cdot P_B^{\text{det}} \qquad \{3.20\}$$

$$\text{where} \quad P_B^{\text{det}} = \frac{2B_e}{\pi\Delta\nu_B} P_B$$

From Equations {3.14} and {3.20}, it can be seen that, on heterodyning

1. The peak rf power for two signals, each of fixed lineshape, is proportional to the product of the power in each.

2. The peak power is proportional to the ratio of rf detection bandwidth to Brillouin spectral width, for a given total Brillouin power.

3. The shape of the rf power spectrum is given by the sum of cross-correlations of the two lineshapes.

With the ESA set to a resolution bandwidth of 5MHz and a video bandwidth of 3MHz, the spatial resolution is dictated by the video bandwidth and the fraction of total power detected at the peak Brillouin frequency, $2B_e/(\pi\Delta\nu_B)$, is dictated by the resolution bandwidth.

3.8 Polarisation Effects

The theory outlined in §3.7 is only valid for two interfering beams of the same polarisation. If the polarisation states are different, however, the interference will not be complete and reduces to zero for orthogonal polarisations. If the polarisation state of the Brillouin backscatter signal were constant, a polarisation controller could be used on the local oscillator to maximise the interference. However, as mentioned in §2.2.4, standard single-mode optical fibre has low, but non-negligible, birefringence and the polarisation states of both the input pulse and the backscatter signal are affected by this. The backscatter signal therefore has a different polarisation and therefore a different heterodyne efficiency depending on its point of origin within the fibre. Fibre birefringence changes only slowly with time so the noise on the trace resembles coherent Rayleigh noise and will not be reduced significantly by temporal averaging. This noise is peculiar to heterodyne detection (or to direct detection using a highly polarisation-sensitive receiver). There is, however, no persistent component of coherent noise in the Brillouin trace due to each scattering centre producing a

different phase shift at the detector. This is because the scattering centres are not fixed in space, as are the density fluctuations in Rayleigh scattering, but occur where there is an interaction with a phonon. Each trace will therefore have different phase noise characteristic and averaging over many traces will remove this component of the noise.

This type of noise can be reduced by using

- Frequency Shift Averaging (FSAV, as mentioned in §2.2.4)
- Two orthogonal polarisations
- Polarisation scrambling

Frequency shift averaging is cumbersome to execute and requires averaging at many separate laser frequencies as well as a lack of frequency sensitive components within the system. It would take 100 separate trace measurements to reduce noise by a factor of 10. Alternatively, two traces may be taken at orthogonal polarisations of either the sensing pulses or local oscillator. It can be shown that if this is reliably achieved, polarisation noise can be eliminated. However, in practice, it is difficult to attain sufficient system stability that the states remain reliably orthogonal without need of frequent re-adjustment. Polarisation scrambling, on the other hand, is a dynamic process whereby the state of polarisation (SOP) of the input, polarised, radiation is continuously varied in time such that, considered over a sufficiently long averaging time, the output radiation interferes as though unpolarised.

3.8.1 Polarisation Scrambler

To achieve perfect scrambling, all states of polarisation on the Poincaré sphere [3.11] must be represented equally or, equivalently, the percentage degree of polarisation, D, defined using the Stokes parameters (S_0, S_1, S_2, S_3) must be zero. This definition is

$$D = 100 \cdot \frac{\sqrt{S_1^2 + S_2^2 + S_3^2}}{S_0} \qquad \{3.21\}$$

where

$$\begin{aligned} S_0 &= \langle E_x^2 \rangle + \langle E_y^2 \rangle \\ S_1 &= \langle E_x^2 \rangle - \langle E_y^2 \rangle \\ S_2 &= \langle 2E_x E_y \cos\Delta\phi \rangle \\ S_3 &= \langle 2E_x E_y \sin\Delta\phi \rangle \\ \Delta\phi &= (\phi_y - \phi_x) \end{aligned} \qquad \{3.22\}$$

for complex amplitudes of x and y components of the electric field given by

$$A_x = E_x e^{i\phi_x} \quad \text{and} \quad A_y = E_y e^{i\phi_y} \qquad \{3.23\}$$

The angle brackets, $\langle\ \rangle$, denote a time average over the measurement interval.

In order to achieve this, the radiation may be passed through a combination of phase plates with temporally varying phase shifts. For example, a scrambler may consist of two variable phase plates with their axes at 45° (a 2-axis scrambler). If a suitable sinusoidally modulating phase difference is provided by each plate, it is possible to achieve near-perfect scrambling. In order to determine the phase shifts which must be applied, the Stokes parameters must be found for the output radiation. In Appendix A, the following expressions were derived for the Stokes parameters of the output radiation from a 2-axis scrambler, in terms of the input radiation properties and the sinusoidally modulating phase differences of the two plates.

$$S_0 = (E_x^{in})^2 + (E_y^{in})^2 \qquad \{A.10\}$$

$$S_1 = \left\langle (E_x^{in})^2 - (E_y^{in})^2 \right\rangle \left\langle \cos(B\cos\omega_2 t) \right\rangle + 2E_x^{in}E_y^{in} \left\langle \sin(B\cos\omega_2 t)\sin(A\cos\omega_1 t - \Delta\phi_{in}) \right\rangle \qquad \{A.11\}$$

$$S_2 = 2E_x^{in}E_y^{in} \left\langle \cos(A\cos\omega_1 t - \Delta\phi_{in}) \right\rangle \qquad \{A.17\}$$

$$S_3 = \left\langle 2\left(\mathrm{Im}(A_y^{out})\mathrm{Re}(A_x^{out}) + \mathrm{Re}(A_y^{out})\mathrm{Im}(A_x^{out})\right) \right\rangle \qquad \{A.18\}$$

where

$$\begin{aligned}
\mathrm{Re}(A_x^{out}) &= \tfrac{1}{2}E_x^{in}\cos(B\cos\omega_2 t + A\cos\omega_1 t) + \tfrac{1}{2}E_y^{in}\cos(B\cos\omega_2 t + \Delta\phi_{in}) \\
&\quad + \tfrac{1}{2}\left(E_x^{in}\cos(A\cos\omega_1 t) - E_y^{in}\cos(\Delta\phi_{in})\right) \\
\mathrm{Im}(A_x^{out}) &= \tfrac{1}{2}E_x^{in}\sin(B\cos\omega_2 t + A\cos\omega_1 t) + \tfrac{1}{2}E_y\sin(B\cos\omega_2 t + \Delta\phi_{in}) \\
&\quad + \tfrac{1}{2}\left(E_x^{in}\sin(A\cos\omega_1 t) - E_y^{in}\sin(\Delta\phi_{in})\right) \\
\mathrm{Re}(A_y^{out}) &= \tfrac{1}{2}E_x^{in}\cos(B\cos\omega_2 t + A\cos\omega_1 t) + \tfrac{1}{2}E_y^{in}\cos(B\cos\omega_2 t + \Delta\phi_{in}) \\
&\quad - \tfrac{1}{2}\left(E_x^{in}\cos(A\cos\omega_1 t) - E_y^{in}\cos(\Delta\phi_{in})\right) \\
\mathrm{Im}(A_y^{out}) &= \tfrac{1}{2}E_x^{in}\sin(B\cos\omega_2 t + A\cos\omega_1 t) + \tfrac{1}{2}E_y^{in}\sin(B\cos\omega_2 t + \Delta\phi_{in}) \\
&\quad - \tfrac{1}{2}\left(E_x^{in}\sin(A\cos\omega_1 t) - E_y^{in}\sin(\Delta\phi_{in})\right)
\end{aligned} \qquad \{A.19\}$$

It can be seen that S_0 of the output radiation merely demonstrates conservation of energy. The scrambler was assumed lossless and so the output intensity equals the input intensity. In order for S_2=0 for any input polarisation state the following condition must be satisfied

$$\begin{aligned}
&\left\langle \cos(A\cos\omega_1 t - \Delta\phi_{in}) \right\rangle = 0 \\
\text{i.e.}\quad &\left\langle \cos(A\cos\omega_1 t)\cos(\phi_{in}) + \sin(A\cos\omega_1 t)\sin(\phi_{in}) \right\rangle = 0 \\
\text{i.e.}\quad &\left\langle \cos(A\cos\omega_1 t) \right\rangle = 0 \quad \text{and} \quad \left\langle \sin(A\cos\omega_1 t) \right\rangle = 0
\end{aligned} \qquad \{3.24\}$$

Solving these last two equations numerically, by integrating over a single period of the modulation, gives

$$A = 0.76548\pi \qquad \{3.25\}$$

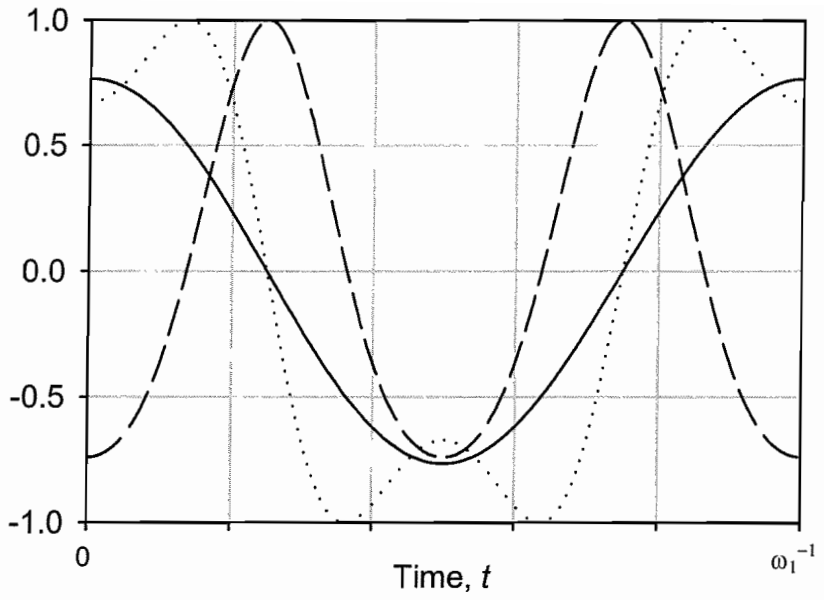

Figure 3.9 Graph showing the functions $\cos(A\cos\omega_1 t)$ and $\sin(A\cos\omega_1 t)$ for A=0.76548π including calculated values of the time average of these functions over 400 points per period showing good agreement with the conditions in Equation {3.24}.

The solutions to these two equations are illustrated in Figure 3.9, where it can be seen that indeed each time average over 400 points in a single period is very small. There is, as yet, no restriction on ω_1. However, in order for S_1=0, both of the following must be satisfied.

$$\langle\cos(B\cos\omega_2 t)\rangle = 0$$
$$\text{and} \qquad \langle\sin(B\cos\omega_2 t)\sin(A\cos\omega_1 t - \Delta\phi_{in})\rangle = 0 \qquad \{3.26\}$$

Now, the first of these conditions gives, as before, the condition

$$B = A = 0.76548\pi \qquad \{3.27\}$$

The second condition is only satisfied if $\omega_2 \neq \omega_1$. This can be seen in Figure 3.10, which shows, for $\Delta\phi_{in} = 0$, the function $\sin(0.76548\pi\cos\omega_2 t)\sin(0.76548\pi\cos\omega_1 t - \Delta\phi_{in})$, over a $10\omega_1^{-1}$ span, for both (a) $\omega_2=\omega_1$ and (b) $\omega_2=(1.1)\omega_1$. It can be seen that it is only in the latter case where the average over the entire waveform (again 400 points per

ω_1^{-1}) is negligible. A plot of these averages versus $\Delta\phi_{in}$ is shown in Figure 3.10(c) and Figure 3.10(d) for $\omega_2=\omega_1$ and $\omega_2=(1.1)\omega_1$, respectively. It can be seen that, in the latter case, the time average is negligible for all input phase differences, $\Delta\phi_{in}$, between *x* and *y* components. It can also be shown that many other values of ω_2/ω_1 also have this property, although $\omega_2/\omega_1=2n-1$ or $\omega_1/\omega_2=2n-1$ should be avoided.

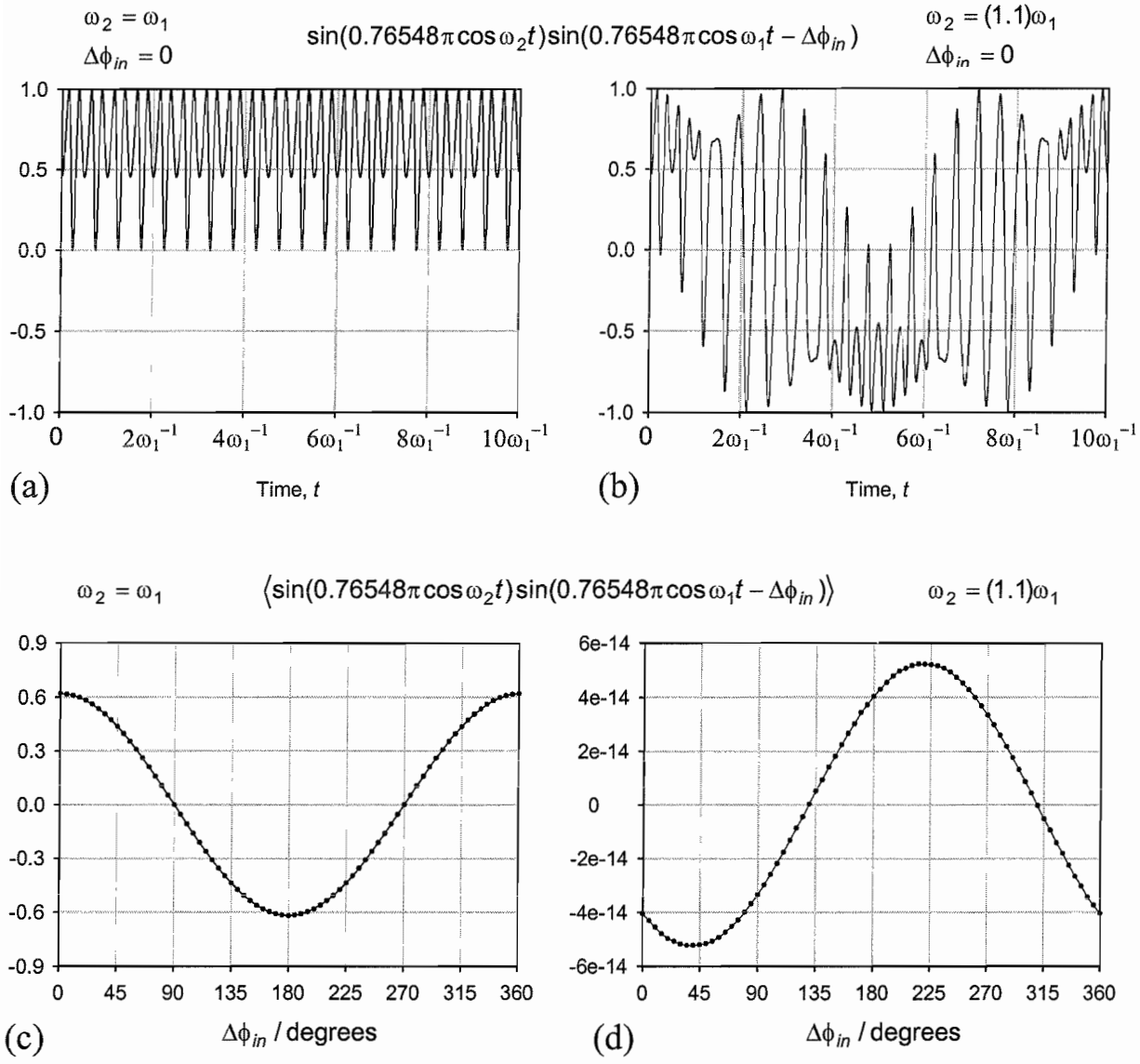

Figure 3.10 Graphs showing the function $\sin(A\cos\omega_1 t)\sin(B\cos\omega_2 t-\Delta\phi_{in})$ for $A=B=0.76548\pi$ for the cases (a) $\omega_2=\omega_1$ and $\Delta\phi_{in}=0$, (b) $\omega_2=(1.1)\omega_1$ and $\Delta\phi_{in}=0$. Also shown are the numerically calculated time averages of this function over 10 periods (ω_1^{-1}) at 400 points per period for (c) $\omega_2=\omega_1$ and $\Delta\phi_{in}=0$, (d) $\omega_2=(1.1)\omega_1$ and $\Delta\phi_{in}=0$.

Now that we have values for A, B, ω_1 and ω_2 which allow $S_1 \approx 0$ and $S_2 \approx 0$, we must check the overall % degree of polarisation, as defined in Equation {3.21}, for these values. This DOP is illustrated in Figure 3.11(b), for all $\Delta\phi_{in}$ and all E_x^{in} components and shows that the scrambling is good independent of the input polarisation state. Figure 3.11(a) shows the equivalent DOP plot for the case $\omega_2 = \omega_1$, which is clearly not satisfactory, since the DOP rises to over 60% for some input polarisation states.

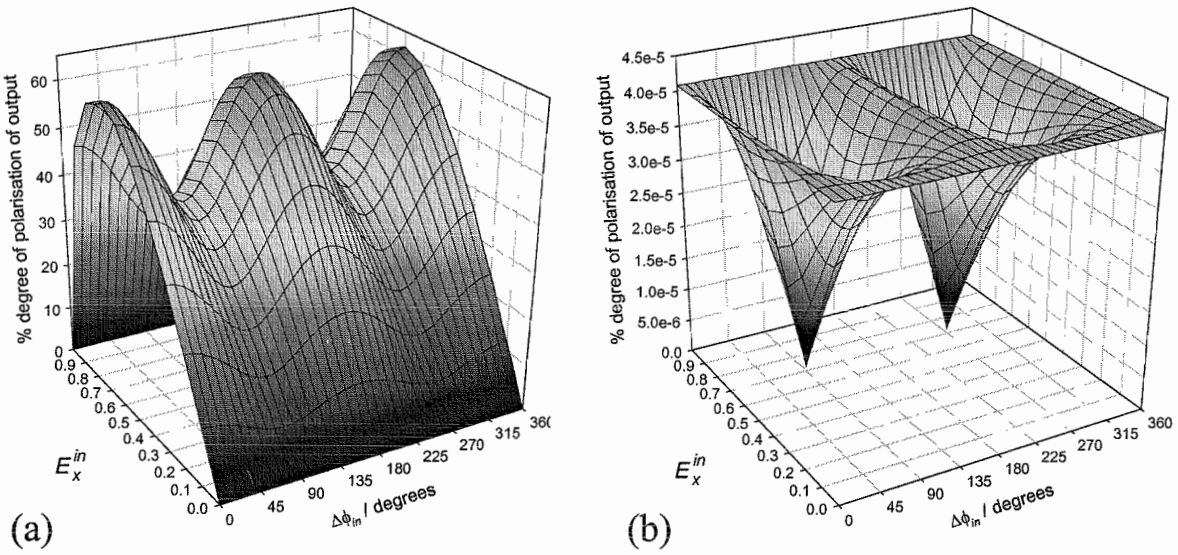

Figure 3.11 Calculated overall degree of polarisation, for all input polarisation states (characterised by E_x^{in} and $\Delta\phi_{in}$) of the output radiation from an ideal 2-axis polarisation scrambler for (a) $\omega_2 = \omega_1$ and (b) $\omega_2 = (1.1)\omega_1$.

Since the actual experimental parameters will not be perfect, it is commonplace to add a third phase plate to the end of the scrambler, at 90° to the first, and modulate its phase difference at a third frequency, ω_3, unrelated to ω_1 and ω_2 and with the same 0.76548π amplitude. The scramblers used in this work are mostly of this 3-axis variety. The phase plates are either liquid crystal cells, to each of which a voltage is applied, or fibre-based, in which either the length of high birefringence fibre is modulated in length or standard fibre is modulated in birefringence, both using piezoelectric transducers.

3.9 Brillouin Frequency Shift Dependence on Source Wavelength

As an initial test of the detection system, heterodyne detection of Brillouin backscattered radiation was carried out cw, in the stimulated regime, to ensure a large signal.

To this end, the 300μW output from a 1550nm-band, tunable, external cavity BT&D semiconductor laser was amplified to 10mW using an EDFA. The laser specifications state a centre wavelength of 1535nm, a tuning range of 40nm and a linewidth of 100kHz. This narrow linewidth is well within the Brillouin gain bandwidth (typically 35MHz) ensuring a lack of linewidth-related increase in stimulated threshold. 5mW of the amplified signal, launched via a 50/50 fibre coupler into a 34km length of standard single-mode fibre, was therefore sufficient to generate significant stimulated scattering (§2.4.4.1). The other half was used as the optical local oscillator signal and mixed with the backscatter using a further 50/50 fibre coupler. The backscattered optical power was monitored via a 5% tap prior to heterodyne mixing. The experimental configuration is shown in Figure 3.12.

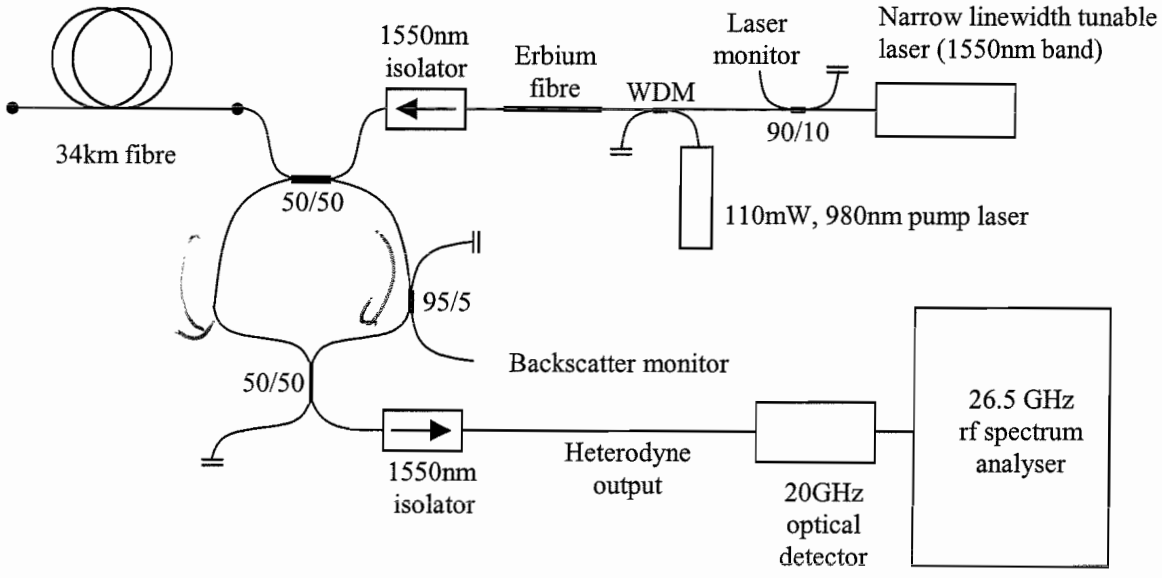

Figure 3.12 Experimental heterodyne configuration for Brillouin frequency shift measurement as a function of pump wavelength. Continuous wave, stimulated Brillouin scattering was generated using 34km fibre and heterodyne measurements made at ~11GHz.

An optical isolator was placed at the heterodyne output to prevent coherent etalon intensity fluctuation effects due to repeated reflections from the cleaved fibre end and what is essentially a Sagnac loop mirror (Appendix B). An angle polished fibre end would have achieved a similar result, but would have complicated optical coupling into the fibre-coupled 20GHz detector.

The heterodyne signal was easily visible and a sample spectrum is presented in Figure 3.13 for an optical local oscillator power of 1.6mW and total backscatter power of 4.6μW at the detector (equivalent to 37.5μW from the fibre itself). The heterodyne peak is situated at 10.86GHz, with a pump wavelength of 1552.4nm.

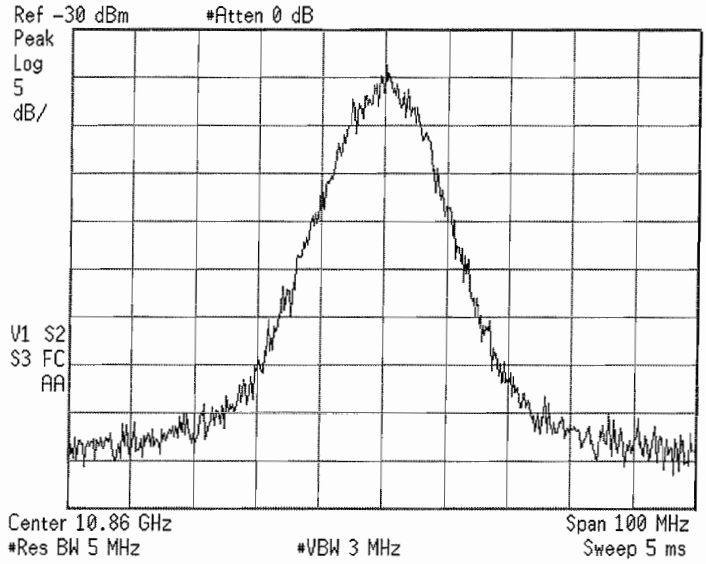

Figure 3.13 Stimulated Brillouin heterodyne lineshape using the experimental arrangement shown in Figure 3.12.

The laser was then tuned over a 30nm range in order to calibrate the Brillouin frequency shift with wavelength. Figure 3.14 shows the dependence of the frequency shift on wavenumber, which is linear with a slope of 1.686MHz·cm (equivalent to a change in Brillouin frequency shift of −7.2MHz per nanometre increase in pump wavelength). This is expected from Equation {2.17} in §2.4.1 and the corresponding value for the product of refractive index and speed of sound within the fibre is calculated as 8430ms^{-1}, giving $V_A = 5774\text{ms}^{-1}$ for $n = 1.46$, which is of the same order as the published values of 5835ms^{-1} (for n=1.46) [3.12] and 5960ms^{-1} [3.13]. For information, the Brillouin frequency shift is 11.0GHz for a pump wavelength of 1532.7nm.

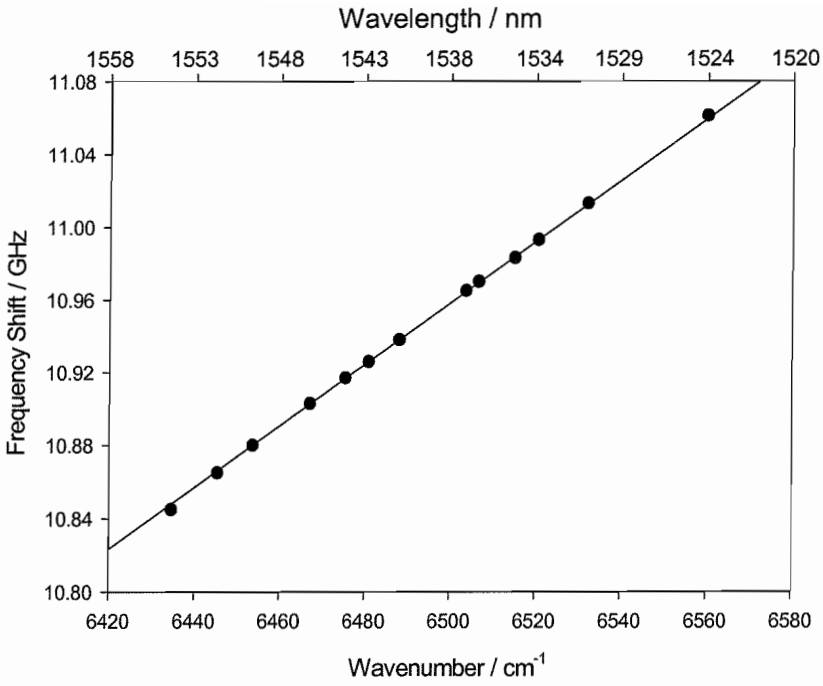

Figure 3.14 Brillouin frequency shift as a function of pump wavenumber as measured using the experimental arrangement in Figure 3.12. Equivalent wavelength values are given to the nearest nm at the top of the plot.

3.10 The First Sensor

The first sensor design, based upon the components detailed in this chapter is shown in Figure 3.15. Radiation from the tunable laser was amplified by EDFA1 and split using a 50/50 coupler into local oscillator and pulse arms. The pulses were formed using a 110MHz downshifting AOM and amplified by EDFA2 before being launched into the sensing fibre via a 3 port optical circulator.

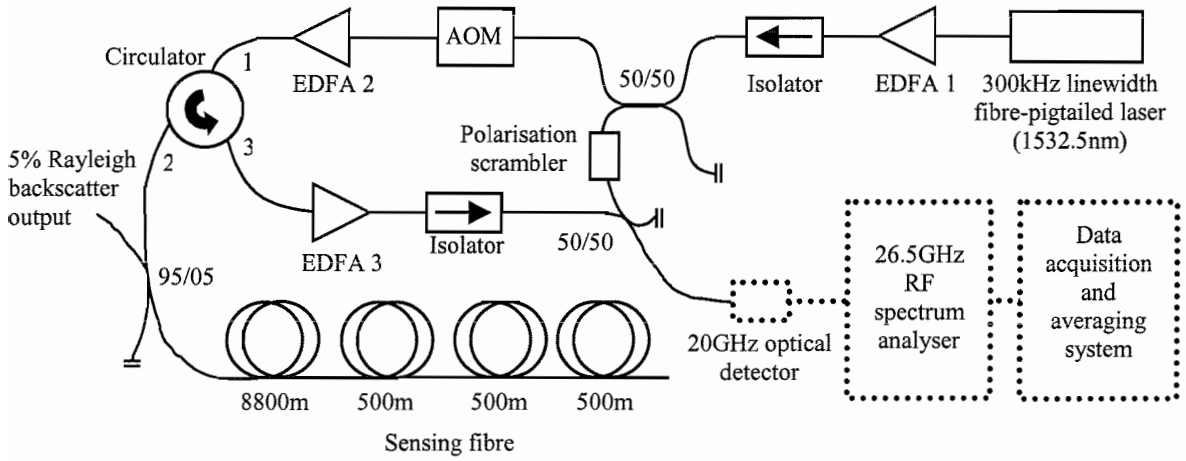

Figure 3.15 The First Sensor.

The backscattered Rayleigh was monitored from a 5% tap before the backscatter returns to the circulator and passed to EDFA3 (small-signal gain 26.4dB) for pre-amplification prior to mixing with the local oscillator. Pre-amplification was necessary to achieve a large enough signal-to-noise ratio for practical sensing purposes (see Chapter Four). The mixed radiation was detected and the spectrum analyser used to form the beat frequency traces. The polarisation state of the local oscillator was scrambled during heterodyne trace collection. The scrambler used was a commercial product, where an independent scrambling voltage was applied to each of three liquid crystals cells. Local oscillator power at the detector was 1mW and the source wavelength was 1532.5nm

The sensing fibre consisted of four fibre sections of 8800m, 500m, 500m and 500m spliced together with the second section being heated to a temperature of 67°C whilst the remaining fibre remained at the ambient room temperature of 22°C. Since the expected Brillouin frequency shift for the wound drums at room temperature for a 1532.5nm source is 11.0GHz, the anti-Stokes signal should be centred at 10.89GHz and the Stokes signal at 11.11GHz due to the 110MHz downshift of the AOM. Pulses of power 150mW and length 200ns were launched down the sensing fibre and sample backscatter traces are shown in Figure 3.16 for both the anti-Stokes radiation and the broad-band Rayleigh (achieved by switching off the tunable laser). Each trace was averaged 65536 times. The recorded backscatter trace at 10.89GHz corresponds approximately to the anti-Stokes peak frequency.

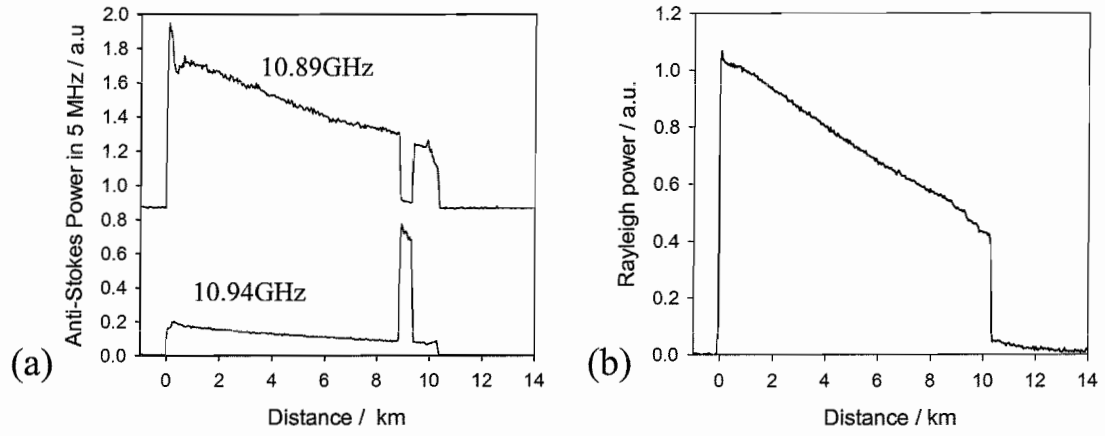

Figure 3.16 Recorded backscatter traces from the sensor illustrated in Figure 3.15. (a) Anti-Stokes traces, taken at both 10.89GHz and 10.94GHz, corresponding to the expected peak frequency shifts of the unheated and heated fibre lengths, respectively. An artificial offset has been added to the 10.89GHz trace to separate the plots, for clarity. (b) Broad-band Rayleigh trace, showing potential capability of the sensor to achieve normalisation for intrinsic fibre loss.

The expected frequency shift for the heated fibre is ~50MHz (at ~1.1MHz/K) and the trace recorded at this frequency indeed shows a peak at the position of the heated fibre with a corresponding trough at 10.89GHz. There is also a peak at the start of the 10.89GHz trace, which can be attributed to a lower Brillouin shift due to absence of strain at this point in the sensing fibre, prior to the wound drums. This also indicates that the peak anti-Stokes frequency for the wound fibre differs from 10.89GHz, which is instead the peak frequency at the fibre's near end.

3.11 Data processing

In order to build up a set of complete distributed spectra, traces must be collected for the whole range of frequencies of interest. The resulting set of frequency data must then be processed in order to determine the Brillouin spectrum at each point along the fibre. Data is collected as an rf voltage, which means that, since the Brillouin power is proportional to rf power, each trace must first be squared before use.

There is an interpulse voltage between successive backscatter traces which must be compensated for. Since the analyser is not stable, the interpulse level and also the gain may be different for each frequency and so, by scaling to this level, which is assumed constant (due to broad-band ASE beat spectra – see Chapter Four) over the small frequency spans used, compensation can be made for changes in gain. The interpulse level is then removed. The efficacy of this procedure may be verified by calculating the Brillouin power backscatter trace and comparing the loss per km to that expected. First, however, the Brillouin power must be extracted from the recorded spectra. There are several potential methods of achieving this.

Peak Power

This is the easiest power measurement to perform and would be valid if the Brillouin spectrum were to remain of the same linewidth and shape for every point along the fibre. However, it has been found that the backscattered Brillouin linewidth and/or shape changes as the pulse propagates down the fibre due to, for example, temperature changes, mild self-phase modulation or variation in temperature or strain within the spatial resolution.

Sum over Frequency Range

This is another, relatively simple measurement to make, where the power in every frequency trace at each point along the fibre is summed, forming a crude integral of the spectrum over the data frequency range. There are also disadvantages to this method of approach, in that the power measurement obtained will be inaccurate if a significant proportion the Brillouin spectrum lies outside the frequency range of interest. This proportion will vary depending on the exact Brillouin shift at that point and so compensation cannot easily be made. Spontaneous Brillouin spectra are Lorentzian in shape (this will be verified in §5.2.3) so the power does not decay quickly with frequency (a Lorentzian has broad wings), and this problem is particularly troublesome. The proportion of the spectrum within the measured frequency range will also depend upon the Brillouin linewidth so problems akin to those for measuring the peak power arise.

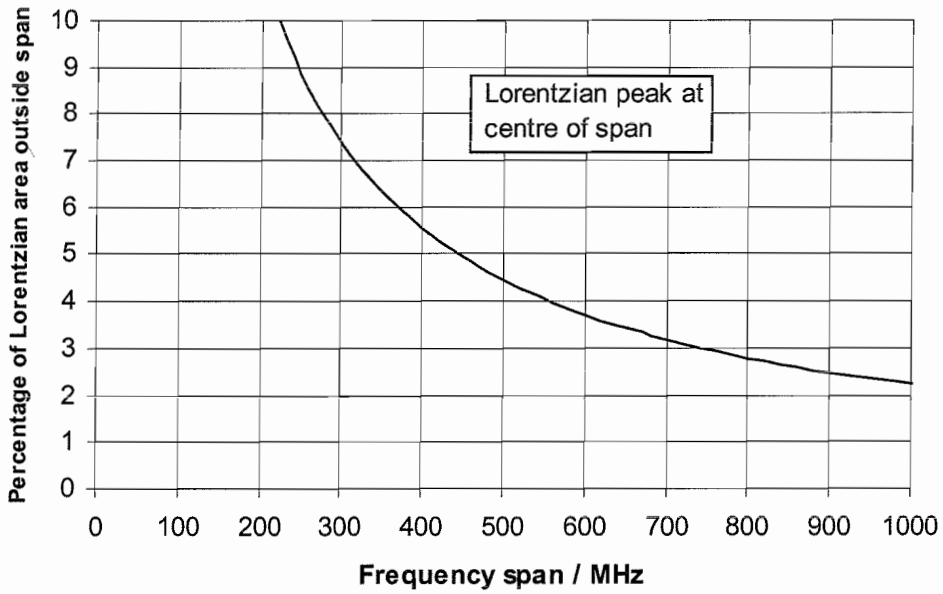

Figure 3.17 Theoretical percentage of Lorentzian area excluded from the integral over a given frequency span as a function of that frequency span. The Lorentzian peak is at the centre of the span.

Figure 3.17 shows the theoretical percentage of the Lorentzian area outside the frequency span of detection for a Lorentzian curve of 35MHz linewidth with its peak at the centre of the span (the integral of a Lorentzian is an arctangent function – see §3.7). It can be seen that even using a 1GHz span (±500MHz) there is still over 2%

of the spectrum excluded from the range. Now, imagine that the range of Brillouin shifts to be measured by the sensor is 200MHz (±100MHz from span centre), corresponding to 200K or 4000με. In this case, for a total span of 300MHz, the percentage excluded Lorentzian area as a function of peak frequency offset from the centre of the span is shown in Figure 3.18. This shows a 5.6% change in excluded area over the 100MHz Brillouin shift range, which is equivalent to over 15K temperature error. In order to reduce this error to 1K, the span must be increased to 648MHz, over three times the frequency shift range to be measured – see Figure 3.19.

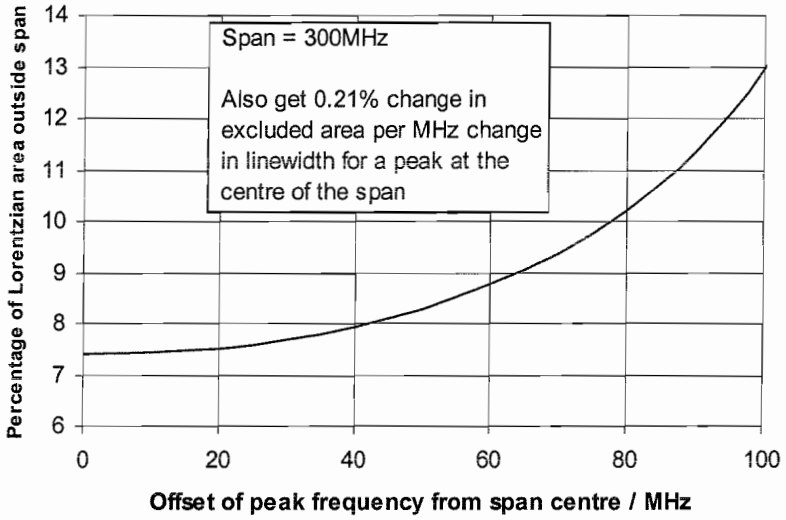

Figure 3.18 Percentage of excluded Lorentzian area as a function of its peak frequency offset from the span centre (for a span of 300MHz and a Lorentzian linewidth of 35MHz)

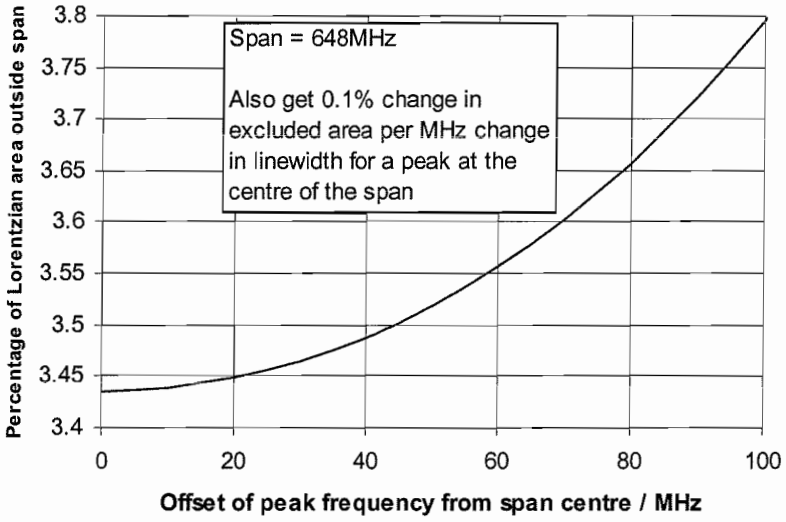

Figure 3.19 Percentage of excluded Lorentzian area as a function of its peak frequency offset from the span centre (for a span of 648MHz and a Lorentzian linewidth of 35MHz)

The change in excluded area may also be calculated for a change in linewidth of a peak at the span centre. For a 300MHz span, the change in excluded area per MHz change in linewidth is 0.21%. For a 648MHz span, the change is 0.1% per MHz change in linewidth. Changes in linewidth of a few MHz are observed for temperature changes of several tens of Kelvin or more over long fibre lengths (see §5.7) and so, even for the larger span, errors in power measurement corresponding to ~1K could be expected due to this effect.

Curve Fitting

Use a curve fitting algorithm and calculate the area under the curve. This method fits a Lorentzian function to the recorded spectral data then mathematically calculates the area under the fitted curve. The area under a Lorentzian curve is proportional to its peak power multiplied by its linewidth. The algorithm chosen was the Levenberg-Marquardt algorithm [3.14] [3.15]. This method has the advantage that the correct area will be determined even if some of the function lies outside the frequency range of the scan, provided there is sufficient data for a good fit. Another advantage to this method is that it also provides the frequency shift information to a higher resolution than the frequency step used in the scan.

Lorentzian curve fitting was therefore chosen as the optimum method of spectrum processing to obtain the required power and frequency shift measurements. Examples of processed spectra will be shown in Chapter Five, along with distributed sensing results, but firstly Chapter Four will provide a theoretical analysis of the sensor's performance.

3.12 Conclusions

In this chapter, the constituents of a prototype microwave coherent Brillouin sensor were described and the preliminary results from such a sensor were presented, although as yet no full sensing results have been demonstrated. The chapter also included a discussion of heterodyne theory, polarisation properties of the backscatter

and processing methods to extract the required frequency shift and power information from the collected data.

The sensor itself will be investigated with a more experimental approach in Chapter Five, where temperature and strain sensing results will be discussed. Firstly, however, Chapter Four will provide a detailed theoretical analysis of the performance of the sensor.

3.13 References

[3.1] J.K.A. Everard: "Coherent detection of stimulated Brillouin backscatter on photoconductive three-wave mixer for sensing applications", *Electronics Letters*, Vol. 25, No. 18, pp. 1236-1237 (August 1989)

[3.2] N.N. Ghogomu and J.K.A. Everard: "Coherent photoconductive detection of Brillouin scattering for temperature sensing", *Electronics Letters*, Vol. 31, No. 18, pp. 1606-1607 (August 1995)

[3.3] T. Okoshi, K. Kikuchi and A. Nakayama: "Novel method for high resolution measurement of laser output spectrum", *Electronics Letters*, Vol. 16, No. 16, pp. 630-631 (July 1980)

[3.4] D. Maydan: "Acoustooptical Pulse Modulators", *IEEE Journal of Quantum Electronics*, Vol. QE-6, No. 1, pp. 15-24 (January 1970)

[3.5] A. Yariv: "Optical Electronics", 4th Edition, *Saunders College Publishing*, ISBN 0-03-053239-6 (1991)

[3.6] H.C. Lefevre: "Single-mode fibre fractional wave devices and polarisation controllers", *Electronics Letters*, Vol. 16, No. 20, pp. 778-780 (September 1980)

[3.7] R.J. Mears, L. Reekie, I.M. Jauncey and D.N. Payne: "Low-noise erbium-doped fibre amplifier operating at 1.54 μm", *Electronics Letters*, Vol. 23, No. 19, pp. 1026-1028 (September 1987)

[3.8] R.I. Laming, S.B. Poole and E.J. Tarbox: "Pump excited-state absorption in erbium-doped fibers", *Optics Letters*, Vol. 13, No. 12, pp. 1084-1086 (December 1988)

[3.9] J.L. Wagener, P.F. Wysocki, M.J.F. Digonnet, H.J. Shaw and D.J. DiGiovanni: "Effects of concentration and clusters in erbium-doped fiber lasers", *Optics Letters*, Vol. 18, No. 23, pp. 2014-2016 (December 1993)

[3.10] L. Reekie, I.M. Jauncey, S.B. Poole and D.N. Payne: "Diode-laser-pumped operation of an Er^{3+}-doped single-mode fibre laser", *Electronics Letters*, Vol. 23, No. 20, pp. 1076-1078 (September 1987)

[3.11] W.A. Shurcliff and S.S. Ballard: "Polarized Light", *D. Van Nostrand*, Section 8, p. 71 (1964)

[3.12] T.-O. Tsun, A. Wada and R. Yamauchi: "Wavelength Dependences of Brillouin Frequency Shifts of Optical Fibres in 1.55μm Wavelength Region", *Electronics Letters*, Vol. 27, No. 19, pp. 1764-1765 (September 1991)

[3.13] Agrawal: "Nonlinear Fiber Optics", Second Edition, *Academic Press* ISBN 0-12-045142-5 (1995)

[3.14] D.W. Marquardt: "An algorithm for least-squares estimation of nonlinear parameters", *Journal of the Society for Industrial and Applied Mathematics*, Vol. 11, No. 2, pp. 431-441 (June 1963)

[3.15] W.H. Press, S.A. Teukolsky, W.T. Vetterling and B.P. Flannery: "Numerical Recipes in C – The Art of Scientific Computing", Second Edn., *Cambridge University Press*, ISBN 0-521-43108-5 (1995)

Chapter Four

Theoretical Analysis of the Sensor

4.1 Introduction

In this chapter we shall consider the performance of three different coherent detection sensors based on the detector and spectrum analyser discussed in the previous chapter and compare them theoretically with three based on direct detection using a double-pass Mach-Zehnder interferometer (§2.4.5.2). We shall compare their performance for identical spatial resolutions (20m) and equal backscattered power (240nW Rayleigh, 4nW anti-Stokes, 4nW Stokes) from the sensing fibre, calculated using Equation {6.3} (an experimentally modified version of Equation {2.6}) for ~160mW pulses at 200ns (the power and pulse length to be used for the sensing measurements presented in Chapter Five). Within both the coherent detection and direct detection subsections, we will consider sensors which detect unamplified backscatter and sensors which use an EDFA to pre-amplify the backscatter prior to detection. In most of these pre-amplified sensors, the amplified backscatter is then filtered using a circulator and fibre Bragg grating combination. This comparison will enable the optimum 11GHz coherent sensing design to be chosen.

Also, we will consider the curve fitting and trace summing methods of total power determination in the chosen coherent sensor and find theoretical relationships between trace signal-to-noise and errors in total power and frequency shift measurement.

4.2 Optical Properties of The Sensing Regimes

4.2.1 Sensor Configurations

The first three sensors to be considered are based on coherent detection and are illustrated in Figure 4.1. In the first sensor (Sensor CU, Figure 4.1(a)), the backscatter

is mixed directly with the local oscillator and no optical amplification is undertaken. In the second sensor (Sensor CA, Figure 4.1(b)), an EDFA is used to amplify the backscatter prior to mixing with the local oscillator. In this case, an extra 50/50 coupler is required to ensure that the LO does not itself pass through the pre-amplifier, causing saturation. The third sensor (Sensor CAF Figure 4.1(c)) also employs pre-amplification, but in this case, a fibre Bragg grating (FBG1) is used to filter the amplified backscatter, reducing the ASE power incident on the detector.

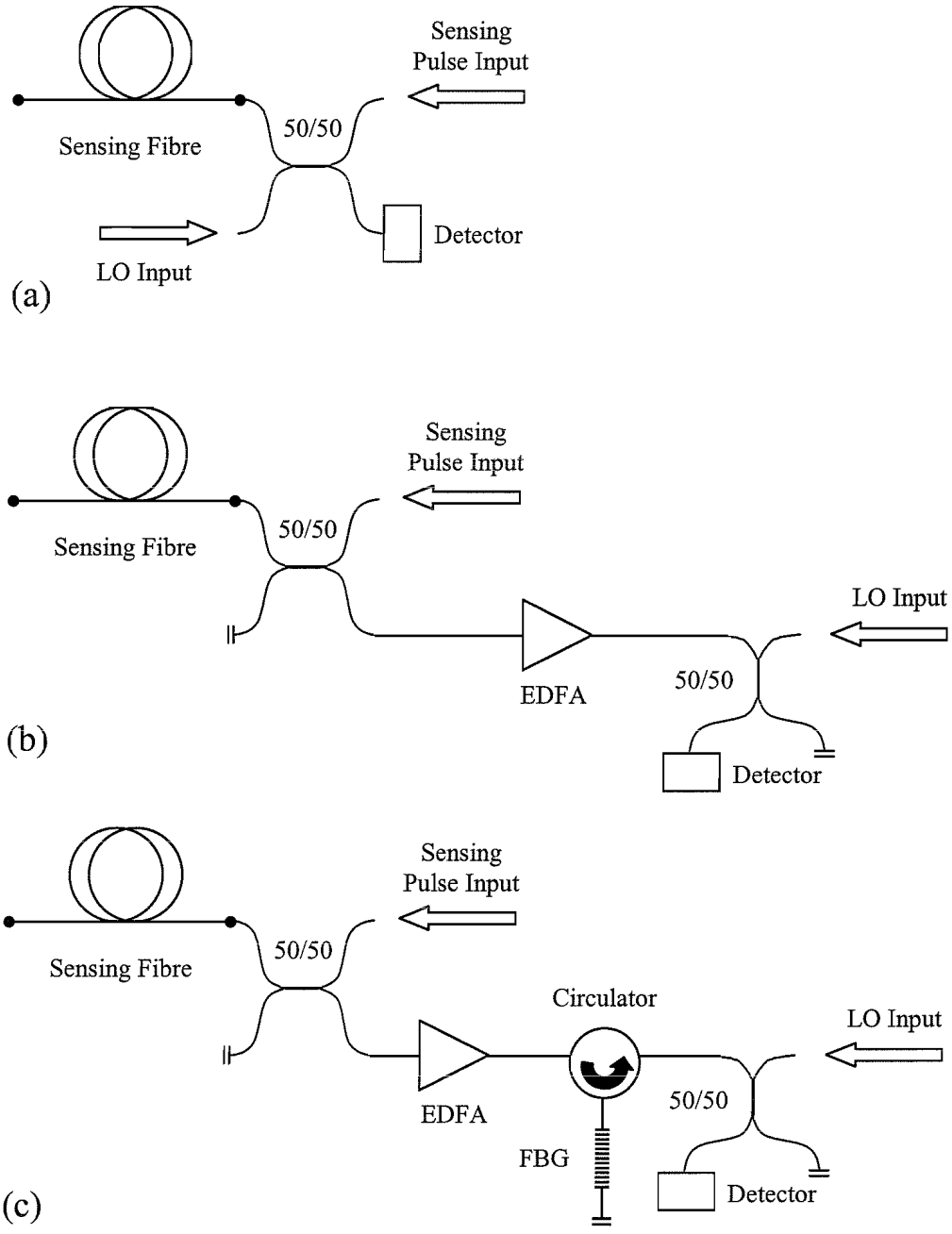

Figure 4.1 Coherent Detection Sensor Configurations

FBG1 is centred on the anti-Stokes frequency and has a linewidth of ~12.8GHz. It causes attenuations of 15dB and 26dB for radiation at the Rayleigh and Stokes frequencies respectively.

The second three sensors are based on direct detection and are illustrated in Figure 4.2. The first of these (Sensor DU, Figure 4.2(a)) is a simple, unamplified direct detection where the backscatter is passed through a double-pass Mach-Zehnder (MZ) interferometer (§2.4.5.2) to filter out the Rayleigh prior to detection of both Stokes and anti-Stokes signals. The second (Sensor DA1, Figure 4.2(b)) employs pre-amplification and filtering of the backscatter prior to passing through the MZ.

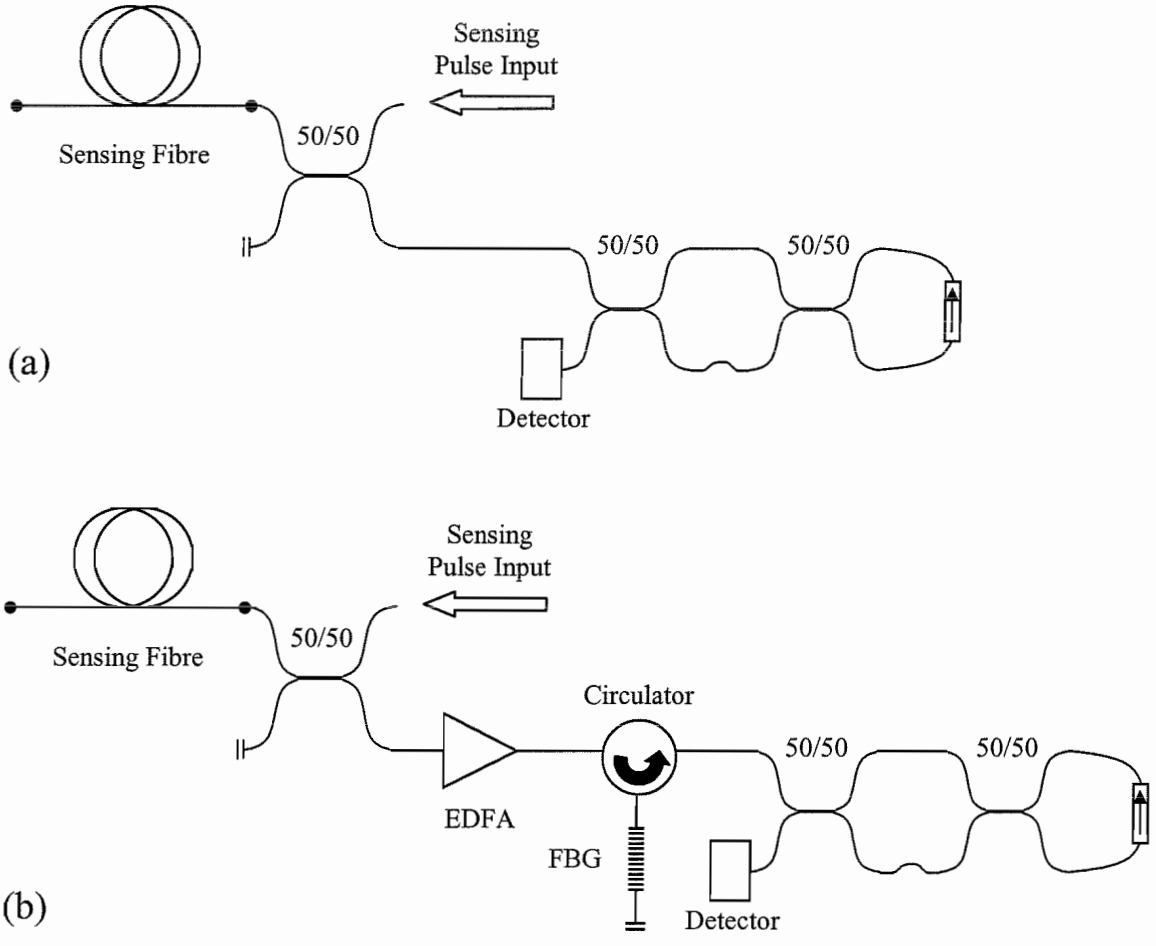

Figure 4.2 Direct Detection Sensor Configurations.

In direct detection optical filtering is essential after amplification since the unfiltered ASE component after the amplifier is ~27dB higher than the maximum amplified Brillouin signal (for a total input Brillouin power of 4nW, a gain of 26.4dB and a total output ASE power of 1mW) which would require a low gain, high noise receiver to avoid saturation and also, even just 1% noise on the ASE signal will correspond to at least 500% noise on the Brillouin signal.

Of course, the MZ will attenuate the unfiltered ASE component by ~0.36 (4.4dB) since the double pass MZ fringe linewidth is 36% of the FSR (see §4.2.2.3), but this still results in an ASE signal 22.6dB larger than the maximum Brillouin signal. Sensor DA1 therefore employs the grating FBG1 mentioned previously, again centred on the anti-Stokes frequency, as in Sensor CAF. This means that the output ASE spectrum from the MZ will consist approximately of a single fringe, centred on the anti-Stokes signal and with linewidth 7.92GHz (=0.36×22GHz). Only the anti-Stokes wavelength is detected in this sensor. In the third direct detection sensor (Sensor DA2, also Figure 4.2(b)), however, both the Stokes and anti-Stokes are detected by using a broader band grating filter (FBG2) centred on the Rayleigh wavelength – this is assumed to have a transmission of unity at the Rayleigh frequency and 0.9 at both Stokes and anti-Stokes frequencies. The bandwidth is such that the ASE spectrum consists of two 7.92GHz fringes, separated by 22GHz.

4.2.2 ASE Powers and Spectra

4.2.2.1 EDFA

This will be used to pre-amplify the backscatter in those sensors which employ this technique. We shall now find a mathematical description of the output ASE power spectrum. According to Desurvire [4.1], the average ASE power spectral density per polarisation mode at the output of an EDFA, $D_{ASE}^{mode,amp}$, is proportional to the gain, G, of the amplifier, for highly inverted EDFAs, such that

$$D_{ASE}^{mode,amp} = E_v G n_{eq} \qquad \{4.1\}$$

where $E_v=h\nu$ is the energy of a photon (which will be approximated as constant over all wavelengths of interest in this analysis and equal to 1.3×10^{-19}J) and n_{eq} is an equivalent noise parameter, corresponding to the number of spontaneous emission photons per mode at the start of the erbium-doped fibre. We will, however, take $D_{ASE}^{mode,amp}$ to be the peak power spectral density and obtain the value of n_{eq} such that this is the case. This is equivalent to merely redefining n_{eq}. In order to determine a practical value for n_{eq} we will use experimental results obtained for the intended pre-amplifier EDFA, which had a small-signal gain, G, of 436.5 (26.4dB) at 1533nm, a total ASE power of ~1mW and the lineshape shown in Figure 4.3. Also shown in this Figure is a fitted double Gaussian curve which will be used to approximate the ASE lineshape.

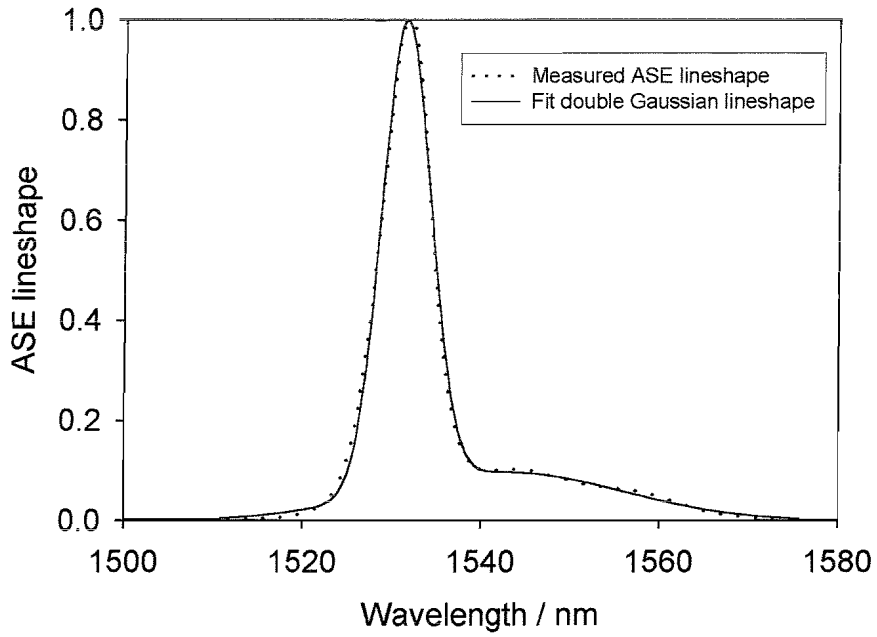

Figure 4.3 ASE lineshape measured experimentally (dotted line) and a fitted double Gaussian curve to approximate this lineshape (solid line).

Fitted curve is

$$L_{ASE}(f)=L^0_{ASE1}\exp(-\ln(2)\cdot(2(f-f_{ASE1})/\Delta\nu_{ASE1})^2)+L^0_{ASE2}\exp(-\ln(2)\cdot(2(f-f_{ASE2})/\Delta\nu_{ASE2})^2)$$

(in terms of frequency, *f*) or

$$L_{ASE}(\lambda)=L^0_{ASE1}\exp(-\ln(2)\cdot(2(\lambda-\lambda_{ASE1})/\Delta\lambda_{ASE1})^2)+L^0_{ASE2}\exp(-\ln(2)\cdot(2(\lambda-\lambda_{ASE2})/\Delta\lambda_{ASE2})^2)$$

(in terms of wavelength, λ)

where $L^0_{ASE1}=0.932$, $L^0_{ASE2}=0.0974$, $f_{ASE1}=195.89$THz, $f_{ASE2}=194.46$THz, $\Delta f_{ASE1}=830$GHz, $\Delta f_{ASE2}=3982$GHz, $\lambda_{ASE1}=1531.46$nm, $\lambda_{ASE2}=1542.73$nm, $\Delta\lambda_{ASE1}=6.49$nm, $\Delta\lambda_{ASE2}=31.11$nm.

The anti-Stokes wavelength is ~1533.08nm (to match a grating used in future experiments) and the Gaussian spectral density profile emitted by the amplifier is given by

$$S_{ASE}^{mode,amp}(f) = D_{ASE}^{mode,amp} L_{ASE}(f)$$
$$= E_v G n_{eq} \left(L_{ASE1}^0 \cdot \exp\left(-\ln(2) \cdot \left(\frac{2(f - \delta f_{ASE1})}{\Delta\nu_{ASE1}} \right)^2 \right) + L_{ASE2}^0 \cdot \exp\left(-\ln(2) \cdot \left(\frac{2(f - \delta f_{ASE2})}{\Delta\nu_{ASE2}} \right)^2 \right) \right) \quad \{4.2\}$$

where f=0 at the anti-Stokes frequency (so $\delta f_{ASE1} = f_{ASE1} - c/(1533.08\times10^{-9})$ and $\delta f_{ASE2} = f_{ASE2} - c/(1533.08\times10^{-9})$). The condition for 0.5mW total ASE power per polarisation mode is

$$P_{ASE}^{mode,amp} = \int_{-\infty}^{\infty} D_{ASE}^{mode,amp} L_{ASE}(f) df = E_v G n_{eq} \sqrt{\frac{\pi}{\ln(2)}} \left(\frac{L_{ASE1}^0 \cdot \Delta\nu_{ASE1}}{2} + \frac{L_{ASE2}^0 \cdot \Delta\nu_{ASE2}}{2} \right) = 0.5\,\text{mW} \quad \{4.3\}$$

and so, for $L_{ASE1}^0 = 0.932$, $L_{ASE2}^0 = 0.0974$, $\Delta\nu_{ASE1} = 830$GHz, $\Delta\nu_{ASE2} = 3982$GHz and G = 26.4dB, n_{eq} is calculated to be 7.17. Since n_{eq} is not constant for different gains, Equation {4.1} cannot be applied to other EDFAs, without knowing their n_{eq}, but we shall use this relation to describe this particular, experimental EDFA. The total ASE power from the EDFA is given by

$$P_{ASE}^{tot,amp} = M \cdot D_{ASE}^{mode,amp} \Delta\nu_{ASE} \quad \{4.4\}$$

where $\Delta\nu_{ASE}$ is an effective ASE linewidth, equivalent to that of a top-hat function (with $L(0)$=1) of the same area (i.e. $\Delta\nu_{ASE} = \sqrt{\frac{\pi}{4\ln(2)}} \left(L_{ASE1}^0 \Delta\nu_{ASE1} + L_{ASE2}^0 \Delta\nu_{ASE2} \right) =$ 1236GHz) and

$$D_{ASE}^{mode,amp} = 4.05\times10^{-16} \text{ W/Hz} \quad \{4.5\}$$

and M is the total number of ASE polarisation modes to be considered (here M = 2, since no polarisation filtering is done prior to detection).

4.2.2.2 ASE Filtering in Coherent Detection

In the coherent detection sensor, Sensor CAF, the ASE is filtered by a fibre Bragg grating of bandwidth $\Delta\nu_{grat}$ centred on the anti-Stokes signal, with transmission

$$T(f) = L_{grat}(f) \qquad \{4.6\}$$

the ASE power spectral density per mode at the detector is then given by, assuming $\Delta\nu_{grat} << \Delta\nu_{ASE}$

$$S_{ASE}^{mode,det}(f) = D_{ASE}^{mode,det} L_{grat}(f) \qquad \{4.7\}$$

where $D_{ASE}^{mode,det} = \alpha_{D_{ASE}} D_{ASE}^{mode,amp}$ and $\alpha_{D_{ASE}}$ is the loss at the grating peak frequency (=anti-Stokes frequency in this case) between the EDFA and the detector, itself dependent on the sensor configuration. The ASE lineshape is reduced from its peak of unity to 0.86 at the anti-Stokes frequency so this component of $\alpha_{D_{ASE}}$ is intrinsic to the grating. The ASE power per mode is given by

$$P_{ASE}^{mode,det} = D_{ASE}^{mode,det} \int_{-\infty}^{\infty} L_{grat}(f) df \qquad \{4.8\}$$

The grating lineshape to be used in the coherent sensor CAF is shown in Figure 4.4. The numerical integral of this lineshape was found to be 14.7GHz. Following the definition of optical bandwidth used in Equation {4.4}, the total power at the detector is therefore

$$P_{ASE}^{tot,det} = M\alpha_{D_{ASE}} \Delta\nu_{grat} \cdot D_{ASE}^{mode,amp} \qquad \{4.9\}$$

where $\Delta\nu_{grat}$ =14.7GHz. As mentioned previously, the Rayleigh and Stokes signals will be attenuated by this filter and have measured power reflectivities of 15dB and 26dB respectively with the grating centred on the anti-Stokes frequency, i.e.

$L_{grat}(-11\,\text{GHz}) = 0.03162$ and $L_{grat}(-22\,\text{GHz}) = 0.0025$. The anti-Stokes frequency has a reflectivity of unity.

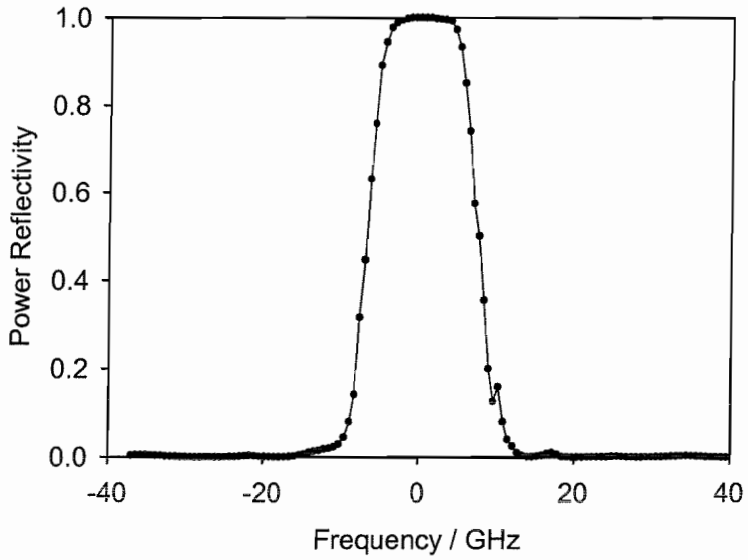

Figure 4.4 Profile of the fibre Bragg grating used in Sensor CAF. The grating is centred on the anti-Stokes frequency (195.68GHz).

4.2.2.3 ASE Filtering in Direct Detection

In this case of direct detection using a MZ filter, the fringe full width at half maximum is 7.92GHz. This corresponds to the ASE transmission profile through a double-pass Mach Zehnder interferometer after FBG filtering to remove undesirable adjacent ASE peaks. The power density per mode is

$$S_{ASE}^{mode,det}(f) = D_{ASE}^{mode,det} L_{grat}(f-\delta) L_{MZ}(f) \qquad \{4.10\}$$

where L_{MZ} is the MZ transfer function, $L_{opt}(f)=L_{grat}(f-\delta)L_{MZ}(f)$ is the output ASE lineshape and δ is the frequency difference between the grating central frequency and the anti-Stokes frequency (at a MZ peak). It is assumed that the peak ASE value is reduced by the transmission through the grating (only applying in the case of Sensor DA2) but that the ASE profile is the shape of a single fringe for Sensor DA1 and the shape of two adjacent fringes for Sensor DA2.

The ideal MZ transfer function is given by (using Equation {2.41})

$$X(\nu) = \left[\tfrac{1}{2} + \tfrac{1}{2}\cos\left(\frac{2\pi(\nu - \nu_0)}{\Delta\nu_{FSR}}\right)\right]^2 \qquad \{4.11\}$$

where $\Delta\nu_{FSR}$=22GHz, $\nu_0 = \nu_{AS}$ and the numerical integral of a single fringe with unity maximum transmission is 8.25GHz (slightly larger than the fringe half-width, which is calculated to be $0.36 \times \Delta\nu_{FSR}$). The numerical integral of two fringes, with 0.9 maximum transmission (due to the preceding grating), is 14.85GHz. So these two values are the effective ASE linewidths ($\Delta\nu_{MZ}$) of the Sensors DA1 and DA2 respectively. The corresponding equation for the total ASE power per mode at the detector is therefore

$$P_{ASE}^{tot,det} = M\alpha_{D_{ASE}} \cdot \Delta\nu_{MZ} \cdot D_{ASE}^{mode,amp} \qquad \{4.12\}$$

The MZ is modelled as having a 2dB intrinsic loss (due to the isolator and splice losses), which is included in $\alpha_{D_{ASE}}$. The attenuation at the Rayleigh frequency is assumed to be 40dB (on top of the 2dB intrinsic loss), although the transmission of the ideal interferometer is zero at this frequency.

The ASE lineshape at the detector satisfies

$L_{opt}(0)=L_{grat}(0)\,L_{MZ}(0)=1\times1=1$	$L_{opt}(0)=L_{grat}(11)L_{MZ}(0)=0.9\times1=0.9$
$L_{opt}(-11)=L_{grat}(-11)L_{MZ}(-11)=0.03162\times0.0001=3.162\times10^{-6}$	$L_{opt}(-11)=L_{grat}(0)L_{MZ}(-11)=1\times0.0001=1\times10^{-4}$
$L_{opt}(-22)=L_{grat}(-22)L_{MZ}(-22)=0.0025\times1=2.5\times10^{-3}$	$L_{opt}(-22)=L_{grat}(-11)L_{MZ}(-22)=0.9\times1=0.9$
(δ = 0) for **Sensor DA1**	(δ = –11GHz) for **Sensor DA2**

The ASE profiles for these two sensors are shown in Figure 4.5, in the summary section, to follow.

4.2.3 Summary

General equations for the total ASE power and the ASE power per mode incident on the detector are given by

$$P_{ASE}^{tot,det} = M\alpha_{D_{ASE}} \cdot \Delta\nu_{opt} \cdot D_{ASE}^{mode,amp} \qquad \{4.13\}$$

and

$$P_{ASE}^{mode,det} = \alpha_{D_{ASE}} D_{ASE}^{mode,amp} \int_{-\infty}^{\infty} L_{opt}(f)df \qquad \{4.14\}$$

where $\Delta\nu_{opt}$ is the optical bandwidth and $L_{opt}(f)$ is the lineshape function of the ASE at the detector (Figure 4.5).

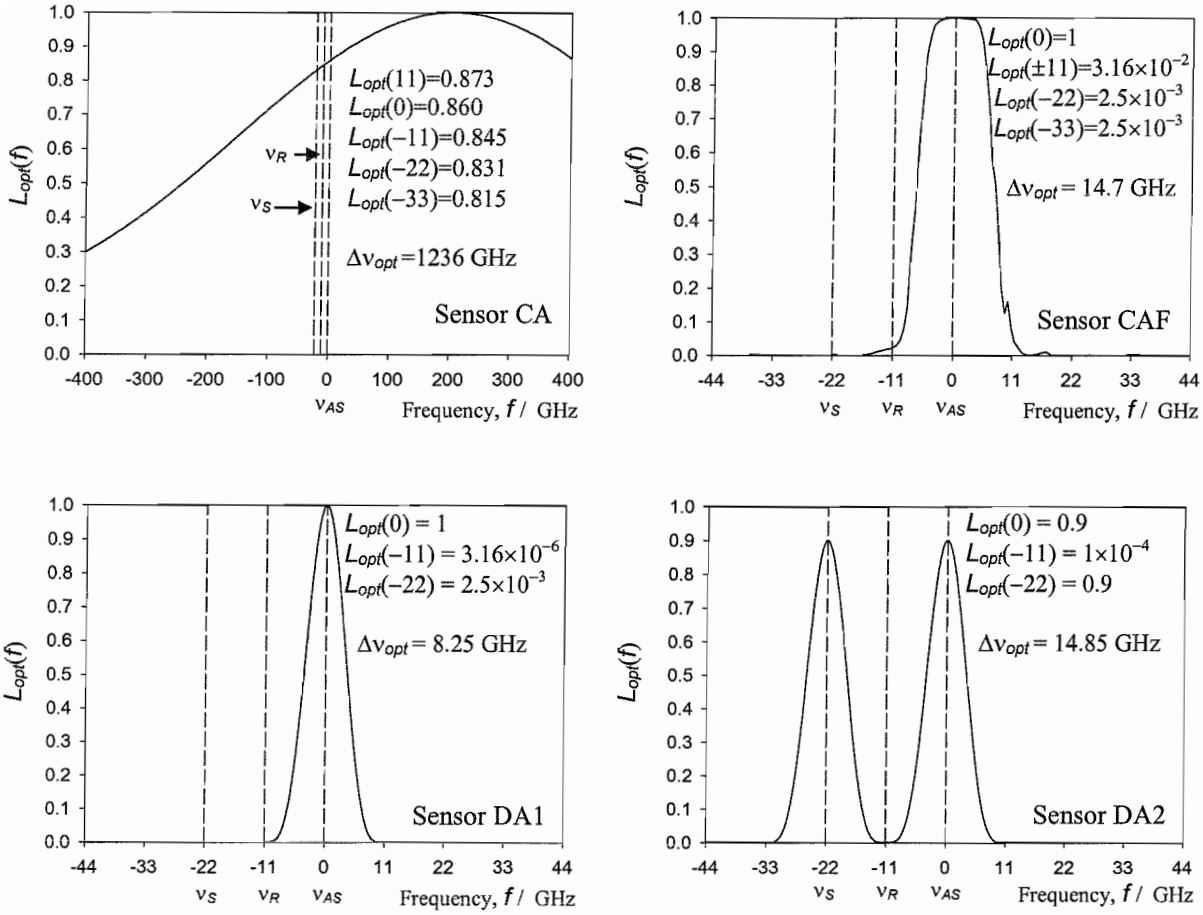

Figure 4.5 ASE profiles for the four sensors under consideration which employ pre-amplification of the backscatter. Useful values of $L_{opt}(f)$ are also included as will be required in §4.3.2.2.

Table 4.1 contains a summary of quantities appearing in the analysis and the values to be used. Where the value is different for each sensor configuration, the reader is referred to the relevant Table or Figure containing the information.

Characteristic	Symbol	Value	Comment
Gain of EDFA / dB	G	26.4	Experimental value (≡ linear gain of 436.5)
ASE peak power spectral density per mode from EDFA / WHz^{-1}	$D_{ASE}^{mode,amp}$	4.05×10^{-16}	Experimental value – see §4.2.2.1
ASE total power per mode from EDFA / mW	$P_{ASE}^{mode,amp}$	0.5	Experimental value – see §4.2.2.1
ASE peak power loss from EDFA to detector	$\alpha_{D_{ASE}}$	see Table 4.2	
ASE total power per mode at the detector	$P_{ASE}^{mode,det}$	see Table 4.3	Equation {4.14}
ASE total power at the detector	$P_{ASE}^{tot,det}$	see Table 4.3	Equation {4.13}
Optical lineshape of ASE	$L_{opt}(f)$	see Figure 4.5	
No. of ASE polarisation modes	M	2	No polariser used
Effective ASE spectral width from EDFA / GHz	$\Delta\nu_{ASE}$	1236	See §4.2.2.1
ASE spectral width at detector	$\Delta\nu_{opt}$	see Table 4.3	
Difference between the zero frequency of the ASE spectrum (ν_{ASE}) and peak of the spectrum of optical component x (ν_x) /GHz	$\Delta\nu_{X\text{-}ASE}$ $=\nu_{ASE}-\nu_x$	10.89 (x=LO) 11 (x=R) 0 (x=AS) 22 (x=S)	$\nu_{ASE}=\nu_{AS}$ (defined as such for all sensors – see Figure 4.5)
Backscattered power at the detector (x = AS, R or S)	$P_x(L)$	see Table 4.2 for P_x^0	$P_x(L)=P_x^0 10^{-(0.2)\gamma L}$
Total power at the detector (x = AS, R and S)	$P_T(L)$	see Table 4.3 for $P_T(0)$	$P_T(L)=P_{LO}+P_{ASE}^{tot,det}+\sum_x P_x^0 10^{-(0.2)\gamma L}$
LO power at detector	P_{LO}	see Table 4.3	to give $P_T(0)$~1.6mW
No. of signal averages	N	-	
Attenuation coefficient / $dBkm^{-1}$	γ	0.2	Typical value
Brillouin frequency shift / GHz	$\delta\nu_B$	11	Experimental value
Brillouin linewidth / MHz	$\Delta\nu_B$	35	Experimental value
Position along fibre / km	L	-	
Temperature of detector / K	T	293	Room temperature
Anti-Stokes Frequency / THz	ν_{AS}	195.68	≡ 1533.08nm
Photon energy / J	E_v	1.3×10^{-19}	
Planck's constant / Js	h	6.626×10^{-34}	
Charge on an electron / C	e	1.602×10^{-19}	
Boltzmann's constant / JK^{-1}	K	1.381×10^{-23}	

Table 4.1 Quantities and experimental values used in the noise analysis.

The sensor-specific tables are shown below. Table 4.2 evaluates the backscattered power at the detector for each sensor based on its construction, along with the ASE peak attenuation from the EDFA to the detector.

Transmission		α_{AS}	α_R	α_S	$\alpha_{D_{ASE2}}^{per\ item}$
EDFA	①	436.5	436.5	436.5	-
Each fibre coupler	②	0.5	0.5	0.5	0.5
Circulator	③	0.5	0.5	0.5	0.5
FBG1	④	1	0.03162	0.0025	0.86
FBG2	⑤	0.9	1	0.9	0.86
Mach-Zehnder	⑥	0.631	0.631×10^{-4}	0.631	0.631

$P_x(L)=P_x^0 10^{-(0.2)\gamma L}$ (x = AS, R or S)		P_{AS}^0	P_R^0	P_S^0	$\alpha_{D_{ASE}}=\frac{D_{ASE}^{mode,det}}{D_{ASE}^{mode,amp}}$	
		Power at detector for L=0 / nW				
From fibre	-	4	240	4	-	-
Sensor CU	②	2	120	2	-	-
Sensor CA	②①②	436.5	26191	436.5	②	0.5
Sensor CAF	②①③④②	218.3	414.0	0.546	③④②	0.215
Sensor DU	②⑥	1.262	0.0076	1.262	-	-
Sensor DA1	②①③④⑥	275.4	0.052	0.689	③④⑥	0.2713
Sensor DA2	②①③⑤⑥	247.9	1.653	247.9	③⑤⑥	0.2713

Table 4.2 Backscattered power and ASE losses between generation and the detector. Maximum backscattered power values (for L=0) at the detector are also given for each sensor to be considered.

Table 4.3 shows the local oscillator, ASE, maximum total backscatter and overall total powers at the detector evaluated using Equation {4.13} and the definition of the total power from Table 4.1.

	P_{LO}	$P_{ASE}^{tot,det}$	$\sum_x P_x^0$	$P_T(0)$	$\Delta\nu_{opt}$
	Power at detector / mW				GHz
Sensor CU	1.6	-	0.000124	1.600	-
Sensor CA	1.08	0.5	0.0271	1.607	1236
Sensor CAF	1.6	0.00256	0.000633	1.603	14.7
Sensor DU	0	-	2.53×10^{-6}	2.53×10^{-6}	-
Sensor DA1	0	0.00181	0.000276	0.00209	8.25
Sensor DA2	0	0.00326	0.000497	0.00376	14.85

Table 4.3 Powers at the detector. For coherent detection, the local oscillator is arranged to be such that the total power incident on the detector is ~1.6mW

4.3 Noise Analysis

4.3.1 Detector Specifications and SNR

The signal-to-noise ratio will always be taken to be that observed on the measured Brillouin signal. Although this may not always be the accepted definition, it is the relevant quantity in this analysis, since it gives a direct measurement of percentage noise on the Brillouin trace.

4.3.1.1 Coherent Detection

The noise characteristics of Brillouin OTDR using direct detection and coherent detection are different. Indeed, the noise in coherent detection systems is dependent on the exact technique used. The measured quantity will always be the anti-Stokes Brillouin signal. With the high-frequency beat measurement, the Stokes will be visible, too, unless filtered out, but the 110MHz AOM frequency shift will introduce a frequency difference of 220MHz between Stokes and anti-Stokes beat frequencies as detected on the ESA.

There are two main types of coherent detection systems. In the first type, where the signal is mixed down to baseband, any noise on the photocurrent remains as an AC signal and so contributes to the trace noise. In the second type, where the signal is mixed down to a fixed IF, bandpass filtered and rectified using a fast rf detector, any noise within the detection bandwidth is also rectified and so converted to a DC level. Any photocurrent noise is therefore not manifested as a noise source on the final voltage trace. The only way in which photocurrent noise contributes to trace noise in this second case is if the noise is amplitude-modulated at a frequency within the detection bandwidth. The detector/ESA combination used in these experiments is an example of this type of detection regime.

The measured output traces from the ESA are proportional to rms rf voltage, however, so we must first consider the noise and DC offset in terms of voltage. The ESA itself contributes a measured rf power offset of –73.5dBm, corresponding to a voltage DC offset of 47.4μV. The rms noise on this ESA-created DC voltage offset is measured

to be 22μV with no trace averaging. To aid comparison between coherent and direct detection, we will now remove the effect of the detector resistance and instead work in terms of current (=*V*/*R*). The ESA offset and noise properties will therefore be stated as

$$\left(i_{off}^{ESA}\right)^2 = 9.0\times10^{-13}\ \mathrm{A}^2$$
$$i_{noise}^{ESA} = 4.4\times10^{-7}\ \mathrm{A} \qquad \{4.15\}$$

We will assume that the any photocurrent noise is not amplitude modulated, i.e. that the noise on the current trace is due only to the ESA-generated noise.

So, we collect a trace proportional to the rms current (voltage). It is, however, the current (voltage) squared which gives a signal proportional to Brillouin power. Consider the following current trace, obtained prior to squaring, with a single Fourier component of noise at frequency *f* on it

$$i+\delta i = \sqrt{i_s^2+i_{off}^2}+\delta i = \sqrt{i_s^2+i_{off}^2}+i_f\cos(2\pi ft+\phi_f) \qquad \{4.16\}$$

where the signal power $P_s \propto i_s^2$ and i_{off}^2 is the dc offset term on the trace corresponding to ESA-generated offset and rectified noise. The rms noise on the trace is therefore, putting $\theta = 2\pi ft+\phi_f$

$$i_f^{rms} = i_f\sqrt{\frac{1}{2\pi}\int_{-\pi}^{+\pi}\cos^2\theta\,d\theta} = \frac{1}{\sqrt{2}}i_f \qquad \{4.17\}$$

On squaring the trace we obtain

$$i^2+\delta(i^2) = \left(i_s^2+i_{off}^2\right)+2\cdot\sqrt{i_s^2+i_{off}^2}\cdot\delta i+(\delta i)^2 \qquad \{4.18\}$$

and the rms error is given by

$$\left(i^2\right)_f^{rms} = 2\cdot\sqrt{i_s^2+i_{off}^2}\cdot i_f\sqrt{\frac{1}{2\pi}\int_{-\pi}^{+\pi}\cos^2\theta\,d\theta} + i_f^2\sqrt{\frac{1}{2\pi}\int_{-\pi}^{+\pi}\cos^4\theta\,d\theta}$$
$$= 2\cdot\sqrt{i_s^2+i_{off}^2}\cdot i_f^{rms} + \sqrt{\frac{3}{2}}\cdot\left(i_f^{rms}\right)^2 \qquad \{4.19\}$$

Now, this will apply to every Fourier component and so the overall noise may be given by

$$\left(i^2\right)_{noise} = 2\cdot\sqrt{i_s^2+i_{off}^2}\cdot i_{noise} + \sqrt{\frac{3}{2}}\cdot\left(i_{noise}\right)^2 \qquad \{4.20\}$$

If the current trace is averaged N times prior to squaring, i_{noise} decreases as $1/\sqrt{N}$, so the noise on the squared current trace (proportional to Brillouin power) is

$$\left(i^2\right)_{noise} = 2\cdot\sqrt{i_s^2+i_{off}^2}\cdot\frac{i_{noise}}{\sqrt{N}} + \sqrt{\frac{3}{2}}\cdot\frac{\left(i_{noise}\right)^2}{N} \qquad \{4.21\}$$

From this, it can be seen that even though a DC current offset does not affect noise on the current trace, it biases the noise on the squared trace – the greater the offset, the greater the noise, for a given signal current.

The ratio of the first and second terms in Equation {4.21} is given by

$$Ratio = \sqrt{\frac{8N(i_s^2+i_{off}^2)}{3}}\cdot\frac{1}{i_{noise}} \qquad \{4.22\}$$

The minimum offset is given by the ESA-generated offset of 9.0×10^{-13} A^2. With a current noise of 4.4×10^{-7} A, no signal and N=1000, this ratio is 111.3 and so the noise term in coherent detection may be expressed, for coherent sensors based on this ESA, as (ignoring the second term in Equation {4.21})

$$\left(i^2\right)_{noise}^{CD} = 2\cdot\sqrt{\left(i_s^{CD}\right)^2+i_{pcn}^2+\left(i_{off}^{ESA}\right)^2}\cdot\frac{i_{noise}^{ESA}}{\sqrt{N}} \qquad \{4.23\}$$

where i_{pcn}^2 is the rms photocurrent noise which is rectified to a DC offset. We are now in a position to calculate an expression for the SNR. The signal current squared, i_s^2, for the trace at the peak Brillouin frequency, is given by (using Equation {3.19})

$$\left(i_s^{CD}\right)^2 = \left(\frac{\eta e}{E_v}\right)^2 \cdot 2P_{LO}P_{AS}\frac{2B_e}{\pi\Delta\nu_B} \qquad \{4.24\}$$

and so the anti-Stokes power SNR for coherent detection is

$$SNR_{CD} = \sqrt{N}\frac{\left(\frac{\eta e}{E_v}\right)^2 \cdot 2P_{LO}P_{AS}\frac{2B_e}{\pi\Delta\nu_B}}{2\cdot\sqrt{\left(i_s^{CD}\right)^2 + i_{pcn}^2 + \left(i_{off}^{ESA}\right)^2}\cdot i_{noise}^{ESA}} \qquad \{4.25\}$$

4.3.1.2 Direct Detection

Finding the SNR for direct detection is less complicated. The total noise on the current trace is due only to photocurrent noise and is given by

$$i_{noise}^{DD} = \frac{1}{\sqrt{N}}\sqrt{i_{pcn}^2} \qquad \{4.26\}$$

The signal current (not the current squared, as for coherent detection) is proportional to Brillouin power and is given simply by

$$i_s^{DD} = \left(\frac{\eta e}{E_v}\right)\cdot\left(P_{AS} + P_S\right) \qquad \{4.27\}$$

So the Brillouin power SNR for direct detection is

$$SNR_{DD} = \sqrt{N}\frac{\left(\frac{\eta e}{E_v}\right)\cdot\left(P_{AS} + P_S\right)}{\sqrt{i_{pcn}^2}} \qquad \{4.28\}$$

4.3.1.3 Summary

The properties of the coherent and direct detection systems are summarised in Table 4.4, some of which need further explanation.

Characteristic	Symbol	Value	
		Coherent Detection	Direct Detection
Detection Bandwidth	B_e	5 MHz	3 MHz
Feedback Resistance	R	50 Ω	various
Quantum Efficiency	η	$0.65/\sqrt{2}$	0.65
Central detection frequency	f_{det}	10.89GHz	1.5MHz
ESA output current noise	i_{noise}^{ESA}	4.4×10^{-7} A	-
ESA output offset	$\left(i_{off}^{ESA}\right)^2$	9.0×10^{-13} A^2	-

Table 4.4 Detection characteristics for both coherent and direct detection regimes. Explanation of some of the figures is found below.

- The bandwidth of the direct detection receiver is only 3MHz, as opposed to 5MHz in the coherent detection case since, once rectified using the RF detector, the heterodyne signal is passed through a 3MHz low-pass filter, which reduces the spatial resolution without reducing the DC offset due to photocurrent noise.

- In order to allow a DC path to ground at the detector output, so as not to damage the ESA, a 3dB RF attenuator is inserted prior to the ESA input. This effectively reduces the quantum efficiency of the detector by a factor of $\sqrt{2}$, as is evident in Table 4.4.

- The central detection frequency is the peak LO-AS beat frequency in coherent detection (equal to 11GHz minus 110MHz, due to the AOM shift). The central detection frequency in direct detection is 1.5MHz, in the centre of the 3MHz bandwidth of the detector.

4.3.2 Noise Components

Now we will find expressions for the noise components of the photocurrent so that we can find and compare the signal to noise ratios for each of the six sensors.

4.3.2.1 Shot Noise and Thermal Noise

The shot noise due to the detection process can be calculated from the following definition (ignoring dark current) [4.2]

$$\begin{aligned} i_{shot}^2 &= 2\eta e^2 B_e \left(\frac{P_T(L)}{E_v} \right) \\ &= 2\eta e^2 B_e \left(\frac{P_{LO} + P_{AS} + P_R + P_S + P_{ASE}^{tot,det}}{E_v} \right) \end{aligned} \qquad \{4.29\}$$

where e is the charge on an electron, h is Planck's constant, $P_T(L)$ is the total power incident on the detector and the other quantities are defined and given experimental values in the Tables on pages 99, 100 and 105.

Using Equation {4.13}, this becomes

$$\boxed{i_{shot}^2 = 2\eta e^2 B_e \left(\frac{P_{LO} + P_{AS} + P_R + P_S}{E_v} + \frac{M\alpha_{D_{ASE}} \Delta\nu_{opt} D_{ASE}^{mode,amp}}{E_v} \right)} \qquad \{4.30\}$$

The thermal (Johnson) noise due to the feedback resistor in the receiver is given by [4.2]

$$\boxed{i_{th}^2 = \frac{4KTB_e}{R}} \qquad \{4.31\}$$

4.3.2.2 ASE Beat Terms

In those sensors employing an EDFA, there are additional terms in the total photocurrent noise, due to the presence of ASE at the detector. These are due to beating of the ASE with the local oscillator (if present), with the anti-Stokes, with the Rayleigh, with the Stokes and with itself. Whilst the thermal noise and the shot noise are white over the detection bandwidth, the ASE beat noises are dependent on the frequency of interest.

Since only one polarisation mode may beat with a polarised beam, the beat photocurrent power spectral densities are given, as a function of rf frequency, using Equation {3.15}, by

$$\partial^2_{x-ASE}(f) = \left(\frac{\eta e}{E_v}\right)^2 \frac{2P_x P^{mode,det}_{ASE}}{\int_{-\infty}^{\infty} L_{opt}(f)\,df} \cdot \left(L_{opt}(f - \Delta\nu_{x-ASE}) + L_{opt}(-f - \Delta\nu_{x-ASE})\right) \qquad \{4.32\}$$

for x=*LO*, *AS*, *R* or *S*. Using Equation {4.14}, the spectral density becomes

$$\partial^2_{x-ASE}(f) = \left(\frac{\eta e}{E_v}\right)^2 \cdot 2P_x \alpha_{D_{ASE}} D^{mode,amp}_{ASE} \left(L_{opt}(f - \Delta\nu_{x-ASE}) + L_{opt}(-f - \Delta\nu_{x-ASE})\right) \qquad \{4.33\}$$

for x=*LO*, *AS*, *R* or *S*.

The ASE-ASE beat is more complicated to calculate because the auto-correlation of the ASE lineshape must be found, since it can not be thought of as a delta function. However, since the ASE power is not two signals but only one, beating with itself, the signals corresponding to the frequencies f and $-f$ in Equation {3.14} (which describes LO-Brillouin heterodyning but is still valid as a basis) are indistinguishable and should not be counted twice – only the first term in this equation is used. However, both polarisation modes contribute to the ASE-ASE beat spectral density; since they both beat with themselves but not with each other, it is doubled.

Equation {3.14} therefore becomes, for ASE-ASE beat (using Equation {4.14})

$$\partial^2_{ASE-ASE}(f) = M\left(\frac{\eta e}{E_\nu}\right)^2 \cdot \frac{2\cdot\left(P^{mode,det}_{ASE}\right)^2}{\left(\int_{-\infty}^{\infty} L_{opt}(\nu)\,d\nu\right)^2} \cdot \int_{-\infty}^{\infty} L_{opt}(\nu)\cdot L_{opt}(\nu+f)\,d\nu$$
$$= 2M\left(\frac{\eta e}{E_\nu}\right)^2 \cdot \left(\alpha_{D_{ASE}} D^{mode,amp}_{ASE}\right)^2 \cdot \int_{-\infty}^{\infty} L_{opt}(\nu)\cdot L_{opt}(\nu+f)\,d\nu \qquad \{4.34\}$$

The autocorrelation will obviously be different for different sensors, depending on the ASE filtering used. For each sensor, the function $F(f)$ is found at $f = f_{det}$ such that

$$\partial^2_{ASE-ASE}(f) = 2M\left(\frac{\eta e}{E_\nu}\right)^2 \cdot \left(\alpha_{D_{ASE}} D^{mode,amp}_{ASE}\right)^2 \Delta\nu_{opt} \cdot F(f) \qquad \{4.35\}$$

Sensor CA

For the double Gaussian ASE lineshape of Sensor CA, Equation {4.34} becomes

$$\partial^2_{ASE-ASE}(f) = 2M\left(\frac{\eta e}{E_\nu}\right)^2 \left(\alpha_{D_{ASE}} D^{mode,amp}_{ASE}\right)^2 \int_{-\infty}^{\infty} \left(L_{ASE1}(\nu)+L_{ASE2}(\nu)\right)\left(L_{ASE1}(\nu+f)+L_{ASE2}(\nu+f)\right)d\nu$$
$$= 2M\left(\frac{\eta e}{E_\nu}\right)^2 \left(\alpha_{D_{ASE}} D^{mode,amp}_{ASE}\right)^2 \left(\int_{-\infty}^{\infty} L_{ASE1}(\nu)L_{ASE1}(\nu+f)d\nu + \int_{-\infty}^{\infty} L_{ASE2}(\nu)L_{ASE2}(\nu+f)d\nu \right.$$
$$\left. + \int_{-\infty}^{\infty} L_{ASE1}(\nu)L_{ASE2}(\nu+f)d\nu + \int_{-\infty}^{\infty} L_{ASE2}(\nu)L_{ASE1}(\nu+f)d\nu \right) \qquad \{4.36\}$$

$$\partial^2_{ASE-ASE}(f) = 2M\left(\frac{\eta e}{E_\nu}\right)^2 \left(\alpha_{D_{ASE}} D^{mode,amp}_{ASE}\right)^2 \sqrt{\frac{\pi}{4\ln(2)}} \cdot \left[\left(L^0_{ASE1}\right)^2 \frac{\Delta\nu_{ASE1}}{\sqrt{2}} \exp\left(\frac{-\ln(2)\cdot 2f^2}{\Delta\nu^2_{ASE1}}\right) \right.$$
$$+ \left(L^0_{ASE2}\right)^2 \frac{\Delta\nu_{ASE2}}{\sqrt{2}} \exp\left(\frac{-\ln(2)\cdot 2f^2}{\Delta\nu^2_{ASE2}}\right) + L^0_{ASE1}L^0_{ASE2} \frac{\Delta\nu_{ASE1}\Delta\nu_{ASE2}}{\sqrt{\Delta\nu^2_{ASE1}+\Delta\nu^2_{ASE2}}} \cdot \qquad \{4.37\}$$
$$\left. \left(\exp\left(\frac{-\ln(2)\cdot 4(f-(f_{ASE1}-f_{ASE2}))^2}{\Delta\nu^2_{ASE1}+\Delta\nu^2_{ASE2}}\right) + \exp\left(\frac{-\ln(2)\cdot 4(-f-(f_{ASE1}-f_{ASE2}))^2}{\Delta\nu^2_{ASE1}+\Delta\nu^2_{ASE2}}\right) \right) \right]$$

where the cross correlation of two Gaussians of different linewidths is given by

$$\int_{-\infty}^{\infty} \exp\left(\frac{-4\ln(2)\nu^2}{\Delta\nu_{ASE1}^2}\right)\exp\left(\frac{-4\ln(2)(\nu+f)^2}{\Delta\nu_{ASE2}^2}\right)d\nu = \sqrt{\frac{\pi}{4\ln(2)}}\cdot\frac{\Delta\nu_{ASE1}\Delta\nu_{ASE2}}{\sqrt{\Delta\nu_{ASE1}^2+\Delta\nu_{ASE2}^2}}\exp\left(\frac{-4\ln(2)\cdot f^2}{\Delta\nu_{ASE1}^2+\Delta\nu_{ASE2}^2}\right) \quad \{4.38\}$$

From this equation, at the beat frequency of 10.89GHz, $F(f_{det})$=0.55.

Sensors CAF, DA1 and DA2

For sensor CAF, the cross-correlation of the grating transmission function, shown in Figure 4.4, was found numerically and a value for $F(f_{det})$ determined as 0.25. Likewise, for sensors DA1 and DA2, cross correlations of the Mach Zehnder fringes were found and $F(f_{det})$ calculated as 0.73 and 0.66 respectively, for f_{det}=1.5MHz.

	f_{det} / GHz	$F(f_{det})$
Sensor CA	10.89	0.55
Sensor CAF	10.89	0.25
Sensor DA1	0.0015	0.73
Sensor DA2	0.0015	0.66

Table 4.5 Values of the function $F(f)$ defined in Equation {4.35} at the detection central frequency f_{det} for each of the sensors employing pre-amplification.

A summary of the values of $F(f_{det})$ is provided in Table 4.5. Until now, we have calculated only the power spectral densities of the ASE beat photocurrent noise components. The corresponding noise components are given, for $B_e << \Delta\nu_{opt}$ as

$$i_{x-ASE}^2 = \left(\frac{\eta e}{E_\nu}\right)^2 \cdot 2P_x\alpha_{D_{ASE}}D_{ASE}^{mode,amp}B_e\left(L_{opt}(f_{det}-\Delta\nu_{x-ASE})+L_{opt}(-f_{det}-\Delta\nu_{x-ASE})\right) \quad \{4.39\}$$

for beat between ASE and x=*LO*, *AS*, *R* or *S* (in the case of direct detection, since the x-ASE beat spectra are broad, f_{det} is assumed to be 0, rather than 1.5MHz) and by

$$i_{ASE-ASE}^2(f) = 2M\left(\frac{\eta e}{E_\nu}\right)^2\left(\alpha_{D_{ASE}}D_{ASE}^{mode,amp}\right)^2\Delta\nu_{opt}B_e\cdot F(f_{det}) \quad \{4.40\}$$

for ASE-ASE beat.

The first of these noise terms is dependent on distance down the fibre, the second is not. Both, however, are dependent on rf frequency, the first through the lineshape function itself, the second through the cross-correlation of the lineshape.

4.3.2.3 Brillouin, Rayleigh and Local Oscillator Self-Beat Terms

Beating of the anti-Stokes Brillouin signal with itself is also a source of photocurrent noise, in a similar way to ASE-ASE beat, as is the self-beating of all the other optical signals reaching the detector (Stokes Brillouin, Rayleigh and local oscillator). Due to the narrow linewidths of all these signals these self beat terms, which are centred at DC, are much more evident at low detection frequencies. The absence of such noise is another advantage of working at an 11GHz beat frequency. Each of these signals is assumed to have a Lorentzian lineshape, with the Stokes and anti-Stokes Brillouin having 35MHz linewidth, the local oscillator having 300kHz linewidth and the Rayleigh having 5MHz linewidth (due to the pulsing). The lineshape of each self-beat function is the autocorrelation of its profile which, for a Lorentzian shape, is another Lorentzian function with twice the linewidth. The self-beat spectral density may be expressed, in a similar way to Equation {4.34}, as

$$\begin{aligned}
\partial^2_{x-x}(f) &= \left(\frac{\eta e}{E_\nu}\right)^2 \cdot \frac{2 \cdot P_x^2}{\left(\int_{-\infty}^{\infty} L_x(\nu)\, d\nu\right)^2} \cdot \int_{-\infty}^{\infty} L_x(\nu) \cdot L_x(\nu + f)\, d\nu \\
&= \left(\frac{\eta e}{E_\nu}\right)^2 \cdot \frac{2 \cdot P_x^2}{\left(\frac{\pi}{2}\Delta\nu_x\right)^2} \cdot \frac{\pi \Delta\nu_x}{4} \cdot \frac{1}{\left(\frac{f}{\Delta\nu_x}\right)^2 + 1} \qquad \{4.41\} \\
&= \left(\frac{\eta e}{E_\nu}\right)^2 \cdot \frac{2 \cdot P_x^2}{\pi \Delta\nu_x} \cdot \frac{1}{\left(\frac{f}{\Delta\nu_x}\right)^2 + 1}
\end{aligned}$$

where $x = AS,\ S,\ R$ or LO.

The corresponding noise component is given by

$$i_{x-x}^2 = \left(\frac{\eta e}{E_v}\right)^2 \cdot \frac{2 \cdot P_x^2}{\pi \Delta \nu_x} \cdot \int_{f_{det}-B_e/2}^{f_{det}+B_e/2} \frac{1}{(f/\Delta \nu_x)^2 + 1} df \qquad \{4.42\}$$

which evaluates as

$$\boxed{i_{x-x}^2 = \left(\frac{\eta e}{E_v}\right)^2 \cdot \frac{2 \cdot P_x^2}{\pi} \cdot \left[\tan^{-1}\left(\frac{f_{det} + \frac{1}{2}B_e}{\Delta \nu_x}\right) - \tan^{-1}\left(\frac{f_{det} - \frac{1}{2}B_e}{\Delta \nu_x}\right)\right]} \qquad \{4.43\}$$

4.3.2.4 Brillouin, Rayleigh and Local Oscillator Cross-Beat Terms

Similarly, the cross beat terms are given by

$$\boxed{\begin{aligned} i_{x-y}^2 = &\left(\frac{\eta e}{E_v}\right)^2 \cdot \frac{2 \cdot P_x P_y}{\pi} \cdot \left[\tan^{-1}\left(\frac{2f_{det} - 2\Delta \nu_{x-y} + B_e}{\Delta \nu_x + \Delta \nu_y}\right) - \tan^{-1}\left(\frac{2f_{det} - 2\Delta \nu_{x-y} - B_e}{\Delta \nu_x + \Delta \nu_y}\right)\right] \\ &+ \left(\frac{\eta e}{E_v}\right)^2 \cdot \frac{2 \cdot P_x P_y}{\pi} \cdot \left[\tan^{-1}\left(\frac{2f_{det} + 2\Delta \nu_{x-y} + B_e}{\Delta \nu_x + \Delta \nu_y}\right) - \tan^{-1}\left(\frac{2f_{det} + 2\Delta \nu_{x-y} - B_e}{\Delta \nu_x + \Delta \nu_y}\right)\right] \end{aligned}} \qquad \{4.44\}$$

where $x = AS,\ S,\ R$ or LO and $y = AS,\ S,\ R$ or LO but $x \neq y$. In coherent detection, the LO-AS beat is the signal to be detected so is not classified as a noise component. The extra terms in this equation, as compared to Equation {4.43}, arise because the interacting signals are distinct and so f is not equivalent to $-f$ in Equation {3.14}.

4.3.3 SNR and Noise Comparisons

Equations {4.30} and {4.31} for shot and thermal noise, Equations {4.39} and {4.40} for ASE beat terms, Equation {4.43} for non-ASE self-beat terms and Equation {4.44} for non-ASE cross beat terms may be used to enable calculation of the SNR for both coherent detection and direct detection.

This is done using Equations {4.25} and {4.28}, where

$$i_{pcn}^2 = i_{shot}^2 + i_{th}^2 + i_{ASE-ASE}^2 + \left(\sum_x i_{x-ASE}^2 \right) + \sum_x i_{x-x}^2 + i_{S-AS}^2 + i_{LO-R}^2 + i_{LO-S}^2 + i_{R-S}^2 + i_{R-AS}^2 \qquad \{4.45\}$$

and the local oscillator terms apply only to coherent detection. Values for all the quantities appearing in these equations appear in the various summary tables presented so far in this chapter. No other detector noise terms will be taken into account in this analysis. We will now compare the performance of the six sensors.

Initially, Sensors DA1 and DA2 will be modelled as having 100kΩ feedback and Sensor DU will be assumed to be an 10MΩ feedback receiver. This will represent a best case scenario for Sensor DU (few detectors use a feedback greater than 10MΩ), since no electronic amplifier noise, dark current noise or any noise source other than shot noise and thermal noise is included in the model. It will become evident that thermal noise is unimportant for the other two direct detection sensors for a wide range of feedback resistance due to the presence of other, dominant noise sources.

Firstly, the total measured trace and the dc offset component for each sensor will be presented, to give an idea as to the magnitude of the offset, on top of which the Brillouin signal rests. These are shown in Figure 4.6. For coherent detection, the offset is caused by the rectified photocurrent noise and the intrinsic ESA DC offset. For direct detection, the offset is caused by other optical powers incident on the detector, primarily ASE power. It can be seen that, considering the pre-amplified sensors, the DC offset is much smaller in the coherent case than the direct case, but that in the unamplified sensors the reverse is true. A lower DC offset means that any additional noise present on the offset makes up a smaller percentage of the Brillouin signal and, in coherent detection, that the bias of the voltage noise after trace squaring is reduced.

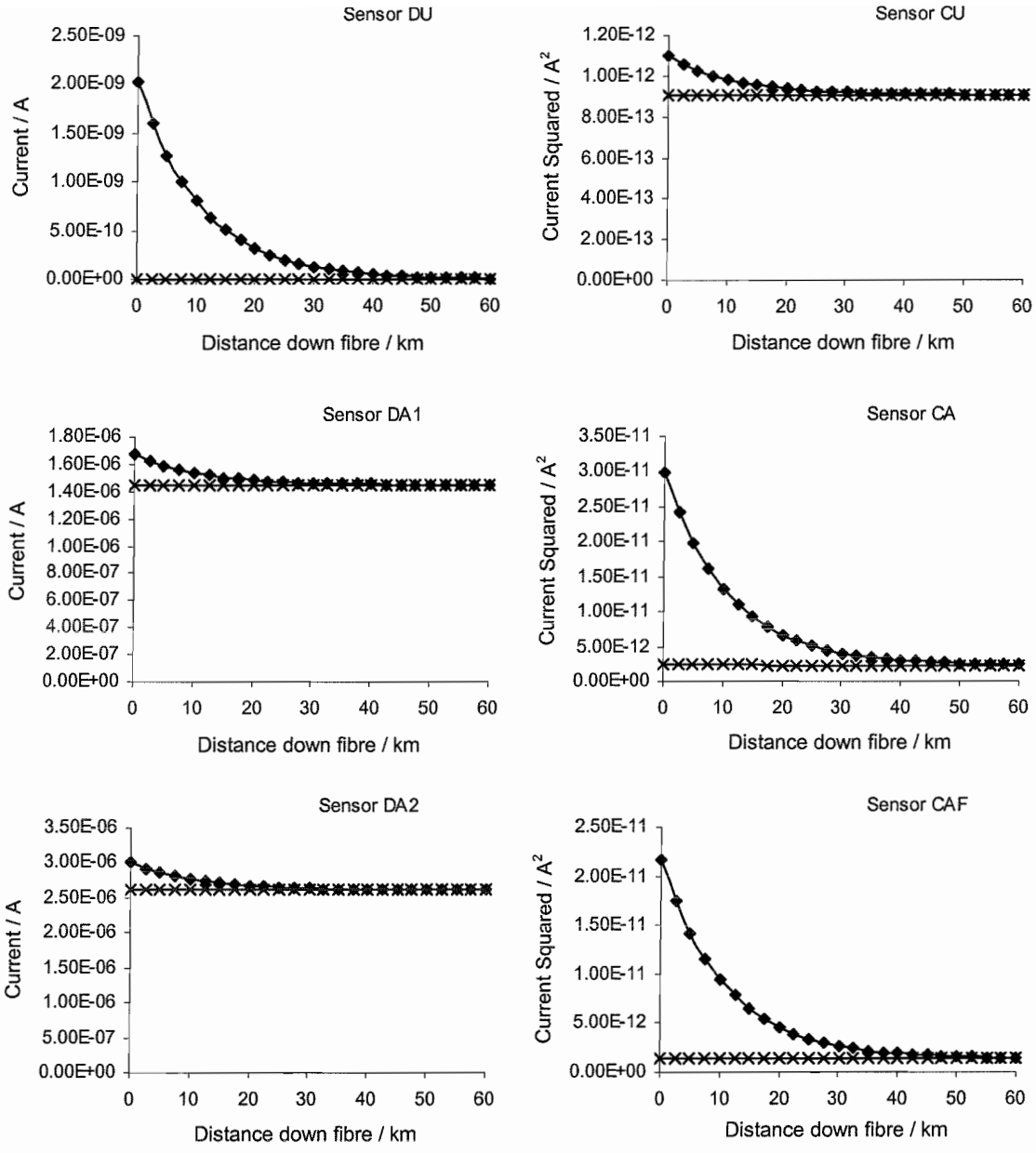

Figure 4.6 Plots of theoretical total recorded trace (diamonds) and DC offset level (crosses) for each of the six sensors. The difference between the two is proportional to Brillouin power.

Now, the signal and noise magnitudes for a single trace acquistion (no averaging, so N=1) will be compared. These are shown in Figure 4.7. It can be seen that all sensors except the unamplified coherent detection sensor have an unaveraged signal to noise ratio greater than 1 at 20km, which bodes well for their sensing abilities. The unamplified coherent sensor, however, has an unaveraged signal to noise ratio of less than 0.21 (i.e. < -6.9dB) and it must therefore be rejected as a sensing candidate.

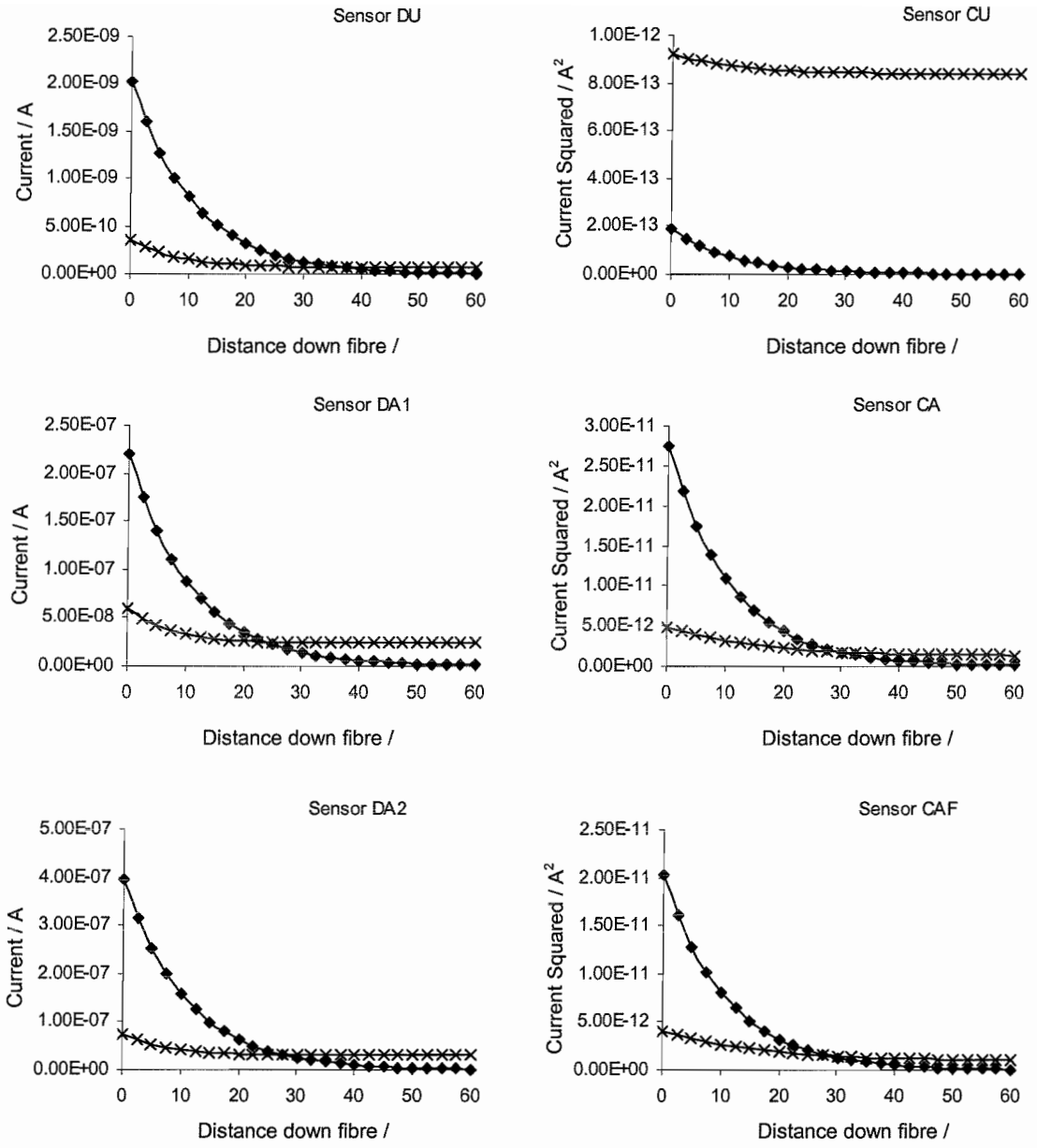

Figure 4.7 Plots of theoretical Brillouin signal power (diamonds) and corresponding theoretical noise level (crosses) with no signal averaging, for each of the six sensors.

It is informative to observe the percentage contributions of the different components of photocurrent noise to the final value of i_{pcn}^2 for each sensor (in the case of the coherent sensors, $(i_{off}^{ESA})^2$ is included and the percentages found relative to $i_{pcn}^2 + (i_{off}^{ESA})^2$). The main contributors only are shown on a linear scale for each sensor in Figure 4.8. In all cases, the sum of the percentages of the plotted noises is greater than 97%. For information and reference, logarithmic plots of every noise component for each sensor are provided in Appendix C.

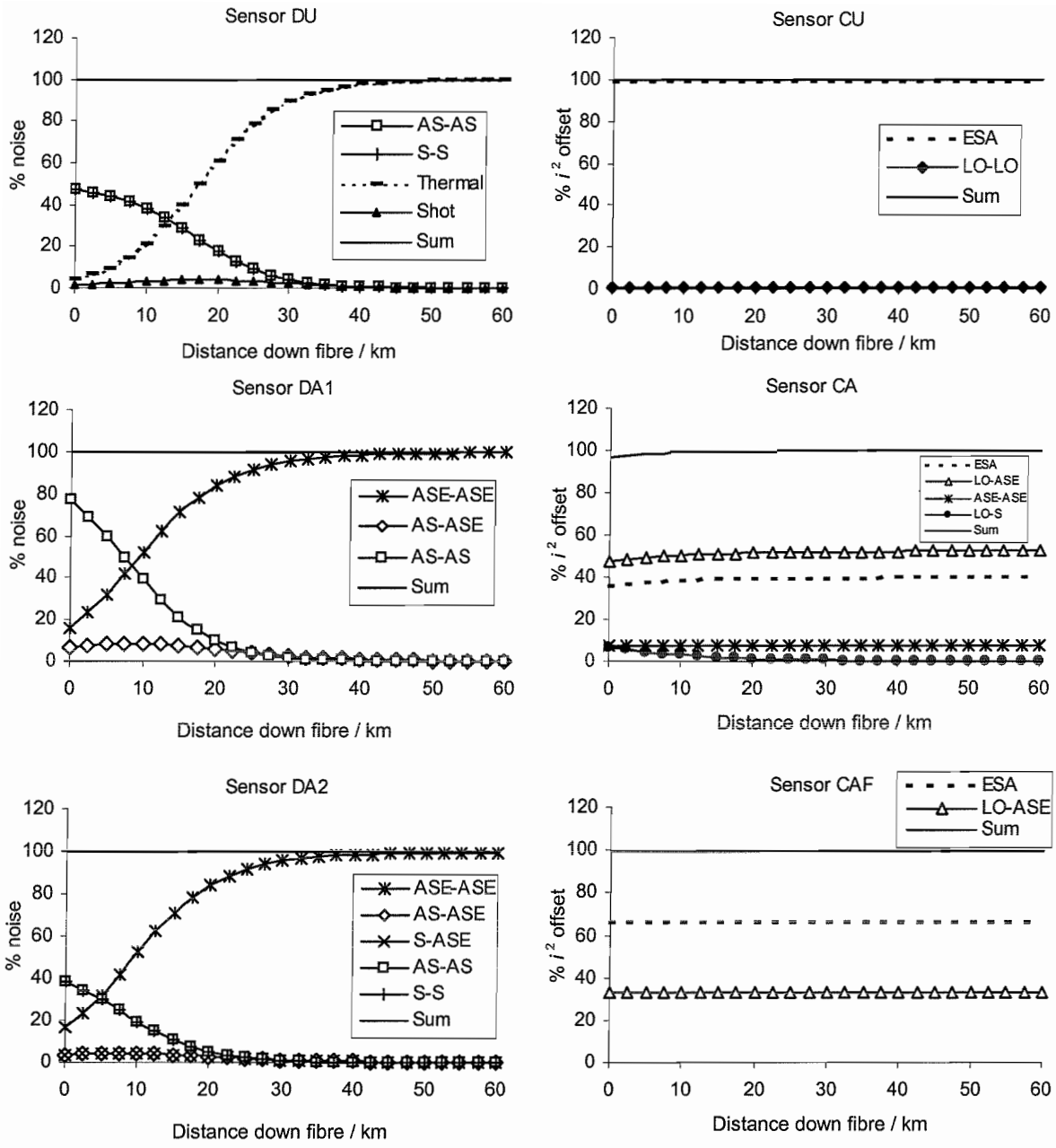

Figure 4.8 Main contributors to the total noise for each sensor. Each component is graphed as a % of the total and the sum of all plotted components, which is greater than 97% for every sensor, is also shown. The totals are i_{pcn}^2 and $i_{pcn}^2 + (i_{off}^{ESA})^2$ for direct and coherent detection respectively.

It can be seen from Figure 4.8 that the dominant noise source, from ~18km down the fibre, for Sensor DU is thermal noise; before this, S-S and AS-AS beat noise dominates, increasing to 94% of the noise at the near end of the fibre. For both the other two direct detection sensors, Brillouin self-beat again dominates at the near end of the fibre, but it is ASE-ASE beat which prevails for most of the 60km length modelled. For coherent detection, ESA noise is significant in all sensors, with sensor CU having nearly a ESA contribution of nearly 99% for the entire fibre length. In the other two coherent sensors, LO-ASE beat is also important, as is ASE-ASE to a lesser extent in sensor CA. It can also be seen that the LO-S beat is non-negligible for this

sensor. This is significant because this adds a component to the final trace DC offset (due to the Stokes heterodyne signal, centred at 11.11GHz) which is dependent on fibre length. This will act to distort the anti-Stokes signal in this sensor and will be discussed later. Sensor CAF, which filters out the Stokes signal, does not suffer from this effect.

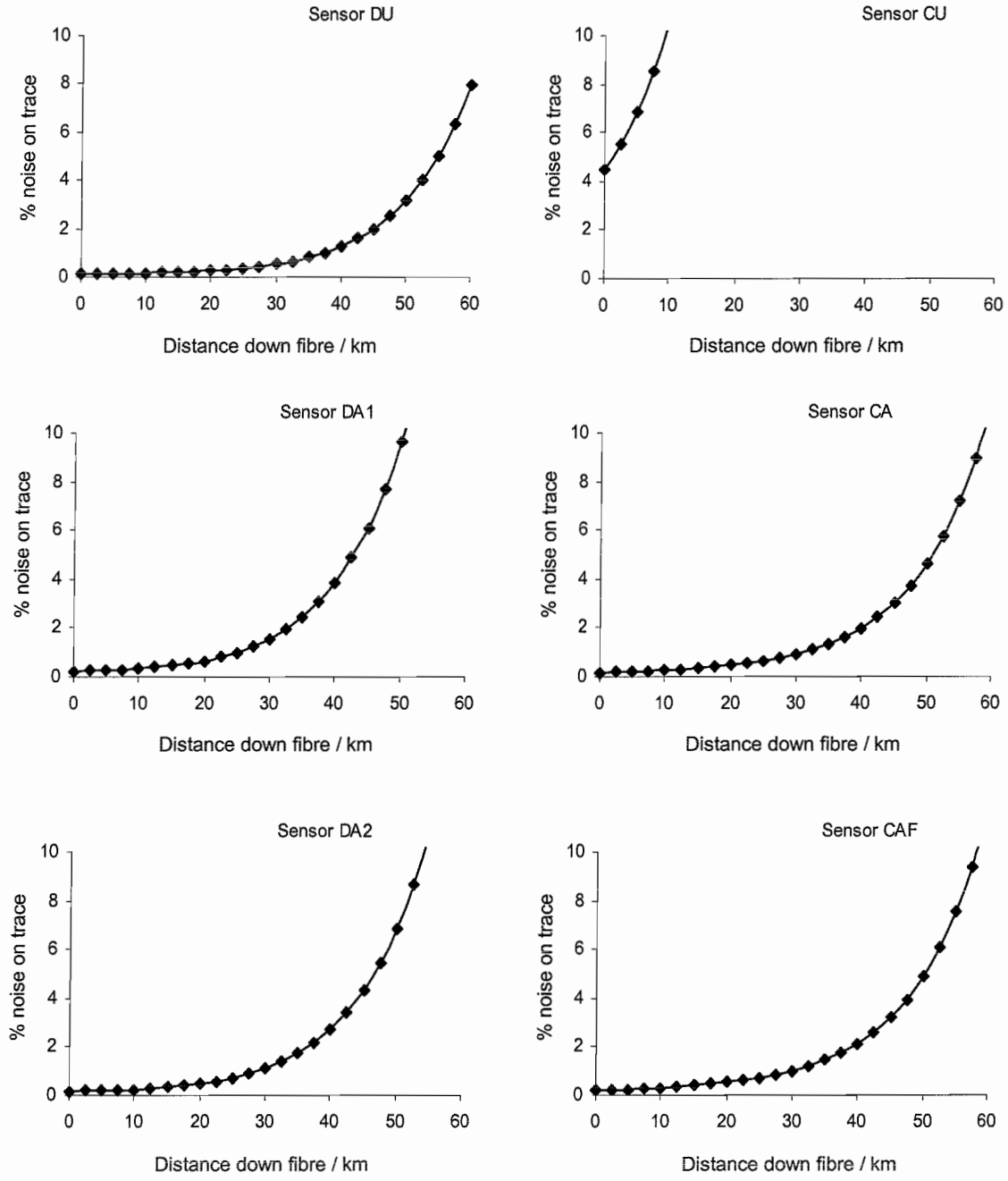

Figure 4.9 Plots of the theoretical percentage noise observed on the measured Brillouin traces as a function of fibre length, for each of the six sensors. The noise is that observed for 12288 (3×4096) averages.

The percentage noise on the Brillouin signal as function of fibre length, for 12288 (3×4096) averages per trace, is shown for each sensor in Figure 4.9. As expected sensor CU performs poorly, with the noise never as low as 4% even at the start of the fibre. The other 5 sensors all show a noise of less than ~1.5% at 30km, with the ideal unamplified 10MΩ direct detection sensor performing only marginally better than the rest. It is perhaps surprising, in this direct detection case, that optical pre-amplification does not improve the signal-to-noise ratio. However, if such a high quality detector as that used in Sensor DU were not available, a sensor with much higher thermal noise (lower gain) could be used, in conjunction with pre-amplification and filtering, in order to improve the SNR to the level exhibited by Sensor DA1 or DA2. For example, with a feedback resistor of 1kΩ, Sensor DA2 exhibits a reduction in SNR of only 0.02dB at the near end and 0.11dB at the far end of the sensing fibre, whereas Sensor DU exhibits a degradation of 13dB at the near end of the fibre and 20dB at the far end. This results in an improvement in SNR due to pre-amplification of 12.6dB at the near end and 16.4dB at the far end of the fibre.

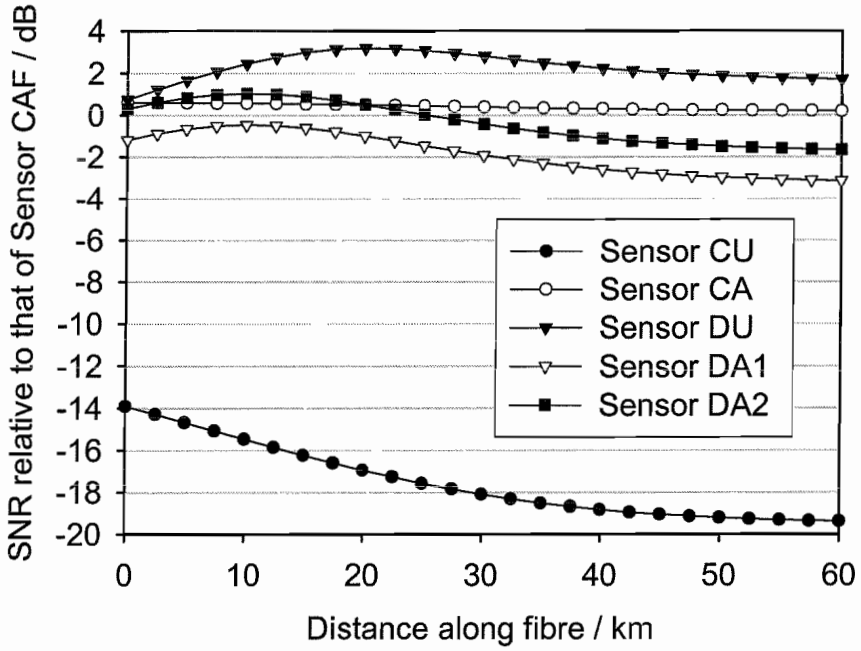

Figure 4.10 Signal-to-noise ratio, relative to that of sensor CAF, of the remaining five sensors, as a function of fibre length.

The SNR for each sensor, relative to that of Sensor CAF, is plotted in Figure 4.10. It can be seen that there is very little difference in SNR for the two amplified coherent sensors, with the unfiltered version having an SNR very slightly larger than the

filtered version (a lower noise does not quite make up for the higher loss between fibre and detector in the latter sensor). Sensor DA2 performs better than Sensor DA1, but only by ~1.5dB, since the increase in signal power is partially negated by an increase in noise due to ASE. It is also evident that even sensor DU never achieves a signal-to-noise ratio better than ~3.2dB above that of Sensor CAF.

An interesting point to note about all the coherent sensors is that detector thermal noise is not a significant proportion of the total photocurrent noise, so emphasis must be placed on other qualities of the detector, such as linearity and gain flatness over the frequency range of interest, rather than noise per se. With a 50Ω resistance, however, the thermal noise is large in any case. Since ESA noise is not negligible in these sensors, it must also be concluded that a less noisy rf detection arrangement is required, in future work, to achieve the maximum potential of this sensing method.

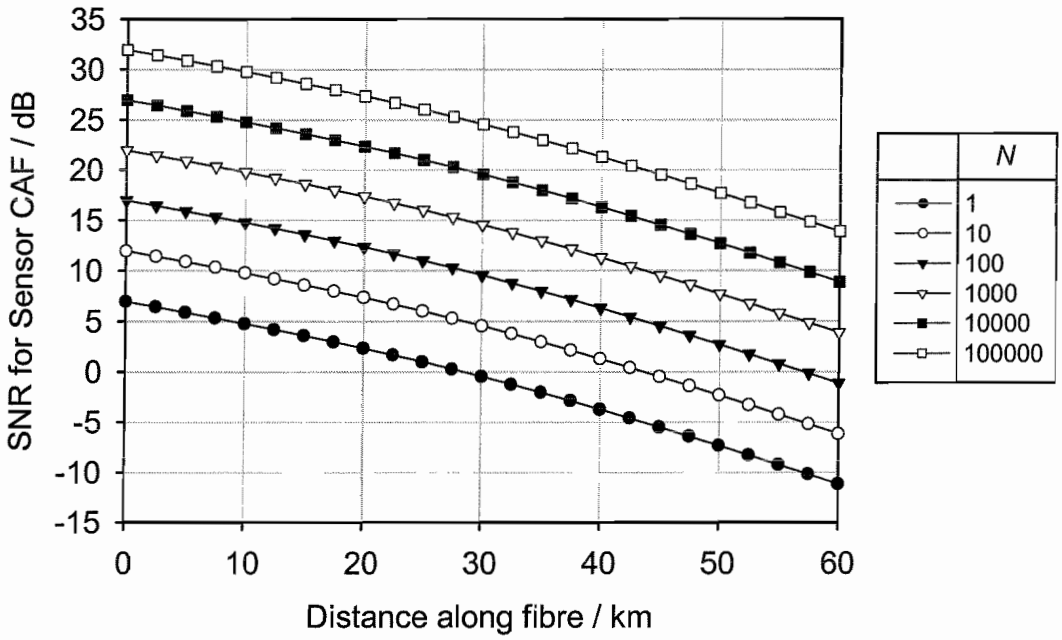

Figure 4.11 Theoretical SNR observed on the central Brillouin trace for sensor CAF as a function of distance along the fibre and number of signal averages, *N*.

For reference, the theoretical SNR on the central Brillouin trace as a function of fibre length for Sensor CAF is shown in Figure 4.11, for different numbers of signal averages, between 1 and 100,000. It can be seen that a ~1% noise (20dB SNR) can theoretically be achieved at 30km for 10,000 averages.

One important consideration with respect to the coherent sensors is the flatness of the DC offset. Firstly, the flatness with distance along the fibre is very important. If the beat terms involving the backscatter signals, other than the desired LO-AS term, are significant in magnitude, the DC offset will change along the trace length and since the interpulse level is not affected, there is no way to compensate for their effect.

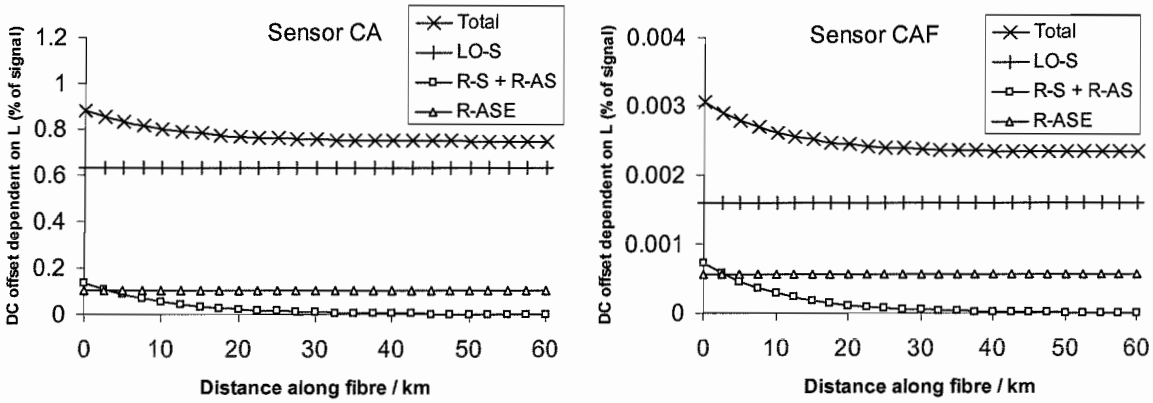

Figure 4.12 Contributions to the DC offset which are dependent on the distance along the fibre for Sensors CA and CAF. The total value and main components are shown as a percentage of the Brillouin signal. Such beat signals are not present in the interval between backscatter traces and remain to distort the signal spectrum after the interpulse offset has been subtracted.

For Sensors CA and CAF, the sum of every trace-dependent contribution to the DC offset was found as a percentage of the signal level at that point along the fibre. This is shown in Figure 4.12, as are the main contributors to this value, which together make up over 90% of the total value. It can be seen that Sensor CA has an offset signal of ~0.8% of the signal level, with most due to the rival Stokes heterodyne signal but, at the near end of the fibre, ~0.3% is due to the sum of R-S and R-AS. These percentages are of the same order as those produced by temperature changes of one or two Kelvin. For Sensor CAF, however, with its Rtwayleigh and Stokes filtering properties, this offset is equivalent to <0.01K.

Of course, the LO-S, R-S and R-AS beat components will all depend strongly on the exact beat frequency measured (frequency scanning spans of several hundred MHz are commonly used). The LO-S beat is centred at 11.11GHz and in Sensor CA, the trace at this point due to LO-S is equal to that for LO-AS at 10.89GHz. For Sensor CAF, however, the LO-S peak trace is only 0.25% of the LO-AS peak trace, almost

entirely removing its distortion effect. R-S and R-AS components are both centred at 11GHz, where their combined peak at the near end of the fibre is ~4.2% of the LO-AS peak for Sensor CA and 0.023% of the LO-ASE peak for sensor CAF. It can be seen that the optical filtering employed by Sensor CAF reduces any distortion on the signal spectrum caused by rival heterodyne signals to less than the equivalent of a change in temperature of 0.7K.

Also, flatness of the interpulse DC offset level, to within a fraction of a percent, over the frequency shift span used allows normalisation of each trace to this level, provided the laser properties are stable, in order to compensate for any instability in gain of the ESA. The interpulse level is affected mostly by the flatness of the ASE spectrum. There are three terms contributing to the interpulse level (excluding ESA offset), which are ASE-ASE, LO-ASE and LO-LO beat terms. LO-LO beat changes by 3.6% over a 220MHz span starting at 10.89GHz, but contributes only 0.12% (Sensor CA) or 0.49% (Sensor CAF) to the total level and so its frequency dependence is negligible. The LO-ASE term is centred on 10.89GHz so it is the flatness of the peak of the ASE spectrum which is important – using the double Gaussian fit, it is calculated to change by only 0.03% over 220MHz for Sensor CA. Sensor CAF will experience a similar change if the peak in the grating transmission function is flat over this frequency range. In Sensor CAF, ASE-ASE beat forms only 0.013% of the total offset, so any change in this term over the frequency span will also be negligible. In Sensor CA, however, it forms 7.7% of the total, but using Equation {4.37} it is found to change only by 8.3×10^{-5} % over 220MHz. It can be readily assumed that the interpulse level will be flat to within 0.03% for both Sensor CA and Sensor CAF.

Finally, it is informative to compare the SNR of Sensor CAF and an equivalent sensor where the only difference is that optical shifting has been employed to ensure the beat frequency between local oscillator and anti-Stokes signal is 100MHz. Plots of the theoretical SNR of each of these sensors are shown in Figure 4.13. It can be seen that the SNR of the 10.89GHz measurement is greater for all fibre lengths than that for the 100MHz beat frequency, with the difference being 3.3dB at the start of the fibre and 8.7dB at the end. This decrease in SNR is due primarily to an increase in LO-LO beat noise – the source self-beat noise – by ~40dB. This type of noise forms 97.7% of the

DC offset along the entire fibre length for the 100MHz beat frequency. Also, this low frequency results in larger backscatter self-beat noise, so optical filtering is still required to reduce the R-R component, in particular from ~1.3% to <0.0005% of the signal level.

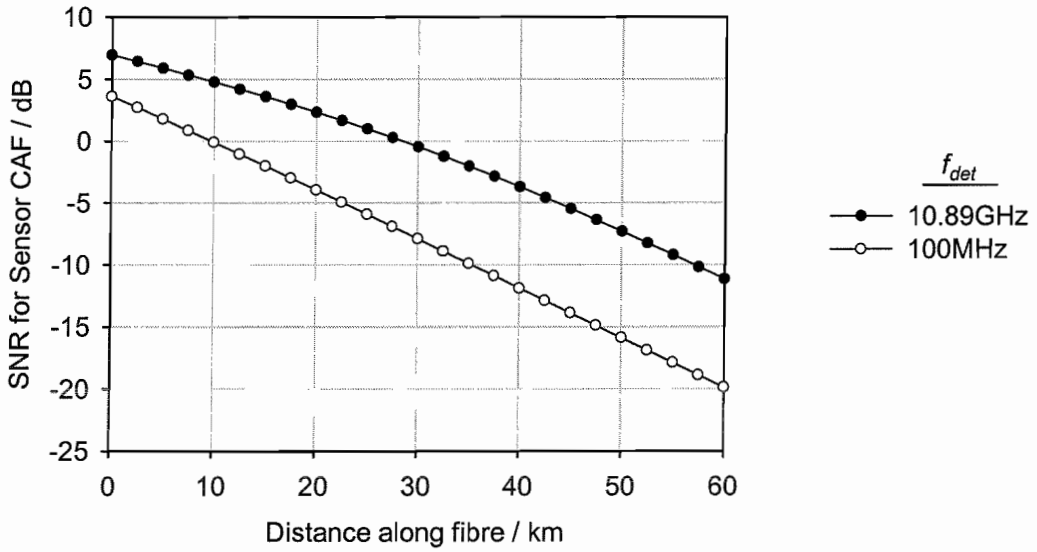

Figure 4.13 Comparison of the behaviour of the coherent detection system of Sensor CAF for two different peak beat frequencies of detection. One frequency is the frequency discussed thus far, 10.89GHz. The other represents a equivalent sensor including optical frequency shifting to ensure the optical local oscillator is 100MHz from the anti-Stokes signal.

4.4 Frequency Shift and Power Errors

Of course, if Brillouin spectroscopy is being undertaken, as in the coherent sensors, the SNR on the central trace will not equal the SNR on the total power. In order to determine the theoretical behaviour of the percentage error in total power, as well as the error in frequency shift, computational modelling was undertaken of the curve fitting process. The theoretical signal level and noise on the central trace, determined earlier in the chapter, were used to create Lorentzian spectra, of specified linewidth (set to 35MHz for these results) and centre frequency, with Gaussian noise of the required standard deviation. These spectra consisted of a specified number of points on the curve, from a specified start frequency, with a specified frequency step, imitating the recorded experimental data. The curve fitting algorithm was applied to the noisy spectra and the deviations from the noiseless curve area (or noiseless frequency shift) of the equivalent curve fitting output parameters were recorded. The

RMS values of these deviations were found, for 1000 consecutive spectra (identical in the absence of noise), each with a different random noise seed for the Gaussian noise generation. Two such RMS values in succession were output from the program and compared for closeness of match.

This model allows the performance of Sensor CAF to be predicted. Firstly, an appropriate frequency step must be chosen. To this end, errors in power and frequency shift were obtained for identical total spans (240MHz) and identical total number of averages (49×4096), i.e. capable of the measuring the same range of frequency shifts in the same collection time, but using different frequency steps. Number of recorded frequencies is equal to span divided by frequency step, plus one. This data is shown in Figure 4.14, for the SNR obtained 30km down the sensing fibre and the peak in the centre of the recorded span.

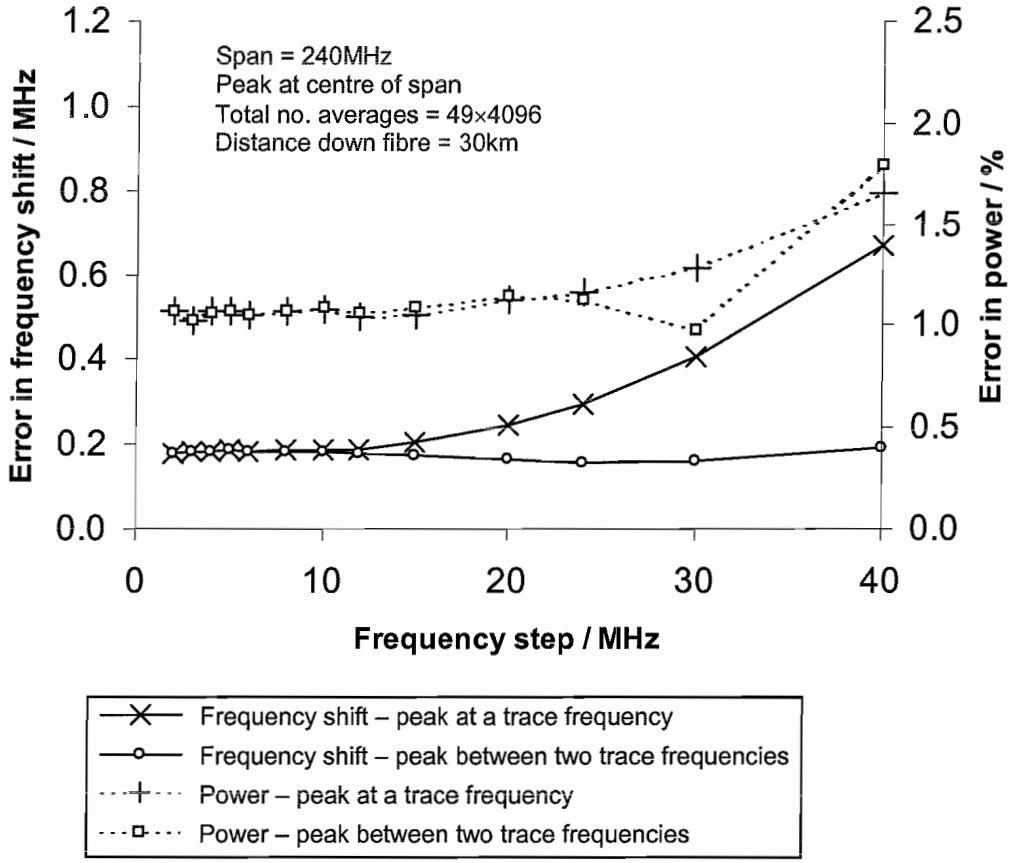

Figure 4.14 Theoretical behaviour of frequency shift error and total power error on the frequency step chosen in the collected data, for identical frequency spans and measurement times. Data is shown for spectra both with their peak at a recorded frequency and with their peak midway between two recorded frequencies.

It can be seen that the sensor has a similar performance for frequency steps up to ~12MHz, after which the sparsity of the data reduces the measurement accuracy. It can also be seen that, above 12MHz, the accuracy of the fit starts to become dependent on the position of the spectral peak with respect to the recorded data. Using this information, a frequency step of 5MHz was chosen, a compromise between less noisy individual traces (and smaller quantity of data) and an improved tolerance of a reduction in spectral width.

Using this frequency step, the dependence of the power and frequency shift errors on total recorded span was modelled. This was again for a spectrum at 30km down the fibre and with its peak in the centre of the span in all cases. Data was found for both 4096 averages per trace (increasing the measurement time for increasing span) and for the same number of total averages (20×4096), independent of span. The resulting data is shown in Figure 4.15.

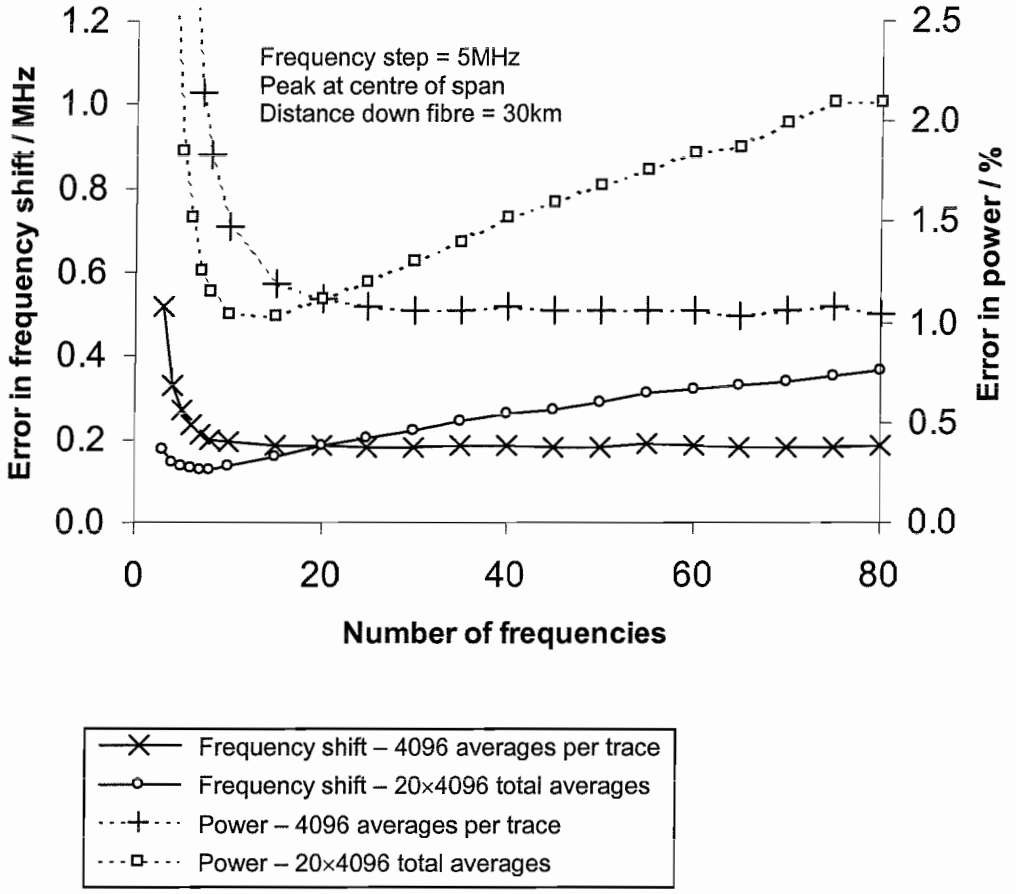

Figure 4.15 Theoretical behaviour of frequency shift error and total power error on the frequency span of collection, for a frequency step of 5MHz. Data is shown for both 4096 averages per trace and for a total number of averages of 20×4096.

In this figure, frequency spans shorter than ~50MHz (11 frequencies) result in a significant increase in both power and frequency shift errors due to incomplete spectral coverage. Above ~100MHz span (21 frequencies), there is little change in error with span, provided that the number of averages per frequency is constant. If, however, the sum of the powers at each frequency were used as the total power, as discussed in §3.11, the extra traces would introduce additional noise, which is another incentive to choose the curve fitting method. For an identical total number of averages, the errors rise with span, as would be expected, doubling between spans of ~100MHz and ~400MHz. Using data such as these, we may predict how many averages must be taken per trace in order to achieve the required frequency shift and power resolution for a given specified frequency shift span.

The results so far have considered a spectrum in the centre of the span. In order to determine the required collection span for a desired range of frequency shifts, we must consider how the position of the peak frequency within the collected span affects the measurement errors. Data for a span of 395MHz (80 frequencies), at 4096 averages per trace, is shown in Figure 4.16. It can be seen that the errors increase for peaks centred at either end of the span and that the span must therefore extend at least 20MHz beyond the required frequency shift measurement range in order to keep the measurement errors within a factor of ~1.3 of those in the centre of the span.

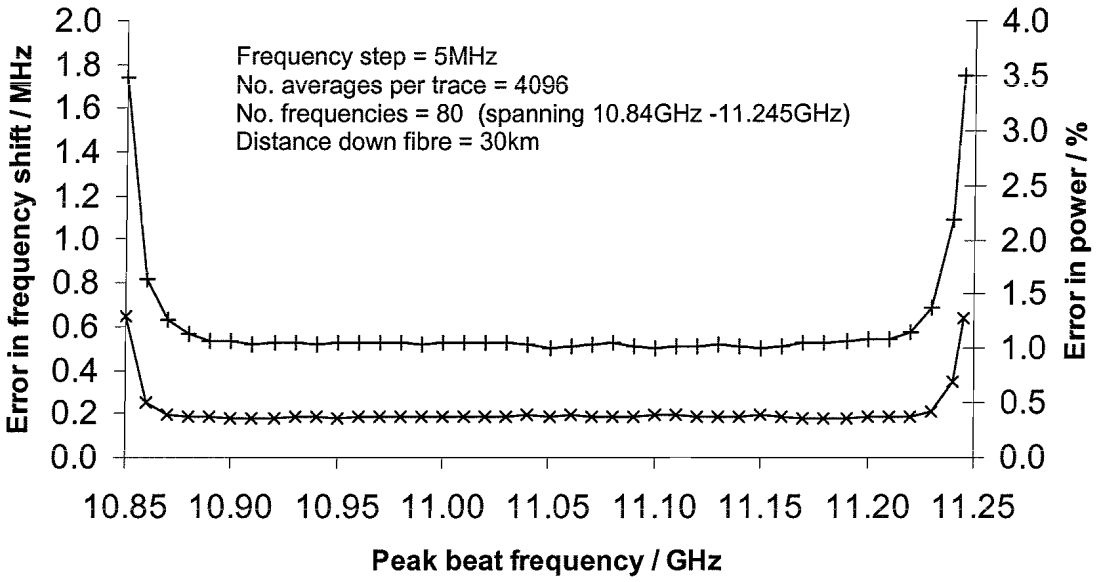

Figure 4.16 Dependence of the errors in frequency shift and power on the position of the spectral peak within the collection span.

Finally, the signal-to-noise ratios of both the total power and the power in the central 5MHz are plotted in Figure 4.17 as a function of fibre length, for a span of 170MHz (35 frequencies) and 4096 averages per frequency.

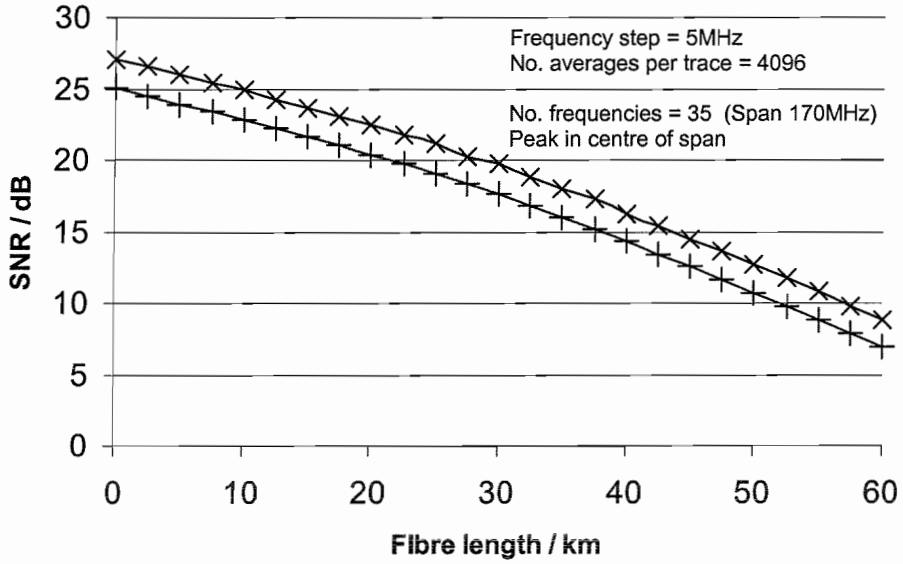

Figure 4.17 Signal-to-noise ratios of both central trace (+) and total power trace (×), as determined by curve fitting, as a function of distance along the fibre.

It can be seen that the SNR improvement is ~2dB for all distances along the fibre, i.e. for a range of central trace SNRs between ~7dB and ~25dB. This is equivalent to the increase which would be caused by taking 2.5 times the number of averages.

4.5 Conclusions

In this chapter, a detailed theoretical analysis of the proposed 11GHz sensor was presented, together with a comparison with direct detection methods. It was found that an optically pre-amplified and filtered coherent sensor has a central trace SNR which is no more than 3.2dB worse than the power SNR of a direct detection, unamplified backscatter sensor using an ideal 10MΩ receiver. It was also found that such a filtered coherent sensor will allow detection of undistorted anti-Stokes spectra, unlike the unfiltered version. Also, the use of an 11GHz beat frequency was demonstrated to improve the central trace SNR by between 3.3dB and 8.7dB compared to that obtained using a 100MHz beat frequency, due to the smaller LO-LO beat noise.

The curve fitting process to determine total power and frequency shift was applied to modelled spectra based on the theoretical signal-to-noise ratios. This enabled the selection of appropriate frequency step and collection span and demonstrated an improvement in SNR, with respect to that of the central trace, of ~2dB, independent of distance along the fibre.

The next chapter will examine the experimental results obtained using the coherent sensor, including comparisons to this theory.

4.6 References

[4.1] E. Desurvire: "Erbium-doped Fiber Amplifiers: Principles and Applications", *John Wiley & Sons Inc.*, ISBN 0-471-58977-2 (1994)

[4.2] A. Yariv: "Optical Electronics", 4th Edition, *Saunders College Publishing*, ISBN 0-03-053239-6 (1991)

Chapter Five

Temperature and Strain Sensing: Experiments

5.1 Introduction

This chapter will deal with many aspects of the sensor's performance, noise characteristics, sensing capability and progressive improvement, along with comparisons to the theory, where appropriate.

Calibrations to find coefficients for the dependences of the Brillouin power and frequency shift on both temperature and strain are provided and simultaneous strain and temperature sensing is discussed. Polarisation noise on the Brillouin trace and coherent noise on the Rayleigh trace are both examined and the signal-to-noise ratio is determined as a function of fibre length as compared to the theoretical dependence.

5.2 Problems with the First Sensor and Their Solutions

Firstly, however, the disadvantages of the first sensor design will be considered, along with their solutions.

5.2.1 Undesirable Heterodyne Peaks

As mentioned in Chapter Four, the existing first sensor (Figure 3.15) will exhibit unwanted peaks due to both Stokes-LO heterodyning and Rayleigh-Stokes and Rayleigh anti-Stokes heterodyning. These phenomena are illustrated in Figure 5.1 for this unfiltered sensor, where the Stokes-LO peak is evident at ~11.11GHz and the Rayleigh-Brillouin peak lies at ~11GHz. In this figure, experimental data is indicated by crosses and the sum of three Lorentzian curves best fitting the data is plotted as a solid line.

From the theory (§4.3.3), the combined R-S and R-AS peak value should be 4.2% of the LO-AS peak value. Since the Stokes signal in the experimental case is slightly stimulated, the theory is modified to say that the combined peak be 2.1% of the sum of the LO-AS and LO-S peaks. In actual fact, it is measured experimentally (using the fitted Lorentzian curves) to be 3.4% of the sum. However, the backscatter is coupled from the fibre via a circulator in this experiment, with a typical port-to-port loss of 1.2dB, rather than 3dB coupler as the theory models. This will act to increase the Rayleigh by a factor of 1.8dB and so our theoretical value rises to ~3.2%. Also, the local oscillator in this case as 1mW, rather than the modelled 1.08mW, increasing he theoretical value still further, to ~3.4%, in agreement with the experiment. However, this last value must again be modified due to the nature of the experimental backscatter trace, which is the average of 15 separate distributed spectra (2048 averages per trace) spanning ~1km at the near end of the fibre. The averaging was performed to help reduce CRN on the central peak, for a more accurate estimate. Since the Rayleigh signal decays by 0.2dB after 0.5km, this new theoretical estimate of 3.4% is also reduced by this amount, to 3.25%, which is still close to the experimental value.

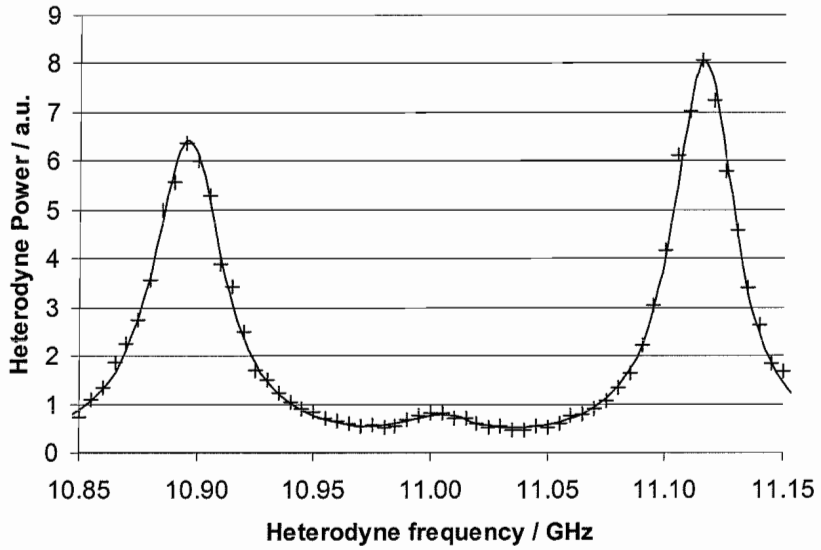

Figure 5.1 Unfiltered spectral output from the first sensor (see Figure 3.15). Three peaks exist in the spectrum, from left to right: signal LO-AS peak, combined R-AS and R-S peak and LO-S peak. The solid line is a fitted triple Lorentzian curve to model the data.

The production of an extra 11GHz peak is the principal method by which the Rayleigh can affect the Brillouin signal in this type of sensor and is much less significant than an equivalent amount of contaminating Rayleigh power in direct detection, since it is the ratio of local oscillator power to Rayleigh power which is important, rather than the ratio of Brillouin power to Rayleigh power

To remove the two spurious peaks in Figure 5.1, the circulator was replaced by a 3dB coupler and moved to the output of EDFA2, where it acted to transmit the amplified backscatter to and from a fibre Bragg grating filter centred on the anti-Stokes wavelength, as in Sensor CAF (discussed in Chapter Four). Now, either the anti-Stokes or Stokes signals could be observed by tuning the narrow-band source so that the relevant backscatter component lay at the grating peak wavelength (1533.08nm). Contact with the heavy, metal optical bench and the use of thermostatically controlled air conditioning both increased the stability of the grating and so no thermal drift problems were encountered. Since a typical FBG central wavelength temperature sensitivity is 10-15pm/K and the grating had a flat transmission peak of width ~50pm, ambient temperature changes of a degree or two were tolerable. Use of a thermally compensated grating package would have reduced this problem still further. A resulting spectrum is shown in Figure 5.2 to demonstrate the effective peak removal.

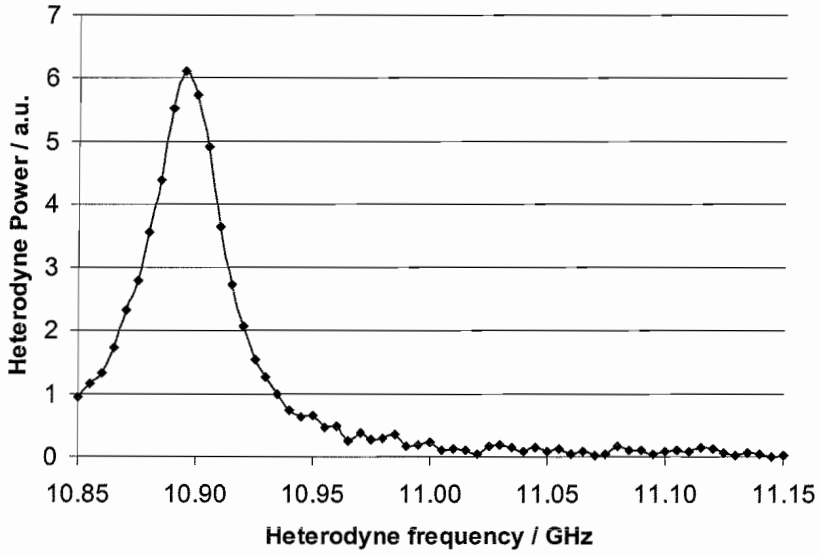

Figure 5.2 Filtered output from the improved sensor, where the Rayleigh and Stokes signals are attenuated by a fibre Bragg grating filter centred on the anti-Stokes wavelength.

5.2.2 Polarisation Noise Due to Incomplete Scrambling

Polarisation noise on the anti-Stokes trace was found to be a problem using the the first sensor, since the polarisation scrambler was faulty and not scrambling effectively. The effect of the scrambler can be seen in Figure 5.3, where central (10.9GHz beat frequency) anti-Stokes power traces are shown for different numbers of signal averages both with and without scrambling. Each trace is completely independent, each with its own separate set of recorded traces.

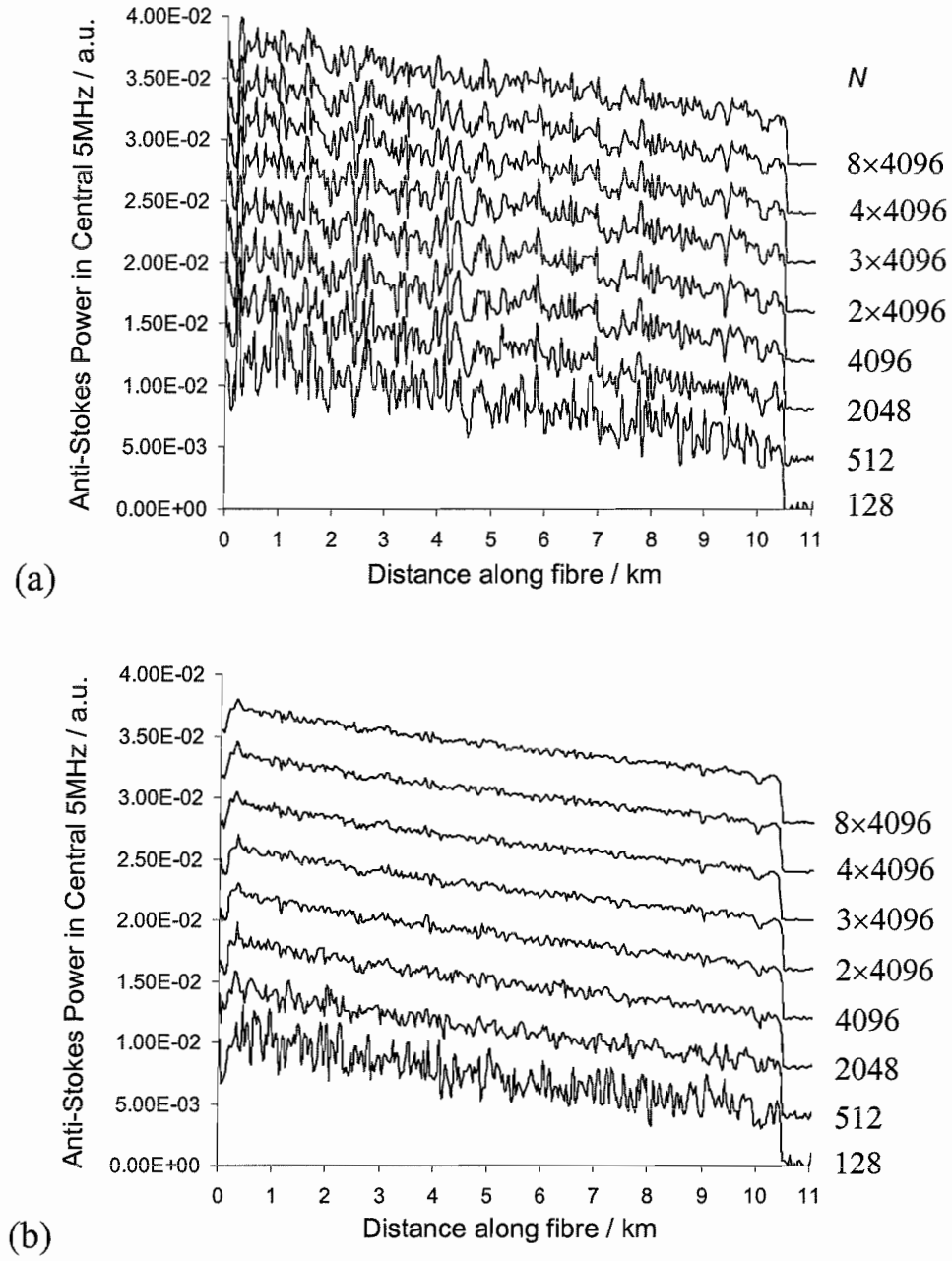

Figure 5.3 Anti-Stokes central frequency power traces for different numbers of averages, *N*, and with (a) scrambler off (b) scrambler on.

It can be seen that the noise is greatly reduced by the action of the scrambler yet there is still marked correlation between the noise in the traces obtained at higher numbers of averages, indicating that polarisation noise is the dominant noise source above ~4096 averages. Figure 5.4 shows the trace noise as a function of number of averages, where the noise is found as the RMS value, over the range 0.5km to 10km, of the percentage deviation from a fitted exponential. This figure shows that the unscrambled signal has ~11% polarisation noise and the scrambled signal has ~3% residual polarisation noise.

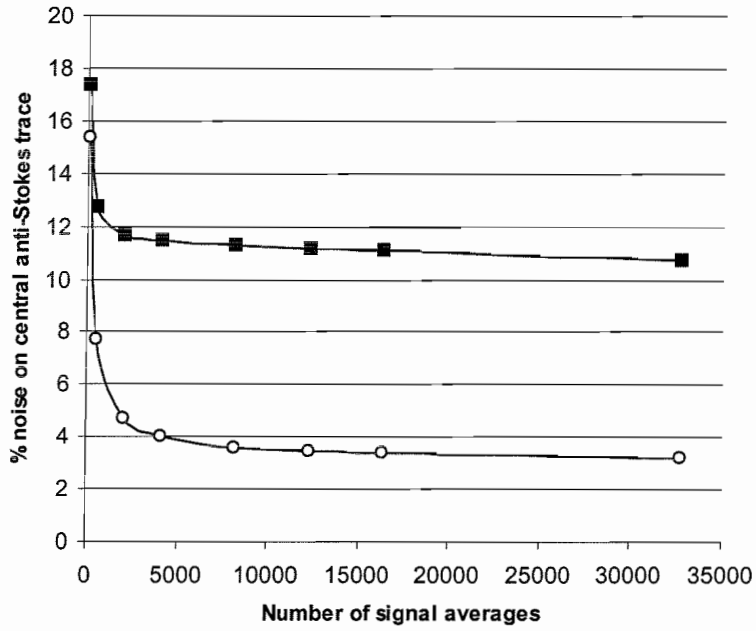

Figure 5.4 RMS power error of the central anti-Stokes trace as a function of number of signal averages. The error is found, in each case, as the RMS deviation from a fitted exponential over the fibre length. Filled squared: scrambler off. Open circles: scrambler on.

In order to reduce this residual component, a further scrambling element was added to the sensor. This was made by winding ~50m of high birefringence fibre tightly round a large piezoelectric cylinder and gluing it in place. A sinusoidal voltage, between the limits of 0 and ~400V, was applied in order to achieve a single fringe polarisation modulation of radiation input at 45° to the fibre axes. This polarisation state was arranged by a polarisation controller situated immediately before the cylinder. This combination was not a true scrambler, but acted as an extra scrambling cell in order to reduce the polarisation noise. The PZT was placed just prior to the sensing fibre.

This extra modulation was sufficient to reduce the residual polarisation noise to less than 1%. A typical residual noise of ~0.8% was observed on the total anti-Stokes power after the introduction of this second "scrambler", which will be evident from the results presented in §5.3 and the subsequent sensing measurements.

5.2.3 The Second Sensor

A 500m section of fibre was removed from its drum, to ensure absence of strain, inserted into the sensing fibre and placed in an oven for temperature measurements. The entire sensing fibre length itself was different for each experiment and will be detailed in the relevant sections. The pulses used in the following experiments were of power 160mW and duration 200ns and the anti-Stokes spectra were recorded.

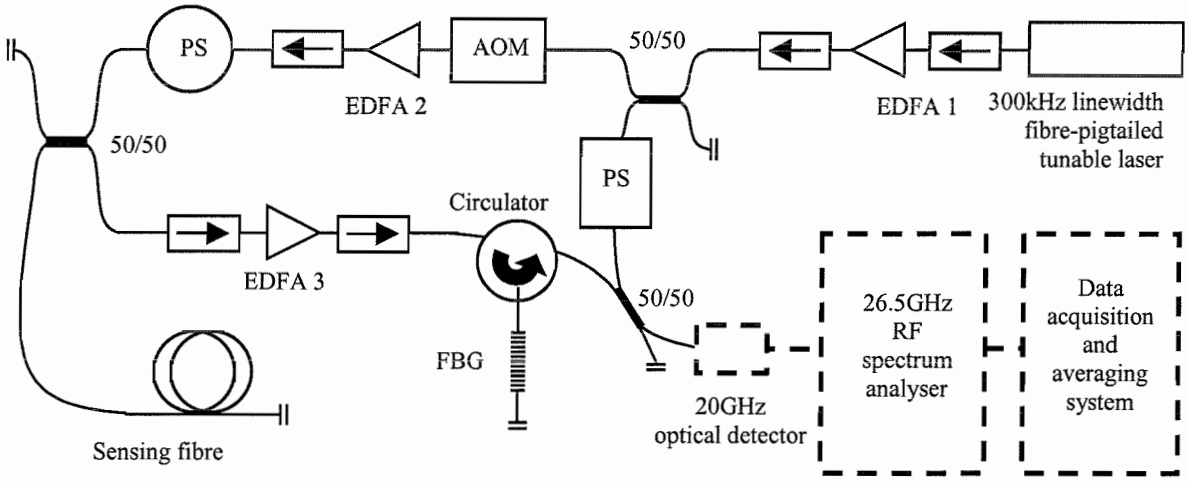

Figure 5.5 The Second Sensor, improved by ASE, Rayleigh and anti-Stokes filtering and the addition of a second polarisation scrambler. Filtering is achieved by a fibre Bragg grating with profile as shown in Figure 4.4 and centre wavelength 1533.08nm at room temperature.

Before discussing the sensing experiments, sample distributed spectra will be presented to check the validity of the Lorentzian curve fitting process. These spectra are shown in Figure 5.6(a) for a 3.5km length, located 25km down a sensing fibre.

The 500m heated portion (at 65°C) is clearly visible, between 26.5km and 27km, due to its frequency shift from the unheated regions (22°C). Figure 5.6(b) shows a single spectrum from this 3.5km section and its corresponding fitted Lorentzian curve.

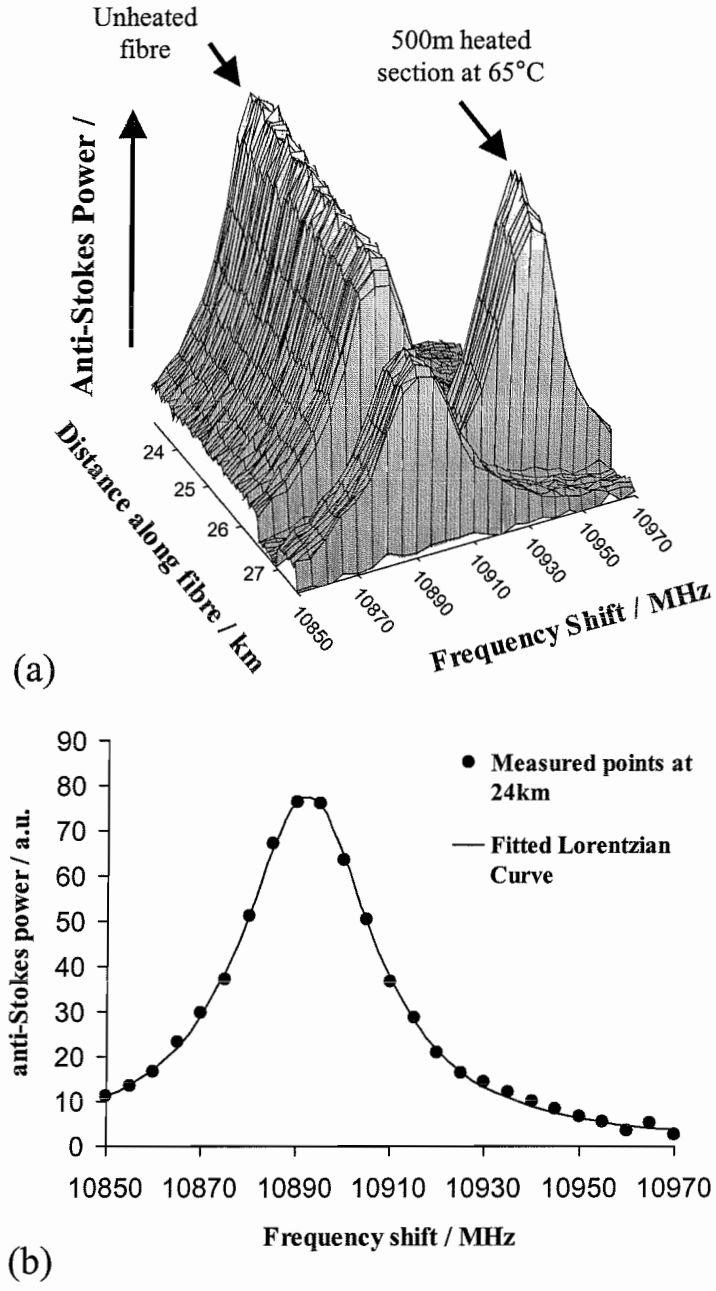

Figure 5.6 (a) Sample distributed anti-Stokes spectra obtained using the third sensor (Figure 5.22) at ~25km down the sensing fibre. A 500m heated section (at 65°C) is easily visible due to its ~45MHz frequency shift with respect to the unheated fibre. (b) Single spectrum, demonstrating the Lorentzian curve fitting process.

To estimate the goodness of fit, the value χ^2/N was calculated, which is defined by

$$\frac{\chi^2}{N} = \frac{1}{N}\sum_{i=1}^{N}\frac{(y_i - f(x_i))^2}{\sigma_i^2} \qquad \{5.1\}$$

for a data set of N points, ($x_{i...N}$, $y_{i...N}$), with standard errors in y of $\sigma_{i...N}$, being modelled to a function $f(x)$. χ^2/N should be roughly equal to 1 for a good fit with the expected noise characteristics, with a closer fit being indicated by a lower value. To obtain an estimate in this case, the noise on each point was assumed to be identical and dominated by electrical noise, which was calculated as the standard deviation of the interpulse traces. The measured value of χ^2/N for Figure 5.6(b) is 0.82, validating the choice of spectral profile.

5.3 Initial Measurements over 57km

The improved sensor (Figure 5.5) was then used with a sensing length of 57km, longer than any length previously reported for single-ended detection of spontaneous Brillouin backscatter, in order to gauge the performance of the sensor. These results will also be compared to the theory developed in the previous chapter. The 57km sensing fibre consisted of five separate fibre lengths: 17500m, 17500m, 17500m, 500m and 4000m, with the 500m section being placed in an oven and unwound from the drum to ensure the absence of strain. The rest of the fibre was kept at the room temperature of 22°C. Distributed anti-Stokes spectra were obtained for a pulse power of 160mW and a pulse duration of 200ns over the entire length of this sensor by recording a series of 25 different backscatter traces, each separated by 5MHz, starting at 10.84GHz; each trace was averaged 4096 times. The resulting backscattered power measurements and frequency shift measurements, obtained using Lorentzian curve fitting, are shown in Figure 5.7, where the oven was set to a temperature of 40°C. The frequency shift due to this 500m heated section is clearly seen at ~53km along the fibre. The frequency shift measurements also emphasise the boundaries between the different fibre sections, with the sharp troughs being attributed to slack fibre between wound drums. It can be seen that each unheated fibre section exhibits a different frequency shift, possibly arising from differences in winding tension or intrinsic fibre properties (acoustic velocity or refractive index).

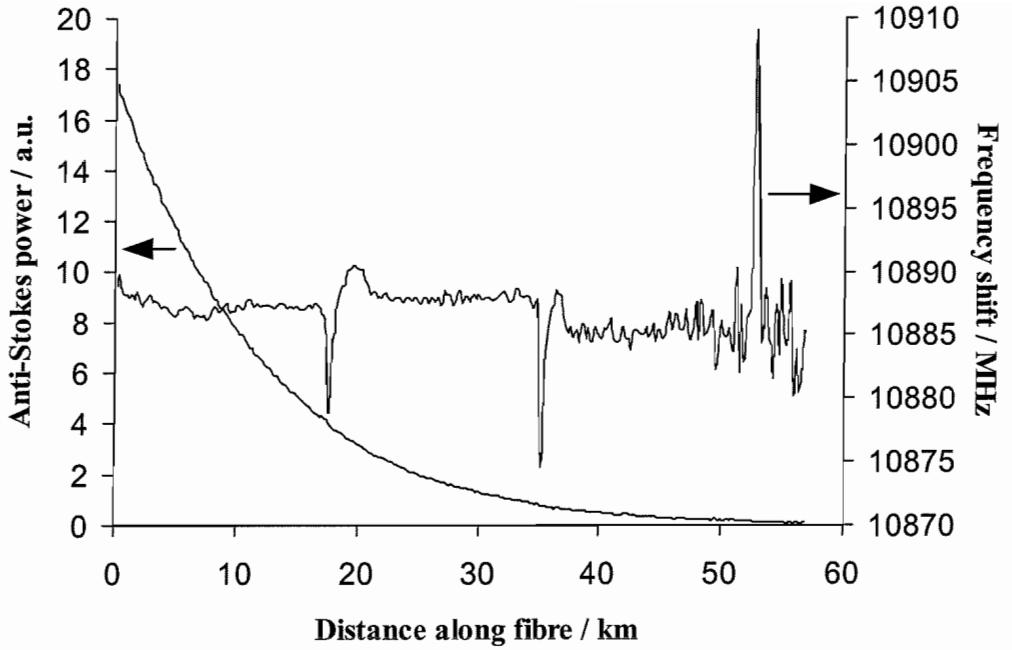

Figure 5.7 Sensing results for the 57km sensing length. Both anti-Stokes power and frequency shift are plotted for an input pulse power of 160mW and duration of 200ns. Lorentzian curve fitting was carried out for 25 frequencies, each separated by 5MHz, with each frequency trace averaged 4096 times.

The sensing fibre was reversed in order to investigate this frequency shift behaviour in comparison to the original fibre configuration. Frequency shift and power measurements (plotted on a dB scale) for the second 17.5km drum are shown in Figure 5.8 for both fibre orientations.

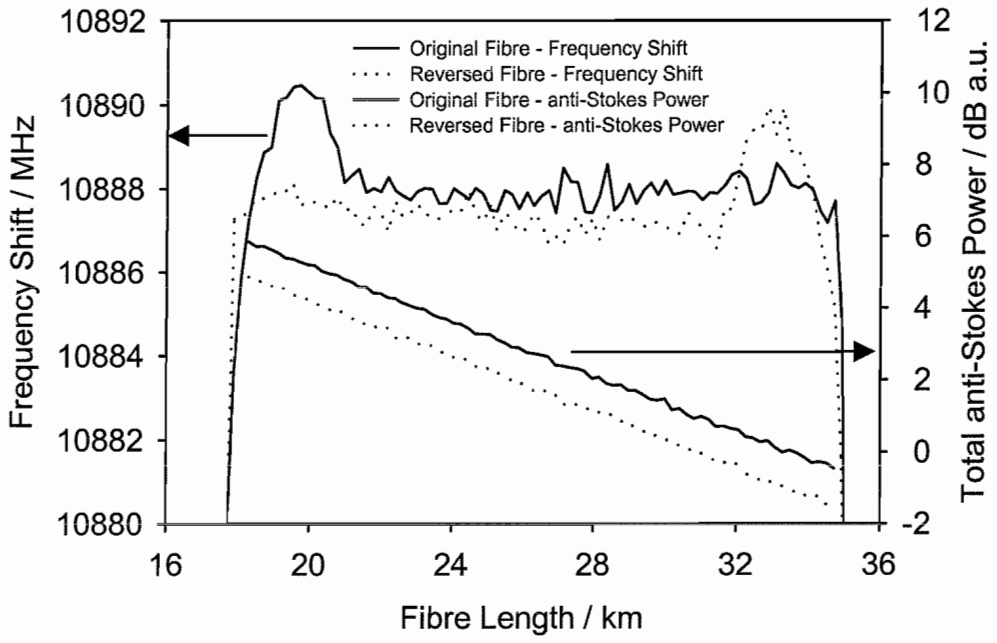

Figure 5.8 Close up of central 17.5km drum in Figure 5.7, along with results taken for the same drum but with the sensing fibre reversed – power traces are offset for clarity.

It can be seen that the behaviour of the frequency shift is the same in each case, although mirror-imaged and the entire spectrum is downshifted by 0.7MHz for the reversed fibre, indicating a reduction in ambient temperature of ~0.7K. It can also be seen that 2.5km of fibre at one end (in fact, this is the portion of fibre wound innermost on the fibre drum) exhibits a frequency shift ~2MHz higher than the rest of the fibre, implying a higher strain during winding for the inner part of the drum (equivalent to ~40με – see §5.9). Indeed, this characteristic is exhibited to some degree for each of the 17.5km drums used in the sensing fibre. The power measurements show the expected exponential decrease with fibre length, with an attenuation of 0.386dB/km (0.193dB/km single-pass), agreeing with the expected value of ~0.4dB/km at 1.53μm. The power trace for the reversed fibre is shifted from the vicinity of the original trace, for clarity.

The RMS noise in both power and frequency shift traces were found over 2km sections (corresponding to 10 data points) located at several positions along the sensing fibre. The power values were found after first normalising the recorded trace to a fitted exponential decay function, one for each separate section of fibre. The noise information is shown in Figure 5.9(a) for the frequency shift and Figure 5.9(b) for the power. The noise levels increase to 1.3MHz and 5.8% at 50km, corresponding to ~1.2°C/28με and ~16°C/6500με respectively. It is clear from this that the power trace is too noisy to allow a useful simultaneous sensor at this distance. It is clear, however, that an unstrained 50km sensing length may be used to measure temperature with better than 1K accuracy for almost all of the sensing length. Figure 5.9(b) indicates that an RMS error of 1.5% would occur at 30km, bringing the temperature error due to the power measurement down to less than 5°C, a reasonable target.

The theoretical values, determined as described in §4.4, are also shown in Figure 5.9, for comparison, using the experimental parameters employed in obtaining this trace. It can be seen that the agreement between the experimental and theoretical errors is good, validating the theory, and that an even closer agreement is obtained if splice losses between fibre drums, measured from Brillouin power traces, are accounted for (0.15dB, 0.4dB, 0.45dB and 0.45dB double-pass for each splice in turn).

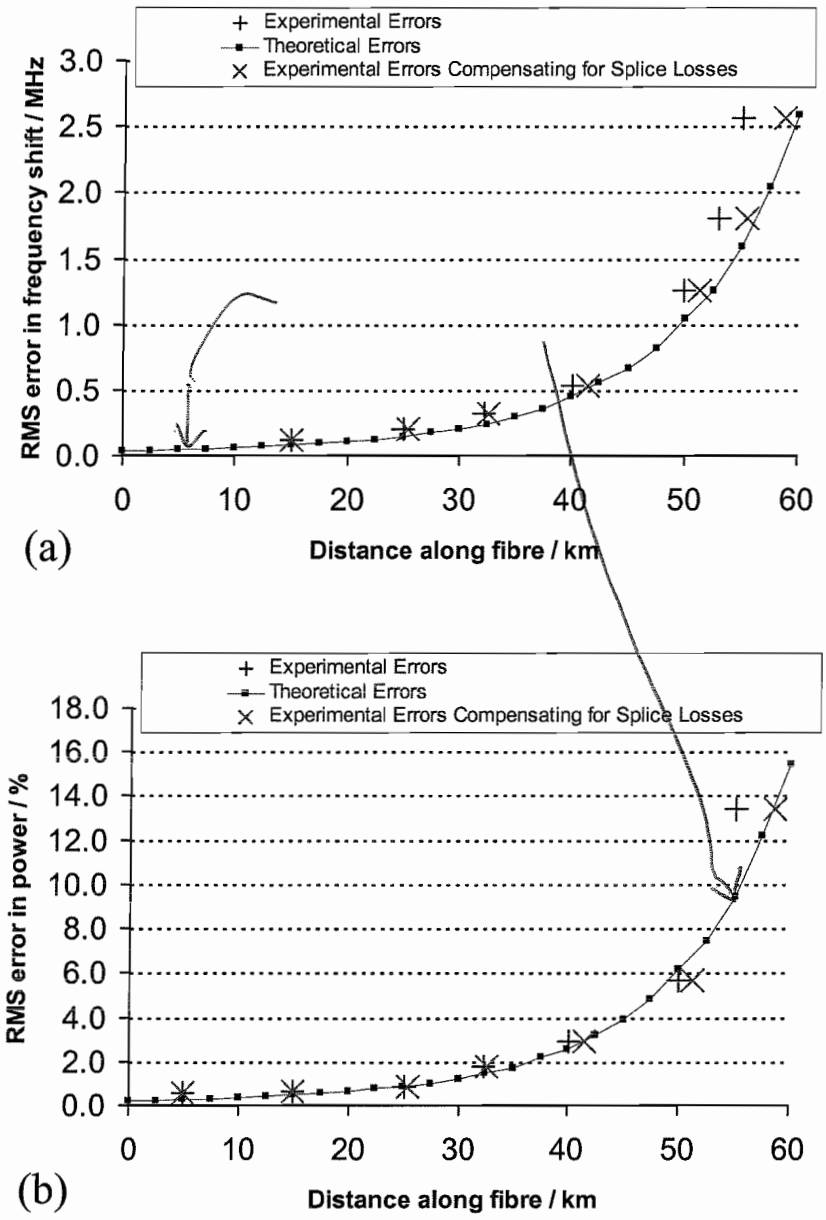

Figure 5.9 Measured experimental RMS noise in (a) frequency shift and (b) anti-Stokes power as a function of sensing distance. Also plotted are theoretical values, for the relevant experimental parameters, calculated as described in §4.4, and the experimental points after compensation for measured splice losses along the sensing length.

On closer inspection of the experimental data in Figure 5.9, the RMS power error is observed to remain at the approximately constant value of 0.7-0.8% for the first 20km of the sensing fibre, over which the backscattered power has decreased by ~8dB. The theoretical resolution is not being achieved at these relatively short distances, indicating the presence of an additional noise source. It is deduced that polarisation noise, which would characteristically contribute a fixed percentage to the noise, has not been fully eliminated and that an even greater degree of scrambling is necessary,

for optimum resolution. The frequency shift RMS error also does not appear to reduce over the first 20km (see Figure 5.7). This is more likely to arise from intrinsic variations in the frequency shift of the fibre. Polarisation noise would not be expected to be significant in frequency shift measurement since an individual spectrum comes from backscatter from a single spatial-resolution-length along the fibre. The detected Brillouin radiation will have a single polarisation state, independent of frequency in the spectrum. Material dispersion (at 0.02 ns nm^{-1} km^{-1}) accounts only for a 0.33ps difference in arrival time at the detector of two 1.53μm signals, separated in frequency by 35MHz, which are emitted at the same time from the end of a 60km fibre. This means that the heterodyne spectra themselves would not be distorted by polarisation noise, although adjacent spectra would be of different intensities.

The results in Figure 5.9 may be used to characterise errors in computed frequency shift and power as functions of the SNR of the central trace. Of course, any such characterisation applies only in the specific experimental circumstances of this particular data set: number and separation of recorded traces will also play a part, as will exact local oscillator power, Brillouin linewidth and incident signal power. It will, however, provide a guide. The relevant plots are presented in Figure 5.10, for the theoretical data shown in Figure 5.9.

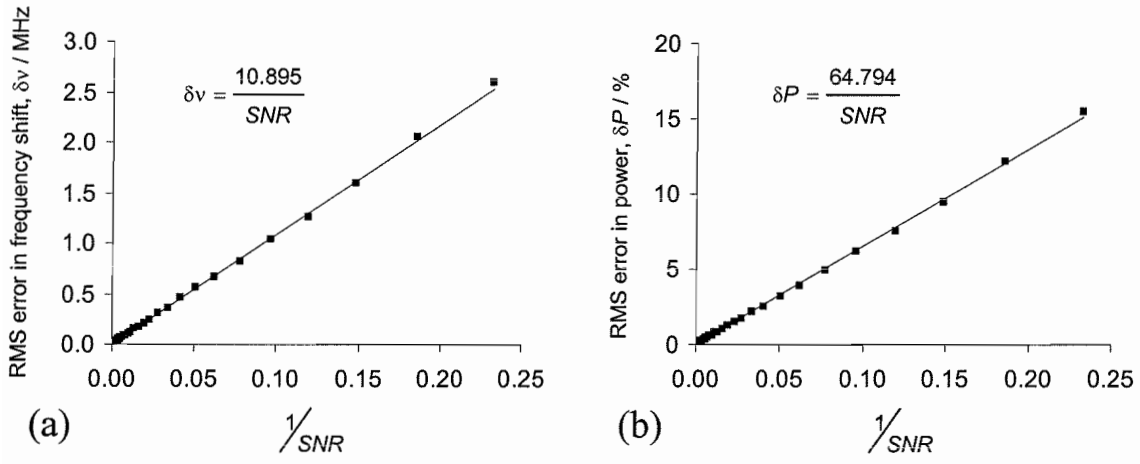

Figure 5.10 Behaviour of theoretical RMS errors in (a) frequency shift and (b) % change in power, obtained after curve fitting, as a function of signal-to-noise ratio (linear, not dB) on the central collected trace. A least squares straight line is fitted to each curve, passing through the origin, with the equation, for each, as indicated in the appropriate figure.

These plots clearly indicate an inverse proportionality of the measured errors on central trace SNR. Interestingly, this disagrees with the relation put forward by Shimizu et al. [5.1], which states that, for coherent detection, the error in frequency shift measurement is inversely proportional to the fourth root of the SNR.

$$\delta\nu_B = \frac{\Delta\nu_B}{\sqrt{2}(SNR)^{1/4}} \qquad \{5.2\}$$

It is reasonable to assume that, given the analysis and the data in this particular case, this equation is flawed, especially since it gives an error as large as $\delta\nu_B$=14MHz for a Brillouin linewidth $\Delta\nu_B$= 35MHz and SNR=10.

5.4 Temperature Calibration

This section will deal with calibration of the sensor, to ensure that its behaviour is consistent with that expected. There should be a linear increase in both frequency shift and power with temperature and the constants of proportionality should ideally agree with previous published calibrations (see §2.4.2).

5.4.1 Oven Temperature Stability

In order to obtain good temperature sensing results, oven stability must be investigated and the built-in temperature readout compared with that of an external reference thermocouple. To that end, the reference thermocouple was inserted into the oven, in close proximity to the fibre under test, and readings of its output and the oven built-in reading were taken during a series of temperature changes. The results were as shown in Figure 5.11. The oven was initially at room temperature and then first set to 35°C. Stabilisation at this temperature was achieved after ~20 minutes and the oven then set to 65°C. This larger temperature difference increased stabilisation time to ~35 minutes. At this point, the oven was reset to 35°C and the cooling time was measured again as ~35 minutes. Agreement between the oven thermocouple (at the roof of the oven) and the monitor thermocouple, at the fibre, was within 1°C after stabilisation at each set temperature.

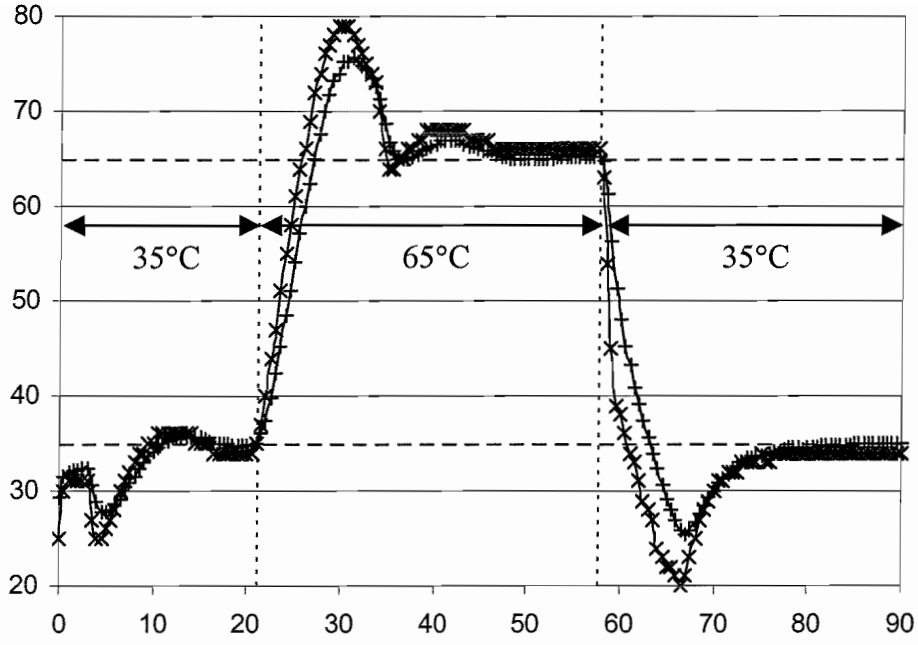

Figure 5.11 Behaviour of oven temperature when set to temperatures of 35°C, 65°C then 35°C again. × Extra thermocouple - next to fibre + Integral thermocouple - near roof of oven.

This investigation suggested that a reasonable minimum delay between change of oven setting and commencement of measurement is ~35 minutes, although the entire fibre must also be allowed to reach thermal equilibrium.

5.4.2 Frequency Shift Dependence

The dependence of Brillouin frequency shift on temperature was determined using the results obtained from the 57km sensing length discussed in §5.3. Distributed Brillouin spectra were recorded using oven temperatures of 60°C, 50°C, 40°C, 30°C and 22°C (room temperature). The resulting frequency shift traces for a 2km length surrounding the 500m heated fibre (53km down the fibre) are shown in Figure 5.12(a). From these traces the RMS frequency shift noise was calculated to be less than 2MHz over the heated fibre section for each oven temperature, with the average error over all five traces being ~1.8MHz. The expected linear relationship between frequency shift and temperature is clearly visible in Figure 5.12(b), with the coefficient of proportionality being 1.07±0.06MHz K^{-1}. This agrees in magnitude with values from other sources [5.2][5.3].

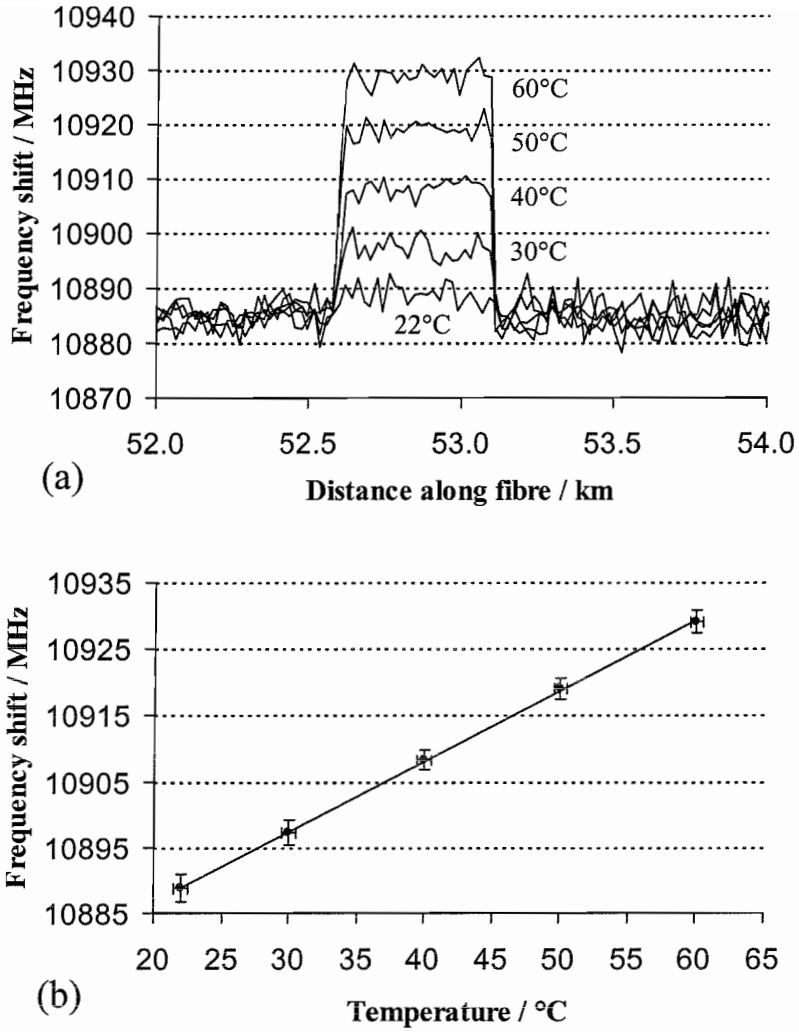

Figure 5.12 (a) Brillouin frequency shift traces obtained from Lorentzian curve fitting to collected spectra using the sensor in Figure 5.5. (b) Corresponding dependence of this shift on temperature, demonstrating a coefficient of proportionality equal to 1.07 ± 0.06 MHz K^{-1}.

5.4.3 Power Dependence

Using the information in §5.3, the sensing length was reduced to 27.4km (four fibre sections of 17500m, 8900m, 500m and 500m, with the third section being heated) in order to demonstrate a long-range sensor capable of measuring power to a useful accuracy (~1%), as well as frequency shift.

Power measurements are more complicated to acquire than frequency shift measurements. A Rayleigh trace must be obtained in order to account for intrinsic fibre losses. This Rayleigh trace was obtained by switching off the source laser (Figure 5.5) and using ASE pulses to generate a broad-band Rayleigh signal. The

Rayleigh power was measured prior to EDFA3 by breaking the splice (32768 averages). This cumbersome method sufficed for these initial results, but prompted the creation of a dual source, which will be discussed in §5.8, enabling sufficient ASE pulse power to be launched that a 95/5 tap could allow measurement of 5% of the Rayleigh signal prior to pre-amplification of the backscatter. Again 25 Brillouin heterodyne frequencies were recorded, separated by 5MHz, but this time the starting frequency was 10.85GHz and each trace was averaged 12288 times. Again, a single Lorentzian was fitted for each point along the fibre. Anti-Stokes backscatter traces for 25°C, 35°C, 45°C, 55°C and 65°C are shown in Figure 5.13 along with the Rayleigh trace, normalised such that the Rayleigh equals the anti-Stokes for the fibre at room temperature.

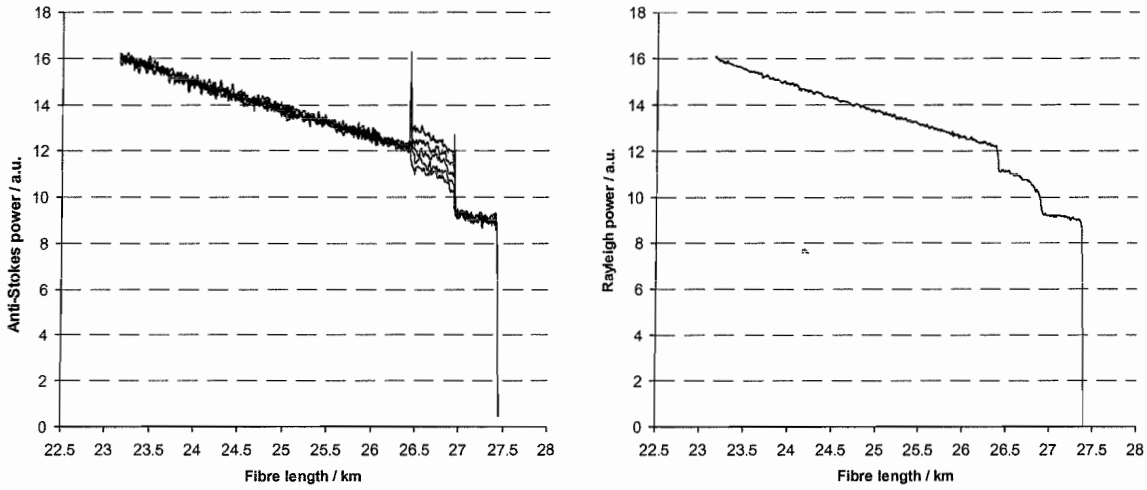

Figure 5.13 Sensing results for the final 4km of a 27.4km fibre. A 500m heated section is evident between 26.5km and 27km. (a) Anti-Stokes Brillouin power traces, found by curve fitting, for five different oven temperatures, 25°C, 35°C, 45°C, 55°C and 65°C. (b) Corresponding broad-band Rayleigh power trace, normalised to the same amplitude as the Brillouin signal.

It can be seen that the noise on the Rayleigh trace is much smaller than that on the Brillouin traces. The anti-Stokes measurements, normalised to the Rayleigh trace, are shown in Figure 5.14(a).

Sharp peaks are evident in the Brillouin traces, on either side of the heated section. These are due to discontinuites in temperature, where double peaks form. However, if the anomalies at either end of the heated section are ignored, another linear relationship with temperature is revealed and is shown in Figure 5.14(b).

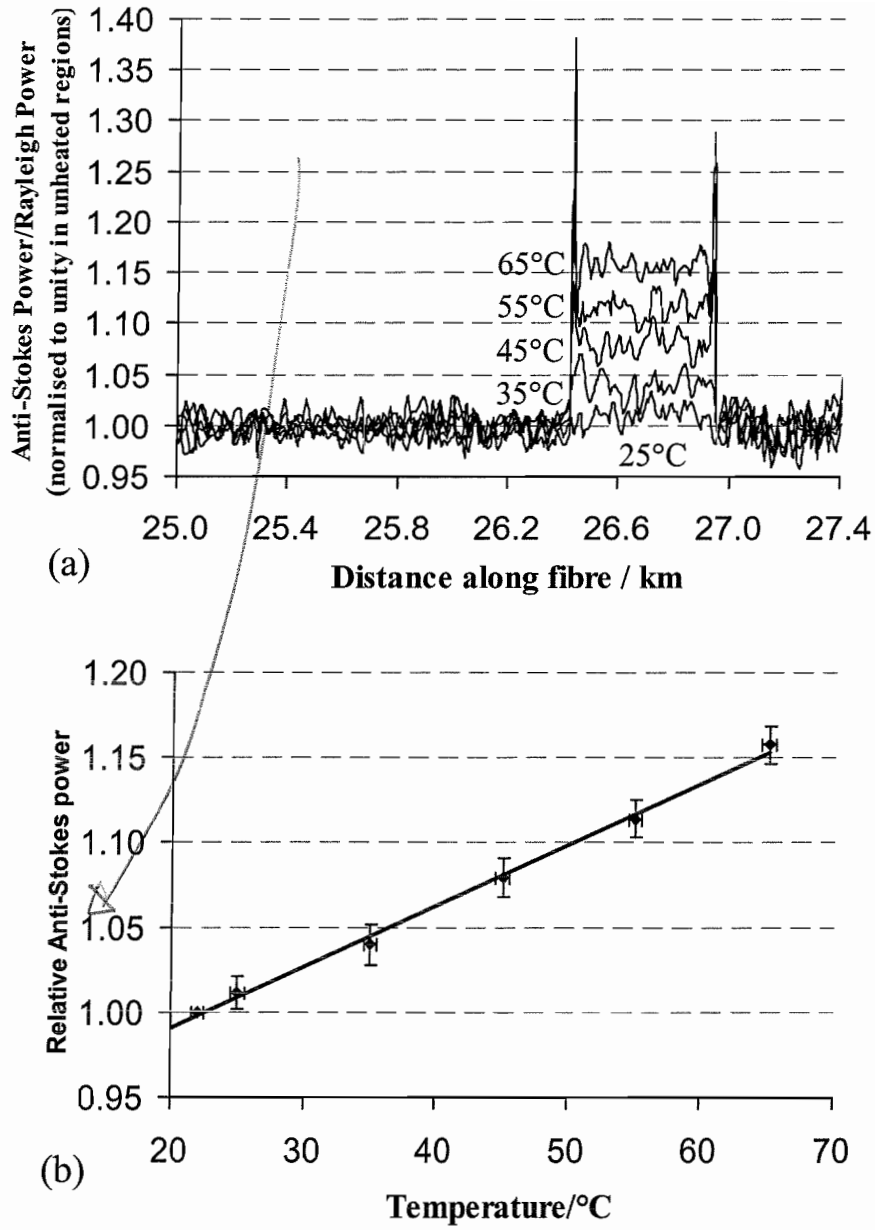

Figure 5.14 Dependence of anti-Stokes power on temperature at 27km down the sensing fibre. (a) Anti-Stokes backscatter traces normalised to a broad-band Rayleigh trace for five different temperatures of a 500m heated fibre section. (b) Mean anti-Stokes power over the heated length as a function of temperature, giving a coefficient of $0.36\pm0.04\%K^{-1}$.

The corresponding coefficient, relating the percentage change in power to temperature, was calculated as $0.36\pm0.04\%K^{-1}$, which again agrees with other sources (see §2.4.2). The RMS error in temperature was found to be less than 3.4K (equivalent to 1.2% power error) at the heated section.

Again, we can compare this result to theory. For 12288 averages per trace, the expected anti-Stokes power noise is 0.6%. However, a polarisation noise component of ~0.8% was observed in Figure 5.9, and the measured noise on the Rayleigh trace,

relative to a fitted exponential, was 0.25%. These errors combine in quadrature to give a total expected error of 1.03%. Actual observed values were 0.98%, 1.20%, 1.16%, 1.11% and 1.12% for the five normalised traces, which are close to the combined predicted error. Again, splice losses have not been accounted for and this would increase the predicted error yet further.

It will now be seen that the artificial peaks either side of the heated region may be removed by fitting a double Lorentzian curve at the transitional points.

5.5 Noise on the Rayleigh Trace

According to theory, the RMS fraction of coherent noise on a Rayleigh trace is given by [5.4] [5.5]

$$\delta\nu_B = \sqrt{\frac{v_g}{4\Delta z \Delta\nu}} \qquad \{5.3\}$$

where v_g is the group velocity of the radiation, Δz is the spatial resolution and $\Delta\nu$ is the effective source bandwidth (the equation was originally derived for frequency shift averaging, but should still apply to a broad-band source, which merely measures all the shifted frequencies simultaneously).

Portions of two measured broad-band Rayleigh traces, each of which have been normalised to a fitted exponential, are shown in Figure 5.15, one for 4×4096 trace averages and one for 16×4096 trace averages. From Equation {5.3}, for a 766GHz (6nm) linewidth ASE pulse and 20m spatial resolution, the fraction of CRN on the trace should be 0.18%. The RMS noise on the 4×4096 average trace is measured as 0.25% and so, if the theory is assumed correct, the non-CRN noise component on this trace is 0.173% (assuming the noises add in quadrature). After four times this number of averages the non-CRN noise component should be halved, but the CRN would be unchanged at 0.18%, and so the total noise should be 0.20%. This is exactly the noise actually measured on the 16×4096 trace, so this theory is supported by these results.

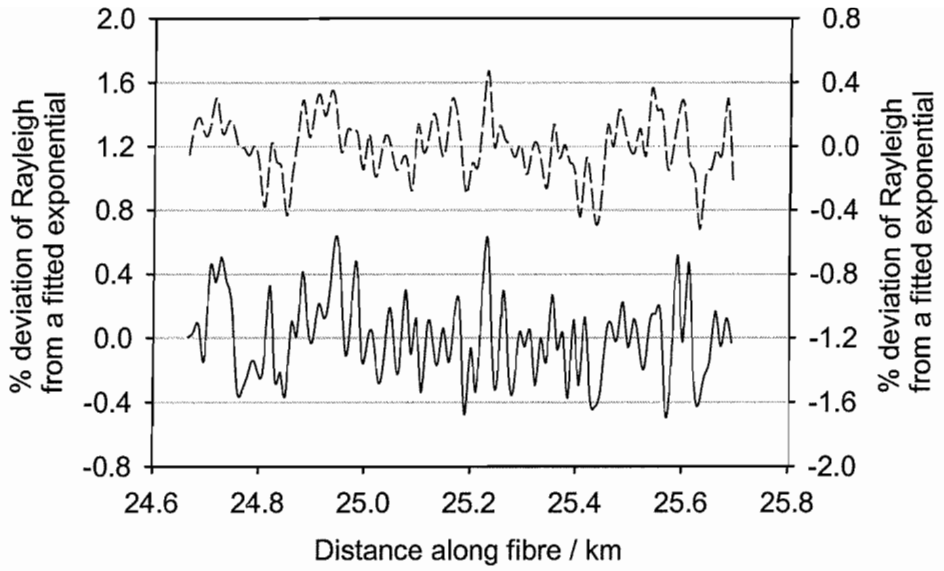

Figure 5.15 Portions of two broad-band Rayleigh traces, normalised to a fitted exponential and the percentage deviation from this calculated. The solid line was recorded after 4×4096 averages and has an RMS noise of 0.25%. The dashed line was recorded after 16×4096 averages and has an RMS noise of 0.20%.

Now we shall briefly look at the coherent noise itself as a function of fibre length, for the narrow-band pulses used in heterodyning. Figure 5.16 is a plot of percentage Rayleigh deviation from a fitted exponential (one for each spliced fibre section) for narrow-band Rayleigh scattering from an entire 30km sensing fibre, for 4×4096 averages. Also plotted is the RMS deviation found over 1km (11 data points).

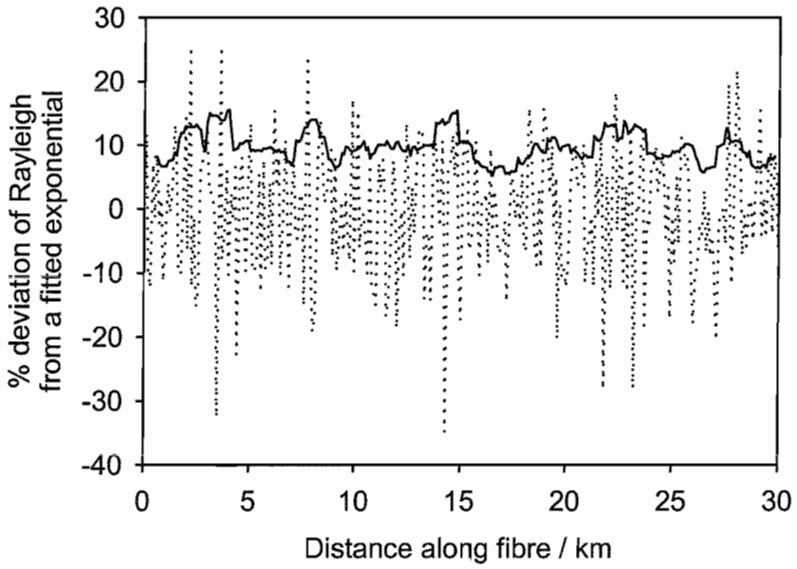

Figure 5.16 Coherent Rayleigh noise for 100ns pulses at 150mW. Rayleigh trace is normalised to a fitted exponential for each section of fibre and the percentage deviation of the backscatter trace found (dotted line). The RMS value of this deviation over 1km (11 data points) is also shown (solid line).

It can be seen that the coherent noise remains at ~10% for the whole trace, independent of fibre length. This percentage does not agree with the theoretical equation above: the pulse linewidth is of the order of 10MHz and so the predicted CRN is 71% (spatial resolution is 10m in this case). This is because the assumptions made in the development of the theory require that $\Delta\nu >> v_g / \Delta z$.

5.6 Multiple Peaks

At points of discontinuity in temperature or strain, there is no longer a single Lorentzian spectrum. Instead double, or even triple peaks may be observed. These points may be dealt with by the fitting of multiple Lorentzian curves, as shown in Figure 5.17. In Figure 5.17(a) a double peak is observed, due to an abrupt temperature change of ~40°C. In Figure 5.17(b) a triple peak is observed: this was taken during a strain measurement and will be discussed further in §5.9. Both traces were taken ~31km down the sensing fibre. In both cases, multiple Lorentzian peaks were fitted successfully to the data; the fitted curves are shown as the solid lines in Figure 5.17.

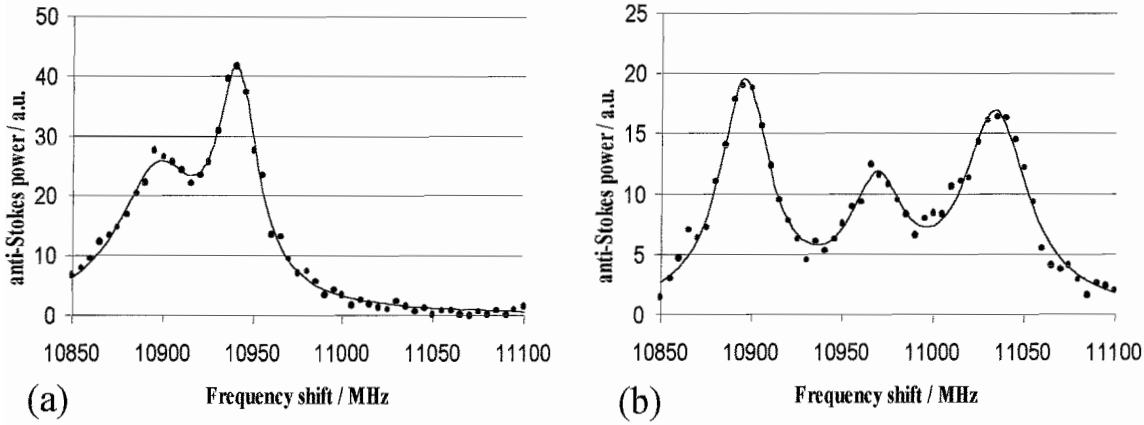

Figure 5.17 Example spectra containing multiple peaks, both observed at ~31km down the sensing fibre. Fitted (a) double and (b) triple Lorentzian curves are shown as solid lines and the experimental data as circles.

χ^2/N values for these two curves, measured as in §5.2.3, are 1.24 and 0.86, showing agreement with the multiple Lorentzian model. Of course, the inclusion of any additional noise sources, such as polarisation noise, would decrease χ^2/N, for any given measured spectrum, since the standard error used in Equation {5.1} would be larger. Automation of the processing may be achieved by, firstly, fitting to each spectrum a single Lorentzian curve; if χ^2/N is high, however, a double-peak may then be tried, or a triple-peak, and so on, until a good fit is obtained.

Using multiple curve fitting, the anomalous peaks in the normalised anti-Stokes power, which are evident in Figure 5.14(a), are removed. The equivalent plot is shown in Figure 5.18.

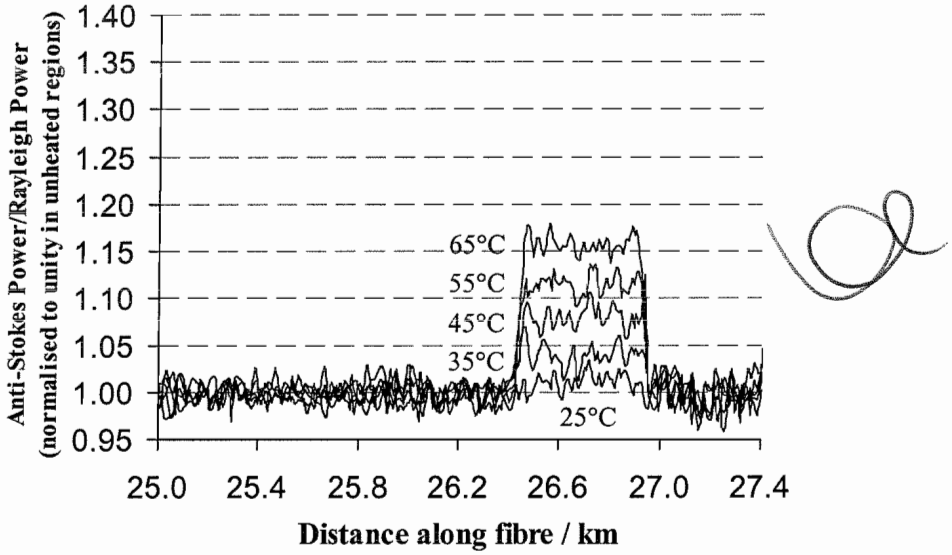

Figure 5.18 Normalised anti-Stokes power trace, using the experimental data for Figure 5.14(a) but employing multiple peak instead of single peak curve fitting.

Multiple curve fitting may also be required even if there are not obviously three peaks in the spectrum. This situation will arise if the differential strain is large enough that the Lorentzian shape is spread signficantly. This situation is shown in Figure 5.19, for a differential strain of 760με per spatial resolution (in this case 20m). In this figure, the experimental data is fitted by a both a single Lorentzian curve (dotted line) and a triple Lorentzian curve (solid line), with the two χ^2/N values being 2.55 and 1.20 respectively. It can be seen that the fit is much improved when a triple curve is used.

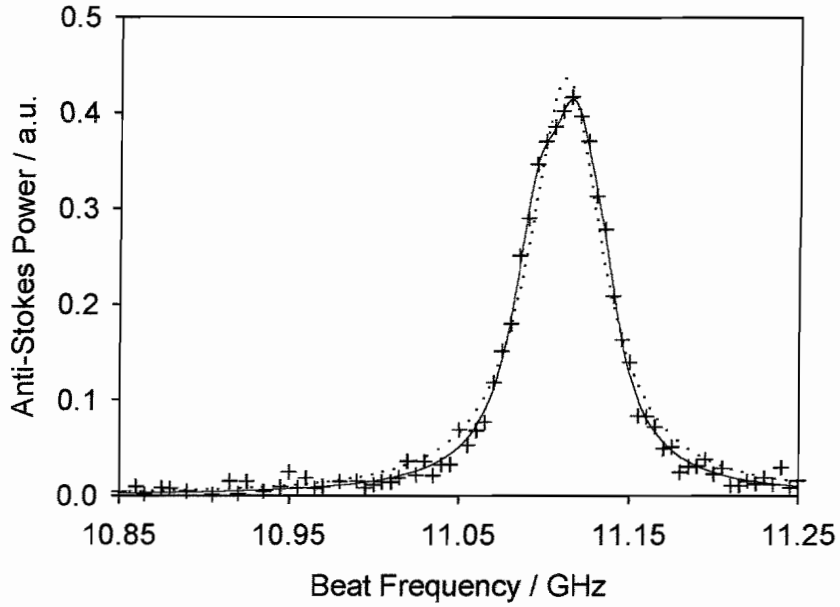

Figure 5.19 Fitting of single and triple Lorentzian curves to the anti-Stokes spectrum, at 31km down the sensing fibre, from a region experiencing high differential strain (~760με or 35MHz per spatial resolution, as measured using the Brillouin frequency shift information). The experimental data is shown by the crosses, a single Lorentzian fit by the dotted line and a triple Lorentzian fit by the solid line.

Of course, for a gradual strain of much more than this, the signal to noise ratio at the peak will decrease and a triple-peaked spectrum would be even less likely to fit the observed spectrum. It is clear that for such cases, the curve fitting method is flawed, although a high χ^2/N value would mark the position of such doubtful points. Despite the fact that a trace summing procedure might provide a more accurate power measurement in these cases, the direct detection of power would be greatly preferred, or perhaps coherent detection of a single trace using a very wide detection bandwidth (greater than 500MHz to avoid excluding a significant portion of the spectrum – see §3.11). This single trace would then provide the Brillouin power to a high accuracy although the noise on the trace would, of course, be increased due to the higher detection bandwidth. This wide bandwidth option is not available using our current detection system.

5.7 Linewidth Dependence on Temperature and Fibre Length

The anti-Stokes linewidth was found to change with temperature. Average linewidth changes for heated fibre sections as a function of temperature are shown in Figure 5.20 for measurements with the heated section at 10km, 26km and 31km.

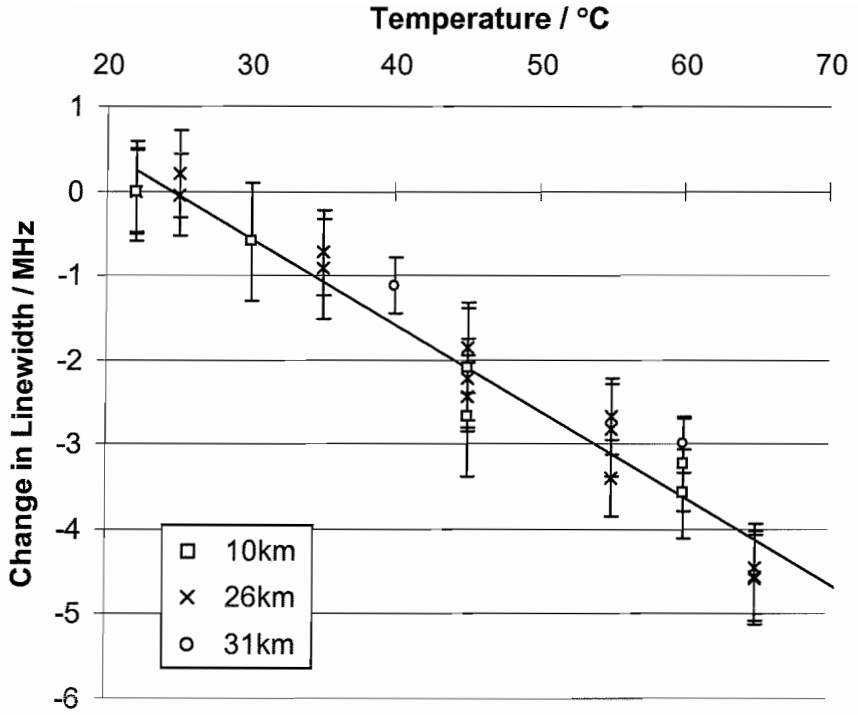

Figure 5.20 Dependence of Brillouin anti-Stokes linewidth, as determined from single Lorentzian curve-fitting measurements, on temperature. Changes in linewidth, relative to that at room temperature, are plotted for the heated section at distances 10km, 26km and 31km down the sensing fibre. The least squares line of best fit for all the data is shown. This line has a coefficient of –0.10 MHz/K.

Looking at this plot, there does not seem to be a large difference in linewidth change with temperature for backscatter from different distances down the fibre. A line of best fit through all the data points is also shown. The corresponding coefficient of –0.10MHz/K is in excellent agreement with the values of –0.12MHz/K and –0.10MHz/K reported for two test fibres investigated by Kurashima et al. in 1990 [5.3], where a linear relationship was also determined between –40°C and +60°C. This reduction in linewidth was attributed to acoustic damping due to three-phonon interactions [5.6].

The dependence on fibre length of the anti-Stokes linewidth, for 160mW pulses at 200ns is shown in Figure 5.21(a). It can be seen that there is an increase in linewidth of ~4MHz over 50km, from ~34MHz to ~38MHz. This is attributed to slight self-phase modulation broadening the sensing pulse spectrum. Figure 5.21(b) shows a Lorentzian fit at 43km to illustrate that the curve fitting process is still valid with such mild SPM. Further discussion of nonlinear effects is presented in Chapter Six.

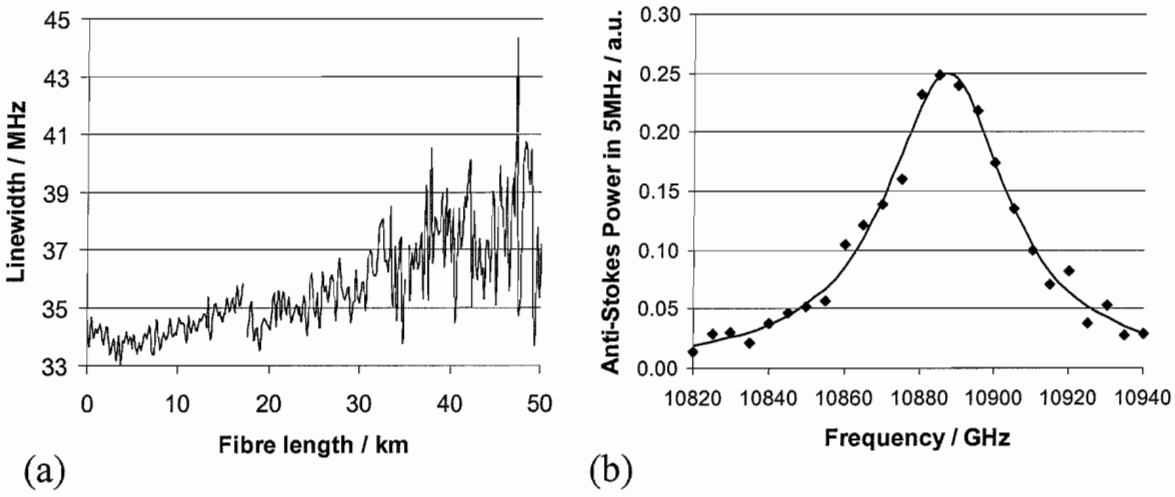

Figure 5.21 (a) Anti-Stokes linewidth, calculated using single Lorentzian curve fitting, dependence on fibre length for 150mW pulses at 200ns. (b) Fitted single Lorentzian curve (solid line) to the spectral data at 43km (from the same data set as (a)).

5.8 Dual Source and the Third Sensor

In order to achieve a versatile sensor for power measurements, a source which is easily switchable between narrow and broad-band operation is required. To this end, modification was made to the first EDFA, such that it would either amplify the source radiation (resulting in narrow-band pulses ~300kHz linewidth) or allow ASE feedback and prevent laser input (resulting in broad-band pulses, ~6nm or 770GHz linewidth). A fibre optic switch was used to toggle between source input and ASE feedback, achieved using a broad-band mirror (a suitably coated, cleaved fibre end). In both cases, the amplifier operated in a saturated regime, with 12mW output in either mode of operation. This dual source is illustrated in Figure 5.22, which shows it in conjuction with the configuration of the next incarnation of the sensor.

The broad-band pulses allow measurement of the Rayleigh signal, which is extracted by a 5% tap coupler at the near end of the sensing fibre. This has replaced the splice breaking method (§5.4.3) since the ASE with feedback was ~9dB larger than the ASE produced with no feedback and merely switching off the source laser. Another modification to the sensor is the addition of a second modulator, to gate the amplified pulses. This prevents interpulse ASE from being launched down the fibre, reducing the ASE offset on the Rayleigh trace.

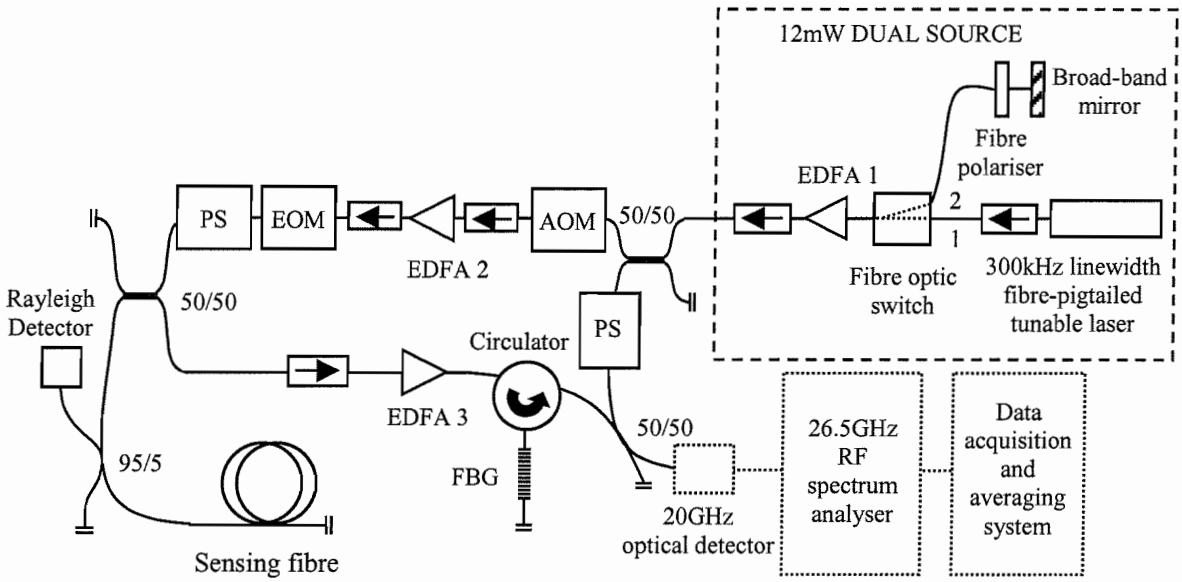

Figure 5.22 The third sensor. A dual source was constructed with two modes of operation. In the first mode, there is narrow-band input to EDFA1 from the laser and 12mW of 300kHz linewidth radiation is output from the source (for Brillouin heterodyne measurement). In the second mode, there is no laser input but instead ASE feedback into EDFA1 and 12mW of ~6nm linewidth radiation is output from the source (for broad-band Rayleigh collection). A second modulator was added to prevent ASE launch down the fibre between pulses.

Primarily, however, the second modulator was introduced in order to ensure that the nonlinear interaction measurements to be presented in Chapter Six were unaffected by the interpulse ASE which would, for example, produce an input signal to be Brillouin amplified, lowering the SBS threshold. The second modulator was initially an integrated electro-optic modulator (EOM), with preceding polarisation controller and polariser, as discussed in §3.4.2. This was replaced by a previously unavailable second AOM for the nonlinear interaction work, since its lower loss (~3dB, as opposed to ~8dB in total for the EOM combination) allowed pulses of higher power to be launched into the fibre. To aid transmission of ASE pulses through the EOM, a fibre polariser was also initially included in the ASE arm of the dual source, ensuring polarisation of the amplified ASE; this was removed when the EOM was abandoned. The third sensor was used to obtain calibrations of frequency shift and power with strain and also simultaneous temperature and strain sensing results.

5.9 Strain Calibration of Brillouin Frequency Shift and Power

To investigate the Brillouin backscatter behaviour with strain and to obtain simultaneous strain and temperature sensing results, a slightly longer fibre was used, of length 31.8km. A fibre of length of 4000m was inserted between the first two sections of the previous sensing fibre (comprising sections of lengths 17500m, 8900m, 500m and 500m) and a 115m strainable section, followed by a 200m length of unstrained fibre, was added at the far end. The heated (unstrained) section (the same 500m length as before) and the strained (unheated) section were therefore situated between 30.4km and 31.6km down the fibre.

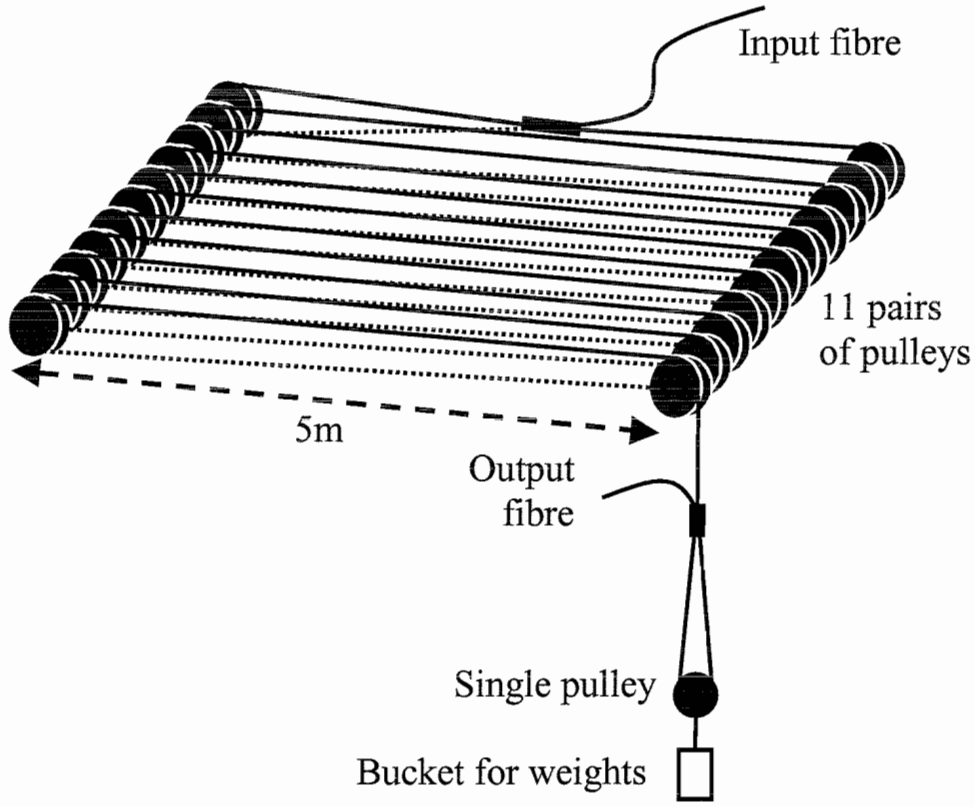

Figure 5.23 Schematic of the strain rig used for calibration and simultaneous strain and temperature sensing.

The 115m fibre section was passed around 11 pairs of pulleys, as illustrated in Figure 5.23, and strained by placing weights inside a plastic container suspended at the end of the rig. The two pulleys in each pair were separated horizontally by ~5m. This configuration inevitably resulted in considerable differential strain across the entire 115m length. Also, since the change in the Brillouin frequency shift induced by the

maximum applied strain (a peak of 4600με ≡ 210MHz) was much larger than that caused by the maximum applied temperature rise (77.5°C ≡ 83MHz), an increase in frequency span of the collected traces was necessary. Since the degree of differential strain was not known, the span was increased to ~400MHz: 80 traces were taken with 5MHz separation, starting at 10.85GHz with 12288 averages per trace. Figure 5.24, a plot of distributed frequency shift for a fibre extension of 48.8cm (equivalent to a strain of 4240με) shows the differential strain clearly. In this figure, the strain varies over a range which corresponds approximately to 50% of the average strain. The effective change in frequency shift due to the applied strain is calculated as the average value over the entire strained region; this change in frequency shift is assumed to arise from a constant strain of 4240με.

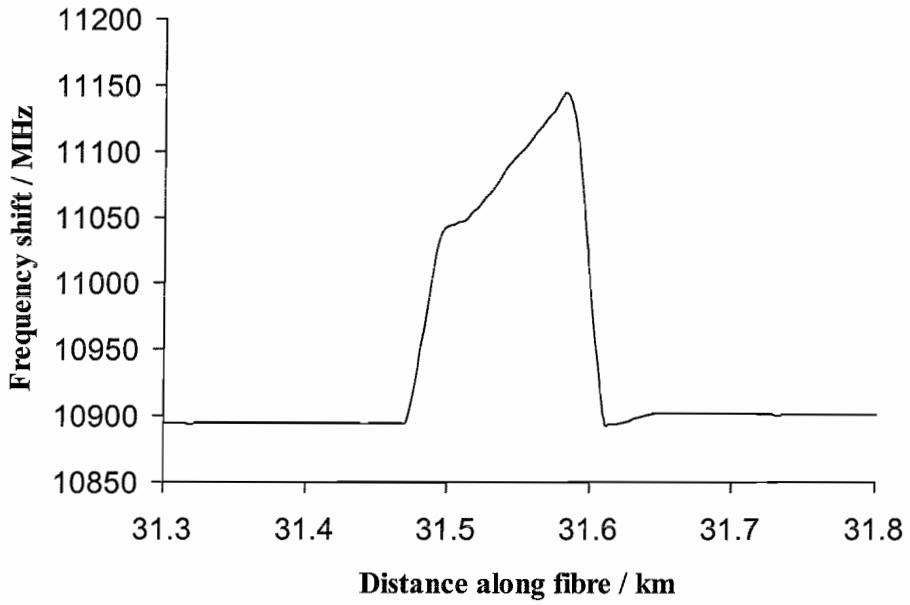

Figure 5.24 Example frequency shift trace due to an applied strain of 4240με.

To determine the two remaining coefficients needed to construct the inverse matrix required for simultaneous sensing (see §2.4.2), both the Brillouin frequency shift and power were calibrated against strain. The response of the frequency shift was linear, having a coefficient of 0.046MHz $\mu\varepsilon^{-1}$, and is shown in Figure 5.25). The power calibration (Figure 5.26) was less conclusive because of the small observed changes in power with strain relative to the noise on each trace. Linear regression of the power

dependence was undertaken, however, and resulted in a coefficient of $-8\pm5\times10^{-4}$ % $\mu\varepsilon^{-1}$. Both of these values agree with previously published results (again, see §2.4.2).

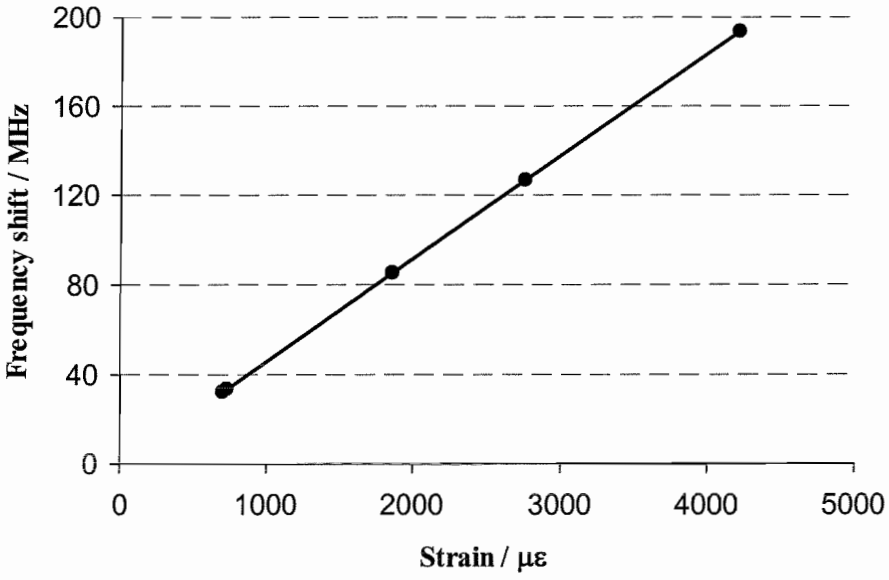

Figure 5.25 Measured dependence of Brillouin frequency shift on applied strain. Coefficient of proportionality is determined as 0.046MHz $\mu\varepsilon^{-1}$.

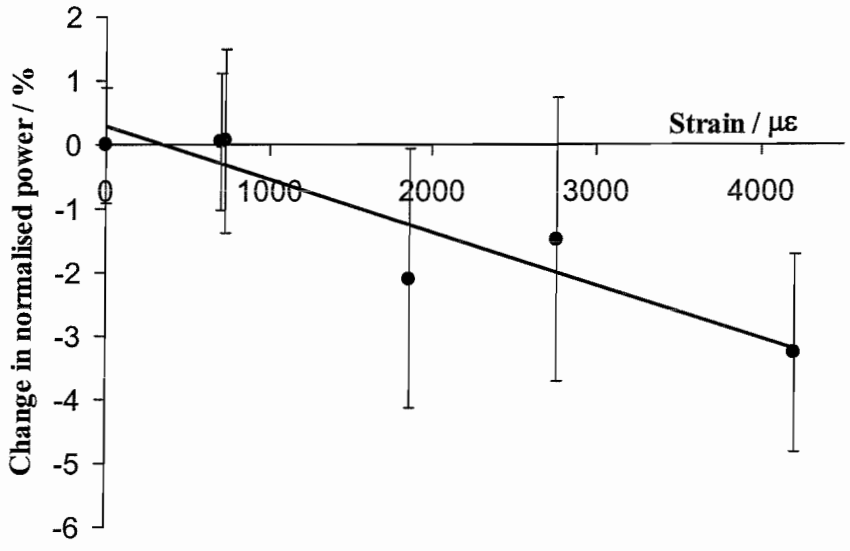

Figure 5.26 Measured dependence of anti-Stokes power on applied strain. Coefficient of proportionality is estimated as $-8 \pm 5\times10^{-4}$ % $\mu\varepsilon^{-1}$.

The precise design of the strain rig results in the generation of the triple peaked spectra shown in Figure 5.17(b) at either end of the strained fibre. This is because, at these points, the same straining force acts upon two fibres simultaneously for a small part of the spatial resolution (~3.5m at the input end and ~1m at the output end), where the fibre is looped around a pulley and secured to itself with wax. This results in the looped fibre bearing only half the strain of the adjacent, fully strained fibre. This results in the formation of an extra peak, situated half-way between the unstrained and fully strained fibre, as is evident in Figure 5.17(b).

5.10 Simultaneous Temperature and Strain Sensing

Simultaneous strain and temperature sensing was undertaken and results obtained for this sensing fibre. In Chapter 2, the following equation, allowing extraction of temperature and strain information from power and frequency shift measurements, was derived

$$\begin{pmatrix} \Delta T \\ \Delta\varepsilon \end{pmatrix} = \frac{1}{\left(C_{P,T}C_{\nu,\varepsilon} - C_{P,\varepsilon}C_{\nu,T}\right)} \begin{pmatrix} C_{\nu,\varepsilon} & -C_{P,\varepsilon} \\ -C_{\nu,T} & C_{P,T} \end{pmatrix} \begin{pmatrix} \Delta P_B^{norm} \\ \Delta\nu_B \end{pmatrix} \qquad \{2.22\}$$

and the corresponding errors were

$$\delta T = \frac{\left|C_{P,\varepsilon}\right| \cdot \delta\nu_B + \left|C_{\nu,\varepsilon}\right| \cdot \delta P_B}{\left|C_{P,T}C_{\nu,\varepsilon} - C_{P,\varepsilon}C_{\nu,T}\right|}, \qquad \delta\varepsilon = \frac{\left|C_{P,T}\right| \cdot \delta\nu_B + \left|C_{\nu,T}\right| \cdot \delta P_B}{\left|C_{P,T}C_{\nu,\varepsilon} - C_{P,\varepsilon}C_{\nu,T}\right|} \qquad \{2.24\}$$

Before presenting the experimental results, the sensor performance in terms of temperature and strain error may be predicted theoretically by Equations {2.24}, using the coefficient values obtained in the calibrations and the values for $\delta\nu_B$ and δP_B calculated as described in §4.4 for noise values computed for 160mW, 150ns pulses with a 1.5mW local oscillator. These predictions are shown in Figure 5.27 and all include a 0.25% contribution by Rayleigh noise. Traces showing the effect of 0.8% polarisation noise on the power trace are also plotted. At ~32km down the fibre, which is the approximate position of the heated and strained fibre (accounting for

splice losses), the predicted temperature and strain errors, including polarisation noise, are 3.9K and 95με, which are within the target resolutions for this work.

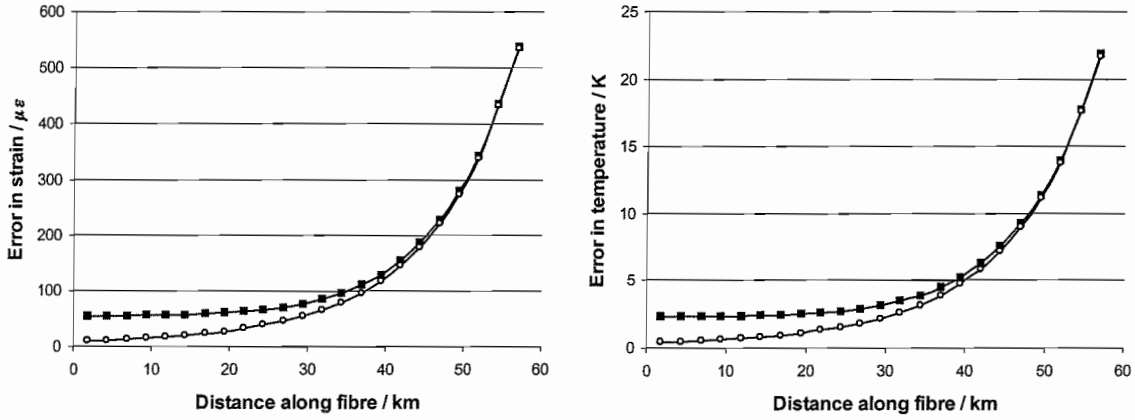

Figure 5.27 Computed theoretical errors in strain and temperature using Equations {2.24} for the theoretical power and frequency shift error data for a 150ns pulse at 160mW and 12288 averages per trace, with the coefficient values being those determined by calibration in this chapter. Filled squares indicate the predicted performance, taking account of 0.8% polarisation noise and 0.25% Rayleigh noise added in quadrature. Open circles show the predicted response in the absence of polarisation noise.

For the simultaneous sensing results, all anti-Stokes power measurements were normalised to the broad-band Rayleigh trace and all frequency shift measurements referenced to that observed with zero strain. Pulses of 150ns and 160mW were launched down the sensing fibre. The frequency shift and the percentage anti-Stokes power change are shown in Figure 5.28 for the heated section at 100°C and the strained section at 730με. The RMS noise on the frequency shift trace, over the 500m heated region, is 0.3MHz and the RMS noise on the power measurement, over this same region, is 1.56%. From Equations {2.24}, the corresponding errors in temperature and strain are given by 4.1°C and 102με, respectively. As a corroboratory measurement, the frequency shift and power RMS noise values for the 500m fibre section between the heated and strained regions were found to be 0.29MHz and 1.49%, resulting in temperature and strain errors of 3.9°C and 97.5με. It can be concluded that the RMS noise on the temperature and strain traces at ~31km along the fibre are ~4°C and ~100με, in good agreement with the theory.

The corresponding derived strain and temperature measurements, found using Equation {2.22}, are shown in Figure 5.29. It can be seen that there is little cross-talk between temperature and strain.

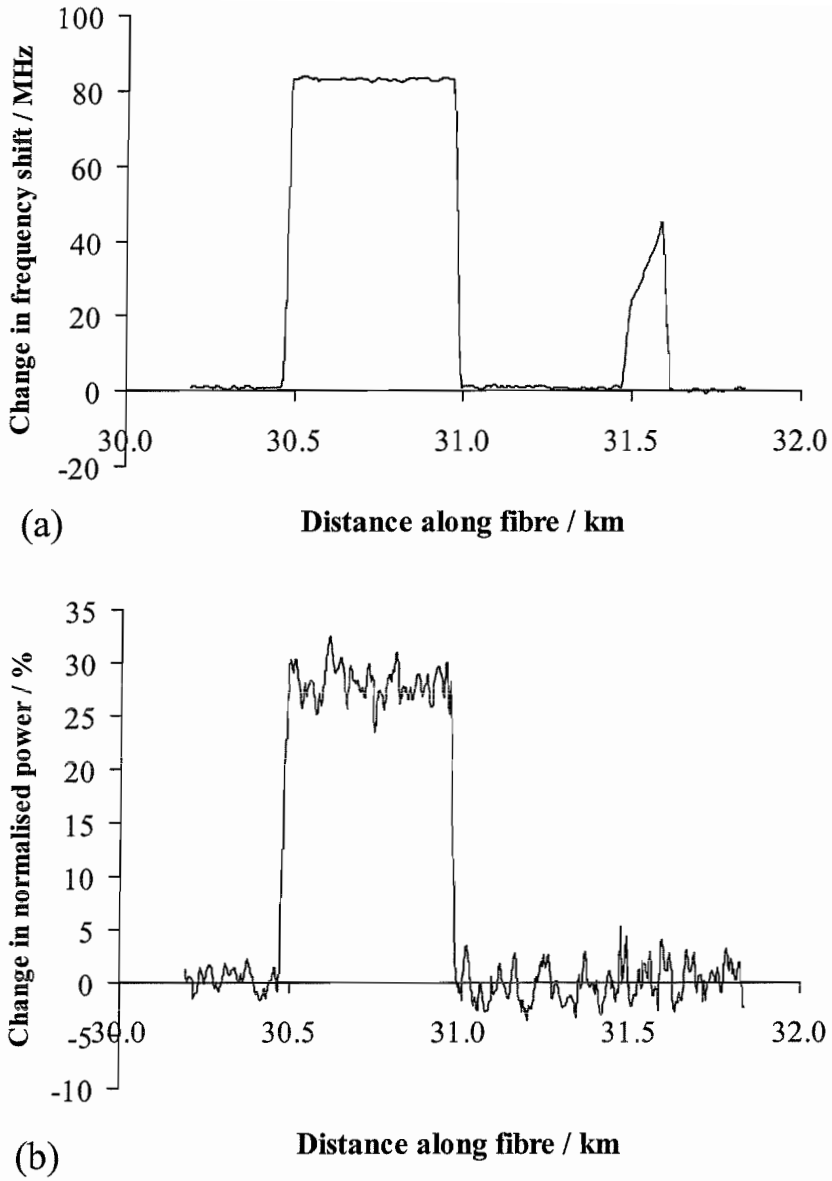

Figure 5.28 Change in frequency shift and change in normalised power for a 1.5km section ~31km down the sensing fibre. This section contains a 500m heated section and a 115m strained section which begin at ~30.5km and 31.5km respectively.

Figure 5.29 also shows that the 100°C temperature of the heated section is measured faithfully by the sensor, despite being outside the range of temperatures used in the power and frequency shift calibration measurements. This indicates that linearity of the Brillouin power and frequency shift with temperature is maintained up to this higher temperature. It is also clear that the noise on both derived traces is dominated by that on the power trace. Indeed, it can be calculated using Equations {2.24} that, for errors of 4°C and 100με, the noise on the power trace is responsible for 99.7% of the temperature error and 94% of the strain error, demonstrating that the power measurements are by far the limiting factor on sensor resolution.

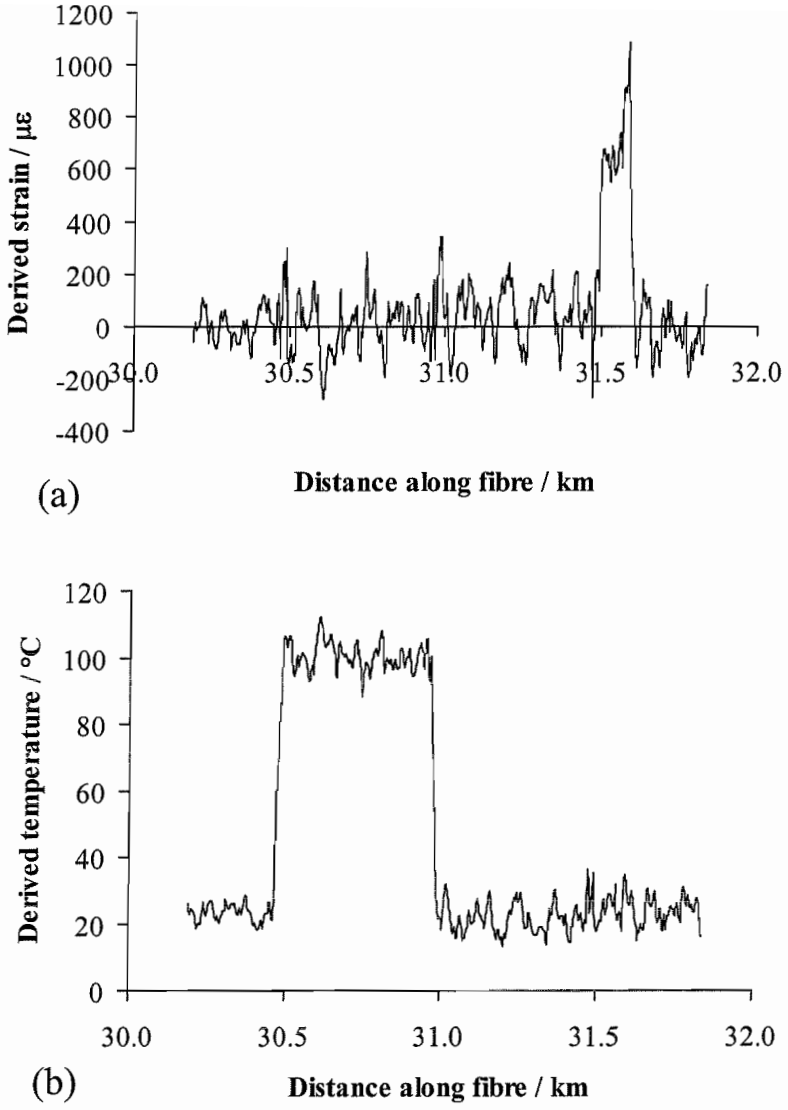

Figure 5.29 Derived temperature and strain information for the data in Figure 5.28, calculated using Equations {2.24}.

It can be seen from Equations {2.24} that, if the error in frequency shift measurement were zero, the temperature error would become

$$\delta T = \frac{\delta P_B}{\left| C_{P,T} - \frac{C_{P,\varepsilon} C_{\nu,T}}{C_{\nu,\varepsilon}} \right|} \qquad \{5.4\}$$

Interestingly, it can be seen that the derived error in temperature would not be merely $\delta T = \delta P_B / |C_{P,T}|$. The mere inclusion of the frequency shift information reduces this error slightly due to the extra term in the denominator ($C_{P,\varepsilon} C_{\nu,T} / C_{\nu,\varepsilon}$ = –0.019 %/K

which is −5.3% of $C_{P,T}$). This means that, if $\delta\nu_B < 0.053 \cdot \delta P_B \cdot |C_{\nu,\varepsilon}| / |C_{P,\varepsilon}|$, a "power only" temperature sensor will actually be improved slightly by including the frequency shift measurement (which is integral to the process in this coherent sensor) and using the simultaneous sensing equation to derive the temperature.

5.11 Measurement Time Considerations

The Fluke digitising oscilloscope, used in all the measurements, completes 4096 averages of a 511-point trace in 50 seconds. This means that an 80-trace spectrum with 12288 averages per trace, as obtained in the simultaneous results, will take 200 minutes to collect. However, the averaging speed may be much faster if superior equipment is used. The actual time taken for 80×12288 consecutive backscatter traces to arrive at the detector, for a repetition rate of 3kHz (allowing sensing up to ~30km to be achieved), is ~328s, a factor of over 36 down on the actual time taken using the oscilloscope. If data acquistion with a dead time between traces of less than 300μs can be achieved, alternate traces may be recorded and the Brillouin spectra may be obtained in only 11 minutes (or ~12.5 minutes if the ~1s taken for the ESA to change frequency is taken into account). This increases the viability of such a sensor.

5.12 Scrambler Replacement

In order to simplify the existing sensor, the two existing polarisation scramblers were replaced by a single commercial scrambler. This new scrambler was based on a fibre squeezing technique using piezo-electric transducers to induce fibre birefringence along different axes to produce a 3-axis scrambler. An electronic driver based on power MOSFET amplification was built for this new scrambler, from a design suggested by Radiodetection Ltd., which provided the required set of three independent 0-60V offset sinusoidal voltages, with different frequencies, for optimum scrambling (see §3.8.1). This scrambler had an insertion loss of only 1dB, rather than 3dB as each of the other two scramblers.

The optimum position of this scrambler was deduced to be just prior to launch into the sensing fibre, after the second modulator. This is because it is only the polarisation

state of the backscatter which is changing with time, in the absence of any scrambling, and so it is only the backscatter which will necessarily undergo polarisation dependent loss (PDL), occurring as it passes through couplers and preamplifier en route to the detector. If, however, the polarisation state of the backscatter arriving at the near end of the sensing fibre is completely scrambled then, even if there is considerable PDL between sensing fibre and detector, resulting in the backscatter at the detector being partially polarised, it will always be polarised in the same way and so the heterodyne efficiency will be unaffected and there will be no polarisation noise.

The performance of the new scrambler is shown in Figure 5.30 for backscatter from a 13.5km fibre. This figure shows the percentage deviation from a fitted exponential of the total anti-Stokes power (10240 averages per trace) and also the power trace itself, on a dB scale, illustrating its exponential decay.

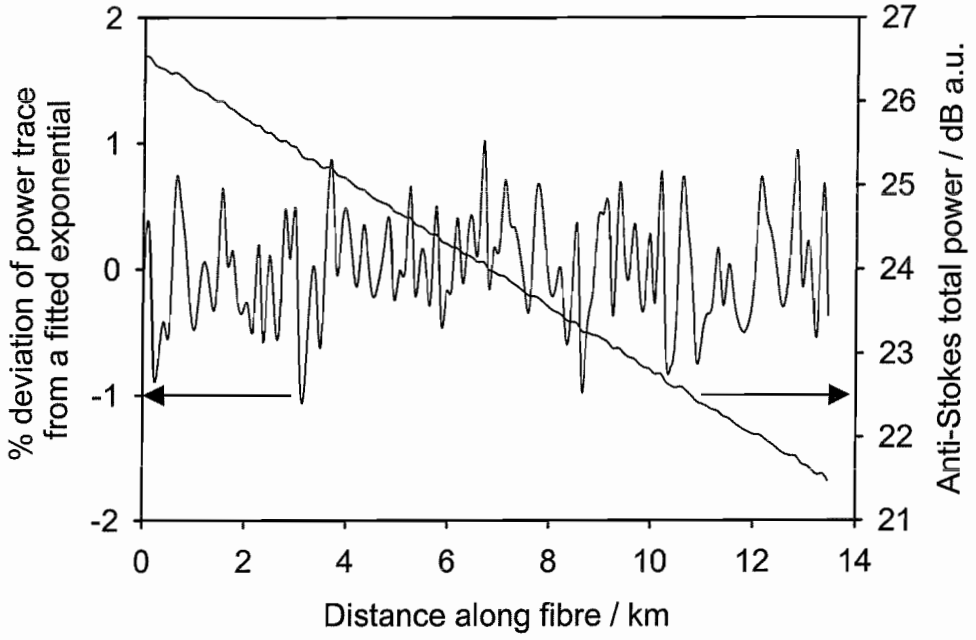

Figure 5.30 Noise characteristic of the total anti-Stokes power obtained using the new scrambler (10240 averages per trace at 5MHz separation). The figure shows both the percentage deviation from a fitted exponential and the total power itself (on a dB scale). The gradient of the fitted exponential gave a single pass attenuation of 0.193dB/km.

The residual polarisation noise was determined as the RMS percentage deviation over the whole fibre length and evaluated to 0.41%, a factor of two smaller than that obtained using the previous scrambling arrangement. This noise is equivalent to a 1.14K temperature error.

New simultaneous results for an average applied strain of 4217με and a temperature of 60°C were obtained and the derived simultaneous temperature and strain distributions are shown in Figure 5.31. Here, the RMS temperature and strain errors are ~2.5K and ~60με, an improvement on previous values of 4K and 100με. These values only apply up to 31.4km, however, since there is a significant increase in error for the strained region and beyond, up to ~3.6K and more than 76με. This time 12288 averages were taken per trace and 201 traces were recorded every 5MHz, giving 1GHz span. Pulses of 200ns duration and 160mW power were used to obtain these results.

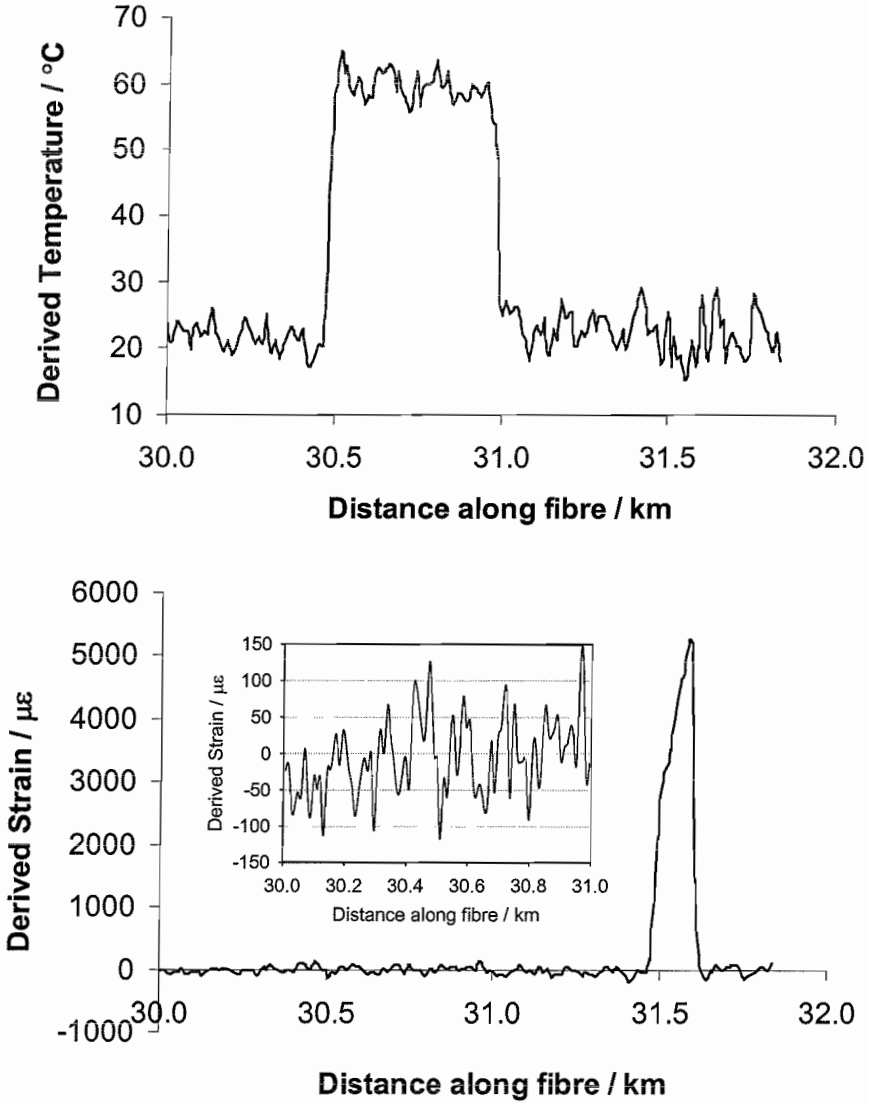

Figure 5.31 Derived temperature and strain information for a simultaneous sensor using the new scrambler. Room temperature was 22°C, oven temperature was 60°C and applied average strain was ~4200με. Inset shows magnification of the derived strain between 30km and 31km down the fibre, to show the noise on the strain trace.

5.13 Satellite Peaks

In certain cases, a Brillouin spectrum, not affected by temperature or strain, may exhibit structure. These satellite peaks may be ascribed to scattering within the cladding, which necessarily has a different composition to the core glass [5.7]. In order for a fibre, of core radius r, to be single-mode at a given wavelength, λ, its V number, defined as

$$V = \frac{2\pi}{\lambda} r(NA) = \frac{2\pi}{\lambda} r\sqrt{n_1^2 + n_2^2} \qquad \{5.5\}$$

must be less than 2.405 ([5.8] p.56). The fraction of power propagating in the cladding is dependent on V and it has been shown [5.9] that for $V<1.4$, more than half of the modal power propagates in the cladding. It is therefore reasonable to assume that low numerical aperture fibres, with a small refractive index difference, will have increased power in their satellite peaks. This is demonstrated by observing the anti-Stokes spectrum obtained from a fibre of numerical aperture of 0.09, rather than the usual single-mode NA of 0.12, as shown in Figure 5.32. The structure seen here cannot be due to the spectrum of the local oscillator or pump pulse since it occurs at the high frequency end of both Stokes and anti-Stokes spectra.

It is obvious that structure within the Brillouin peak will be detrimental in sensing applications, especially using coherent detection. Of course, it is possible to fit a curve to the structured spectrum and use this model as a basic spectral curve, rather than a simple Lorentzian, but this would require that this structure does not change along the fibre. Allowance must be made for any change in fibre type and moreover, the percentage of light in the cladding changes with temperature, complicating matters still further. It is clear that large NA fibre should be used if possible

Such satellite peaks may also arise from structure in the refractive index profile of the core – two peaks have been observed for core profiles with a central dip in refractive index [5.10][5.11]. Another possibility is the contribution of more than one acoustic mode to the scattering, occurring when the longitudinal acoustic velocity is greater in the cladding than in the core, notably in GeO_2 doped fibres [5.12], which could also explain the spectrum in Figure 5.32.

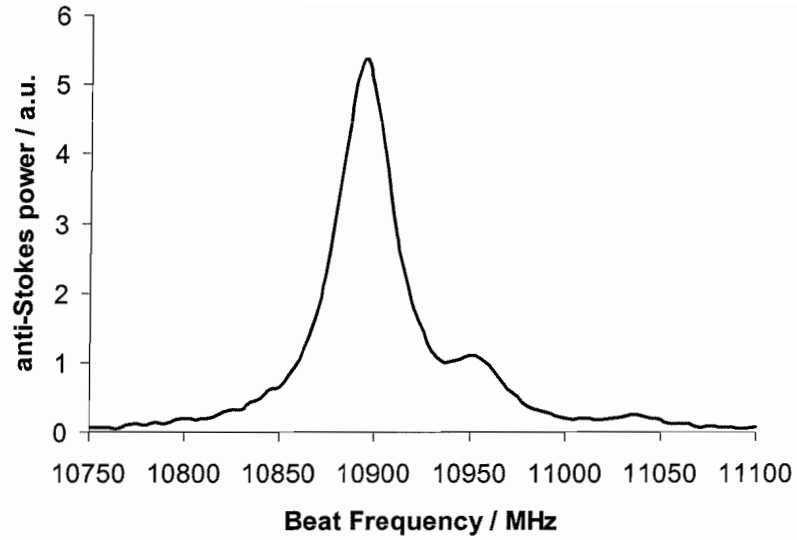

Figure 5.32 Anti-Stokes spectrum from a single-mode fibre with a numerical aperture of 0.09.

5.14 Conclusions

This chapter has demonstrated the operation of the 11GHz beat frequency coherent temperature and strain sensor, along with experimental observation of noise and mention of special processing considerations. Simultaneous temperature and strain sensing has been undertaken, which has ultimately led to a strain resolution of less than 100με and a temperature resolution of less than 4K.

Calibrations of the temperature and strain dependence of the Brillouin frequency shift and power have resulted in coefficients which are supported by existing experiment. The behaviour of Brillouin linewidth with temperature was also as expected, decreasing at –0.1MHz/K.

A dual source has been designed in order to enable easy conversion between narrow-band and broad-band operation for the collection of Brillouin and Rayleigh traces respectively.

The next chapter will deal with the onset of nonlinear phenomena, which limit the launched pulse power and hence backscatter signal to noise ratio for a given spatial resolution.

5.15 References

[5.1] K. Shimizu, T. Horiguchi, Y. Koyamada and T. Kurashima: "Coherent Self-Heterodyne Brillouin OTDR for Measurement of Brillouin Frequency Shift Distribution in Optical Fibers", *Journal of Lightwave Technology*, Vol. 12, No. 5, pp. 730-736 (May 1994)

[5.2] T.R. Parker, M. Farhadiroushan, V.A. Handerek and A.J. Rogers: "Temperature and strain dependence of the power level and frequency of spontaneous Brillouin scattering in optical fibers", *Optics Letters*, Vol. 22, No. 11, pp. 787-789, (June 1997)

[5.3] T. Kurashima, T. Horiguchi and M. Tateda: "Thermal effects of Brillouin gain spectra in single-mode fibers", *IEEE Photonics Technology Letters*, Vol. 2, No. 10, pp. 718-720, (October 1990)

[5.4] K.R.C.P. De Souza: "Fibre Optic Distributed Sensing Based on Spontaneous Brillouin Scattering", *PhD Thesis*, University of Southampton, U.K. (June 1999)

[5.5] K. Shimizu, T. Horiguchi and Y. Koyamada: "Characteristics and Reduction of Coherent Fading Noise in Rayleigh Backscattering Measurement for Optical Fibers and Components", *Journal of Lightwave Technology*, Vol. 10 No. 7 pp. 982-987 (July 1992)

[5.6] A.S. Pine: "Brillouin Scattering Study of Acoustic Attenuation in Fused Quartz", *Physical Review*, Vol. 185, No. 3, pp. 1187-1193, (September 1969)

[5.7] N.L. Rowell, P.J. Thomas, H.M. van Driel and G.I. Stegeman: "Brillouin spectrum of single-mode optical fibers", *Applied Physics Letters*, Vol. 34, No. 2, pp. 139-141, (January 1979)

[5.8] J.M. Senior: "Optical Fiber Communications", Second Edition, *Prentice Hall*, ISBN 0-13-635426-2 (1992)

[5.9] R. Olshansky: "Propagation in glass optical waveguides", *Review of Modern Physics*, Vol. 51, No. 2, pp. 341-366 (1979)

[5.10] N. Shibata, R.G. Waarts and R.P. Braun: "Brillouin-gain spectra for single-mode fibers having pure-silica GeO_2-doped, and P_2O_5-doped cores", *Optics Letters*, Vol. 12, No. 4, pp. 269-271, (April 1987)

[5.11] R.W. Tkach, A.R. Chraplyvy and R.M. Derosier: "Spontaneous Brillouin Scattering For Single-Mode Optical-Fibre Characterisation", *Electronics Letters*, Vol. 22, No. 19, pp. 1011-1013, (September 1986)

[5.12] N. Shibata, K. Okamoto and Y. Azuma: "Longitudinal acoustic modes and Brillouin-gain spectra for GeO_2-doped-core single-mode fibers", *Journal of the Optical Society of America B*, Vol. 6, No. 6, pp. 1167-1174, (June 1989)

Chapter Six

Nonlinear Effects and Threshold Powers

6.1 Introduction

This chapter will concentrate on the nonlinear effects observed when high input powers are launched into the sensing fibre. These include stimulated Brillouin scattering (SBS), stimulated Raman scattering (SRS), self-phase modulation (SPM) and four wave mixing (FWM).

The SBS threshold will be determined for continuous wave input radiation and the result compared to theory. Also, an experimental and theoretical analysis will be undertaken for pulsed input (pulse duration between 50ns and 300ns). This analysis will discuss the effect of the nonlinear interactions on the measurement of distributed Brillouin spectra for the purpose of temperature and strain sensing.

6.2 Continuous Wave Stimulated Brillouin Scattering

Preliminary Brillouin characterisation was undertaken to observe the onset of cw stimulated scattering. The experimental arrangement is the same as that in Figure 3.12. The observed total backscatter power as a function of input power (both calculated to be those existing at the near end of the generating fibre itself) is shown in Figure 6.1. The result is monotonically increasing, as would be expected, with the relationship becoming linear at low input powers. A straight line passing through the origin of slope 7.88×10^{-4} fits this linear relationship and represents the contribution of Rayleigh scattering to the backscatter power. This backscatter characteristic may be compared with the theory by using Equation {2.4}, for a pulsed pump, as the basis for determining the Rayleigh backscattered power due to a cw pump launched down a fibre of length L_{cw}.

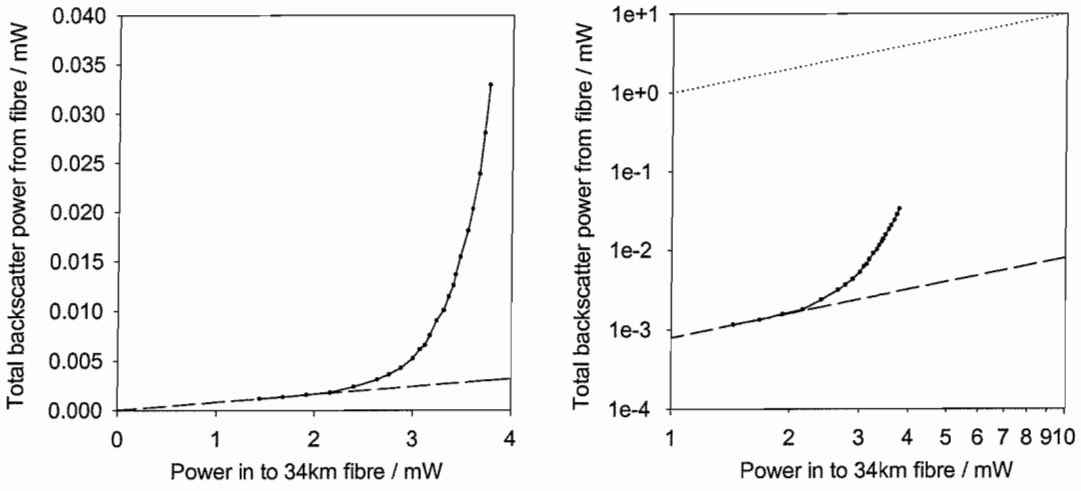

Figure 6.1 Backscattered power from 34km single-mode fibre as a function of cw input power on both linear and logarithmic scales. The dashed lines indicate the contribution of Rayleigh scattering, with the rest being due to stimulated Brillouin scattering. The dotted line represents 100% conversion efficiency.

From this equation, the cw Rayleigh will be given by the integral

$$P_R^{cw} = \tfrac{1}{2} P_i^{cw} S v_g \gamma_R \int_0^{2L_{cw}/v_g} e^{-\gamma v_g t} dt = \tfrac{1}{2} P_i^{cw} S \frac{\gamma_R}{\gamma} \left(1 - e^{-2\gamma L_{cw}}\right) \qquad \{6.1\}$$

and since in the 1.5μm band $\gamma \approx \gamma_R$, this becomes

$$P_R^{cw} = \tfrac{1}{2} P_i^{cw} S \left(1 - e^{-2\gamma_R L_{cw}}\right) = \tfrac{1}{2} P_i^{cw} \frac{(NA)^2}{4n^2} \left(1 - e^{-2\gamma_R L_{cw}}\right) \qquad \{6.2\}$$

and so the theoretical slope, for $\gamma_R = 4.6\times10^{-5}$ m^{-1} and a 34km length of fibre with an NA of 0.12 and a refractive index of 1.46, as used in the example calculation in §2.2.2, is therefore 8.07×10^{-4}. This agrees well with the value of 7.88×10^{-4} obtained in the experiment, with the capture fraction, $S = (NA)^2/(4n^2)$ differing by only ~2.4% in the two cases. Using this experimental data, Equation {2.6} for a pulsed input is modified to

$$P_R(t) = 7.58 \cdot E_P \cdot \exp(-2\gamma x) \qquad \{6.3\}$$

with the new capture fraction being S=1.648×10^{-3}.

The cw stimulated scattering threshold for this fibre type and length (effective length is ~16.3km) is given theoretically as 1.3mW, if the polarisation state of the pump is maintained down the fibre length (using Equation {2.28}, as quoted by Agrawal [6.1]). In the original reference [6.2] cited by Agrawal, this threshold is defined by Smith as the input power for which the backward stimulated Stokes power at the entrance face equals the input pump power. It is obvious from Figure 6.1 that the predicted threshold is much too low to fit the experimental results.

Further investigation of Smith's analysis shows use of the assumption that the pump wave is depleted only by the fibre's linear losses and not by stimulated scattering. This assumption is clearly invalid at his chosen "threshold" condition. Moreover, his threshold scenario is physically impossible due to the fundamental requirement for conservation of energy. The numerical factor of 21 appearing in his Brillouin threshold equation, quoted by Agrawal, is dependent upon fibre properties, including the fibre loss (and therefore pump wavelength). Since Smith calculated (in 1972) the threshold for a loss of 20dBkm^{-1}, rather than the value appropriate to this experiment of 0.2dBkm^{-1}, the final result is affected.

Perhaps a more suitable definition of Brillouin threshold would be the input power for which the Brillouin backscatter is equal to the Rayleigh backscatter at the input face. In order to determine the effect of this change in definition, we must consider the theoretical equation satisfied by the backscatter, as derived by Smith, which is

$$B_{eff}\left(\frac{\nu_s KT}{\nu_a}\right)\frac{\exp\left(\dfrac{g_B P(0)}{\alpha_P A_{eff}}\right)}{\left(\dfrac{g_B P(0)}{\alpha_P A_{eff}}\right)} = P(0) \qquad \{6.4\}$$

where B_{eff} is the effective gain bandwidth, given by

$$B_{eff} = \frac{\sqrt{\pi}}{2}\frac{\Delta\nu_{fwhm}^{Brill}}{\left(P(0)g_B/\alpha_P A_{eff}\right)^{1/2}} \qquad \{6.5\}$$

for an input power $P(0)$ at the start of the fibre.

Descriptions of the symbols and typical values are given in Table 6.1. The quantity $1/\alpha_P$, the effective length of an infinitely long fibre, is replaced by L_{eff}

$$L_{eff} = \frac{1}{\alpha_P}\left[1 - \exp(-\alpha_P L)\right] \qquad \{6.6\}$$

for finite fibre lengths. Equations {6.4} and {6.5} may be rearranged to give

$$\frac{\sqrt{\pi}}{2}\left(\frac{\nu_s KT}{\nu_a}\right)\left(\frac{g_B L_{eff}}{A_{eff}}\right)\Delta\nu_{fwhm}^{Brill} = \left(\frac{g_B L_{eff} P_{threshold}^{SBS}}{A_{eff}}\right)^{5/2} \exp\left(-\frac{g_B L_{eff} P_{threshold}^{SBS}}{A_{eff}}\right) \qquad \{6.7\}$$

and the solution to this equation is

$$P_{threshold}^{SBS} = \frac{K_{SBS} A_{eff}}{g_B L_{eff}} \qquad \{6.8\}$$

where $K_{SBS} = 21$ for the values used by Smith (Equation {2.27}).

Symbol	Description	Value
$P(0)$	Power input to fibre	-
K	Boltzmann's constant	1.38×10^{-23} JK^{-1}
T	Absolute temperature	298 K
ν_a	Frequency of acoustic phonon	11.0 GHz
ν_s	Frequency of Stokes Brillouin photon	195.7 THz
g_B	Peak Brillouin gain	5×10^{-11} mW^{-1}
A_{eff}	Fibre effective area	6×10^{-11} m^2
α_P	Pump absorption coefficient	5×10^{-5} m^{-1}
$\Delta\nu_{fwhm}^{Brill}$	Full width at half maximum of the Brillouin gain profile	35 MHz

Table 6.1 Quantities appearing in Equations {6.4} and {6.5}, as well as subsequent derived equations, along with typical values for the fibre and source used in the experiments in this work.

For the values in Table 6.1, for modern standard single-mode fibres, $K_{SBS} = 17.55$ and the threshold power is ~1.3mW. Effective area has been increased to 60μm^2 because this is the value appropriate to our fibre. However, we must now introduce the new threshold definition (Brillouin backscatter equal to the Rayleigh at the fibre input) and so Equation {6.7} becomes (using Equation {6.2})

$$\frac{\sqrt{\pi}}{2}\left(\frac{\nu_s KT}{\nu_a}\right)\left(\frac{g_B L_{eff}}{A_{eff}}\right)\Delta\nu_{fwhm}^{Brill}\left(\frac{8n^2}{(NA)^2\left(1-e^{-2\gamma_R L_{cw}}\right)}\right)=\left(\frac{g_B L_{eff} P_{threshold}^{SBS}}{A_{eff}}\right)^{5/2}\exp\left(-\frac{g_B L_{eff} P_{threshold}^{SBS}}{A_{eff}}\right) \quad \{6.9\}$$

resulting in K_{SBS} = 8.63, which gives a value for the threshold of 0.633mW. This seems much too low to fit the experimental results, since the actual observed threshold is ~3mW.

At this point, the Brillouin gain itself must be called into question. The value of 5×10^{-11}m/W applies only to fused silica. It has been shown that the Brillouin gain spectra of optical fibre differ from that of fused silica and that the gain coefficient itself is also changed. Tsun et al. [6.3] present experimental evidence that the gain coefficient is approximately inversely proportional to the Brillouin linewidth. Since our Brillouin spectra have a linewidth of ~35MHz, compared to only 16MHz for fused silica at 1.55μm [6.4], the gain coefficient would be expected to be smaller than 5×10^{-11}m/W. Based on the work of Tsun et al., the expected gain coefficient for our fibre is ~1.9×10^{-11}m/W. Using this value in our threshold estimation we instead get K_{SBS} = 9.95 and a corresponding threshold power of 1.92mW, which is closer to our observed value.

Now we must consider polarisation effects. According to van Deventer and Boot [6.5], for a linearly polarised pump, the spontaneous Brillouin backscatter is 33.3% polarised, parallel to the direction of polarisation of the pump. They showed that this is due to the gain in this direction being twice that in the orthogonal direction. SBS will therefore have a lower threshold in this parallel direction than in the orthogonal one and this polarisation will dominate the backscatter once stimulated scattering ensues (hence the observation that high pump power SBS has the properties of an identical polarisation reflector). This parallel polarised backscatter will experience a gain coefficient which is $\frac{2}{3}$ of the above-quoted value (which is valid only if the polarisation states of pump and backscatter are identical for the entire fibre length), i.e. 1.27×10^{-11}m/W. This results in K_{SBS}=10.48 and a theoretical threshold power of 3.03mW, which agrees very well with our observed value of ~3mW.

6.3 Nonlinear Effects in Coherent Sensing: Theory and Experiment

In order to determine threshold powers for distributed sensing, the third sensor (Figure 5.22 with two AOMs, rather than one AOM and one EOM) was used to obtain distributed anti-Stokes, Stokes and narrow-band Rayleigh heterodyne spectra. These spectra were recorded for a series of pulse durations (50ns, 100ns, 150ns, 200ns, 250ns and 300ns) at a range of pulse powers. We shall now consider the different nonlinear effects which may contribute to distortion of the frequency shift and power traces obtained.

6.3.1 Stimulated Brillouin Scattering

6.3.1.1 Theory

When using pulsed input and if the pulse duration is less than the beat length of the fibre, the polarisation state will be maintained throughout the pulse and the gain coefficient may reach its maximum value, as discussed in §6.2, which is 1.9×10^{-11}m/W. Indeed, it will do this for any linear polarisation state [6.5]. It is therefore this maximum gain coefficient which will dictate the minimum threshold for SBS to be achieved. The threshold powers are given in Table 6.2 below for g_B $=1.9\times10^{-11}$m/W and $L_{eff} = L_{cw}$ =5m, 10m, 20m and 30m, and are calculated in the same way as the cw values in §6.2.

L_{eff} / m	Pulse length / ns	K_{SBS}	$P^{SBS}_{threshold}$ / W	Threshold pulse energy / nJ
5	50	8.3	5.24	262
10	100	9.13	2.88	288
20	200	9.95	1.57	314
30	300	10.43	1.1	330

Table 6.2 Threshold values for the onset of stimulated Brillouin scattering for different spatial resolutions. Threshold is defined as the input pulse power which results in a Stokes power equal to the Rayleigh power at the near end of the sensing fibre.

It can be seen that SBS will not be significant in anti-Stokes Brillouin DOFS for spatial resolutions of 30m or below until powers above 1W are incident, since pump depletion due to Brillouin scattering is less than that due to captured Rayleigh

scattering (over 55dB down on the pump even for L_{eff}=30m – using Equation {2.4}) at lower input powers. Stimulated scattering is all in the backward direction due to reflection from the moving grating, so capture fraction is irrelevant in this case.

6.3.1.2 Experiment

In order to support this theory, the total Stokes power was compared to the total anti-Stokes power at the near end of the sensing fibre. The results, which give a maximum magnitude of the effects of SBS, are shown in Figure 6.2. It can be seen that for the pulse energies used in these experiments, up to ~120nJ (~400mW for 300ns duration), the Stokes power is never more than 2.5 times that of the anti-Stokes. Whilst this SBS would result in distortion of any combined power trace, it will not affect measurement of the spontaneous anti-Stokes power alone, since its contribution to pump depletion is tiny (the total Brillouin power is only 1.75 times its entirely spontaneous value, which itself is only 1/30th of the captured Rayleigh power). The increase in Stokes power with input pulse energy can be seen to be approximately linear over this small range.

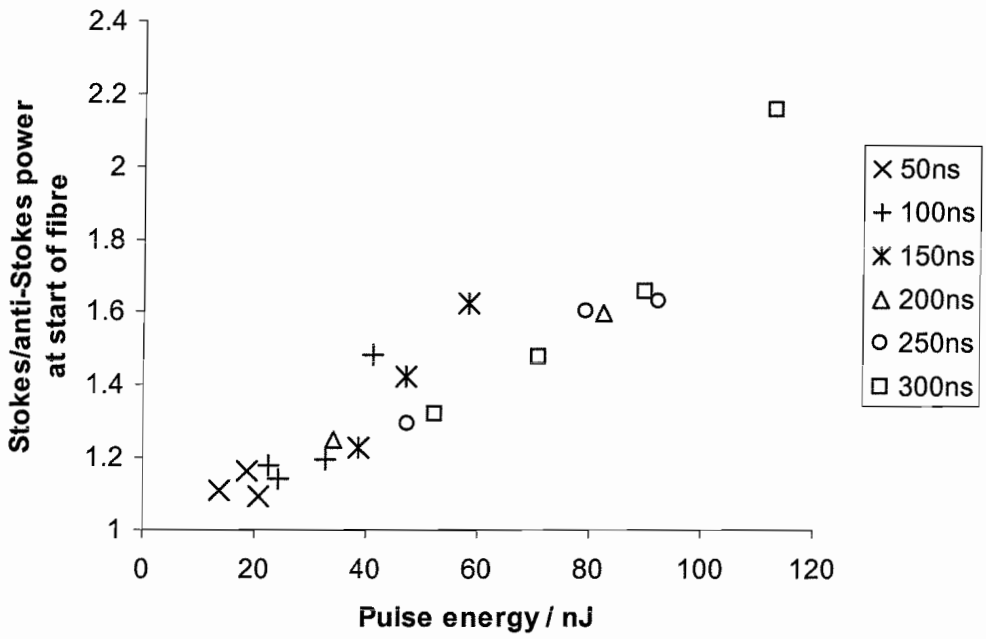

Figure 6.2 Evidence of mild stimulated Brillouin scattering at the near end of the sensing fibre as a function of pulse energy for six different pulse durations between 50ns and 300ns. It can be seen that for the pulse energies of up ~120nJ used in these experiments (~400mW at 300ns) the Stokes backscattered power is not more than 2.5 times that of the anti-Stokes.

6.3.2 Stimulated Raman Scattering

6.3.2.1 Theory

The equivalent expression to Equation {6.7} for forward stimulated Raman scattering is, again from Smith's analysis [6.2]

$$\frac{100}{X}\cdot\frac{\sqrt{\pi}}{2}(h\nu_s)\left(\frac{g_R L_{eff}}{A_{eff}}\right)\Delta\nu_{fwhm}^{Raman}=\left(\frac{g_R L_{eff} P_{threshold}^{SRS}}{A_{eff}}\right)^{3/2}\exp\left(-\frac{g_R L_{eff} P_{threshold}^{SRS}}{A_{eff}}\right) \qquad \{6.10\}$$

which is the equation which must be satisfied for the output Raman power to be equal to X percent of the pump power at the end of the fibre, assuming the pump and Stokes attenuation coefficients are equal. The solution for this is of the same form as that for Brillouin scattering

$$P_{threshold}^{SRS}=\frac{K_{SRS}A_{eff}}{g_R L_{eff}} \qquad \{6.11\}$$

Using $g_R = 6.4\times10^{-14}$ m W^{-1} (using $g_R = 9.2\times10^{-14}$ m W^{-1} at 1.064μm [6.6] and the fact that g_R is inversely proportional to wavelength), $\Delta\nu_{fwhm}^{Raman}$ = 5 THz, $A_{eff} = 60\times10^{-12}$ m^2 and $\alpha_P = 5\times10^{-5}$ m^{-1}, Equation {6.9} may be solved numerically to find the thresholds for X=100 and X =0.36 (a depletion equivalent to 1K temperature change). These thresholds are plotted in Figure 6.3 and listed numerically in Table 6.3.

It can be seen that the value of K_{SRS} ~16 predicted by Smith for X =100 is still valid for these experimental parameters. This is for identical interacting polarisations – for scrambled polarisations, the threshold will be raised by a factor of 2 [6.1]. Experiments have already been attempted at 1550nm to measure the Raman threshold. Barnard et al. [6.7] showed no significant Raman generation for 13ns pulses for powers of less than 8W through 12km fibre. The walkoff length (Equation {2.29}) for these pulses was 5.65km and the corresponding effective length 4.8km, for their fibre (0.25dB/km). The theory predicts a threshold of 3.32W, which doubled for scrambled polarisation is 6.64W.

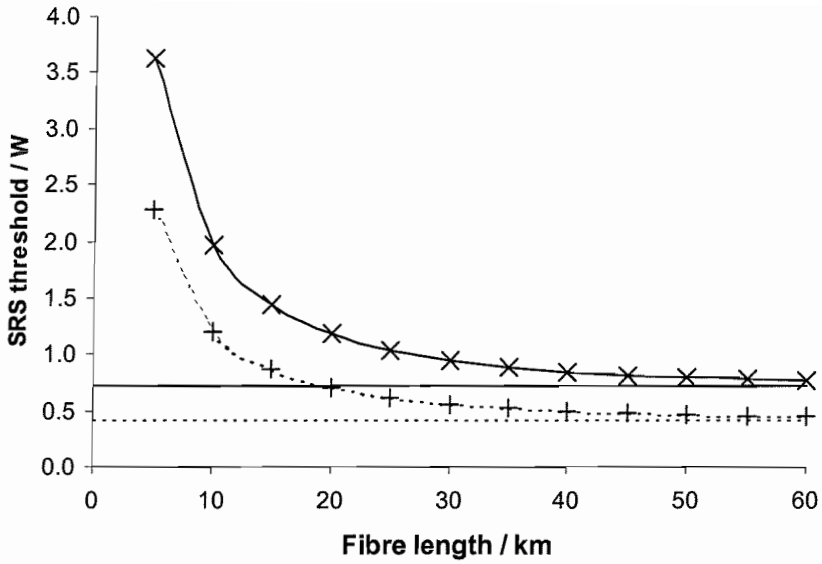

Figure 6.3 Calculated Raman threshold, using Equation {6.10}, as a function of fibre length if the polarisation state of the pump is maintained for the entire length and there is no pulse walkoff. × X=100 + X=0.36 Horizontal lines correspond to values for infinite fibres.

Fibre length L / km	Fibre effective length L_{eff} / km	Threshold for X=100		Threshold for X=0.36	
		K_{SRS}	$P^{SRS}_{threshold}$ / W	K_{SRS}	$P^{SRS}_{threshold}$ / W
5	4.42	17.08	3.618	10.75	2.279
10	7.87	16.44	1.959	10.08	1.201
15	10.55	16.12	1.432	9.73	0.865
20	12.64	15.92	1.180	9.52	0.706
25	14.27	15.79	1.037	9.38	0.616
30	15.54	15.69	0.947	9.28	0.560
35	16.52	15.62	0.886	9.20	0.522
40	17.29	15.57	0.844	9.15	0.496
45	17.89	15.53	0.814	9.11	0.477
50	18.36	15.51	0.792	9.08	0.463
55	18.72	15.49	0.775	9.05	0.453
60	19.00	15.47	0.763	9.03	0.446
∞	20.00	15.41	0.722	8.97	0.421

Table 6.3 Numerical values of the data plotted in Figure 6.3, along with values of K_{SRS}.

The observed threshold is yet higher than this, probably due to the fact that the theory does not take into account pump depletion, when in fact it must be halved if X=100. Taking theory and these experimental results into account, we would not expect to observe significant Raman scattering for pump powers less than ~1W, well above the pulse powers we are looking at in the experiments.

6.3.2.2 Experiment

As expected, no evidence of SRS was found. Even for a pulse power of 400mW and a pulse length of 300ns, there was no evidence of any 1.64μm radiation emitted at the fibre output. Also, no significant change was observed, at any point along the fibre, in the attenuation coefficient of direct detected backscattered Rayleigh signal for increasing pump powers.

6.3.3 Self Phase Modulation

As shown in the previous sections, neither SBS nor SRS have been observed to be significant for the range of pulse powers and durations used in the experiments. However, self-phase modulation (§2.4.4.2) was indeed observed and the resulting distortion to the anti-Stokes spectra was found to be important.

6.3.3.1 Theory

The extent of self-phase modulation is characterised by a nonlinear length, L_{NL}

$$L_{NL} = \frac{1}{\gamma P_0} \qquad \{6.12\}$$

which is defined such that the phase shift induced by the peak pulse power, P_0 (i.e. the maximum phase shift) is given by [6.1]

$$\phi_{max} = \frac{L_{eff}}{L_{NL}} = \gamma P_0 L_{eff} \qquad \{6.13\}$$

In this equation, γ is the nonlinearity parameter

$$\gamma = \frac{2\pi\nu_0}{cA_{eff}} n_2 \qquad \{6.14\}$$

where n_2 is the nonlinear index, which is typically ~2.5 m^2 W^{-1} for standard single-mode fibre (Appendix B in [6.1]). This gives $\gamma = 1.7$ W^{-1} km^{-1} for a pump frequency, ν_0, of 195.7 THz and an effective area of 60μm^2.

The electric field pulse shape due to SPM as the pulse propagates down the fibre is given by

$$U(L,t) = U(0,t)\exp[i\,\phi_{NL}(L,t)] \qquad \{6.15\}$$

where $U(0,t)$ is the input temporal electric field pulse shape, normalised such that its amplitude is unity at the time of the pulse peak power. The nonlinear phase shift is given by

$$\phi_{NL}(L,t) = |U(0,t)|^2 \frac{L_{eff}}{L_{NL}} \qquad \{6.16\}$$

where

$$L_{eff} = \frac{1}{\alpha}[1-\exp(-\alpha L)] \qquad \{6.17\}$$

The shape of the pulse spectrum, $S(\nu)$ as the pulse propagates is given by the modulus squared of the Fourier transform of the field pulse shape amplitude, i.e.

$$S(\nu) = \left| \int_{-\infty}^{\infty} U(0,t)\exp[i\,\phi_{NL}(L,t) + i2\pi(\nu-\nu_0)t]dt \right|^2 \qquad \{6.18\}$$

We will now consider the theoretical spectral evolution of the pulse using these equations. The pulse spectrum at any point depends entirely on the frequency chirp on the initial pulse and the initial source spectral width. We will here be assuming, for simplicity, that the pulse is from a purely AM modulated monochromatic source and so starts out with no chirp.

The output spectral shape of an initially Gaussian pulse is shown in Figure 6.4 for different values of ϕ_{max}, where $S(\nu)$ is found computationally. These spectra apply equally to any pulse duration (Gaussian FWHM, W_0) since all quantities are suitably

normalised. The value of ϕ_{max} depends on the pulse peak power and the fibre length. The absolute spectral spread depends on the pulse duration. Contours of ϕ_{max} are shown in Figure 6.5 for fibre lengths from 4km - 20km and up to 1W peak power, assuming γ = 1.7 W^{-1} km^{-1}, enabling the theoretical spectrum to be deduced, in conjunction with Figure 6.4.

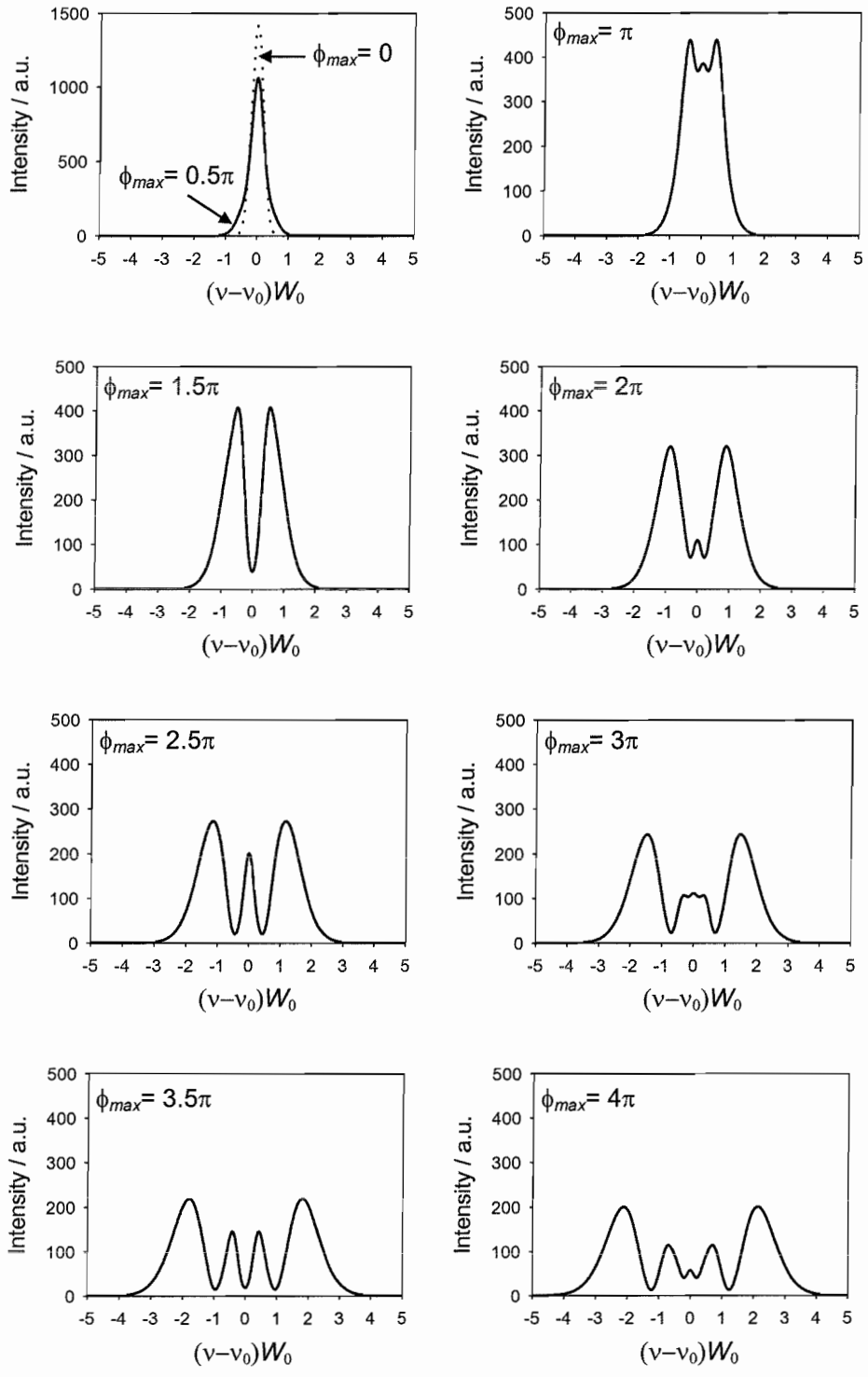

Figure 6.4 Spectral evolution of an input unchirped Gaussian pulse as ϕ_{max} increases.

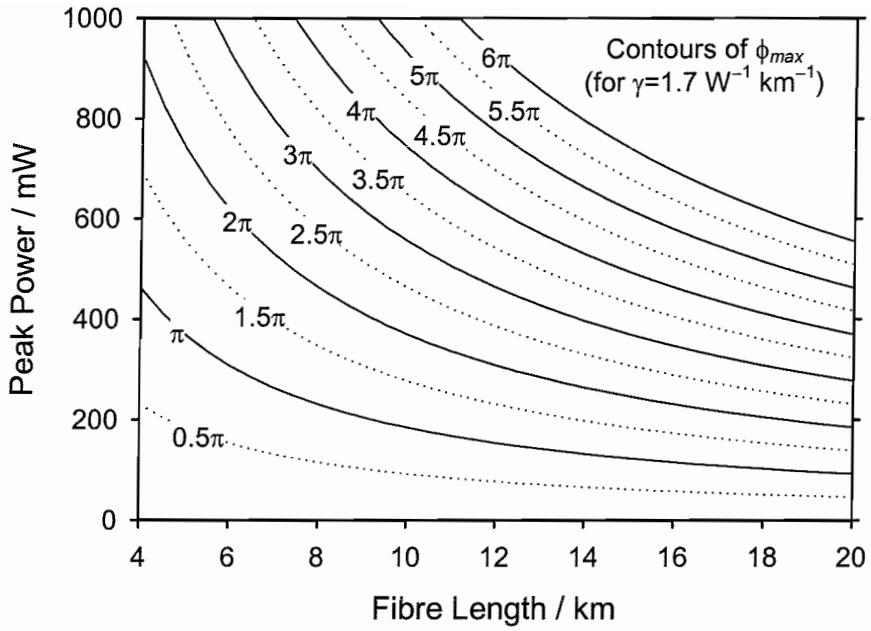

Figure 6.5 Contours of ϕ_{max} for peak powers up to 1W and fibre lengths from 4-20km, assuming γ=1.7 W^{-1} km^{-1}.

In order to compute the effect of SPM on the Brillouin backscatter, the cross-correlation of the output pulse spectrum with a 35MHz-linewidth Lorentzian curve was calculated numerically. A Lorentzian curve was then fitted to this cross-correlation and the difference between the areas under the two curves was found.

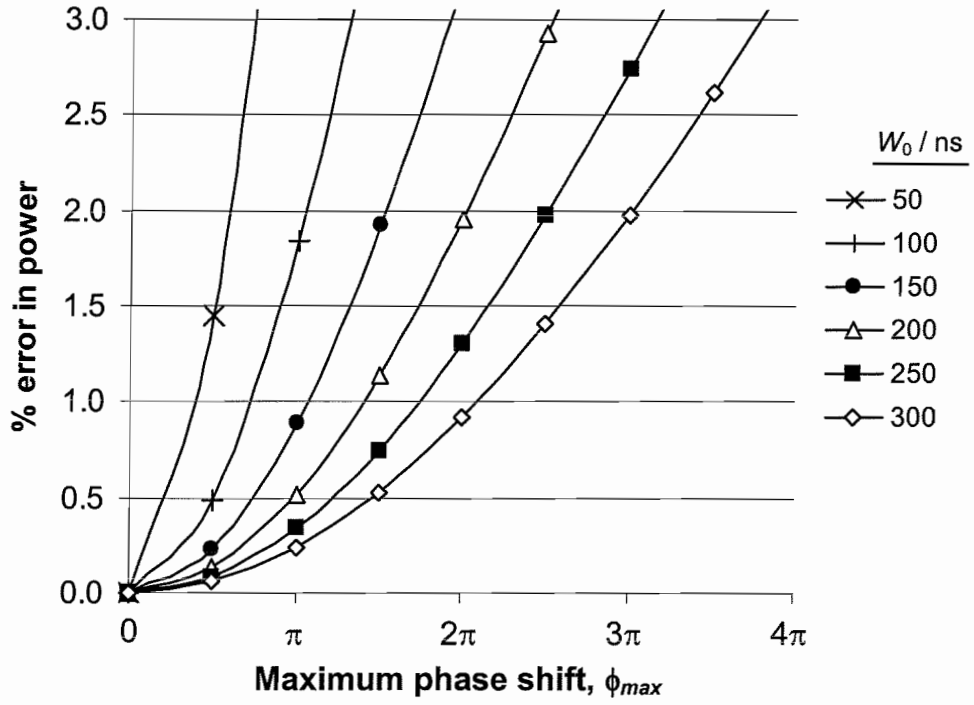

Figure 6.6 Percentage error in curve-fit power as a function of the maximum phase shift, ϕ_{max}, induced by a Gaussian pulse of different durations (FWHM, W_0). This error in power is relative to the curve fit power at the near end of the fibre.

However, when recording a backscatter trace, the distortion observed is effectively that relative to the initial recorded power, so even though the original power estimate may not be good, it is how the error in power evolves relative to this initial value which defines the distortion on the trace. The percentage error in measured power, relative to this initial value, is therefore plotted in Figure 6.6 as a function of ϕ_{max} for different pulse durations.

It can be seen that, if an arbitrary threshold value of 1% change in power is chosen (equivalent to ~2.8K), a threshold value for ϕ_{max} may be deduced from this figure for each pulse duration. This threshold information is plotted in Figure 6.7 and has an approximately linear dependence on pulse duration of $\sim 0.007\pi$ ns^{-1}. In order to convert the ϕ_{max} thresholds into peak power thresholds, the fibre length must be taken into account. Figure 6.8 shows the theoretical threshold power as a function of pulse duration for fibre lengths between 10km and infinity. It can be seen that even for a pulse of 300ns and a fibre length of 10km, the theoretical threshold power is less than 500mW.

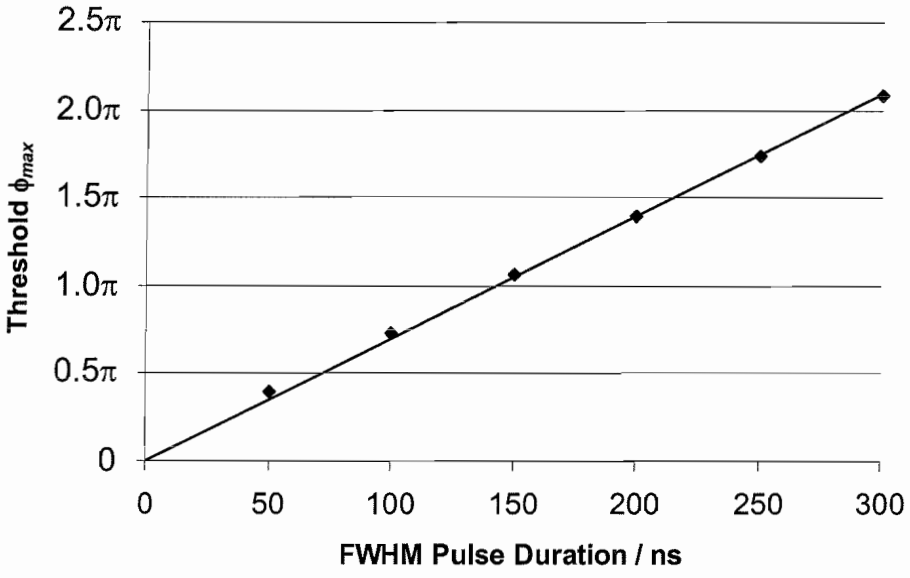

Figure 6.7 Calculated threshold value for ϕ_{max} as a function of Gaussian pulse FWHM duration. This threshold is equivalent to an change in curve-fit power due to SPM of 1%.

It can be seen that the threshold power decreases to below 100mW for a 50ns pulse duration, with a power of less than 50mW being necessary for the longest fibres at this pulse length. This means that in order to decrease spatial resolution from 20m to 5m for a 15km sensor, the pulse duration must be decreased by 6dB and the pulse

power by 5.5dB, resulting in a SNR drop of 11.5dB, for the same detector, which is indeed problematic.

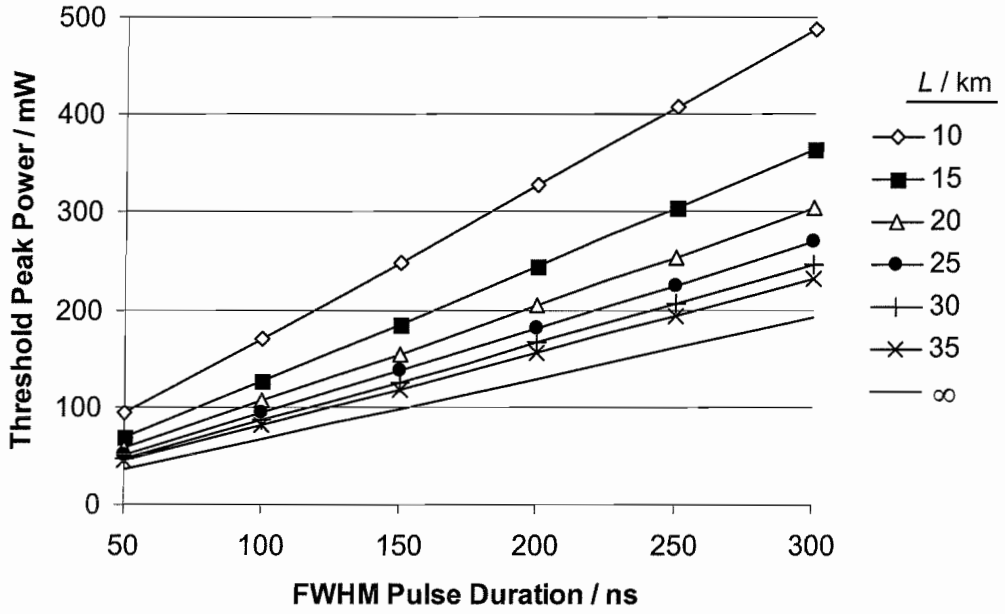

Figure 6.8 Threshold peak powers, calculated from the ϕ_{max} threshold values shown in Figure 6.7, as a function of Gaussian pulse FWHM for a range of different fibre lengths.

This particular threshold power, however, is only appropriate to the curve fitting method of power measurement, which is very sensitive to distortion of the spectral shape. If 5m spatial resolution is required, it is therefore likely that other techniques would be more appropriate to determine the Brillouin power, such as trace summing or direct detection methods.

Whilst these theoretical threshold powers provide some idea of the magnitude of spectral distortion which would be experienced by an incident unchirped Gaussian pulse, in practice there are other considerations to be addressed. Since the Gaussian pulse is symmetrical in time, the phase shift induced by it is also symmetrical in time, as is the pulse spectrum and therefore the central frequency of the pulse remains constant for the whole fibre length. However, in practice, an input pulse is not symmetrical and so the central frequency of its spectrum will change as it propagates and therefore so will the central frequency of its backscattered Brillouin spectrum. The magnitude of this effect depends entirely on the initial pulse shape and chirp and is best investigated experimentally.

6.3.3.2 Experiment

In order to observe the effect of SPM in distributed sensing, distributed narrow-band Rayleigh spectra were recorded for various pulse lengths and powers. Pulse rise time was 20-25ns in all cases. Theoretical spectra due to SPM alone may be calculated using the original pulse shape as $U^2(0,t)$ and finding the Fourier transform (Equation {6.18}) numerically. This ignores any chirp on the pulse and the cw spectrum of the source itself, but will give an idea as to the theoretical magnitude of the frequency spreading. To simulate the 5MHz resolution bandwidth filter of the ESA, each point is then replaced by the average of all those surrounding it within 2.5MHz on either side. As an example, a set of experimental distributed Rayleigh spectra using a 50ns pulse of 400mW peak power (centred at 220MHz, due to two 110MHz downshifting AOMs) is shown in Figure 6.9 and compared to the equivalent set of theoretical spectra which would arise from such an input pulse shape. It can be seen that the magnitude of the theoretical spectral broadening is qualitatively correct, as compared to the experiment, validating the value of γ=1.7 W^{-1} km^{-1} used in the modelling, lending credence to the theoretical discussion of the previous section.

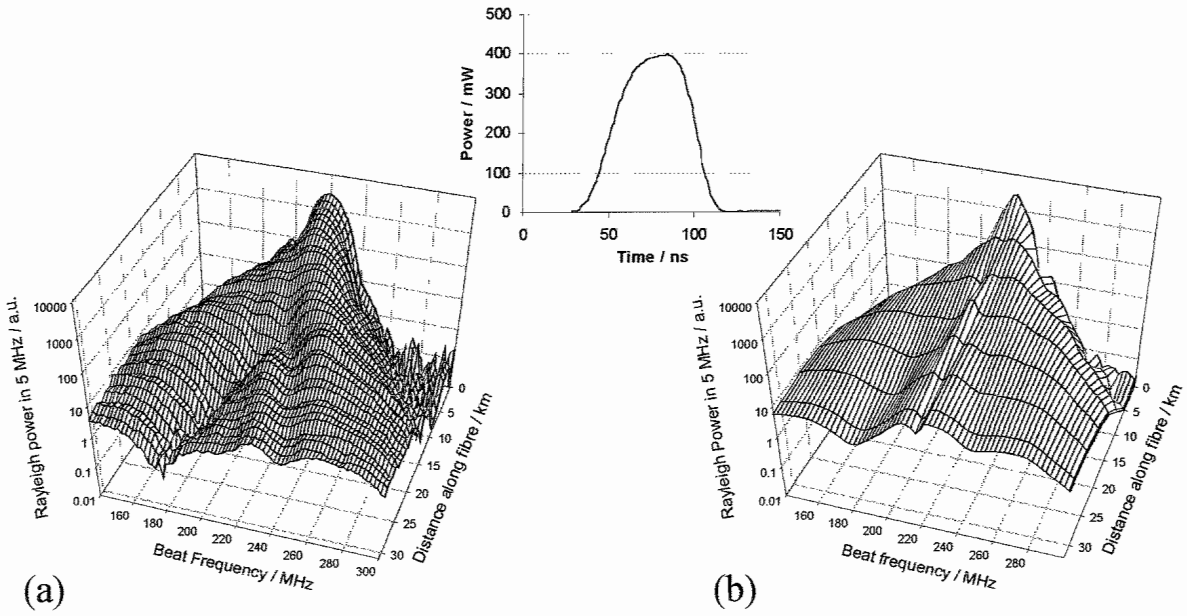

Figure 6.9 (a) Experimental and (b) Theoretical distributed narrow-band Rayleigh spectra obtained for a 50ns, 400mW peak power input pulse (inset). The theoretical spectra are those due only to self-phase modulation and are calculated numerically using the inset pulse shape and Equation {6.18} assuming the pulse is due to a purely AM modulated, monochromatic source.

On closer examination of the data in the plots in Figure 6.9, however, it is clear that another process is occurring simultaneously with SPM. If the total Rayleigh power within the 160MHz bandwidth (between beat frequencies of 140MHz and 300MHz) is found, by summing all the constituent traces, and then normalised to the expected exponential decay, such that the normalised power at the near end of the trace is unity, the resulting experimental and theoretical traces are very different.

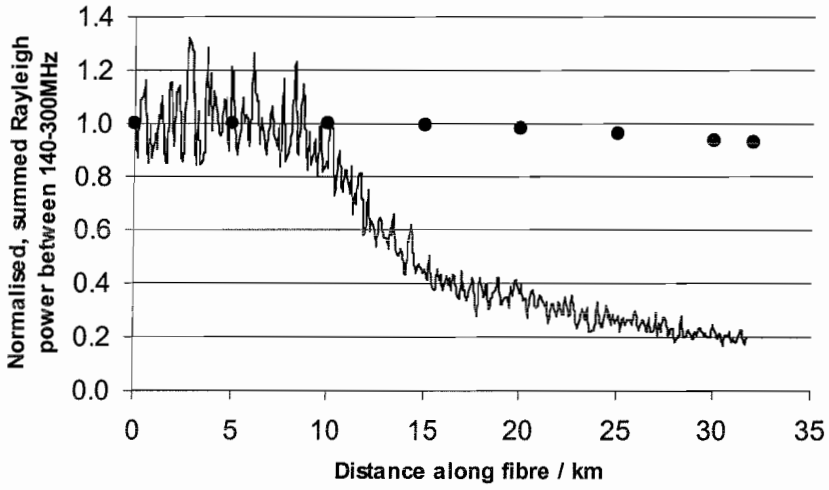

Figure 6.10 Behaviour of the narrow-band Rayleigh heterodyne power, summed over the frequency range 140MHz-300MHz, after normalising the trace to the expected exponential decay, such that the normalised power is unity at the start of the fibre. Solid line – experimental trace. Circles – theoretical prediction.

These two normalised power plots are shown in Figure 6.10, where it can be seen that, theoretically, only ~8% of the total power should be outside this bandwidth by the end of the ~32km fibre. Instead, experimentally, the equivalent figure is found to be 80%. Further evidence that there is another process at work beyond 10km into the fibre, is that the CRN on the direct-detected Rayleigh trace (4×4096 averages) decreases with distance beyond this point, for this pulse shape and power. This can be seen in Figure 6.11, which shows percentage deviation of Rayleigh power from a fitted exponential. The CRN starts at ~10% but decreases to ~2% by the end of the fibre. The solid line in this figure corresponds to the RMS noise, taken over 3km, along the length of the fibre.

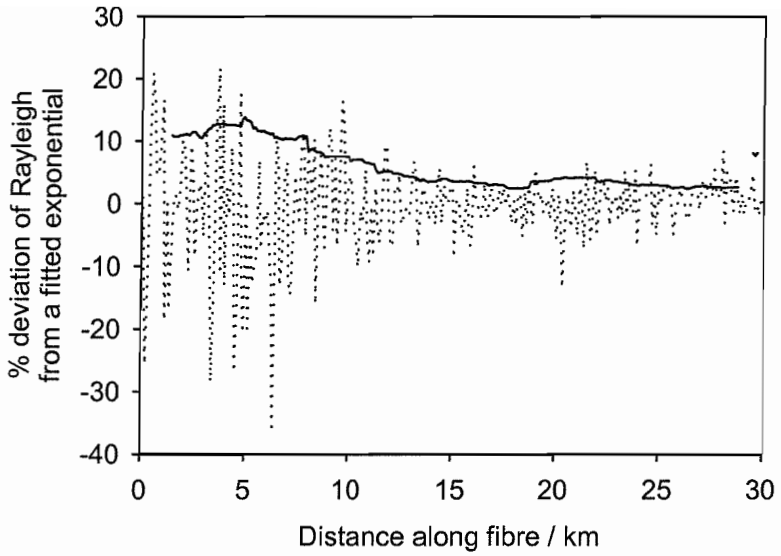

Figure 6.11 Behaviour of the noise on the direct-detected Rayleigh trace corresponding to the 400mW peak power, 50ns pulse inset in Figure 6.9. Dotted line – experimental Rayleigh trace. Solid line – RMS error in Rayleigh power, taken over 3km, along the fibre length.

This information may be used to calculate the percentage of narrow-band radiation which must be present in order to result in this degree of CRN. For example, if the noise is reduced from 10% at the near end of the fibre to 2% at the far end, it is assumed that only 20% of the total backscattered power is narrow-band by this point. If this calculated information is plotted on the same graph as the experimental trace in Figure 6.10, agreement can be seen, as shown in Figure 6.12. Slightly better agreement is seen if the equivalent graph is plotted for a 400mW peak power 100ns pulse. Any discrepancy might be ascribed to inaccuracies in the CRN trace.

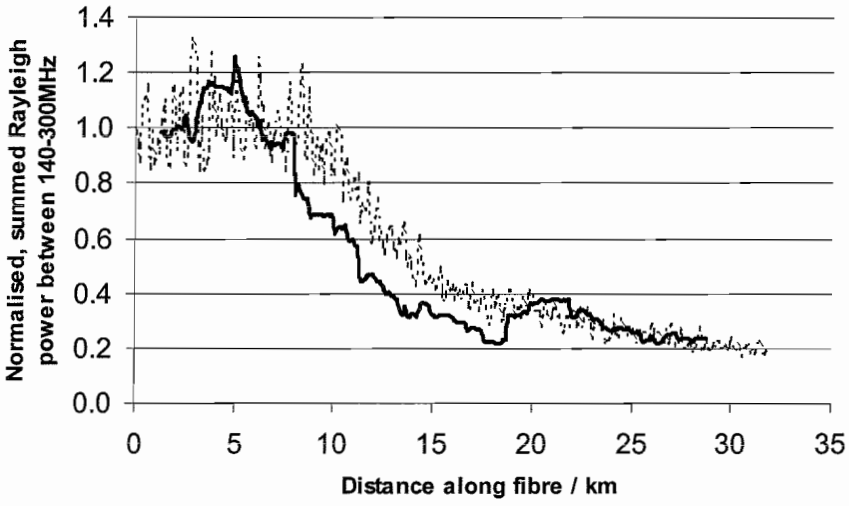

Figure 6.12 Rayleigh depletion for 400mW peak power, 50ns pulse. Dotted line: same data as plotted in Figure 6.10, showing Rayleigh power within a 160MHz bandwidth about the initial pulse peak frequency as a function of fibre length. Solid line: predicted fraction of narrow-band Rayleigh radiation by examination of reduction in CRN along the fibre length.

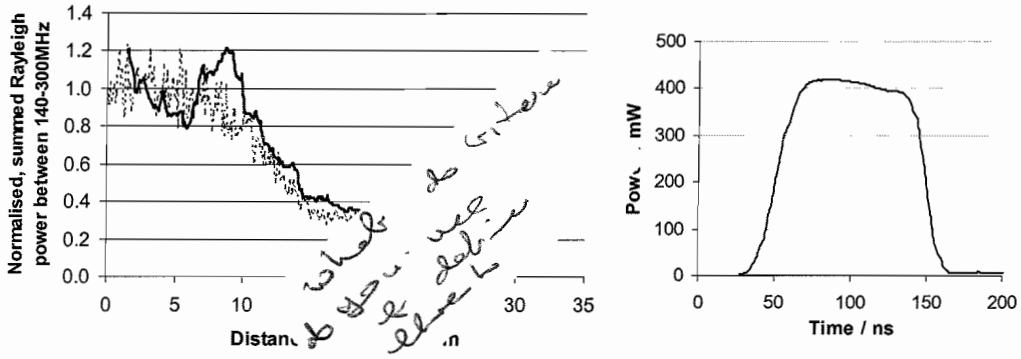

Figure 6.13 (a) Equivalent plot to that of Figure 6.12 but for the pulse shape shown in (b)

Such pump depletion has been observed by Izumita et al. when using EDFA-amplified pulses in coherent optical time-domain reflectometry [6.8], which they showed to be due to four wave mixing (FWM) of the signal and residual ASE on the amplified sensing pulse. This FWM gives rise to new frequencies located in two peaks, one on either side of the Rayleigh frequency. What is more, they estimated the FWM threshold power to be ~316mW for 100ns pulses and ~300mW for 1μs pulses when using a 100km test fibre. These threshold values are low enough to assume that this is the phenomenon we observe here.

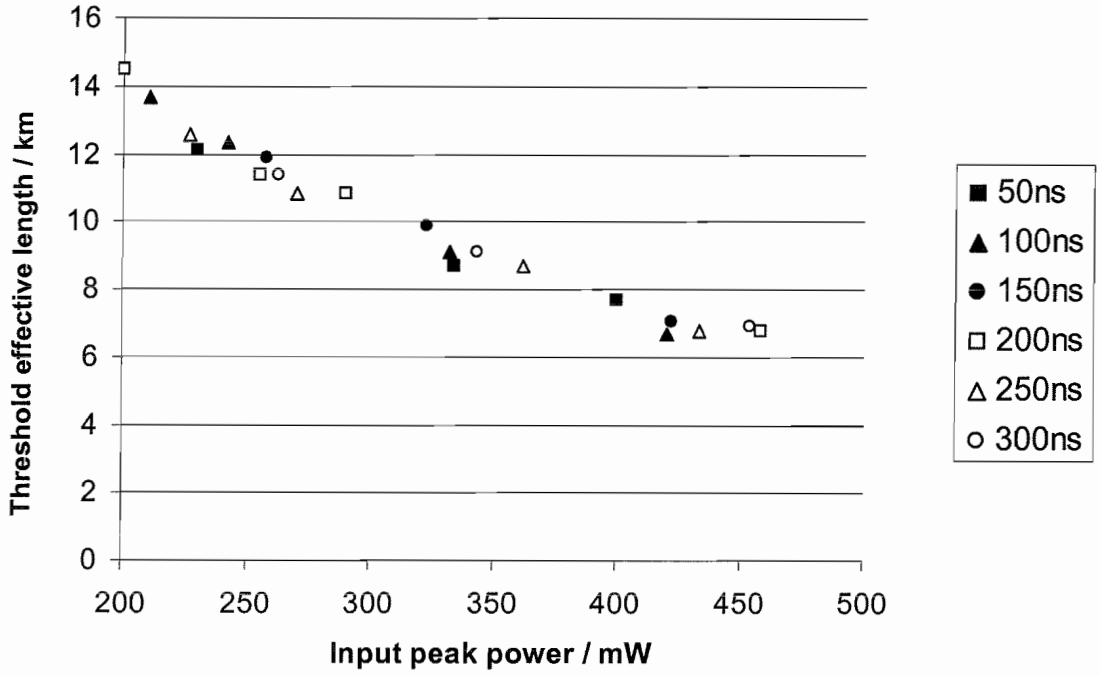

Figure 6.14 Threshold effective length, at which pump depletion due to four wave mixing of the pump pulse with residual ASE begins, as a function of input pulse peak power.

We may use such experimental Rayleigh traces as that in Figure 6.10 to estimate a FWM threshold for different pulse durations and fibre lengths. The threshold effective lengths, where significant Rayleigh depletion begins, are estimated for a range of peak powers and pulse lengths and plotted as a function of peak power in Figure 6.14. As the threshold effective length increases, the depletion is much reduced and for the lower pulse powers, at ~200mW, the threshold length was instead estimated using anti-Stokes power measurements, where the noise was much reduced.

It can be seen that there is no significant dependence of the threshold length on pulse duration. The dependence on peak power may be clarified by looking at a plot of reciprocal threshold effective length as a function of peak power, shown in Figure 6.15 for the data above. The relationship is linear, indicating a similar threshold relationship as for Brillouin and Raman scattering (Equations {6.8} and {6.11}), which evaluates numerically to

$$P_{threshold}^{FWM} / W = \frac{3.0}{L_{eff} / km} \qquad \{6.19\}$$

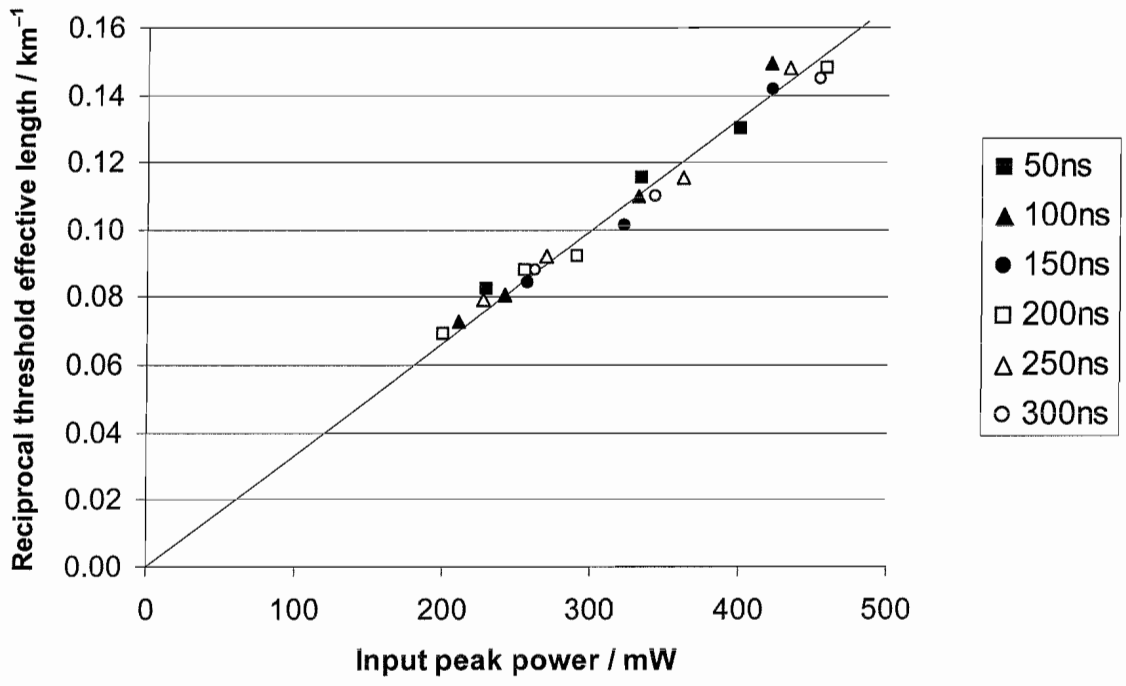

Figure 6.15 Reciprocal threshold effective length as a function of input pulse peak power, showing a linear relationship. Solid line shows the line of best fit, passing through the origin, which has gradient 0.332 $km^{-1}W^{-1}$.

The magnitude of the pump depletion observed at the output of the 32km sensing length was also determined as a function of input pulse peak power and is illustrated in Figure 6.16. For the lower pump powers, this depletion was hidden in the coherent noise and set arbitrarily to zero for the purposes of this analysis.

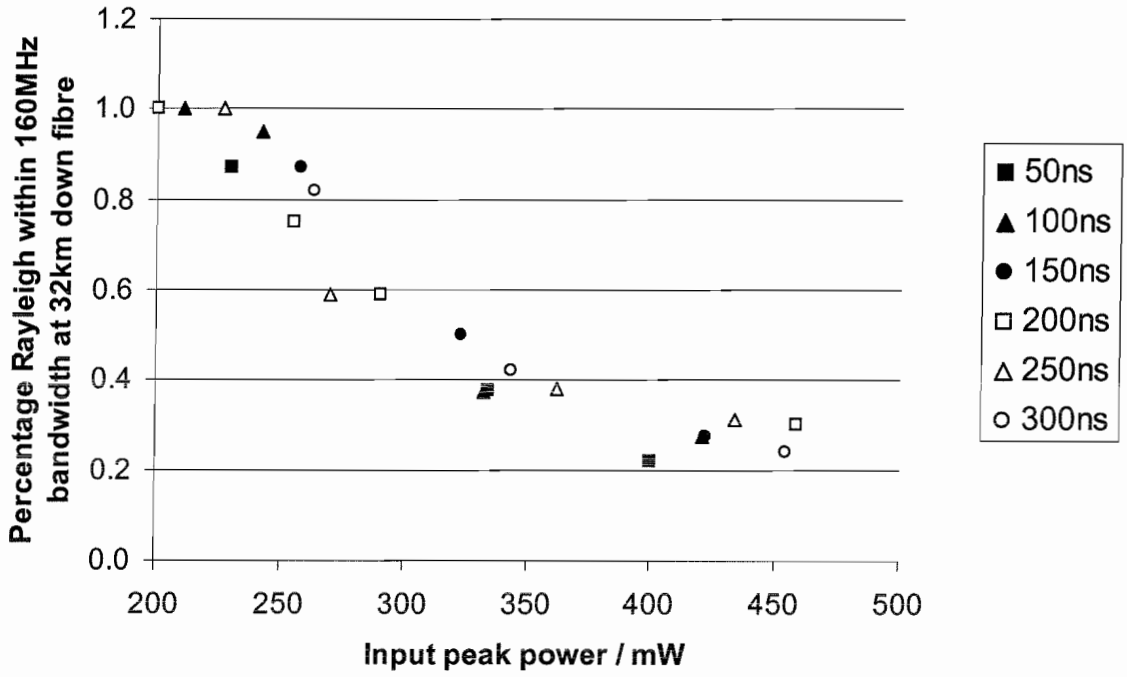

Figure 6.16 Fraction of backscattered Rayleigh power from 32km of sensing fibre within a 160MHz bandwidth centred at 220MHz. This allows pump depletion to be estimated, since Rayleigh power is proportional to pump power.

From this figure, it can be seen that the pump is depleted by 3dB at an incident peak pulse power of between 300 mW and 330 mW, in very close agreement with the experimental thresholds of 316 mW and 300 mW obtained by Izumita et al. [6.8].

Since the FWM is virtually eliminated at an input power of 200mW, the effect of self-phase modulation may be estimated by considering the frequency shift error at this power for each pulse duration. At these low powers, the systematic error in frequency shift (compared to the frequency shift measured using 135mW, 150ns pulses) due to SPM is approximately linear with fibre effective length, with the values observed at 32km being shown in Figure 6.17.

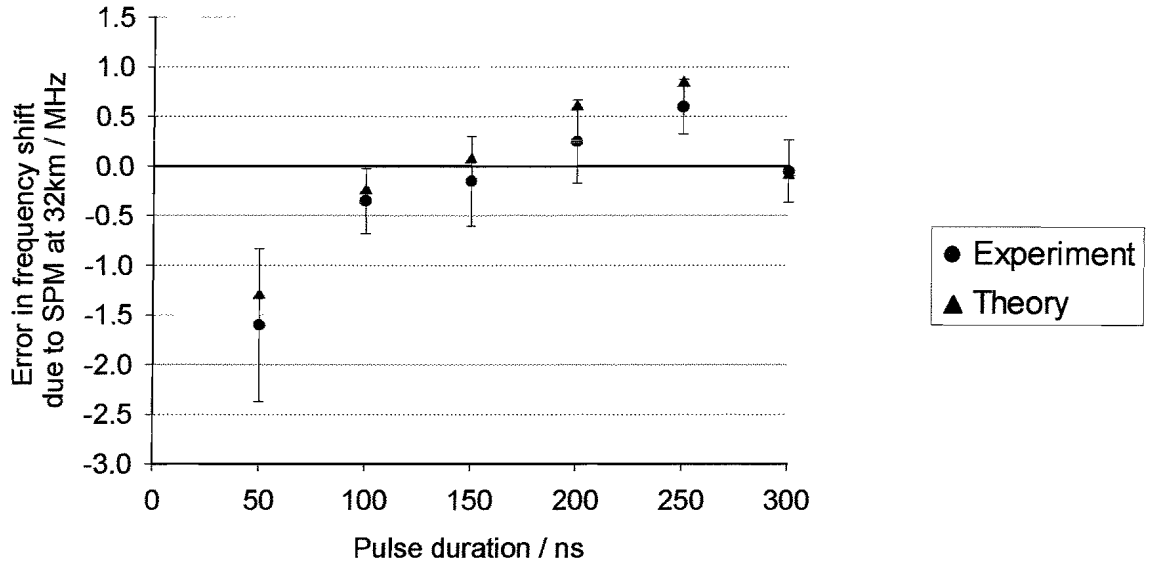

Figure 6.17 Systematic error in frequency shift due to SPM at the end of 32km fibre, for an input peak pulse power of 200mW, as a function of pulse duration. Circles – experimental results Triangles – theoretical numerical computation of the frequency shift error using the measured input pulse shape and Equation {6.18}. The error bars show the RMS noise on the experimental frequency shift traces at the end of the fibre.

This figure shows broad agreement between theory and experiment with the largest discrepancy being 0.35MHz. Frequency errors of less than ±0.5MHz are evident for pulses of 100ns or longer at this 200mW power whereas 50ns pulses result in errors of less than ±1MHz. In contrast, the equivalent plot for 400mW input power, shown in Figure 6.18, displays much less agreement due to the influence of four wave mixing, which becomes more significant for the shorter pulse lengths where the spectrum becomes more widely spread.

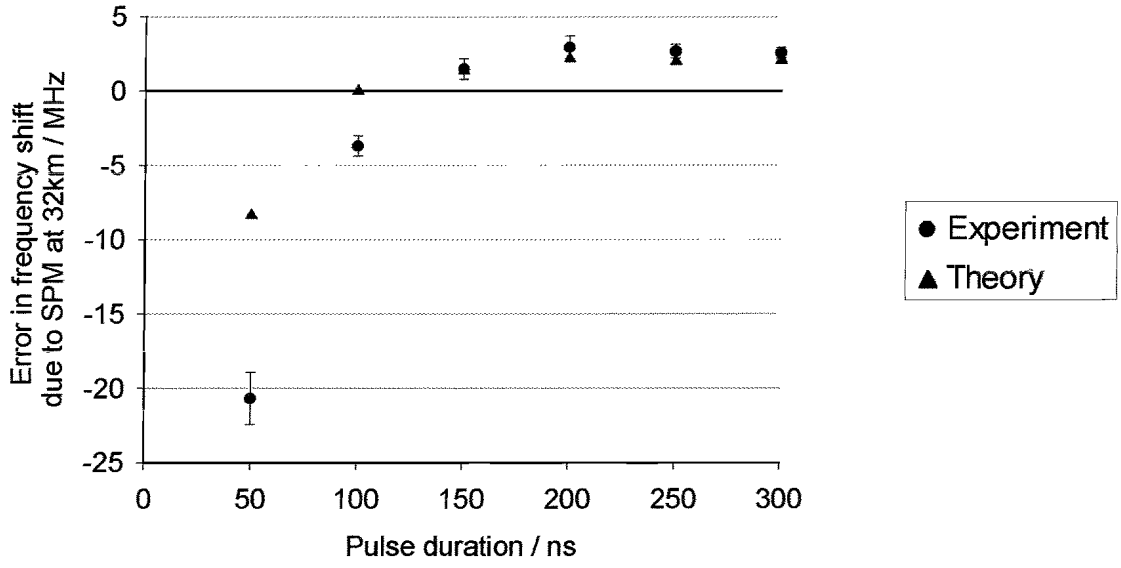

Figure 6.18 Equivalent plot to Figure 6.17 for 400mW input pulses.

The true performance of the sensor, however, is measured by the anti-Stokes curve fitting results. Curve fitted total power traces, relative to that obtained for 150ns 135mW pulses, are shown in Figure 6.19 for various pulse powers and durations, along with theoretical predictions, calculated by curve fitting to the cross-correlation of the theoretical Rayleigh spectrum with a 35MHz Lorentzian peak.

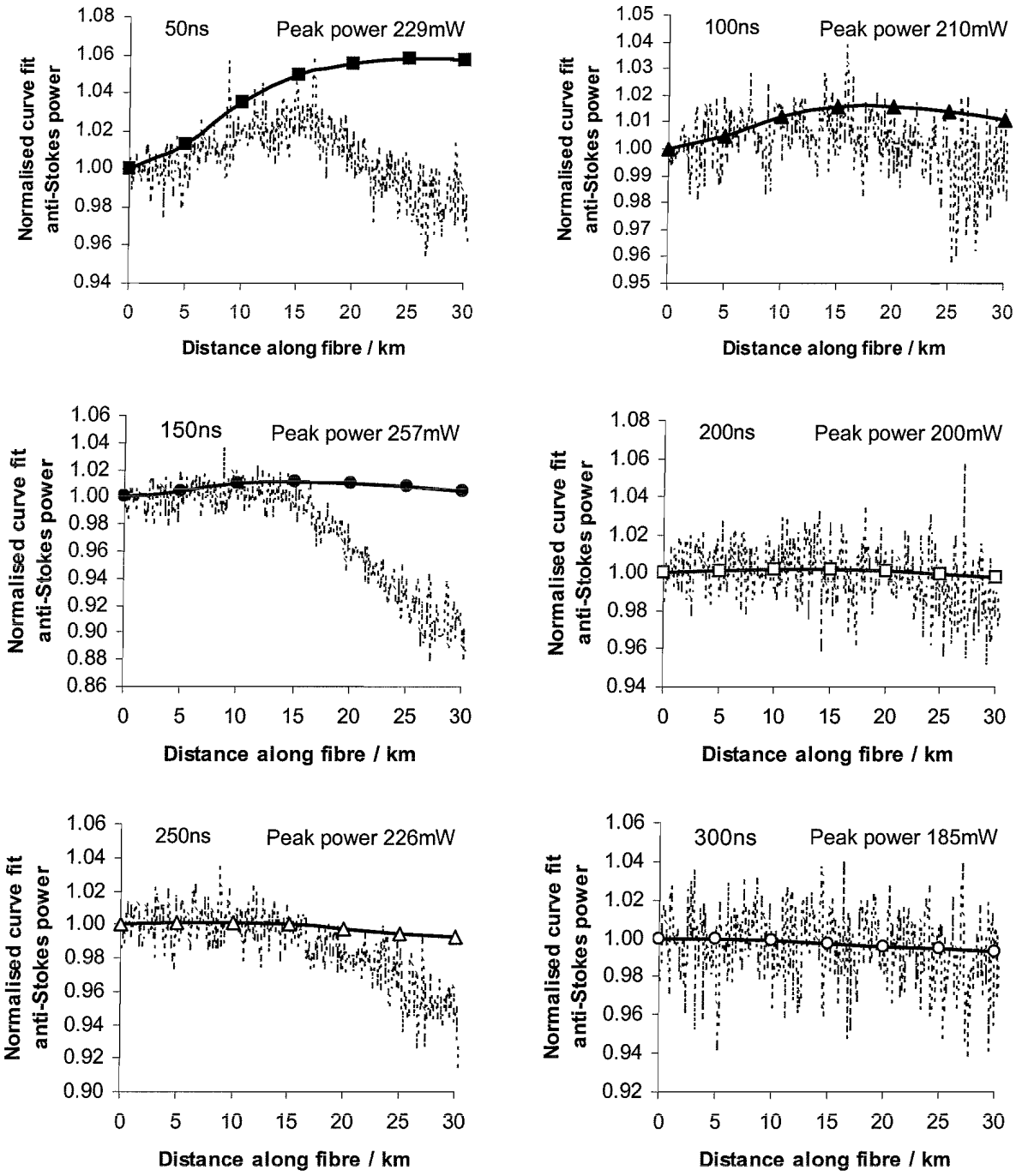

Figure 6.19 Curve-fitted anti-Stokes power normalised to that obtained for 150ns, 135mW pulses. Dotted lines: experimental traces Solid lines: theoretical traces due to SPM alone, based on input pulse shapes and numerical cross-correlation of the resulting Rayleigh spectra with a 35MHz Lorentzian, followed by curve fitting (Symbol key is that in Figure 6.16).

It is demonstrated that the powers closely follow the theoretical predictions up to ~15km, after which depletion due to FWM is evident. By subtracting the actual value from the theory, we can obtain an approximation to the depletion caused by FWM. These results are shown in Figure 6.20 for each trace as a function of peak power, every 5km.

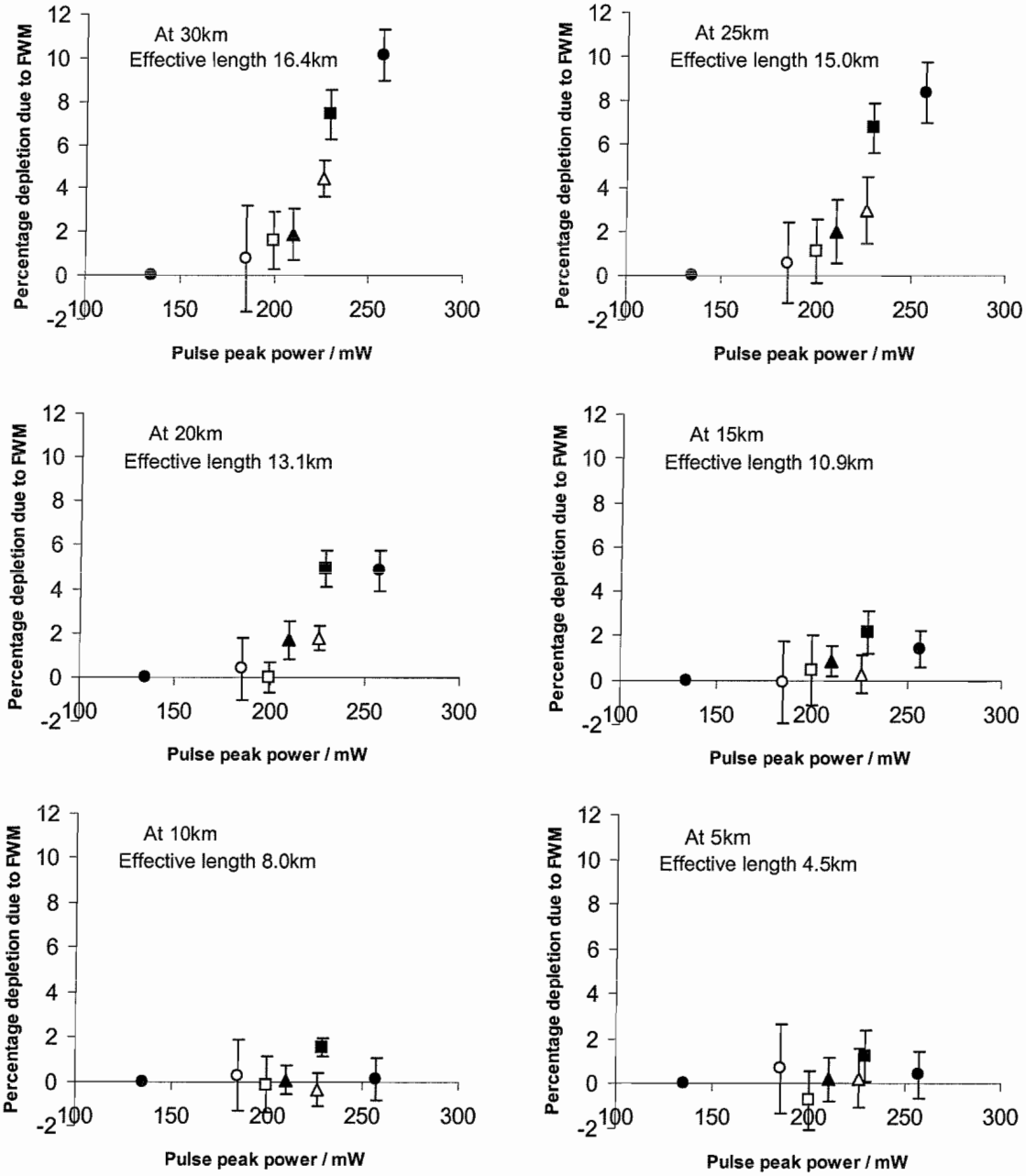

Figure 6.20 FWM-induced, curve-fitted anti-Stokes power depletion as a function of pulse power for different fibre lengths. Data is that in Figure 6.19, with the experimental value being subtracted from the theoretical value, due to SPM alone. (Symbol key is that in Figure 6.16).

The behaviour of the theoretical curve-fit powers shown in Figure 6.19 (but un-normalised to the 135mW, 150ns trace) may be compared to the theoretical behaviour of Gaussian pulses with the same FWHM and peak power, in order to judge the relative magnitudes of the power errors. This comparison, between the expected SPM behaviour of the experimental pulse shapes and ideal Gaussian pulse shapes, is shown in Figure 6.21.

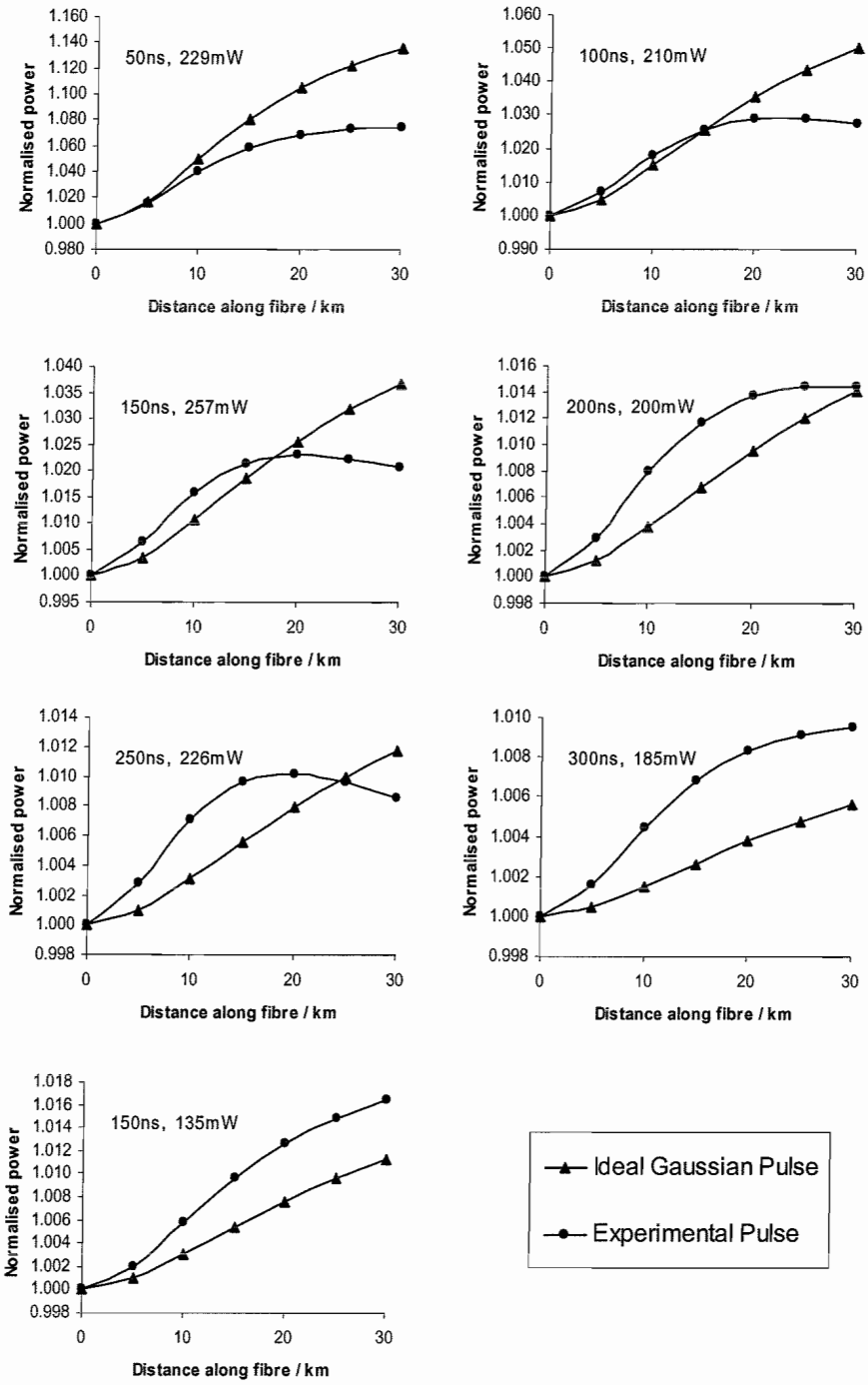

Figure 6.21 Comparison of theoretical curve-fit power error due to SPM, as a function of distance along the fibre, for both experimental pulse shapes and ideal Gaussian pulses with the same peak power and FWHM.

This figure shows that, perhaps surprisingly – due to the fast 20-25ns rise and fall time of the experimental pulses – the expected SPM-induced power error is never as much as a factor of two away from that predicted for equivalent Gaussian pulses. Indeed, for shorter pulses and longer fibre lengths, the experimental pulses clearly out-perform the Gaussian pulses. In any case, such evidence further supports the use of the Gaussian-based SPM threshold power estimates shown graphically in Figure 6.8. To get a qualitative feel for why the experimental pulse performs better than the equivalent ideal Gaussian pulse, the computed Rayleigh spectra which would be observed at 30km down the fibre are shown in Figure 6.22 for the 257mW, 150ns pulse. Whilst the experimental pulse indeed shows greater frequency spreading, most of these frequency components are at a low power and the central peak is relatively undisturbed. In the Gaussian case, the single input peak has become two, with total spread being larger than that of the remaining single peak in the experimental case.

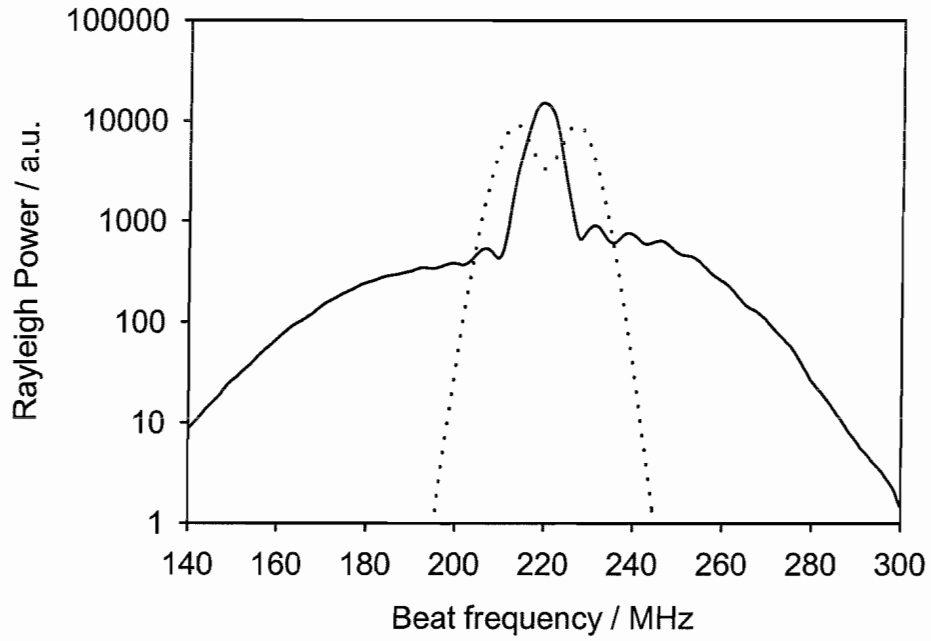

Figure 6.22 Theoretical SPM-induced Rayleigh spectra at 30km down the fibre due to a 257mW, 150ns pulse. Solid line – experimental pulse. Dotted line – equivalent Gaussian pulse.

The other quantity affected by SPM is the frequency shift measurement, which is not subject to error in the case of the ideal symmetric Gaussian pulse. The experimental pulses, however, do affect these measurements and this will now be considered.

Equivalent frequency shift plots to the power traces of Figure 6.19 are presented in Figure 6.23. All frequency shift traces are adjusted such that the value at the near end of the fibre is the same, compensating for any ambient temperature variations. Here there is less departure from theory – the experimental value is always within 1MHz of the predicted value. The deviation from the 150ns, 135mW reference shift is greatest for 50ns pulse but still less than 3MHz over 30km. In the other cases, the deviation is less than 1MHz.

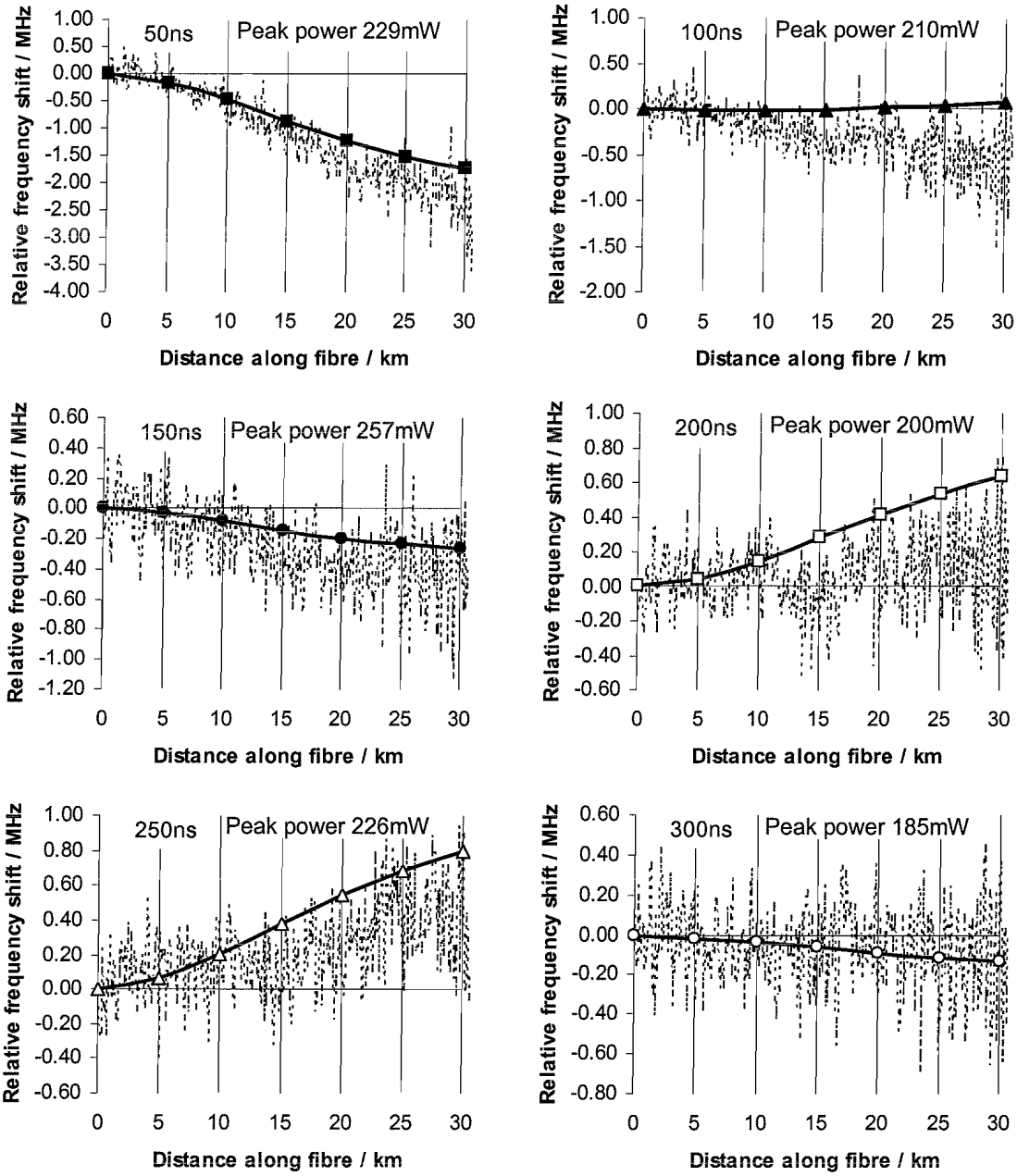

Figure 6.23 Curve-fitted anti-Stokes frequency shift, as a deviation from the shift obtained for 150ns, 135mW pulses. Dotted lines: experimental traces Solid lines: theoretical traces due to SPM alone, based on input pulse shapes and numerical cross-correlation of the resulting Rayleigh spectra with a 35MHz Lorentzian, followed by curve fitting (Symbol key is that in Figure 6.16). This figure is the frequency shift analogue of Figure 6.19.

It can be concluded that FWM has less of an impact on frequency shift measurements than on power measurements as the power is increased above ~200mW. Since SPM has a significant effect on the frequency shift, compared to the noise levels we are achieving, in certain cases (for example the 50ns pulses), the need for pulse symmetry is obvious, although it may be possible to compensate theoretically for any SPM errors at these low powers since the agreement with theory is reasonable.

6.4 Summary and Conclusions

This chapter has a presented theoretical and experimental investigation into nonlinear optical phenomena which affect distributed Brillouin sensing using spectroscopy of the anti-Stokes power. Also, continuous wave stimulated Brillouin scattering was found to exhibit a threshold power consistent with a modified version of existing theory.

It has been demonstrated that the two most important nonlinear effects in this application are self-phase modulation (SPM), which distorts the spectra, and four wave mixing (FWM) of the high power narrow-band sensing pulse with residual ASE, which results in pump depletion.

Frequency shift measurements are affected by both SPM and FWM, with the latter acting to deplete the central, high intensity spectral peak of the pump pulse, thereby increasing the effect of any SPM-induced satellite peaks. The frequency shift error would theoretically be zero for a perfectly symmetrical pulse shape, so this is a desirable feature of any sensing system measuring this quantity.

Four wave mixing has a more profound effect on the power measurements and so it would be ideal to use pulses which have not been amplified by an EDFA, or by using EDFAs with lower gain or greater efficiency. A high power 1550nm cw source laser would be instrumental in achieving such a reduction. Optical filtering of the input pulses could also mitigate this process by attenuating the broad-band input radiation. The theoretical power error due to SPM was found to be of similar magnitude for both experimental and ideal Gaussian pulses, for which a threshold analysis was presented.

6.5 References

[6.1] G.P. Agrawal: "Nonlinear Fiber Optics", Second Edition, *Academic Press*, ISBN 0-12-045142-5 (1995)

[6.2] R.G. Smith: "Optical Power Handling Capacity of Low Loss Optical Fibers as Determined by Stimulated Raman and Brillouin Scattering", *Applied Optics*, Vol. 11, No. 11, pp. 2489-2494 (November 1972)

[6.3] T.-O. Tsun, A. Wada, T. Sakai and R. Yamauchi: "Novel method using white light spectral probe signals to measure Brillouin gain spectra of pure silica core fibres", *Electronics Letters*, Vol. 28, No. 8, pp. 247-249 (January 1992)

[6.4] N. Shibata, Y. Azuma, T. Horiguchi and M. Tateda: "Identification of longitudinal acoustic modes guided in the core region of a single-mode optical fiber by Brillouin gain spectra measurements", *Optics Letters*, Vol. 13, No. 7, pp. 595-597 (July 1988)

[6.5] M. O. van Deventer and A.J. Boot: "Polarization properties of Stimulated Brillouin Scattering in Single-Mode Fibers", *Journal of Lightwave Technology*, Vol. 12, No. 4, pp. 585-590 (April 1994)

[6.6] C. Lin, L.G. Cohen, R.H. Stolen, G.W. Tasker and W.G. French: "Near-infrared sources in the 1-1.3μm region by efficient stimulated Raman emission in glass fibres", *Optics Communications*, Vol. 20, No. 3, pp. 426-428 (1977)

[6.7] C.W. Barnard, P. Myslinski, X. Pan and J. Chrostowski: "Limitations Imposed by Stimulated Raman Scattering of 1550nm High-Energy Pulse Transmission", *Journal of Lightwave Technology*, Vol. 13, No. 2, pp. 115-119 (February 1995)

[6.8] H. Izumita, Y. Koyamada, S.-i. Furukawa and I. Sankawa: "The Performance Limit of Coherent OTDR Enhanced with Optical Fiber Amplifiers due to Optical Nonlinear Phenomena", *Journal of Lightwave Technology*, Vol. 12, No. 7, pp. 1230-1238 (July 1994)

Chapter Seven

Conclusions

7.1 Summary and Conclusions

This work has presented both theoretical and experimental work in the area of temperature and strain sensing using coherent detection of spontaneous Brillouin backscatter. The main focus of this research was to develop a such a sensor working at a beat frequency of ~11GHz. The spatial resolution was fixed at 20m, due to limitations of the spectrum analyser used.

A detailed theoretical analysis of the noise properties of spontaneous Brillouin sensors showed that optical pre-amplification of the signal was necessary for the coherent detection system available. It also showed that this pre-amplified sensor, working at a beat frequency of 11GHz exhibited in a theoretical central trace signal-to-noise ratio that was up to ~9dB larger than that for a 100MHz beat frequency, all other things being equal. This analysis also showed that this same SNR was no more than 3dB lower than that obtained in direct detection using an ideal receiver with 10MΩ feedback. The effects of Lorentzian curve fitting, to extract frequency shift and total power measurements, were modelled in order to determine the behaviour of the errors in these quantities as a function of central trace SNR, frequency step and span of collected traces. It was determined that a 5MHz step in frequency was a good choice and that the collection span should extend at least 30MHz either side of the required range of frequency shifts to be measured.

Theory and experiment both showed that optical filtering of the amplified signal was necessary in order to remove both the Stokes heterodyne peak (which could itself be observed subsequently by tuning of the source laser) and the Rayleigh-Brillouin beat spectrum from anti-Stokes signal. A fibre Bragg grating filter was shown to remove these unwanted features effectively. The ratio of unfiltered Rayleigh-Brillouin peak

power to Stokes heterodyne peak power (which is dependent on the ratio of Rayleigh power to local oscillator power at the detector) was observed experimentally to be approximately the predicted theoretical value.

Polarisation noise on the Brillouin signal was observed at a level of ~11% with no polarisation scrambling. This polarisation noise was finally reduced to a residual value of ~0.4% after optimisation of scrambling within the sensor. Coherent noise on the ~6nm broad-band normalising Rayleigh trace was found to agree with theory at 0.18%.

Distributed sensing measurements were made over 57km, believed to be the longest sensing length for single-ended measurements then published, where a frequency shift resolution of less than 3MHz was maintained for the entire fibre length and less than 0.5MHz for the first 40km. Power measurements, however, were viable only up to ~30km, if an equivalent temperature resolution of less than 5K were required. The frequency shift and power errors obtained experimentally for this sensing length agreed very well with theoretical predictions.

Power measurements over a sensing length of 27.4km provided the first calibration, to our knowledge, of Brillouin power with temperature using a heterodyne sensor. Also, this sensing length was believed to be the longest yet reported for single-ended spontaneous Brillouin power measurements. Coefficients of the temperature dependence of Brillouin power and frequency shift were found to be 0.36±0.04 %/K and 1.07±0.06 MHz/K respectively. Subsequently, strain measurements yielded strain coefficients of 0.046 MHz/με and –8±5 %/με. Fitting of a double or triple Lorentzian peaks was found necessary at points of discontinuity in temperature or strain and in places where the differential strain (or potentially temperature) within the spatial resolution was significant.

Simultaneous temperature and strain measurements were also obtained, believed to be the first such measurements using coherent detection of spontaneous Brillouin power and frequency shift, for a sensing length of 31.8km. A temperature resolution of less than 4K and a strain resolution of less than 100με were obtained at the far end of the

fibre, surpassing in range previous simultaneous spontaneous Brillouin sensors. To our knowledge, the maximum range then reported was 15km (using direct detection) although at 10m spatial resolution, where a resolution of 4K and 290με were obtained [7.1].

The behaviour of the Brillouin linewidth with both temperature and distance along the fibre was investigated. The linewidth was found to decrease with temperature in an approximately linear fashion at a rate of approximately –0.1 MHz/K, agreeing with previous measurements [7.2]. The linewidth increased slightly with distance down the fibre (~4MHz over 50km) probably as a result of mild self-phase modulation.

The effects of nonlinear phenomena on the distributed sensing measurements were also investigated, as the pulse power was increased, for several different pulse durations. Self-phase modulation (SPM) and four wave mixing (FWM) of the pump pulse with residual ASE were found to be the most significant of these effects, which acted to distort the Brillouin spectra and cause pump depletion, respectively. In the absence of significant FWM, theoretical SPM modelling gave good agreement with observed experimental results. It was also found that the theoretical SPM error in power measurement was of a similar magnitude for equivalent experimental and ideal Gaussian pulses, allowing a Gaussian pulse SPM model to provide an estimate of the appropriate threshold power. Continuous wave stimulated Brillouin scattering was also shown experimentally to have a threshold power close to that predicted by a modified version of existing theory.

7.2 Future Work

The primary limitation of the coherent sensor, as it stands, is its spatial resolution. In order to improve this, a new sensing system must be built from scratch with a larger effective detection bandwidth, which will ideally involve a higher intermediate frequency. This requirement for redesign has the advantage that each component may be optimised for our particular application and noise levels should be greatly decreased.

Given the complicated curve-fitting process for obtaining Brillouin power traces using coherent spectroscopy, it would be much simpler if a direct detection method could be used for this purpose and the results subsequently combined with heterodyne frequency shift measurements. This would complicate the optics (e.g. addition of a Mach-Zehnder interferometer), but ensure that the same detector could be used for both the Brillouin and broad-band Rayleigh measurements, improving normalisation accuracy. Such a method would be increasingly necessary for shorter spatial resolutions, where the effects of SPM are more pronounced.

Further investigation into nonlinear phenomena would also be useful, to observe the effect of reduced ASE on the four-wave mixing threshold. Pulse shaping techniques could be used to determine experimentally the effects of different temporal pulse profiles on self-phase modulation. Such pulse shaping could at least be used to minimise the frequency shift error caused by SPM by allowing symmetrical pulses to be launched into the sensing fibre.

7.3 References

[7.1] H.H. Kee, G.P. Lees and T.P. Newson: "All-fiber system for simultaneous interrogation of distributed strain and temperature sensing by spontaneous Brillouin scattering", *Optics Letters*, Vol. 25, No. 10, pp. 695-697 (May 2000)

[7.2] T. Kurashima, T. Horiguchi and M. Tateda: "Thermal effects of Brillouin gain spectra in single-mode fibers", *IEEE Photonics Technology Letters*, Vol. 2, No. 10, pp. 718-720, (October 1990)

Appendix A Polarization Scrambling

This Appendix will discuss, theoretically, the action of a two-axis polarisation scrambler and calculate the output Stokes parameters. The Jones matrix, *M*, describing the scrambler is given by the matrix for a phase plate with fast axis vertical premultiplied by the matrix for a phase plate at 45°.

$$M = \frac{1}{2}\cdot\begin{pmatrix}(e^{i\beta}+1) & (e^{i\beta}-1)\\ (e^{i\beta}-1) & (e^{i\beta}+1)\end{pmatrix}\begin{pmatrix}e^{i\alpha} & 0\\ 0 & 1\end{pmatrix} = \frac{1}{2}\cdot\begin{pmatrix}(e^{i\beta}+1)e^{i\alpha} & (e^{i\beta}-1)\\ (e^{i\beta}-1)e^{i\alpha} & (e^{i\beta}+1)\end{pmatrix} \quad \{A.1\}$$

This means that for general input *x* and *y* complex amplitudes of $A_x^{in} = E_x^{in}$ and $A_y^{in} = E_y^{in}e^{i\Delta\phi_{in}}$ the output polarisation state is given by

$$\begin{pmatrix}A_x^{out}\\ A_y^{out}\end{pmatrix} = \frac{1}{2}\cdot\begin{pmatrix}(e^{i\beta}+1)e^{i\alpha} & (e^{i\beta}-1)\\ (e^{i\beta}-1)e^{i\alpha} & (e^{i\beta}+1)\end{pmatrix}\begin{pmatrix}E_x^{in}\\ E_y^{in}e^{i\Delta\phi_{in}}\end{pmatrix} = \begin{pmatrix}\frac{1}{2}(e^{i\beta}+1)e^{i\alpha}E_x^{in} + \frac{1}{2}(e^{i\beta}-1)E_y^{in}e^{i\Delta\phi_{in}}\\ \frac{1}{2}(e^{i\beta}-1)e^{i\alpha}E_x^{in} + \frac{1}{2}(e^{i\beta}+1)E_y^{in}e^{i\Delta\phi_{in}}\end{pmatrix} \quad \{A.2\}$$

Now, the phase shift induced by each plate is a function of time, such that

$$\alpha = A\cos\omega_1 t$$
$$\beta = B\cos\omega_2 t \quad \{A.3\}$$

and so the complex amplitudes of the resultant *x* and *y* polarisations are given by

$$A_x^{out} = E_x^{out}e^{i\phi_x^{out}} = \tfrac{1}{2}(e^{iB\cos\omega_2 t}+1)e^{iA\cos\omega_1 t}E_x^{in} + \tfrac{1}{2}(e^{iB\cos\omega_2 t}-1)E_y^{in}e^{i\Delta\phi_{in}} \quad \{A.4\}$$

and

$$A_y^{out} = E_y^{out}e^{i\phi_y^{out}} = \tfrac{1}{2}(e^{iB\cos\omega_2 t}-1)e^{iA\cos\omega_1 t}E_x^{in} + \tfrac{1}{2}(e^{iB\cos\omega_2 t}+1)E_y^{in}e^{i\Delta\phi_{in}} \quad \{A.5\}$$

In order to calculate the degree of polarisation of the output radiation, its Stokes parameters need to be calculated. These are given by

$$\begin{aligned} S_0 &= \left\langle (E_x^{out})^2 \right\rangle + \left\langle (E_y^{out})^2 \right\rangle \\ S_1 &= \left\langle (E_x^{out})^2 \right\rangle - \left\langle (E_y^{out})^2 \right\rangle \\ S_2 &= \left\langle 2E_x^{out} E_y^{out} \cos(\Delta\phi_{out}) \right\rangle \\ S_3 &= \left\langle 2E_x^{out} E_y^{out} \sin(\Delta\phi_{out}) \right\rangle \\ \Delta\phi_{out} &= (\phi_y^{out} - \phi_x^{out}) \end{aligned} \qquad \{A.6\}$$

with the corresponding percentage degree of polarisation is given by

$$D = 100 \cdot \frac{\sqrt{S_1^2 + S_2^2 + S_3^2}}{S_0} \qquad \{A.7\}$$

Firstly, the quantities $(E_x^{out})^2$ and $(E_y^{out})^2$ will be calculated, in order to determine the first two Stokes parameters. Each may be found as the product of the corresponding complex amplitude and its complex conjugate.

$$(E_x^{out})^2 = A_x^{out} A_x^{out^*} = \frac{1}{4} \cdot \left((e^{iB\cos\omega_2 t} + 1) e^{iA\cos\omega_1 t} E_x^{in} + (e^{iB\cos\omega_2 t} - 1) E_y^{in} e^{i\Delta\phi_{in}} \right) \cdot \left((e^{-iB\cos\omega_2 t} + 1) e^{-iA\cos\omega_1 t} E_x^{in} + (e^{-iB\cos\omega_2 t} - 1) E_y^{in} e^{i\Delta\phi_{in}} \right)$$

$$\begin{aligned} &= \tfrac{1}{4}(e^{iB\cos\omega_2 t} + 1)(e^{-iB\cos\omega_2 t} + 1)(E_x^{in})^2 \\ &\quad + \tfrac{1}{4}(e^{iB\cos\omega_2 t} - 1)(e^{-iB\cos\omega_2 t} - 1)(E_y^{in})^2 \\ &\quad + \tfrac{1}{4}(e^{iB\cos\omega_2 t} + 1) e^{iA\cos\omega_1 t} E_x^{in} (e^{-iB\cos\omega_2 t} - 1) E_y^{in} e^{i\Delta\phi_{in}} \\ &\quad + \tfrac{1}{4}(e^{-iB\cos\omega_2 t} + 1) e^{-iA\cos\omega_1 t} E_x^{in} (e^{iB\cos\omega_2 t} - 1) E_y^{in} e^{i\Delta\phi_{in}} \end{aligned}$$

$$\begin{aligned} &= \tfrac{1}{2}\left((E_x^{in})^2 + (E_y^{in})^2\right) + \tfrac{1}{2}\left((E_x^{in})^2 - (E_y^{in})^2\right)\cos(B\cos\omega_2 t) \\ &\quad - \tfrac{1}{2} i \sin(B\cos\omega_2 t) e^{iA\cos\omega_1 t} E_x^{in} E_y^{in} e^{i\Delta\phi_{in}} \\ &\quad + \tfrac{1}{2} i \sin(B\cos\omega_2 t) e^{-iA\cos\omega_1 t} E_x^{in} E_y^{in} e^{i\Delta\phi_{in}} \end{aligned}$$

$$\begin{aligned} &= \tfrac{1}{2}\left((E_x^{in})^2 + (E_y^{in})^2\right) + \tfrac{1}{2}\left((E_x^{in})^2 - (E_y^{in})^2\right)\cos(B\cos\omega_2 t) \\ &\quad - \tfrac{1}{2} i E_x^{in} E_y^{in} \sin(B\cos\omega_2 t)\left(e^{i(A\cos\omega_1 t - \Delta\phi_{in})} - e^{-i(A\cos\omega_1 t - \Delta\phi_{in})}\right) \end{aligned}$$

$$= \tfrac{1}{2}\left((E_x^{in})^2 + (E_y^{in})^2\right) + \tfrac{1}{2}\left((E_x^{in})^2 - (E_y^{in})^2\right)\cos(B\cos\omega_2 t) - \tfrac{1}{2} i E_x^{in} E_y^{in} \sin(B\cos\omega_2 t) 2i \sin(A\cos\omega_1 t - \Delta\phi_{in})$$

$$= \tfrac{1}{2}\left((E_x^{in})^2 + (E_y^{in})^2\right) + \tfrac{1}{2}\left((E_x^{in})^2 - (E_y^{in})^2\right)\cos(B\cos\omega_2 t) + E_x^{in} E_y^{in} \sin(B\cos\omega_2 t)\sin(A\cos\omega_1 t - \Delta\phi_{in})$$

So, for x and similarly for y

$$(E_x^{out})^2 = \tfrac{1}{2}\left((E_x^{in})^2 + (E_y^{in})^2\right) + \tfrac{1}{2}\left((E_x^{in})^2 - (E_y^{in})^2\right)\cos(B\cos\omega_2 t) + E_x^{in} E_y^{in} \sin(B\cos\omega_2 t)\sin(A\cos\omega_1 t - \Delta\phi_{in}) \quad \{A.8\}$$

$$(E_y^{out})^2 = \tfrac{1}{2}\left((E_x^{in})^2 + (E_y^{in})^2\right) - \tfrac{1}{2}\left((E_x^{in})^2 - (E_y^{in})^2\right)\cos(B\cos\omega_2 t) - E_x^{in} E_y^{in} \sin(B\cos\omega_2 t)\sin(A\cos\omega_1 t - \Delta\phi_{in}) \quad \{A.9\}$$

Using these two equations, expressions for S_0 and S_1 may be obtained.

$$S_0 = \left\langle (E_x^{out})^2 \right\rangle + \left\langle (E_y^{out})^2 \right\rangle = (E_x^{in})^2 + (E_y^{in})^2 \quad \{A.10\}$$

$$S_1 = \left((E_x^{in})^2 - (E_y^{in})^2\right)\left\langle \cos(B\cos\omega_2 t)\right\rangle + 2E_x^{in}E_y^{in}\left\langle \sin(B\cos\omega_2 t)\sin(A\cos\omega_1 t - \Delta\phi_{in})\right\rangle \quad \{A.11\}$$

To find S_2, an expression for $2E_x^{out}E_y^{out}\cos(\Delta\phi_{out})$ must be found. This may be rewritten as

$$2E_x^{out}E_y^{out}\cos(\Delta\phi_{out}) = 2E_x^{out}E_y^{out}\left(\cos(\phi_y^{out})\cos(\phi_x^{out}) + \sin(\phi_y^{out})\sin(\phi_x^{out})\right) = 2\left(\mathrm{Re}(A_y^{out})\mathrm{Re}(A_x^{out}) + \mathrm{Im}(A_y^{out})\mathrm{Im}(A_x^{out})\right) \quad \{A.12\}$$

Now, the real and imaginary parts of the output polarisation states may be calculated.

The real part of the complex amplitude along the *x* axis is

$$\begin{aligned}\mathrm{Re}(A_x^{out}) &= \tfrac{1}{2}(A_x^{out} + A_x^{out^*}) = \tfrac{1}{4}\left[(e^{iB\cos\omega_2 t}+1)e^{iA\cos\omega_1 t}E_x^{in} + (e^{iB\cos\omega_2 t}-1)E_y^{in}e^{i\Delta\phi_{in}}\right.\\ &\quad \left. + (e^{-iB\cos\omega_2 t}+1)e^{-iA\cos\omega_1 t}E_x^{in} + (e^{-iB\cos\omega_2 t}-1)E_y^{in}e^{-i\Delta\phi_{in}}\right]\\ &= \tfrac{1}{4}\left[E_x^{in}(e^{i(B\cos\omega_2 t + A\cos\omega_1 t)} + e^{-i(B\cos\omega_2 t + A\cos\omega_1 t)}) + E_x^{in}(e^{iA\cos\omega_1 t} + e^{-iA\cos\omega_1 t})\right.\\ &\quad \left. + E_y^{in}(e^{i(B\cos\omega_2 t + \Delta\phi_{in})} + e^{-i(B\cos\omega_2 t + \Delta\phi_{in})}) - E_y^{in}(e^{i\Delta\phi_{in}} + e^{-i\Delta\phi_{in}})\right]\\ &= \tfrac{1}{2}\left[E_x^{in}\cos(B\cos\omega_2 t + A\cos\omega_1 t) + E_y^{in}\cos(B\cos\omega_2 t + \Delta\phi_{in})\right.\\ &\quad \left. + \left(E_x^{in}\cos(A\cos\omega_1 t) - E_y^{in}\cos(\Delta\phi_{in})\right)\right]\end{aligned} \quad \{A.13\}$$

Similarly along the *y* axis

$$\begin{aligned}\mathrm{Re}(A_y^{out}) &= \tfrac{1}{2}\left[E_x^{in}\cos(B\cos\omega_2 t + A\cos\omega_1 t) + E_y^{in}\cos(B\cos\omega_2 t + \Delta\phi_{in})\right.\\ &\quad \left. - \left(E_x^{in}\cos(A\cos\omega_1 t) - E_y^{in}\cos(\Delta\phi_{in})\right)\right]\end{aligned} \quad \{A.14\}$$

The imaginary part of the complex amplitude along the *x* axis is

$$\begin{aligned}\mathrm{Im}(A_x^{out}) &= \tfrac{1}{2i}(A_x^{out} - A_x^{out^*}) = \tfrac{1}{4i}\left[(e^{iB\cos\omega_2 t}+1)e^{iA\cos\omega_1 t}E_x^{in} + (e^{iB\cos\omega_2 t}-1)E_y^{in}e^{i\Delta\phi_{in}}\right.\\ &\quad \left. - (e^{-iB\cos\omega_2 t}+1)e^{-iA\cos\omega_1 t}E_x^{in} - (e^{-iB\cos\omega_2 t}-1)E_y^{in}e^{-i\Delta\phi_{in}}\right]\\ &= \tfrac{1}{4i}\left[E_x^{in}(e^{i(B\cos\omega_2 t + A\cos\omega_1 t)} - e^{-i(B\cos\omega_2 t + A\cos\omega_1 t)}) + E_x^{in}(e^{iA\cos\omega_1 t} - e^{-iA\cos\omega_1 t})\right.\\ &\quad \left. + E_y^{in}(e^{i(B\cos\omega_2 t + \Delta\phi_{in})} - e^{-i(B\cos\omega_2 t + \Delta\phi_{in})}) - E_y^{in}(e^{i\Delta\phi_{in}} - e^{-i\Delta\phi_{in}})\right]\\ &= \tfrac{1}{2}\left[E_x^{in}\sin(B\cos\omega_2 t + A\cos\omega_1 t) + E_y^{in}\sin(B\cos\omega_2 t + \Delta\phi_{in})\right.\\ &\quad \left. + \left(E_x^{in}\sin(A\cos\omega_1 t) - E_y^{in}\sin(\Delta\phi_{in})\right)\right]\end{aligned} \quad \{A.15\}$$

and similarly along *y*

$$\begin{aligned}\mathrm{Im}(A_y^{out}) &= \tfrac{1}{2}\left[E_x^{in}\sin(B\cos\omega_2 t + A\cos\omega_1 t) + E_y^{in}\sin(B\cos\omega_2 t + \Delta\phi_{in})\right.\\ &\quad \left. - \left(E_x^{in}\sin(A\cos\omega_1 t) - E_y^{in}\sin(\Delta\phi_{in})\right)\right]\end{aligned} \quad \{A.16\}$$

So, from Equation {A.12}

$$
\begin{aligned}
2E_x^{out}E_y^{out}\cos(\Delta\phi_{out}) &= 2\left(\mathrm{Re}(A_y^{out})\mathrm{Re}(A_x^{out})+\mathrm{Im}(A_y^{out})\mathrm{Im}(A_x^{out})\right)\\
&= \tfrac{1}{2}\left(E_x^{in}\cos(B\cos\omega_2 t + A\cos\omega_1 t) + E_y^{in}\cos(B\cos\omega_2 t+\Delta\phi_{in})\right)^2\\
&\quad + \tfrac{1}{2}\left(E_x^{in}\sin(B\cos\omega_2 t + A\cos\omega_1 t) + E_y^{in}\sin(B\cos\omega_2 t+\Delta\phi_{in})\right)^2\\
&\quad - \tfrac{1}{2}\left(E_x^{in}\cos(A\cos\omega_1 t) - E_y^{in}\cos(\Delta\phi_{in})\right)^2\\
&\quad - \tfrac{1}{2}\left(E_x^{in}\sin(A\cos\omega_1 t) - E_y^{in}\sin(\Delta\phi_{in})\right)^2\\
&= \tfrac{1}{2}(E_x^{in})^2\cos^2(B\cos\omega_2 t + A\cos\omega_1 t) + \tfrac{1}{2}(E_y^{in})^2\cos^2(B\cos\omega_2 t+\Delta\phi_{in})\\
&\quad + \tfrac{1}{2}(E_x^{in})^2\sin^2(B\cos\omega_2 t + A\cos\omega_1 t)) + \tfrac{1}{2}(E_y^{in})^2\sin^2(B\cos\omega_2 t+\Delta\phi_{in})\\
&\quad - \tfrac{1}{2}(E_x^{in})^2\cos^2(A\cos\omega_1 t) - \tfrac{1}{2}(E_y^{in})^2\cos^2(\Delta\phi_{in})\\
&\quad - \tfrac{1}{2}(E_x^{in})^2\sin^2(A\cos\omega_1 t) - \tfrac{1}{2}(E_y^{in})^2\sin^2(\Delta\phi_{in})\\
&\quad + E_x^{in}E_y^{in}\cos(B\cos\omega_2 t + A\cos\omega_1 t)\cos(B\cos\omega_2 t+\Delta\phi_{in})\\
&\quad + E_x^{in}E_y^{in}\sin(B\cos\omega_2 t + A\cos\omega_1 t)\sin(B\cos\omega_2 t+\Delta\phi_{in})\\
&\quad + E_x^{in}E_y^{in}\cos(A\cos\omega_1 t)\cos(\Delta\phi_{in})\\
&\quad + E_x^{in}E_y^{in}\sin(A\cos\omega_1 t)\sin(\Delta\phi_{in})
\end{aligned}
$$

$$
\begin{aligned}
2E_x^{out}E_y^{out}\cos(\Delta\phi_{out}) &= E_x^{in}E_y^{in}[\cos(B\cos\omega_2 t + A\cos\omega_1 t)\cos(B\cos\omega_2 t+\Delta\phi_{in})\\
&\quad + \sin(B\cos\omega_2 t + A\cos\omega_1 t)\sin(B\cos\omega_2 t+\Delta\phi_{in})]\\
&\quad + E_x^{in}E_y^{in}[\cos(A\cos\omega_1 t)\cos(\Delta\phi_{in}) + \sin(A\cos\omega_1 t)\sin(\Delta\phi_{in})]\\
&= E_x^{in}E_y^{in}\cos(A\cos\omega_1 t - \Delta\phi_{in}) + E_x^{in}E_y^{in}\cos(A\cos\omega_1 t - \Delta\phi_{in})
\end{aligned}
$$

and therefore S_2 is given by

$$
S_2 = \left\langle 2E_x^{out}E_y^{out}\cos(\Delta\phi_{out})\right\rangle = 2E_x^{in}E_y^{in}\left\langle\cos(A\cos\omega_1 t - \Delta\phi_{in})\right\rangle \qquad \{\mathbf{A.17}\}
$$

In a similar way to Equation {A.12}, S_3 is found from

$$
\begin{aligned}
S_3 &= \left\langle 2E_x^{out}E_y^{out}\sin(\Delta\phi_{out})\right\rangle = \left\langle 2E_x^{out}E_y^{out}\left(\sin(\phi_y^{out})\cos(\phi_x^{out}) - \cos(\phi_y^{out})\sin(\phi_x^{out})\right)\right\rangle\\
&= \left\langle 2\left(\mathrm{Im}(A_y^{out})\mathrm{Re}(A_x^{out}) + \mathrm{Re}(A_y^{out})\mathrm{Im}(A_x^{out})\right)\right\rangle
\end{aligned} \qquad \{\mathbf{A.18}\}
$$

This equation does not simplify as readily as that for S_2 so it will be left in this format and coupled with the expressions for the real and imaginary parts calculated previously as

$$\mathrm{Re}(A_x^{out}) = \tfrac{1}{2}E_x^{in}\cos(B\cos\omega_2 t + A\cos\omega_1 t) + \tfrac{1}{2}E_y^{in}\cos(B\cos\omega_2 t + \Delta\phi_{in}) + \tfrac{1}{2}\left(E_x^{in}\cos(A\cos\omega_1 t) - E_y^{in}\cos(\Delta\phi_{in})\right)$$

$$\mathrm{Im}(A_x^{out}) = \tfrac{1}{2}E_x^{in}\sin(B\cos\omega_2 t + A\cos\omega_1 t) + \tfrac{1}{2}E_y\sin(B\cos\omega_2 t + \Delta\phi_{in}) + \tfrac{1}{2}\left(E_x^{in}\sin(A\cos\omega_1 t) - E_y^{in}\sin(\Delta\phi_{in})\right)$$

{A.19}

$$\mathrm{Re}(A_y^{out}) = \tfrac{1}{2}E_x^{in}\cos(B\cos\omega_2 t + A\cos\omega_1 t) + \tfrac{1}{2}E_y^{in}\cos(B\cos\omega_2 t + \Delta\phi_{in}) - \tfrac{1}{2}\left(E_x^{in}\cos(A\cos\omega_1 t) - E_y^{in}\cos(\Delta\phi_{in})\right)$$

$$\mathrm{Im}(A_y^{out}) = \tfrac{1}{2}E_x^{in}\sin(B\cos\omega_2 t + A\cos\omega_1 t) + \tfrac{1}{2}E_y^{in}\sin(B\cos\omega_2 t + \Delta\phi_{in}) - \tfrac{1}{2}\left(E_x^{in}\sin(A\cos\omega_1 t) - E_y^{in}\sin(\Delta\phi_{in})\right)$$

Equations {A.10}, {A.11}, {A.17}, {A.18} and {A.19} are used in §3.8.1 to calculate the optimum values of the parameters A, B, ω_1 and ω_2 to achieve good scrambling.

Appendix B Sagnac Loop Mirror

A Sagnac loop mirror is formed by simply joining the two output ports of a 2×2 fibre coupler (Figure B.1), with the reflectivity depending on the split ratio of the coupler.

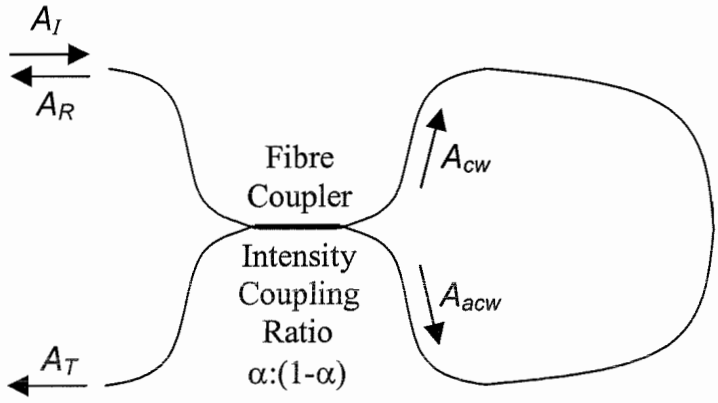

Figure B.1 Sagnac Loop Mirror Reflector. The reflectivity depends upon the coupling ratio, α, and ignoring any loss and any nonlinear or birefringent effects within the loop, $R = 4\alpha(1-\alpha)$.

The reflectivity of the Sagnac loop may be calculated by considering complex amplitudes. In Figure B.1, A_I, A_R and A_T are the complex amplitudes of the incident, reflected and transmitted waves respectively. On passing through the coupler, the clockwise (cw) propagating wave exhibits no phase change, however the anti-clockwise (acw) propagating wave, which has been coupled across, exhibits a $\pi/2$ phase change, due to the nature of the coupling. The cw and acw waves then each propagate around the loop and back to the coupler, where the cross-coupled wave again undergoes a $\pi/2$ phase change. Interference between coupled beams then causes reflected and transmitted waves of intensity dependent on the coupling ratio, α.

In the absence of nonlinear effects, the phase changes due to propagation will be identical for both arms and the reflectivity of the loop may be calculated by considering only the phase and amplitude changes due to the coupler.

The clockwise and anticlockwise complex amplitudes are therefore given by

$$A_{cw} = \sqrt{(1-\alpha)} \cdot A_I \quad , \qquad A_{acw} = e^{i\frac{\pi}{2}} \cdot \sqrt{\alpha} \cdot A_I = i\sqrt{\alpha} \cdot A_I \qquad \{\mathbf{B.1}\}$$

When the waves pass back through the coupler, the complex amplitudes of the transmitted and reflected waves therefore become

$$\begin{aligned} A_T &= \sqrt{(1-\alpha)} \cdot \sqrt{(1-\alpha)} \cdot A_I + i\sqrt{\alpha} \cdot i\sqrt{\alpha} \cdot A_I = (1-2\alpha)A_I \\ A_R &= i\sqrt{\alpha} \cdot \sqrt{(1-\alpha)} \cdot A_I + \sqrt{(1-\alpha)} \cdot i\sqrt{\alpha} \cdot A_I = 2i\sqrt{\alpha} \cdot \sqrt{(1-\alpha)} \cdot A_I \end{aligned} \qquad \{\mathbf{B.2}\}$$

and so the intensity transmittance, T, and reflectance, R, may be expressed as

$$\begin{aligned} T &= \frac{|A_T|^2}{|A_I|^2} = (1-2\alpha)^2 \\ R &= \frac{|A_R|^2}{|A_I|^2} = 4\alpha \cdot (1-\alpha) \end{aligned} \qquad \{\mathbf{B.3}\}$$

It can be seen that for a coupling ratio $\alpha = 0.5$, the mirror is theoretically 100% reflecting. As was noted previously, nonlinear effects have been ignored, however, for very unbalanced couplers, a high intensity may propagate in one direction round the loop and a small intensity in the other. This may result in nonlinear refractive index changes and departure from the formulae calculated above. Any attenuation within the loop has also been ignored, for simplicity. Since none of the previous discussion is wavelength dependent, the mirror is obviously broad-band, limited only by the bandwidth of the coupler itself.

Appendix C Full Theoretical Noise Breakdowns

This appendix is a collection of graphs of all components which contribute to the total theoretical noise, for the six sensors discussed in Chapter Four.

Where more than one noise component has the same or very similar magnitude, the symbols representing the conflicting components are alternated along the length of the trace, for clarity.

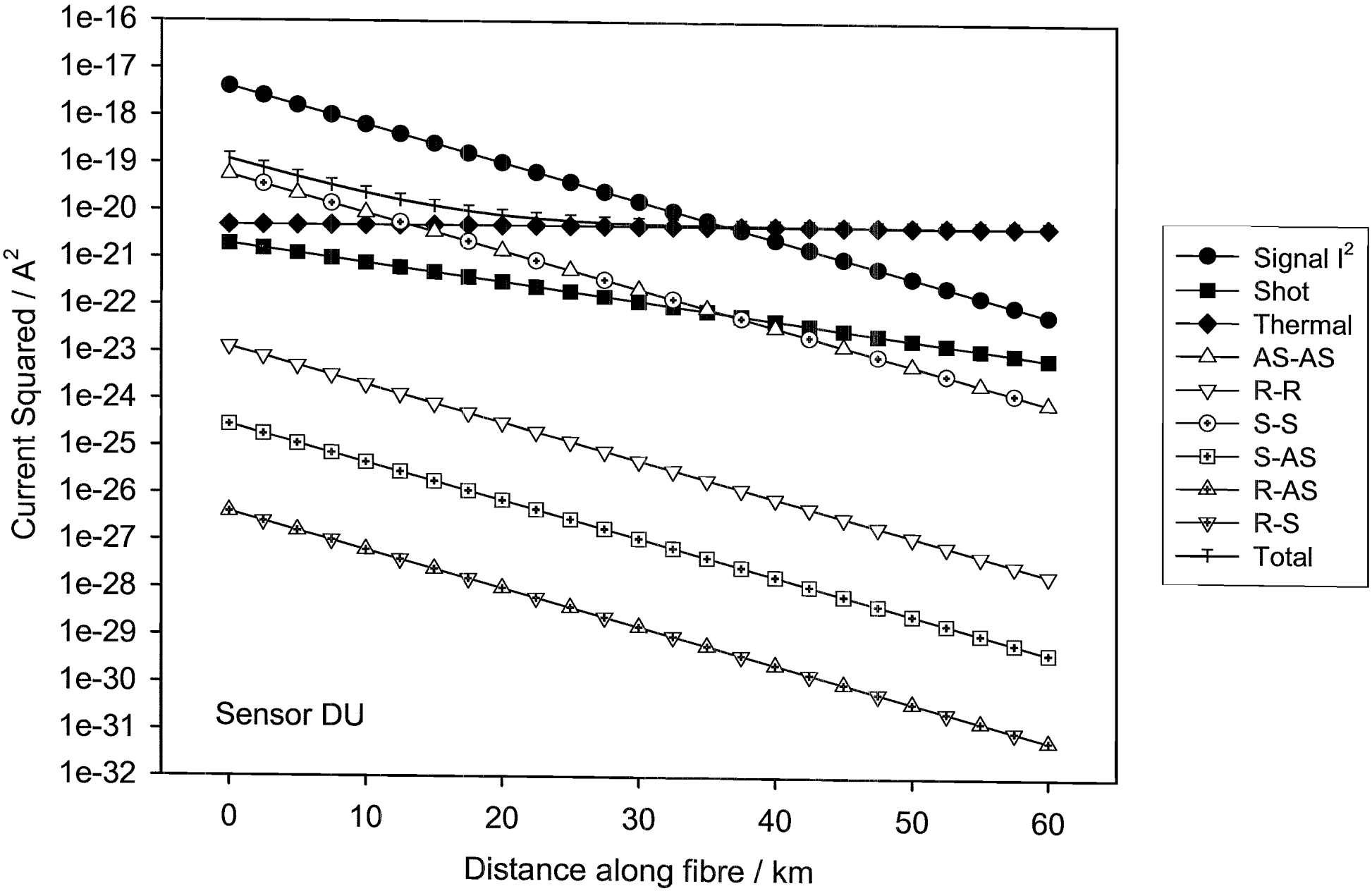
1e-16
1e-17
1e-18
1e-19
1e-20
1e-21
1e-22
1e-23
1e-24
1e-25
1e-26
1e-27
1e-28
1e-29
1e-30
1e-31
1e-32
Current Squared / A2
0
10
20
30
40
50
60
Distance along fibre / km
Sensor DU
Signal I2
Shot
Thermal
AS-AS
R-R
S-S
S-AS
R-AS
R-S
Total

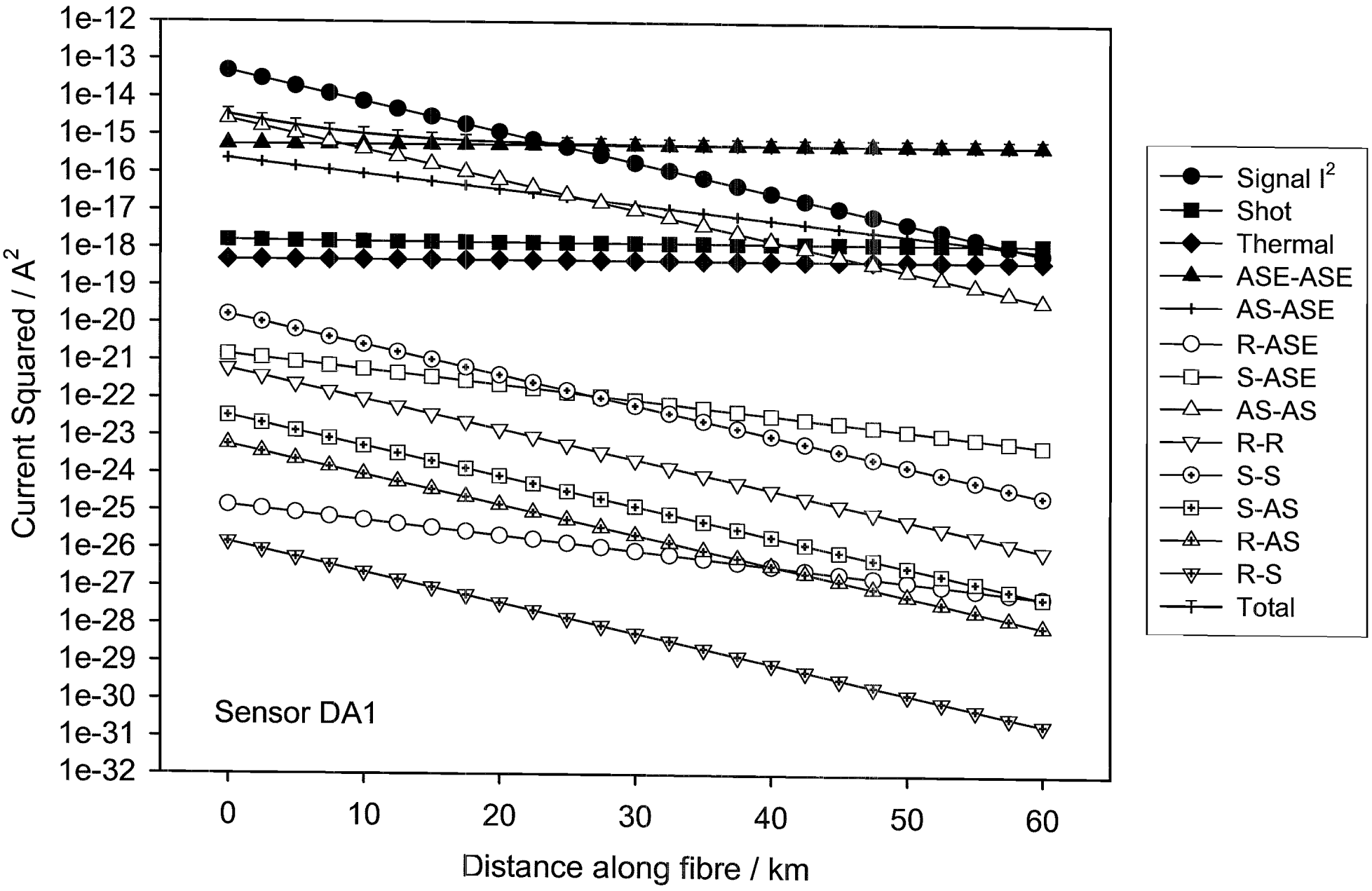
1e-12
1e-13
1e-14
1e-15
1e-16
1e-17
1e-18
1e-19
1e-20
1e-21
1e-22
1e-23
1e-24
1e-25
1e-26
1e-27
1e-28
1e-29
1e-30
1e-31
1e-32
Current Squared / A2
0
10
20
30
40
50
60
Distance along fibre / km
Sensor DA1
Signal I2
Shot
Thermal
ASE-ASE
AS-ASE
R-ASE
S-ASE
AS-AS
R-R
S-S
S-AS
R-AS
R-S
Total

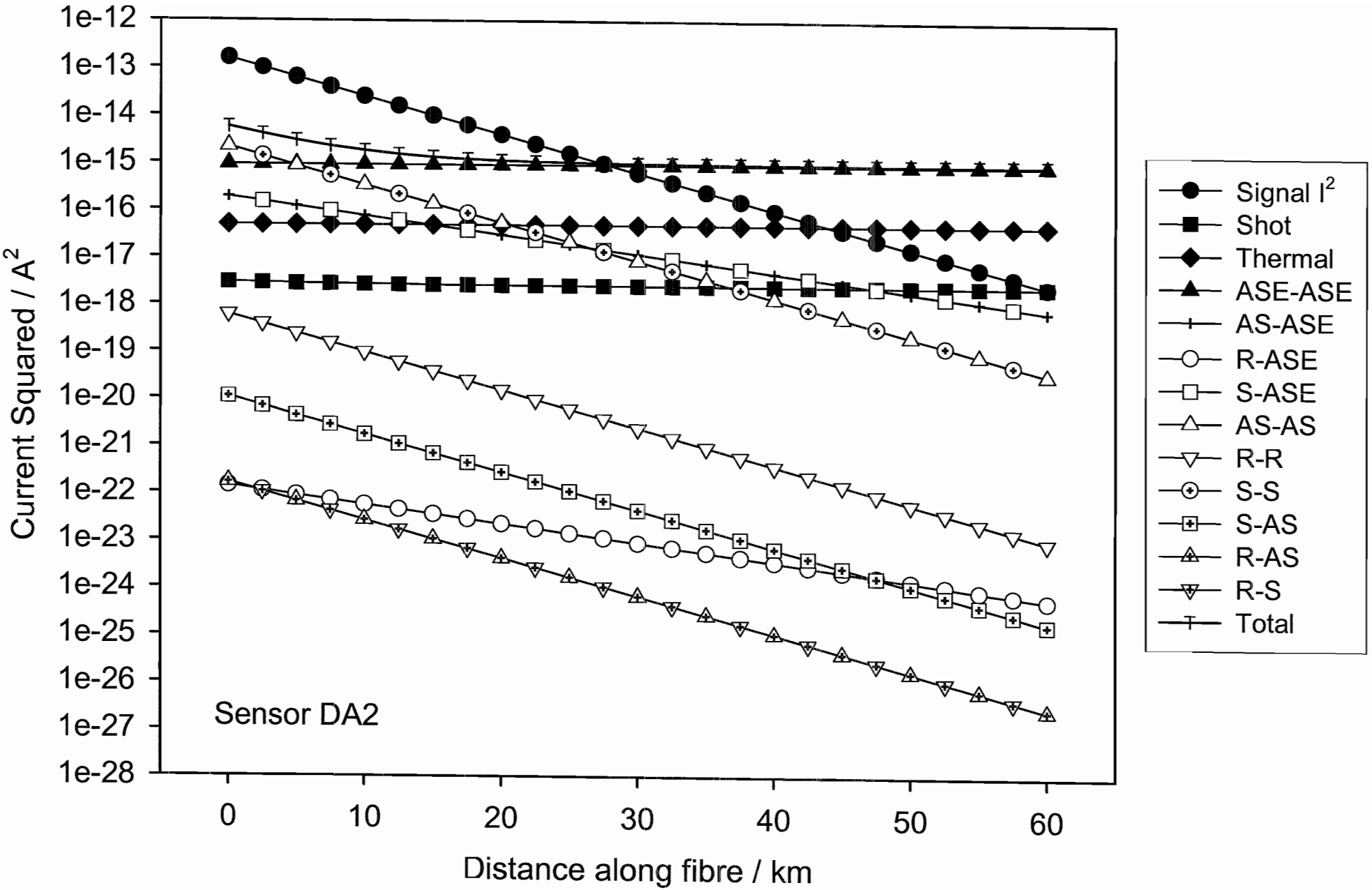
1e-12
1e-13
1e-14
1e-15
1e-16
1e-17
1e-18
1e-19
1e-20
1e-21
1e-22
1e-23
1e-24
1e-25
1e-26
1e-27
1e-28
Current Squared / A2
0
10
20
30
40
50
60
Distance along fibre / km
Sensor DA2
Signal I2
Shot
Thermal
ASE-ASE
AS-ASE
R-ASE
S-ASE
AS-AS
R-R
S-S
S-AS
R-AS
R-S
Total

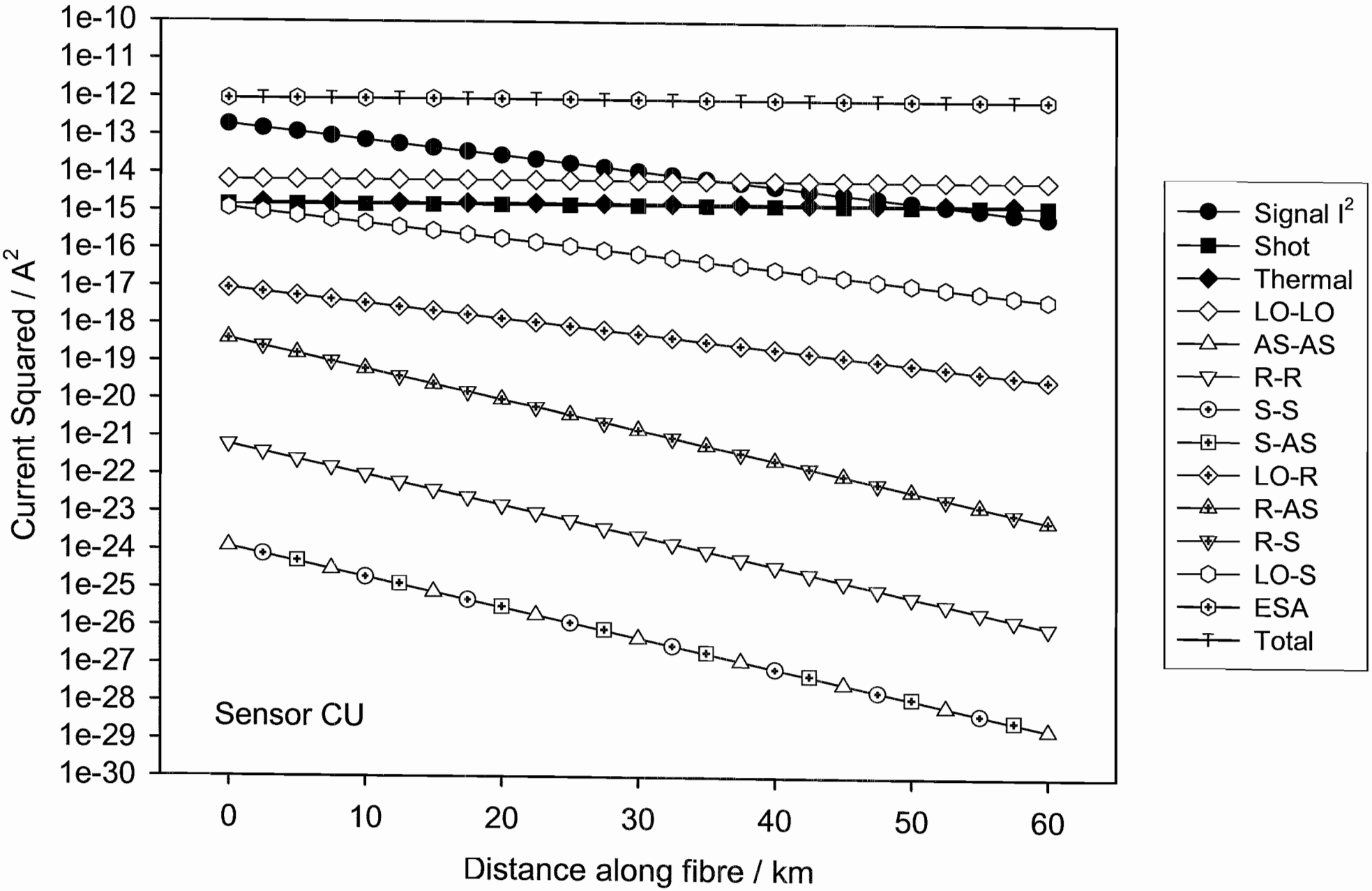
1e-10
1e-11
1e-12
1e-13
1e-14
1e-15
1e-16
1e-17
1e-18
1e-19
1e-20
1e-21
1e-22
1e-23
1e-24
1e-25
1e-26
1e-27
1e-28
1e-29
1e-30
Current Squared / A2
Sensor CU
0
10
20
30
40
50
60
Distance along fibre / km
Signal I2
Shot
Thermal
LO-LO
AS-AS
R-R
S-S
S-AS
LO-R
R-AS
R-S
LO-S
ESA
Total

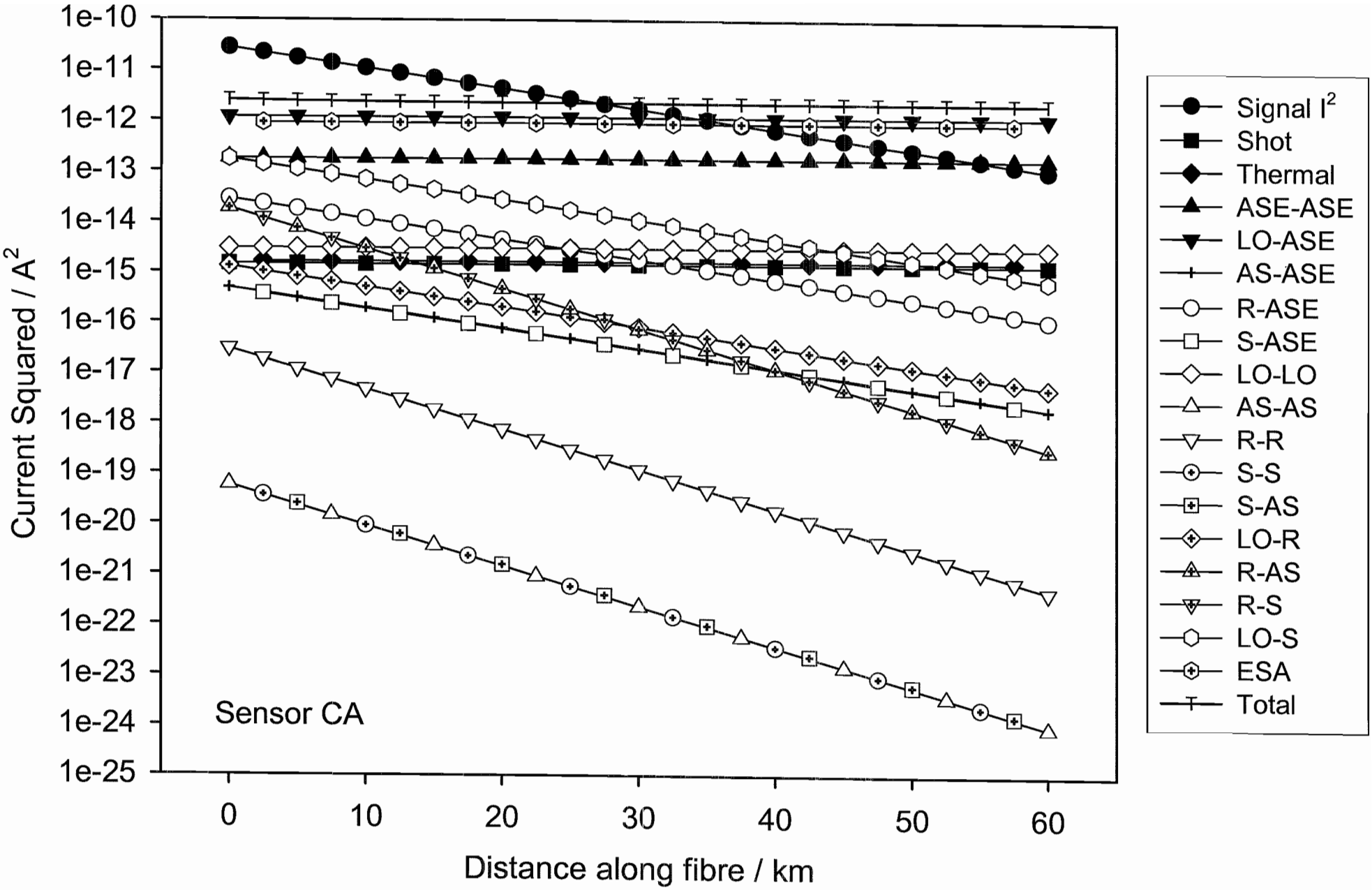
Current Squared / A^2
1e-10
1e-11
1e-12
1e-13
1e-14
1e-15
1e-16
1e-17
1e-18
1e-19
1e-20
1e-21
1e-22
1e-23
1e-24
1e-25
0
10
20
30
40
50
60
Distance along fibre / km
Sensor CA
Signal I^2
Shot
Thermal
ASE-ASE
LO-ASE
AS-ASE
R-ASE
S-ASE
LO-LO
AS-AS
R-R
S-S
S-AS
LO-R
R-AS
R-S
LO-S
ESA
Total

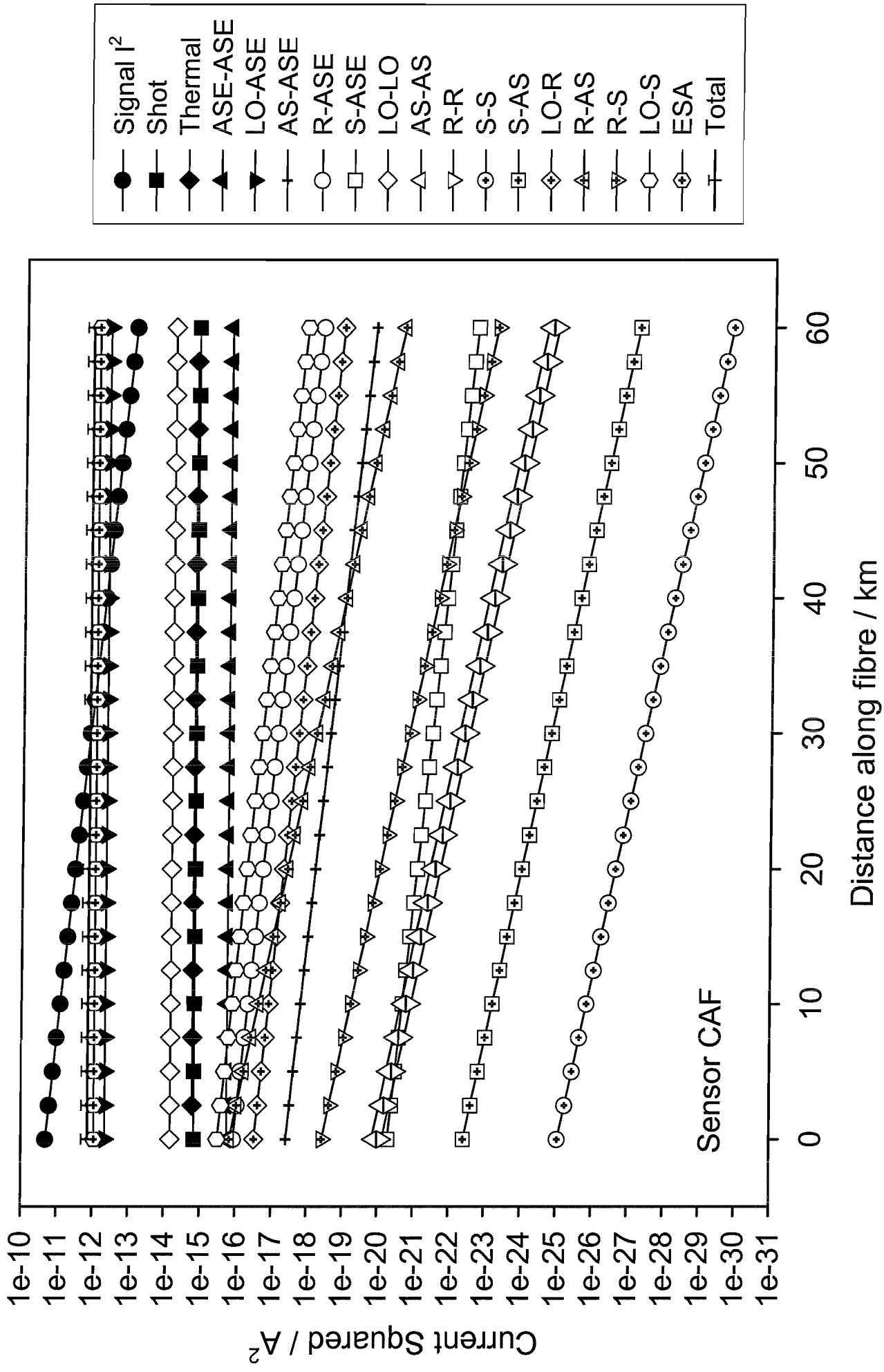
Signal I²
Shot
Thermal
ASE-ASE
LO-ASE
AS-ASE
R-ASE
S-ASE
LO-LO
AS-AS
R-R
S-S
S-AS
LO-R
R-AS
R-S
LO-S
ESA
Total
Sensor CAF
Current Squared / A²
Distance along fibre / km
1e-10
1e-11
1e-12
1e-13
1e-14
1e-15
1e-16
1e-17
1e-18
1e-19
1e-20
1e-21
1e-22
1e-23
1e-24
1e-25
1e-26
1e-27
1e-28
1e-29
1e-30
1e-31
0
10
20
30
40
50
60

List of Publications

1) S.M.Maughan, H.H.Kee and T.P.Newson: "Novel Distributed Fibre Sensor Using Microwave Heterodyne Detection of Spontaneous Brillouin Backscatter", *14th International Conference on Optical Fibre Sensors (OFS2000)*, pp. 780-783 (Venice, October 2000)

2) S.M.Maughan, H.H.Kee and T.P.Newson: "57-km single-ended spontaneous Brillouin-based distributed fiber temperature sensor using microwave coherent detection", *Optics Letters*, Vol. 26, No. 6, pp. 331-333 (March 2001)

3) S.M.Maughan, H.H.Kee and T.P.Newson: "A Calibrated 27-km Distributed Fiber Temperature Sensor Based on Microwave Heterodyne Detection of Spontaneous Brillouin Backscattered Power", *Photonics Technology Letters*, Vol. 13, No. 5, pp. 511-513 (May 2001)

4) S.M.Maughan, H.H.Kee and T.P.Newson: "Simultaneous distributed fibre temperature and strain sensor using microwave coherent detection of spontaneous Brillouin backscatter", *Measurement Science and Technology*, Vol. 12, No. 7, pp. 834-842 (July 2001)

Featured in:

- Opto and Laser Europe, Issue 84, p. 21 (May 2001)